

# **Dynamic Two-Phase Flow in Porous Media and its Implications in Geological Carbon Sequestration**

---

by

**Luqman K. Abidoye**

Thesis

Submitted in partial fulfilment of the requirements

for the award of

Doctor of Philosophy (PhD) degree of Loughborough University

**November 2014**

© by **Luqman K. Abidoye**

## DEDICATION

This thesis is dedicated to my late father,

***Alhaji Yunusa Abidoye***

## ABSTRACT

Two-phase flow in porous media is an important subsurface process that has significant impacts on the global economy and environments. To study two-phase system in porous media, capillary pressure ( $P^c$ ), relative permeability ( $K_r$ ), bulk electrical conductivity ( $\sigma_b$ ) and bulk relative permittivity ( $\epsilon_b$ ) are often employed as characterization parameters. Interestingly, all of these parameters are functions of water saturation ( $S$ ). However, the non-uniqueness in the  $P^c$ - $S$ ,  $K_r$ - $S$ ,  $\sigma_b$ - $S$  and  $\epsilon_b$ - $S$  relationships pose considerable challenges in employing them for effective monitoring and control of the two-phase flow processes. In this work, laboratory scale experiments and numerical simulations were conducted to investigate the factors and conditions contributing to the non-uniqueness in the above relationships for silicone oil-water and supercritical  $\text{CO}_2$ -water flow in porous media, with a special emphasis on geological carbon sequestration.

Specifically, the dynamic capillary pressure effect, which indicates the dependence of the  $P^c$ - $S$  relationship on the rate of change of saturation ( $\partial S/\partial t$ ) during two-phase flow in porous media was investigated. Using a silicone oil-water system, the dynamic capillary pressure effect was quantified in term of the parameter named the dynamic coefficient,  $\tau$ , and it was found to be dependent on the domain scale and the viscosity ratio of the two fluids. It was found that  $\tau$  increases with the domain scale and the viscosity ratio. It is inversely affected by  $\partial S/\partial t$ , which is related to the degree of resistance to the fluid motion, namely, viscosity. In almost all cases,  $\tau$  was found to decrease monotonically with an increase in water saturation,  $S$ . An order increase in magnitude of  $\tau$  was observed as the domain scale increases from 4cm scale to 8cm in height. A similar order of increase in  $\tau$  was observed in the 12cm high domain scale. There is an order increase in the value of  $\tau$  for the silicone oil-water system as the viscosity ratio increases from 200 to 500. For the supercritical  $\text{CO}_2$  ( $\text{scCO}_2$ ) and water system in porous media, the experiments and numerical simulations showed that  $\tau$  increases with rising system temperature and decreasing porous media permeability.

Dimensionless analysis of the silicone oil-water experimental results showed that by constructing non-dimensional groups of quantities expressing a relationship among different variables on which  $\tau$  depends, it is possible to summarise the experimental results and determine their functional relationship. A generalised scaling relationship for  $\tau$  was derived from the dimensionless analysis which was then validated against independent literature data. The exercise showed that the  $\tau$ - $S$  relationship obtained from the literature and the

scaling relationship match reasonably well. This work also demonstrated the applicability of an artificial neural network (ANN) as an alternative computational platform for the prediction of the domain scale dependence of  $\tau$ .

The dependence of the  $K_r$ - $S$  relationship on  $\partial S/\partial t$  was also investigated. The results showed that the  $K_r$ - $S$  curve under dynamic flow condition is different from that under the quasi-static condition.  $K_r$  for water ( $K_{rw}$ ) increases with increasing water saturation and decreases with the increase in viscosity ratio while  $K_r$  for silicone oil ( $K_{rnw}$ ) increases with decreasing water saturation as well as with the increase in viscosity ratio. Also,  $K_{rw}$  decreases while  $K_{rnw}$  increases with the increasing boundary pressure.

However, the  $\varepsilon_b$ - $S$  and  $\sigma_b$ - $S$  relationships were found to be independent of  $\partial S/\partial t$  for the scCO<sub>2</sub>-water system in carbonate and silicate porous media. Nevertheless, the  $\varepsilon_b$  and  $\sigma_b$  values decrease as the water saturation decreases in the two porous media samples. While  $\varepsilon_b$  decreases with increase in temperature in silica sand, the trend in the limestone showed a slight increase with temperature, especially at high water saturation. Also, the  $\varepsilon_b$ - $S$  relationship is shown to be affected by pressure in silica sand increasing with the pressure of the domain. On the contrary, the  $\sigma_b$ - $S$  relationship increases as the temperature increases with more significance at higher water saturation in the silica sand sample.

This work further demonstrated the application of a membrane in the monitoring of the CO<sub>2</sub> in geological sites used for carbon sequestration. Commercial silicone rubber coupled with a pressure transducer showed potential in the detection of CO<sub>2</sub> leakage from geological sites. The response of the device in terms of the mass of permeated gas, permeability and gas flux were investigated for both CO<sub>2</sub> and N<sub>2</sub>. In addition, the monitoring of potable water contamination in a shallow aquifer by the migrating or leaking of CO<sub>2</sub> is demonstrated with the combination of the pH analysis, geoelectrical measurement techniques and the membrane-sensor system.

Overall, the work in this PhD research demonstrated robust applications of two-phase systems' characterization parameters under different scenarios in the porous media. Implications of the findings in this work to the monitoring and control of two-phase systems in porous media are expatiated.

**Keywords:** Two-phase flow, Dynamic capillary pressure effect, Porous Media, Silicone Oil, Supercritical CO<sub>2</sub>, Geoelectrical Characterization, Bulk Electrical Conductivity, Bulk Relative permittivity, Silica Sand, Limestone, Silicone Rubber, Numerical Simulation

## ACKNOWLEDGEMENTS

All praises and adoration belong to Almighty Allah, The Most Merciful, The Most Compassionate. I thank Him for guidance and provisions for my PhD programme.

Many thanks to my sponsor, Petroleum Technology Development Fund (PTDF) for giving me the financial support to undertake the research. My appreciation goes to my supervisors-Dr Diganta Das and Prof. Chris Rielly. I appreciate the efforts of Dr Diganta Das for setting the ball rolling. I am very grateful for his thorough critique of my work and the provision of technical guidance in the course of various investigations. I also acknowledge the various inputs of the technicians led by Mr. Tony Eyre, whose experience was key to the successful operation of high-pressure experimental rig. This appreciation also extends to the staff of the Chemical Engineering department support office, especially Mrs Yasmin Kosar for her particularly filial disposition. Their quick and friendly responses to various requests served as encouragements. I acknowledge the contributions and collaborations of Kamal Khudaida and Gaurav Goel in this research work. Similarly, positive influences of my various intimate friends like Maina Wairagu, Faiz Mahdi, Mambo Abdulhameed, Abdulkadir Hussein Sheik and other research colleagues in the Department of Chemical Engineering, will remain indelible in my mind.

I beseech the forgiveness and blessings of Allah for my late Father. I beg Allah to put him in paradise. My appreciation goes to my Mum and siblings for being supportive of my endeavours at home and abroad.

Finally, I remain indebted to my wife and children, for their endurance and supports during my frequent overseas sojourns in the course of my PhD research.

## TABLE OF CONTENTS

<b>ABSTRACT</b>	<b>I</b>
<b>ACKNOWLEDGEMENTS</b>	<b>III</b>
<b>TABLE OF CONTENTS</b>	<b>IV</b>
<b>LIST OF FIGURES</b>	<b>IX</b>
<b>LIST OF TABLES</b>	<b>XV</b>
<b>NOMENCLATURE</b>	<b>XVI</b>
<b>PUBLICATIONS</b>	<b>XVIII</b>
<b>CHAPTER ONE</b>	<b>1</b>
<b>1. INTRODUCTION</b>	<b>1</b>
1.1 Background	1
1.2 Motivation for research	2
1.3 Research questions	3
1.4 Specific aims	4
1.5 Contributions to knowledge	4
1.6 Thesis structure	5
<b>CHAPTER TWO</b>	<b>8</b>
<b>2. GEOLOGICAL CARBON SEQUESTRATION IN THE CONTEXT OF TWO-PHASE FLOW IN POROUS MEDIA: A REVIEW*</b>	<b>8</b>
2.1 Introduction	8
2.2 Characteristics of the geological sites	12
2.2.1 Porosity and pore size distribution	13
2.2.2 Intrinsic, relative and effective permeability	15
2.2.3 Threshold pressure (bubbling pressure)	17
2.2.4 Wettability	18
2.3 <i>In situ</i> trapping mechanisms of injected CO <sub>2</sub>	20
2.3.1 Structural trapping	20
2.3.2 Residual trapping	21
2.3.3 Solubility trapping	22
2.3.4 Mineral trapping	24
2.4 Modelling and simulations of scCO <sub>2</sub> -brine-rock system	25
2.5 P <sup>c</sup> -S-K <sub>r</sub> relationships and phase characteristics in scCO <sub>2</sub> -brine system	28
2.5.1 Effects of viscosity and density ratios of CO <sub>2</sub> on P <sup>c</sup> -S-K <sub>r</sub> relationships	28
2.5.2 Instability in the displacement of fluid/fluid interface in scCO <sub>2</sub> -brine-porous media system	30
2.5.3 Influence of pressure, dissolution and wettability on P <sup>c</sup> -S-K <sub>r</sub>	33
2.5.4 P <sup>c</sup> -S-K <sub>r</sub> relationships in consolidated porous rocks	34
2.6 Leakage risks and monitoring	34
2.7 Summary	37
<b>CHAPTER THREE</b>	<b>41</b>

<b>3. SCALE DEPENDENT DYNAMIC CAPILLARY PRESSURE EFFECT FOR TWO-PHASE FLOW IN POROUS MEDIA IN RELATION TO FLUID VISCOSITY RATIO*</b>	<b>41</b>
<b>3.1 Introduction</b>	<b>41</b>
<b>3.2 Materials and methods</b>	<b>47</b>
3.2.1 Porous medium, domain size and fluid property	47
3.2.2 Experimental methods	47
3.2.3 Dynamic and equilibrium experiments on two-phase flow	49
3.2.4 Calculation of dynamic coefficient ( $\tau$ )	51
3.2.5 Averaging approach	52
<b>3.3 Results and discussions</b>	<b>53</b>
3.3.1 $P^c$ -S and $\partial S/\partial t$ – S relationships for different fluid viscosity ratios	55
3.3.1.1 $P^c$ -S relationships	55
3.3.1.2 $\partial S/\partial t$ -S relationships: Influences of fluid properties and porous domain characteristics	56
3.3.2 Scale Dependency of $\tau$ -S relationships for Different Fluid Viscosity Ratios	58
3.3.3 Influence of the similar pressure gradient on domain scale dependence of $\tau$ -S	67
3.3.4 $\tau$ scaling factor ( $\tau_r$ )	68
3.3.5 Non-dimensional analysis of dynamic coefficient using the Buckingham's II theorem	70
<b>3.4 Summary</b>	<b>76</b>
<b>CHAPTER FOUR</b>	<b>78</b>
<b>4. SCALE DEPENDENCY OF DYNAMIC RELATIVE PERMEABILITY CURVES IN RELATION WITH FLUID VISCOSITY AND DYNAMIC CAPILLARY PRESSURE EFFECT*</b>	<b>78</b>
<b>4.1 Introduction</b>	<b>78</b>
<b>4.2 Materials and methods</b>	<b>83</b>
4.2.1 Porous medium, domain size and fluid properties	83
4.2.2 Methods of averaging and parameters calculation	83
4.2.3 Relative permeability calculation	83
4.2.4 Dynamic coefficient ( $\tau$ ) calculation	84
<b>4.3 Results and discussions</b>	<b>84</b>
4.3.1 $P^c$ -S and $\partial S/\partial t$ -S relationships for different domain scales	84
4.3.2 Effects of viscosity ratio on relative permeability-saturation relationship	86
4.3.3 Effects of boundary pressure on dynamic relative permeability-saturation relationship	88
4.3.4 Effects of domain size on dynamic relative permeability-saturation relationship	89
4.3.5 Effects of location on relative permeability-saturation relationship	89
4.3.6 Comparison of static and dynamic relative permeability-saturation relationships	91
4.3.7 Comparison of mobility ratio ( $m$ ) and dynamic coefficient ( $\tau$ )	91
<b>4.4 Summary</b>	<b>93</b>
<b>CHAPTER FIVE</b>	<b>94</b>
<b>5. ARTIFICIAL NEURAL NETWORK (ANN) MODELLING OF SCALE DEPENDENT DYNAMIC CAPILLARY PRESSURE EFFECTS IN TWO-PHASE FLOW IN POROUS MEDIA*</b>	<b>94</b>
<b>5.1 Introduction</b>	<b>94</b>
<b>5.2 Modelling approaches</b>	<b>97</b>
5.2.1 ANN	97

5.2.1.1	Data sources and pre-processing	98
5.2.1.2	ANN development	98
5.2.2	Linear (LR) and non-linear (NLR) regression models	100
5.2.3	Models performance testing criteria	102
5.2.4	Prediction of domain scale dependency of $\tau$ -S relationships	103
<b>5.3</b>	<b>Results and discussions</b>	<b>103</b>
5.3.1	ANN configurations	103
5.3.2	Prediction of $\tau$ -S relationships	108
5.3.3	Domain scale dependency of $\tau$ -s relationships	111
<b>5.4</b>	<b>Summary</b>	<b>116</b>
<b>CHAPTER SIX</b>		<b>118</b>
<b>6.</b>	<b>DYNAMIC CAPILLARY PRESSURE EFFECTS IN SUPERCRITICAL CO<sub>2</sub>-WATER FLOW SYSTEM: EXPERIMENTS AND NUMERICAL SIMULATIONS*</b>	<b>118</b>
6.1	Introduction	118
6.2	Methodology	120
6.2.1	Fluids and porous Materials	120
6.2.2	Sample holder for porous domains and instruments	121
6.2.3	Dynamic and equilibrium experiments	123
6.2.4	Numerical Simulation	125
6.2.5	Averaging Method	129
6.2.6	Calculation of dynamic coefficient ( $\tau$ )	130
<b>6.3</b>	<b>Results and discussions</b>	<b>131</b>
6.3.1	Experimental results	131
6.3.2	Dynamic effects in $P^c$ -S relationship for supercritical CO <sub>2</sub> -water system	131
6.3.3	Displacement pattern in supercritical CO <sub>2</sub> -water system in porous media	133
6.3.4	Dynamic coefficient ( $\tau$ ) for supercritical CO <sub>2</sub> -water system in coarse sand sample: Influence of temperature	134
6.3.5	Effect of porous media permeability on $\tau$	136
6.3.6	Numerical analyses	138
<b>6.4</b>	<b>Dynamic <math>P^c</math> effects in scCO<sub>2</sub>-water system and errors in the estimate of aquifer storage capacity</b>	<b>141</b>
<b>6.5</b>	<b>Summary</b>	<b>142</b>
<b>CHAPTER SEVEN</b>		<b>143</b>
<b>7.</b>	<b>GEOELECTRICAL CHARACTERIZATION OF CARBONATE AND SILICATE POROUS MEDIA IN THE PRESENCE OF SUPERCRITICAL CO<sub>2</sub>-WATER FLOW*</b>	<b>143</b>
7.1	Introduction	143
7.2	Materials and methods	147
7.2.1	Unconsolidated porous materials	147
7.2.2	Instrumentations and sample holder set up	147
7.2.3	Experimental procedure	149
7.2.3.1	Equipment set up	149
7.2.3.2	Dynamic and quasi static drainage experiments	150
7.2.4	Bulk relative permittivity ( $\epsilon_b$ ) and electric conductivity ( $\sigma_b$ ) measurements	151
<b>7.3</b>	<b>Results and discussions</b>	<b>152</b>
7.3.1	Relative permittivity	152

7.3.1.1	Effect of pressure	154
7.3.1.2	Effect of porous media sample chemical properties	155
7.3.1.3	Effect of temperature	156
7.3.2	Electrical conductivity	157
7.3.3	Salt concentration	160
7.3.4	Mathematical description of results	161
<b>7.4</b>	<b>Summary</b>	<b>163</b>
<b>CHAPTER EIGHT</b>		<b>165</b>
<b>8. POTENTIAL OF SILICONE RUBBER MEMBRANE IN THE MONITORING OF SUBSURFACE GASES AND ITS APPLICATIONS IN GEOLOGICAL CARBON SEQUESTRATION*</b>		<b>165</b>
<b>8.1</b>	<b>Introduction</b>	<b>165</b>
<b>8.2</b>	<b>Materials and methods</b>	<b>169</b>
8.2.1	Porous domain and materials	169
8.2.2	Instruments and sample holder set up	169
8.2.3	Experimental design	171
8.2.4	Calculation of mass transfer parameters	173
<b>8.3</b>	<b>Results and discussions</b>	<b>176</b>
8.3.1	Gas permeation in the membrane	177
8.3.2	Gas flux across the membrane	179
8.3.3	Membrane permeability to gases	181
8.3.4	Distinguishing criterion for permeated gas	182
<b>8.4</b>	<b>Summary</b>	<b>184</b>
<b>CHAPTER NINE</b>		<b>186</b>
<b>9. PH, GEOELECTRICAL AND MEMBRANE FLUX PARAMETERS FOR THE MONITORING OF WATER-SATURATED SILICATE AND CARBONATE POROUS MEDIA CONTAMINATED BY CO<sub>2</sub> *</b>		<b>186</b>
<b>9.1</b>	<b>Introduction</b>	<b>187</b>
<b>9.2</b>	<b>Methodology</b>	<b>190</b>
9.2.1	Porous domain and materials	190
9.2.2	Instrumentations and sample holder	190
9.2.3	Experimental Procedure	191
9.2.3.1	Equipment set up	191
9.2.3.2	Design of the experimental conditions	192
9.2.3.3	pH measurement	193
9.2.4	Time domain reflectometry	193
9.2.5	Calculation of CO <sub>2</sub> flux through the non-porous membrane	195
<b>9.3</b>	<b>Results and discussions</b>	<b>195</b>
9.3.1	Change in pH of the water-saturated domain contaminated by CO <sub>2</sub>	196
9.3.2	Bulk relative permittivity of the water-saturated domain in the presence of CO <sub>2</sub>	198
9.3.3	Bulk electrical conductivity of the water-saturated domain in the presence of CO <sub>2</sub>	200
9.3.4	Diffusion of CO <sub>2</sub> in the water-saturated domain and its permeation through silicone rubber membrane	202
9.3.5	A mathematical expression between pH and $\sigma_b$	203
<b>9.4</b>	<b>Summary</b>	<b>205</b>
<b>CHAPTER TEN</b>		<b>206</b>

<b>10. CONCLUSIONS AND RECOMMENDATIONS</b>	<b>206</b>
<b>10.1 Conclusions</b>	<b>206</b>
10.1.1    Silicone oil/water system	206
10.1.2    CO <sub>2</sub> /water system	208
<b>10.2 Recommendations for future work</b>	<b>209</b>
<b>REFERENCES</b>	<b>211</b>
<b>APPENDIX A    MATERIAL CHARACTERIZATIONS</b>	<b>A1</b>
<b>A.1 Particle characterization</b>	<b>A1</b>
A.1.1    Sieve analysis	A1
A.1.2    Microscope scan	A4
A.1.3    Absolute density	A8
<b>A.2 Particle bed permeability</b>	<b>A8</b>
<b>APPENDIX B    CALIBRATION OF TDR</b>	<b>B1</b>
<b>B.1 Time domain reflectometry</b>	<b>B1</b>
B.1.1    Relative permittivity	B1
B.1.2    Electrical conductivity (EC)	B4
B.1.3    TDR calibration procedure	B4
B.1.4    Probe offset determination	B5
B.1.5    Volumetric Water Correlation	B7
B.1.6    Data logger set up	B7
<b>APPENDIX C    CALIBRATION OF THE PRESSURE TRANSDUCERS</b>	<b>C1</b>
<b>APPENDIX D    SAMPLE DATALOGGER PROGRAM</b>	<b>D1</b>
<b>APPENDIX E    NUMERICAL SIMULATION</b>	<b>E1</b>

## LIST OF FIGURES

Figure 2.1: Carbon dioxide sequestration operations at pilot and commercial scales worldwide (Michael et al. 2010).....	10
Figure 2.2: Relative permeability curves for CO <sub>2</sub> (blue) and water (red) (Pistone et al. 2011). .....	17
Figure 2.3: Wettability index of liquid as a function of contact angle ( $\alpha$ ): $\alpha > 90^\circ$ (non-wetting liquid), $\alpha < 90^\circ$ (wetting liquid). The possibility of $\alpha=0^\circ$ (perfectly wetting) is not shown. ....	19
Figure 2.4: Mechanisms of CO <sub>2</sub> Trapping with time (Benson and Cole 2008). ....	20
Figure 2.5: Various mechanisms of CO <sub>2</sub> trapping in the reservoir (Bentham 2006).....	21
Figure 2.6: Solution pH as a function of solubility of CO <sub>2</sub> in brine (Espinoza et al. 2011). ....	22
Figure 2.7: CO <sub>2</sub> solubility as a function of salinity (Chang et al. 1998).....	23
Figure 2.8: Density and viscosity of water and CO <sub>2</sub> with depth (Espinoza et al. 2011) .....	28
Figure 2.9: Capillary number and the displacement in the two-phase system (a) high viscosity ratio ( $\log m = 1.9$ ), (b) low viscosity ratio ( $\log m = -4.7$ ). Vertical axis represents the saturation of the displacing phase (Lenormand et al. 1988). ....	32
Figure 3.1: A schematic diagram of experimental set up showing different core scale domains (i.e., 4cm, 8cm and 12cm) used in this work. Only primary drainage experiment is conducted in this study. ....	53
Figure 3.2: Replicate desaturation rate as a function of average domain saturation at 20 kPa imposed pressure in a 4cm cell for viscosity ratio of 200.....	55
Figure 3.3: Capillary pressure and saturation relationship for quasi-static and dynamic conditions in 4cm cell for silicone oil of different viscosity ratios: (A) 200 (B) 500 (C) 1000. .	56
Figure 3.4: Desaturation patterns at different sections and domain scales for viscosity ratio of 200 at 20kPa imposed pressure: (A) 8cm cell (B) 12cm cell (C) Top sections in each of 4, 8 and 12cm cells (D) Bottom sections in each of 8 and 12cm cells (E) Bottom of 8cm cell compared to the middle of 12cm cell (F) Domain scales of 4, 8 and 12cm cells. ....	60
Figure 3.5: Desaturation patterns at different sections and domain scales for 500 viscosity ratio at 20kPa imposed pressure: (A) 8cm cell (B) 12cm Cell (C) Top sections in each of 4, 8 and 12cm cells (D) Bottom sections in each of 8 and 12cm cells (E) Bottom of 8cm cell compared to the middle of 12cm cell (F) Domain scales of 4, 8 and 12cm cells. ....	61
Figure 3.6: Desaturation patterns at different sections and domain scales for 1000 viscosity ratio at 20 kPa imposed pressure: (A) 8cm cell (B) 12cm Cell (C) Top sections in each of 4, 8 and 12cm cells (D) Bottom sections in each of 8 and 12cm cells (E) Bottom of 8cm cell compared to the middle of 12cm cell (F) Domain scales 4, 8 and 12cm cells. ....	62
Figure 3.7 : Comparison of Intercept and Origin fitting approaches on magnitude of dynamic coefficient for a viscosity ratio of 200 in a 4cm cell. ....	63
Figure 3.8: Dynamic coefficients and saturation relationship for the silicone oil-water system: (A) 8cm cell, 200 viscosity ratio (B) 12cm cell, 200 viscosity ratio (C) 12 cm cell, 500 viscosity ratio (D) 200, 500 and 1000 viscosity ratio silicone oil in 4 cm cell (E) Top sections of 4 and 8 cm cells for 200 viscosity ratio (F) Domain scales for 4, 8 and 12 cm cells, 200 viscosity ratio. Domain scale $\partial S / \partial t$ obtained from balance readings. ....	64
Figure 3.9: Influence of similar pressure gradient ( $\Delta P$ ) on domain scale dependence of ....	68
Figure 3.10: Influence of similar pressure gradient ( $\Delta P$ ) on domain scale dependence of ..	68

Figure 3.11: $\tau$ scaling factor in 8cm high cell for different viscosity ratios (A) viscosity ratio of 200 (B) viscosity ratio of 500 (C) viscosity ratio of 1000. ....	70
Figure 3.12: $\tau$ scaling factor in 12cm high cell for different viscosity ratios: (A) viscosity ratio of 200 (B) viscosity ratio of 500 (C) viscosity ratio of 1000. ....	71
Figure 3.13: Derivation and validation of a scaling relationship obtained from dimensional analysis (A) relationship between the dimensionless groups for 200, 500 and 1000 viscosity ratio (B) calibration of the scaling relationship using data in this work for all viscosity ratios and additional literature data reported by Das and Mirzaei (2012) (C) comparison of the relationship between the dimensionless groups for the parameters used by Bottero (2009) and predictions by equation (3.13) for the same parameters (D) comparison of $\tau$ -S data from Bottero (2009) and predictions by equation (3.13) for the same parameters. ....	76
Figure 4.1: Comparison of dynamic coefficient - water saturation curves for water and silicone oil with three differing silicone viscosities (0.65, 5 and 200 cSt respectively). Data for silicone oil with 0.65 and 5 cSt are taken from Goel and O'Carroll (2011) and the remaining data for 200 cSt are from Das and Mirzaei (2013). Goel and O'Carroll (2011) used sand having a mean permeability of $1.42 \times 10^{-11} \text{ m}^2$ . Das and Mirzaei (2013) used two different sands with mean permeabilities of $8.7 \times 10^{-10} \text{ m}^2$ (coarse sand) and $3.1 \times 10^{-10} \text{ m}^2$ (fine sand). ....	82
Figure 4.2: $P^c$ -S and $\partial S/\partial t$ -S patterns in the 8 and 12 cm high domains with 200 cSt silicone oil at 10 kPa boundary pressure. ....	86
Figure 4.3: Relative permeability-water saturation curves for water and silicone oil with two different viscosities (200 and 1000 cSt respectively) for 8 cm high domain and boundary pressure of 10 kPa.....	87
Figure 4.4: Relative permeability-water saturation curves for water and silicone oil (200 cSt) for the 12 cm high domain and boundary pressures of 10 and 20 kPa. ....	89
Figure 4.5: Relative permeability-water saturation curves for water and silicone oil (200 cSt) for boundary pressure of 10 kPa in the 8 and 12 cm domains.....	90
Figure 4.6: Relative permeability-water saturation curves for water and silicone oil (200 cSt) for boundary pressure of 10 kPa in the 8 cm high domain. ....	90
Figure 4.7: Comparison of static and dynamic relative permeability vs. water saturation curves for water and silicone oil (1000 cSt) for the 12 cm high domain. ....	91
Figure 4.8: Plots of mobility ratio ( $m$ ) and dynamic coefficient ( $\tau$ ) as a function of water saturation with 200cSt silicone oil at the top boundary pressure of 10kPa for the 8 and 12cm high domains. ....	92
Figure 4.9: Plots of mobility ratio ( $m$ ) and dynamic coefficient ( $\tau$ ) as a function of water saturation with 1000cSt silicone oil at the boundary pressure of 10kPa for the 8 and 12cm high domains. ....	92
Figure 5.1: (A) Training and (B) post-training regression analysis using ANN [9-13-15-1]..	105
Figure 5.2: (A) Training and (B) post-training regression analysis using ANN [9-15-17-1]..	106
Figure 5.3: Average absolute relative error (AARE) for ANN, linear (LR) and non-linear (NLR) regression models. ....	109
Figure 5.4: Sum squared error (SSE) for ANN, linear (LR) and non-linear (NLR) regression models.....	110
Figure 5.5 Model output efficiency for ANN, linear (LR) and non-linear (NLR) regression models.....	110

Figure 5.6: Threshold statistics (TS) for ANN, linear (LR) and non-linear (NLR) regression models.....	111
Figure 5.7: The dynamic coefficient values from ANN structures output and target data against water saturation using ANN [9-13-15-1].....	112
Figure 5.8: The dynamic coefficient values from ANN structures output and target data against water saturation using ANN [9-15-17-1].....	112
Figure 5.9: The dynamic coefficient values from ANN structures output and target data against water saturation using ANN [9-10-10-1].....	113
Figure 5.10: The dynamic coefficient values from ANN structures output and target data against water saturation using ANN [9-11-13-1].....	113
Figure 5.11: The dynamic coefficient against the water saturation values for the entire dataset and the predictions by linear regressions structure.....	114
Figure 5.12: The dynamic coefficient against the water saturation values for the entire dataset and the predictions by non-linear regression structures.....	114
Figure 5.13: Prediction of dynamic coefficient values against water saturation for the original, 10%, and 20% increase in domain size using the ANN [9-13-15-1]. Data for the original domain size were obtained from Das and Mirzaei (2012) where the oil viscosity is 200 cSt. ....	115
Figure 5.14: Prediction of dynamic coefficient values against water saturation for the original, 10%, and 20% increase in domain size using ANN [9-13-15-1]. Data for original domain size were obtained from Goel and O'Carroll (2011) where the oil viscosity is 5 cSt. ....	115
Figure 5.15: Dynamic coefficient values against water saturation for the original, 10% and 20% increase in domain size using ANN [9-13-15-1]. Data for original domain size were obtained from the in-house laboratory experiments (Abidoeye and Das 2014) where the oil viscosity is 500 cSt. ....	116
Figure 6.1: (A) High pressure experimental set-up for the scCO <sub>2</sub> -water system (B) Configuration of .....	126
Figure 6.2: P <sup>c</sup> -S relationship under dynamic and quasi static conditions in (A) coarse sand at 40°C, (B) coarse sand at 50°C, (C) coarse sand at 40°C with 0.1% surfactant. All dynamic experiments are conducted at 80.5 bar.....	132
Figure 6.3: Desaturation rate in coarse sand at 40°C and 50°C, and coarse sand at 40°C saturated with 0.1% surfactant. All dynamic experiments conducted at 80.5 bar.....	134
Figure 6.4: Dynamic coefficients in coarse sand at 40°C, coarse sand at 50°C, and coarse sand saturated with 0.1% surfactant at 40°C. All dynamic experiments conducted at 80.5 bar. ....	136
Figure 6.5: (A) P <sup>c</sup> -S relationships for the scCO <sub>2</sub> -water system under dynamic and quasi static condition in fine sand (CH30) at 40°C (B) Comparison of dynamic P <sup>c</sup> -S relationship for scCO <sub>2</sub> -water system in coarse and finer silica sand at 40°C. (C) Comparison of desaturation rate in coarse and fine silica sand at 40°C (D) Comparison of dynamic coefficients in coarse and fine silica sand at 40°C. All dynamic experiments conducted at 80.5 bar. ....	137
Figure 6.6: P <sup>c</sup> -S curves from the numerical simulations of the dynamic and quasi static displacements of water by scCO <sub>2</sub> in the coarse sand medium (A) at 40°C (B) at 50°C.....	139
Figure 6.7: Numerically and experimentally determined $\tau$ -S relationships in the coarse sand medium at (A) 40°C (B) 50°C (C) comparison of $\tau$ -S at 40 and 50°C. Dynamic experiments and simulations are conducted at 80.5bar.....	139

Figure 6.8: (A) Numerically determined $P^c$ -S relationship in the fine sand medium at 40°C (B) Numerically and experimentally determined $\tau$ -S relationship in the fine sand medium at 40°C (C) Comparison of numerically determined $\tau$ -S relationship in the fine and coarse sand media at 40°C. Dynamic experiments and simulations conducted at 80.5 bar.....	140
Figure 7.1: (A) High-pressure experimental set-up for the scCO <sub>2</sub> -water system (B) Schematics of TDR measurement system. ....	149
Figure 7.2: A photograph of the sample holder showing the TDR probes with insulation (cell internal diameter: 10cm, sample height: 4cm).....	151
Figure 7.3: Reproducibility plot of $\epsilon_b$ -S relationship for CO <sub>2</sub> -water-silica sand system. ....	153
Figure 7.4: Drainage under quasi static and faster injection rate (5 ml/min) in scCO <sub>2</sub> -water-silica sand system at 80 bar and 40°C. ....	153
Figure 7.5: Effect of pressure on $\epsilon_b$ -S relationship in CO <sub>2</sub> -water-silica sand system.....	154
Figure 7.6: Effect of porous media chemical properties on $\epsilon_b$ -S relationships in scCO <sub>2</sub> -water-silica/limestone sand system.....	155
Figure 7.7: Effect of temperature on $\epsilon_b$ -S relationships in CO <sub>2</sub> -water-silica sand system....	156
Figure 7.8: Effect of temperature on $\epsilon_b$ -S relationships at 80 bar in the scCO <sub>2</sub> .limestone (Trucal 6)-water system. ....	156
Figure 7.9: Effect of CO <sub>2</sub> injection rates on $\sigma_b$ -S relationships in the scCO <sub>2</sub> -water-silica sand system (5% NaCl). ....	158
Figure 7.10: Effect of media sample types on $\sigma_b$ -S relationships in the CO <sub>2</sub> -water-sand system at 5% NaCl. ....	158
Figure 7.11: Effect of temperature on $\sigma$ -S relationships in CO <sub>2</sub> -brine system in silica sand at 5% NaCl. ....	159
Figure 7.12: Effect of temperature on $\sigma_b$ -S relationships in limestone (Trucal 6) (5% NaCl). ....	159
Figure 7.13: $\sigma_b$ -S relationships at different salt concentrations at 40°C in limestone (Trucal 6). ....	160
Figure 7.14: $\sigma_b$ -S relationships at different salt concentrations at 50°C in limestone (Trucal 6). ....	160
Figure 7.15: Prediction of the $\epsilon_b$ values using nonlinear regression in water-silica sand system ....	163
Figure 7.16: Comparisons of model predictions of the $\epsilon_b$ values in silica sand and limestone. ....	163
Figure 8.1: Photographs of (A) The sample holder showing silica sand and pressure transducer (B) Steel holder showing the pressure transducer and the silicone rubber sheet (metal cap not shown). Sample holder size: internal diameter=10cm, sample height=4cm	170
Figure 8.2: High-pressure experimental set-up for the investigation of gas migration in the porous media using membrane-sensor system (The set-up is slightly different from Figure 7.1) .....	171
Figure 8.3: Scans of (A) Fresh (B) Used (experiment at 67.5 bar, 31.25°C, i.e., 200m depth) silicone rubber membrane using FEGSEM (LEO 1530VP, Carl Zeiss SMT, Oberkochen, Germany).....	173
Figure 8.4: Simultaneous responses of the two pressure transducers to the CO <sub>2</sub> gas that permeated through the membrane at imposed conditions corresponding to 250m depth...	176
Figure 8.5: Mass of permeated gas (N <sub>2</sub> ) under conditions that mimic different depths. ....	178

Figure 8.6: Mass of permeated gas (CO <sub>2</sub> ) through the membrane under conditions that mimic different depths .....	178
Figure 8.7: Mass of permeated gases (CO <sub>2</sub> and N <sub>2</sub> ) through the membrane under similar conditions .....	179
Figure 8.8: Change in the flux of permeated gas (N <sub>2</sub> ) under conditions that mimic different depths.....	180
Figure 8.9: Change in the flux of permeated gas (CO <sub>2</sub> ) under conditions that mimic different depths.....	181
Figure 8.10: Models of mass permeation rate for different gases at different geological depths for application in the distinction of the presence of the different gases in the porous medium.....	183
Figure 9.1: (A) Schematic diagram of experimental rig for the investigation of CO <sub>2</sub> -contamination of water in porous media. (B) Photograph of the sample holder showing silica sand, pressure transducer and TDR (C) Steel holder showing the pressure transducer and the silicone rubber sheet (metal cap not shown). Sample holder size: internal diameter=10cm, sample height=4cm. ....	194
Figure 9.2: Hypothetical representation of geological sediment with potable water aquifers located at different depths. This work considers the effect of aquifer depth on CO <sub>2</sub> contamination of water-saturated aquifer. ....	195
Figure 9.3: Replicate experimental results showing the three stages of changes in pH for water-saturated silica sand contaminated by CO <sub>2</sub> at conditions corresponding to 200m depth. ....	197
Figure 9.4: Replicate experiments for bulk relative permittivity of water-saturated silica sand contaminated by CO <sub>2</sub> at conditions corresponding to 100m depth. ....	199
Figure 9.5: Bulk relative permittivity for water-saturated limestone contaminated by CO <sub>2</sub> at conditions corresponding to 50 and 200m depths. ....	199
Figure 9.6: Replicate experiments showing bulk electrical conductivity of water-saturated silica sand contaminated by CO <sub>2</sub> at conditions corresponding to 100m depth.....	201
Figure 9.7: Bulk electrical conductivity of water-saturated limestone at conditions corresponding to 50 and 200m depths.....	201
Figure 9.8: Permeation of CO <sub>2</sub> into silicone rubber membrane via diffusion through water-saturated silica sand. ....	202
Figure 9.9: CO <sub>2</sub> flux through the silicone rubber membrane via diffusion through water-saturated silica sand. ....	203
Figure 9.10: Comparison of the ratios of the bulk electrical conductivity ( $\sigma_{br}$ ) from the experiments and mathematical predictions .....	204
Figure A.1: Plot of % mass retention on each sieve versus average sieve.....	A3
Figure A.2: Semi-log plot of % finer particle mass against average particle .....	A3
Figure A.3: Plot of % mass retention on each sieve versus average sieve.....	A4
Figure A.4: Semi-log plot of % finer particle mass against average particle .....	A4
Figure A.5: Microscope scan (DA 14/25) (Magnification:x4).....	A5
Figure A.6: Microscope scan (DA 30) (Magnification:x4).....	A5
Figure A.7: Histogram of particle size distribution based on imageJ analysis of microscope scan of particles (DA 14/25).....	A6

Figure A.8: Histogram of particle size distribution based on imageJ analysis of microscope scan of particles (DA 30)	A7
Figure A.9: Set up of constant-head permeameter for permeability experiment	A9
Figure A.10: Permeability of the sand blend	A9
Figure B.1: Wave reflection in TDR probe visualised with PCTDR (a) in air, (b) in water .....	B3
Figure B.2: A schematic overview of the mini-TDR with triple-rod probe and coax cable ....	B4
Figure B.3: TDR instruments and the interconnections .....	B5
Figure B.4: Plots of aqueous saturation, ( $S_w$ ) against square root of relative permittivity, $\sqrt{K_a}$ . (A) mini TDR1 (B) mini TDR2 (C) mini TDR3 .....	B10
Figure C.1: DPI calibrator with pump used in the calibration of the pressure transducers. ..	C2
Figure C.2: Voltage output from the pressure transducers in response to the applied pressure (low-pressure pressure transducers).....	C2

## LIST OF TABLES

Table 2.1: Wettability indices for oil-water indices (Pentland 2011) .....	19
Table 2.2: Typical $P^c$ -S- $K_r$ experiments for scCO <sub>2</sub> -brine/water system in the literature (d: diameter L: Length).....	36
Table 3.1: Fluid and material properties used in the experiments in this work.....	48
Table 5.1: Statistics of the input and output variables .....	101
Table 5.2: Slope and correlation coefficient for different ANN configurations (single and double hidden layered ANN structures) .....	107
Table 6.1: Fluid and Material Properties .....	124
Table 6.2: Boundary conditions for different displacement cases used in the simulation....	127
Table 6.3: Equations used for the simulation .....	128
Table 6.4: Number of nodes and nodal spacing for the domain used for numerical simulation .....	129
Table 7.1: Material Properties .....	148
Table 7.2: The electrical conductivity of the water used in the experiments .....	161
Table 8.1: List of Experimental Conditions and State of CO <sub>2</sub> .....	173
Table 9.1: List of conditions which were experimentally simulated in this study .....	192
Table 9.2: Changes in pH of water-saturated silicate and carbonate porous media in the presence of CO <sub>2</sub> at various depths .....	198
Table A.1: Sieve analysis for coarse silica sand particles .....	A1
Table A.2: Sieve analysis for fine silica sand particles .....	A2
Table A.3: Distribution coefficients in the silica sand samples.....	A2
Table B.1: Probe Offset for the mini-TDR probes.....	B7
Table B.2: Parameters for $S_w$ calculation from fifth order polynomial equation ( $x=\sqrt{Ka}$ ).....	B10

## NOMENCLATURE

<b>Symbol/ Abbreviation</b>	<b>Description</b>	<b>Unit</b>
A	Area	m <sup>2</sup>
c	Concentration of fluid in solid	kg m <sup>-3</sup>
D	Diffusion coefficient	
d	Cell Diameter	m
g	Acceleration due to gravity	m s <sup>-2</sup>
K	Permeability	m <sup>2</sup>
K <sub>r</sub>	Relative permeability	-
K <sub>T</sub>	Overall mass transfer coefficient	kg/(m <sup>2</sup> .hr.bar)
k <sub>g</sub>	Gas boundary mass transfer coefficient	kg/(m <sup>2</sup> .hr.bar)
k <sub>m</sub>	Membrane layer mass transfer coefficient	kg/(m <sup>2</sup> .hr.bar)
J	Mass rate of transfer per unit area	kg/(m <sup>2</sup> .hr)
L	Length or depth	m
m	Mass of gas	kg
nw	Non wetting phase	
$\Delta P$	Pressure gradient	Pa
P <sup>C</sup>	Capillary pressure	Pa
P <sup>C,dyn</sup>	Dynamic capillary pressure	Pa
P <sup>C,equi</sup>	Quasi static capillary pressure	Pa
P	Permeability of membrane	Kg.m/(m <sup>2</sup> .hr.bar)
p	Pressure	Pa
R <sub>g</sub>	Rate of gas permeation	kg s <sup>-1</sup>
Q	Volume flow rate	m <sup>3</sup> s <sup>-1</sup>
S	Water saturation	-
S <sub>rw</sub>	Irreducible water saturation	-
S <sup>eff</sup>	Effective water saturation	-
t	Time	s
$\tau$	Dynamic coefficient	Pa s
$\sigma$	Electrical conductivity	( $\Omega$ m) <sup>-1</sup>
$\sigma_b$	Bulk electrical conductivity	( $\Omega$ m) <sup>-1</sup>
$\sigma_{bi}$	Initial value of $\sigma_b$ before the injection of CO <sub>2</sub>	-
$\sigma_{br}$	Ratio of the steady state value of $\sigma_b$ to the initial value of $\sigma_b$ ( $\sigma_{bi}$ )	-
$\epsilon$	Relative permittivity	-
$\epsilon_b$	Bulk relative permittivity	-
$\phi$	Porosity	-
$\mu$	Fluid viscosity	Pa s
$\mu_r$	Fluid-fluid viscosity ratio	-
$\rho$	Fluid density	kg m <sup>-3</sup>
$\rho_r$	Fluid-fluid density ratio	-
$\rho_s$	Solid density	kg m <sup>-3</sup>
$\rho_b$	Bulk density	kg m <sup>-3</sup>
$\partial S/\partial t$	Rate of change of saturation	s <sup>-1</sup>

$\delta$	Pore diameter	m
$\delta_m$	Thickness of the membrane	m
$V_m$	Volume of the gas that passes through the membrane	$m^3$
w	Wetting phase	
TDR	Time domain reflectometry	-
PT	Pressure transducer	-
scCO <sub>2</sub>	Supercritical CO <sub>2</sub>	-
PTFE	Polytetrafluoroethylene	

## PUBLICATIONS

### ACCEPTED/PUBLISHED ARTICLES

1. **Abidoeye, L.K.**, Das, D.B., and Khudaida, K., (2015). Geological carbon sequestration in the context of two-phase flow in porous media: A review. *Critical Reviews in Environmental Science and Technology*, DOI: 10.1080/10643389.2014.924184 (in press) (**Chapter 2**).
2. Das, D.B., Gill, B.S., **Abidoeye, L.K.**, and Khudaida, K., (2014). Numerical Simulation of Dynamic Effect in Capillary Pressure-Saturation Relationship for Supercritical Carbon dioxide-Water Flow in Porous Domain, *AIChE Journal*, 60(12), pp. 4266-4278, DOI 10.1002/aic.14577.
3. **Abidoeye, L.K.**, and Das, D.B., (2014). Scale-dependent dynamic capillary pressure effect for two-phase flow in porous media. *Advances in Water Resources*, 74, pp. 212–230, DOI: 10.1016/j.advwatres.2014.09.009 (**Chapter 3**).
4. **Abidoeye, L.K.**, and Das, D.B (2015). pH, Geoelectrical and Membrane Flux Parameters for the Monitoring of Water-Saturated Silicate and Carbonate Porous Media Contaminated by CO<sub>2</sub>, *Chemical Engineering Journal*, 262, pp. 1208–1217, DOI: 10.1016/j.cej.2014.10.036 (**Chapter 9**).
5. **Abidoeye, L.K.**, and Das, D.B (2015). Artificial Neural Network (ANN) Modelling of Scale Dependent Dynamic Capillary Pressure Effects in Two-Phase Flow in Porous Media, *Journal of Hydroinformatics* (Accepted) (**Chapter 5**)

### ARTICLES UNDER REVIEW

1. Goel, G., **Abidoeye, L.K.**, Das, D.B., and Chahar, B.R. Scale dependency of dynamic relative permeability curves in relation with fluid viscosity and dynamic capillary pressure effect. *Environmental Fluid Mechanics* (submitted) (**Chapter 4**).
2. **Abidoeye, L.K.**, and Das, D.B. Dynamic capillary pressure effects in supercritical CO<sub>2</sub>-Water flow system: Experiments and numerical Simulations. *AIChE Journal* (submitted) (**Chapter 6**).
3. **Abidoeye, L.K.**, and Das, D.B. Geoelectrical characterization of carbonate and silicate porous media in the presence of supercritical CO<sub>2</sub>-water flow, *Geophysical Journal International* (submitted) (**Chapter 7**).

4. **Abidoeye, L.K.**, and Das, D.B. Potential of Silicone Rubber Membrane in the Monitoring of Subsurface Gases and its Applications in Geological Carbon Sequestration. Industrial & Engineering Chemistry Research (submitted) (**Chapter 8**).

## CONFERENCES/SEMINARS

### Oral presentation:

1. **Abidoeye, L.K.**, and Das, D.B., (2013). Dynamic effects in Capillary Pressure-Saturation Relationship for CO<sub>2</sub>-Water-Sand System: Application to CO<sub>2</sub> Sequestration. Presentation at the 3rd United Kingdom Carbon Capture and Storage (UKCCSC) Winter School, University of Edinburgh, Edinburgh, United Kingdom, January 8th -11th , 2013.
2. **Abidoeye, L.K.**, and Das, D.B., (2013). Dynamic Effects in Two-Phase Flow: Application to Geological Sequestration: PhD Seminar at Loughborough University, October 1st, 2013.
3. **Abidoeye, L.K.**, and Das, D.B., (2012). Experimental determination of dynamic effect for CO<sub>2</sub>-H<sub>2</sub>O flow in porous medium: application to CO<sub>2</sub> sequestration. Presentation at the 2nd United Kingdom Carbon Capture and Storage (UKCCSC) Winter School, Cambridge centre for carbon capture and storage, University of Cambridge, Cambridge, UK, January 10th-12th, 2012.
4. **Abidoeye, L.K.**, and Das, D.B., (2014). Multistage characterization of CO<sub>2</sub>-H<sub>2</sub>O system in the carbonate and silicate porous media. Presentation at the 1<sup>st</sup> North Sea Young CCS Researchers Conference, Amsterdam, 17-18 June 2014.

### Poster presentations

1. **Abidoeye, L.K.**, and Das, D.B., (2014). Multi-Parameter Characterizations of CO<sub>2</sub>-Water System in Silicate and Carbonate Porous Media. Poster presentation at the UKCCSRC biannual meeting themed 'CCS and Industry' held at the School of Engineering, Cardiff University, United Kingdom. September 10<sup>th</sup> to 11<sup>th</sup>, 2014.
2. **Abidoeye, L.K.**, and Das, D.B., (2014). Scale-dependent dynamic capillary pressure effect for two-phase flow in porous media in relation to fluid viscosity ratio. Poster presentation at the XX. International Conference on Computational Methods in Water Resources (CMWR), University of Stuttgart, Stuttgart, Germany, June 10<sup>th</sup>-13<sup>th</sup>, 2014.

3. **Abidoeye, L.K.**, and Das, D.B., (2014). Artificial Neural Network (ANN) Modelling of Scale Dependent Dynamic Capillary Pressure Effects in Two-Phase Flow in Porous Media. Poster presentation at the XX. International Conference on Computational Methods in Water Resources (CMWR), University of Stuttgart, Stuttgart, Germany, June 10<sup>th</sup>-13<sup>th</sup>, 2014.
4. **Abidoeye, L.K.**, and Das, D.B., (2014). Dynamic Effects in Supercritical CO<sub>2</sub> - Water System: Application to Geological CO<sub>2</sub> Sequestration. Poster presentation at the XX. International Conference on Computational Methods in Water Resources (CMWR), University of Stuttgart, Stuttgart, Germany, June 10<sup>th</sup>-13<sup>th</sup>, 2014.
5. Goel, G., **Abidoeye, L.K.**, Das, D B., Chahar, B.R., and Singh, R., (2013). Scale dependency of dynamic relative permeability curves in relation with fluid viscosity and dynamic capillary pressure effect. Poster presentation at the XX. International Conference on Computational Methods in Water Resources (CMWR), University of Stuttgart, Stuttgart, Germany, June 10<sup>th</sup>-13<sup>th</sup>, 2014.
6. **Abidoeye, L.K.**, and Das, D.B., (2014). Multistage characterization of CO<sub>2</sub>-H<sub>2</sub>O system in the carbonate and silicate porous media. Poster presentation at the Research That Matters: Research Challenges in Focus, hosted by the Graduate School, Loughborough University, Loughborough, UK on 18<sup>th</sup> June, 2014.

#### **In attendance**

1. United Kingdom Carbon Capture and Storage Research Centre (UKCCSRC) Biannual Meeting titled: Carbon Capture, Cross Cutting Issues and Carbon Storage with Pact Facilities Field trip, Sheffield, UK. April 8/9, 2013.
2. Potential environmental effects of CO<sub>2</sub> leakage in the marine and terrestrial environment: Understanding, monitoring, mitigation workshop, Nottingham Centre for Carbon Capture and Storage, University of Nottingham, Nottingham, UK, 21st Feb., 2012.
3. Carbon Capture and Storage, The Geological Society, London, A joint meeting between the Geological Society and AAPG, November 22 and 23, 2011.

# CHAPTER ONE

## INTRODUCTION

### 1.1 Background

Instances of fluid flow through porous medium are commonly encountered in the flow of groundwater through aquifers, flow of petroleum or gas through reservoir rock matrices as well as in the percolation of water through the common household sponge. It is also come across in the permeation of a fluid phase through a selective permeable membrane, e.g., silicone rubber (Scholes et al. 2014). Aside the case of single-phase fluid flow in porous medium, multiphase system consisting of more than one fluid phase is also common in the subsurface. They can arise from the contamination of groundwater by oil spill or radioactive wastes (Ekre et al. 2014; Markatos 2012).

Two-phase flow in the porous medium is a familiar phenomenon in many chemical, petroleum and environmental problems, where one fluid is displaced by another. A common example is the subsurface contamination by the non-aqueous phase liquids, NAPLs (e.g., oils, perchloroethylene (PCE), etc.), produced and accidentally spilt by various chemical process industries (Sweijen et al. 2014; Yang et al. 2013). They may remain in the subsurface for hundreds of years and constitute environmental threat worldwide (Das et al. 2007).

Characterising the two-phase flow system in the porous medium relies upon the relationships among various fluids and the porous medium properties. To perform the characterization of immiscible two-phase flow system in the porous medium, the traditional approach employs the capillary pressure ( $P^c$ ), saturation ( $S$ ) and relative permeability ( $K_r$ ) relationships ( $P^c$ - $S$ - $K_r$ ) to describe the system.  $P^c$  and  $K_r$  for wetting and non-wetting phases are parameters of key importance in modelling the two-phase flow processes encountered during flow of immiscible phases in the underground (Aggelopoulos and Tsakiroglou 2008) and they constitute key parameters used to history match and design field-scale fluid injection projects using reservoir simulators (Doughty 2007).

Apart from the  $P^c$ - $S$ - $K_r$  relationships, geoelectrical measurement techniques are also utilised to monitor the two-phase system in the porous medium. Common electrical parameters employed in the study of the two-phase flow systems in the porous medium include the bulk electrical conductivity ( $\sigma_b$ ) and the relative permittivity ( $\epsilon_b$ ) of the fluid-fluid-porous media system. Relative permittivity is a measure of the electrical polarization of a material when an

electric field is applied across it, while the electrical conductivity ( $\sigma$ ) is a measure of the conduction current, developed by an electric field through a material (Solymar et al. 2014; Keller 1966). Interestingly, the capillary pressure ( $P^c$ ), relative permeability ( $K_r$ ), bulk electrical conductivity ( $\sigma_b$ ) and the relative permittivity ( $\epsilon_b$ ) of two-phase flow systems in the porous medium are functions of the water saturation ( $S$ ) (Plug et al. 2007b). Thus, they can be employed in the investigations of the oil and water flow through the rock matrix in order to enhance the control of the secondary oil recovery process. Also, in the geological carbon sequestration process, the parameters can be applied in the monitoring of the displacement of brine by injected  $\text{CO}_2$  in the saline aquifer.

However,  $P^c$ - $S$ - $K_r$ ,  $\epsilon_b$ - $S$  and  $\sigma_b$ - $S$  relationships for two-phase flow systems exhibit non-uniqueness (Kalaydjian 1992; Hassanizadeh and Gray 1993; Das et al. 2006; Plug et al. 2007b). Non-uniqueness in the above relationships refers to the variations in their behaviours under seemingly similar conditions (e.g., same porosity or permeability of the porous material). Investigations and understanding of the factors causing non-uniqueness in the above relationships are relevant to the effective control and monitoring of subsurface two-phase processes.

The aim of this work is to experimentally and numerically investigate the factors and conditions causing non-uniqueness in the characterization functions ( $P^c$ - $S$ ,  $K_r$ - $S$ ,  $\epsilon_b$ - $S$  and  $\sigma_b$ - $S$ ) for two-phase flow in the porous media. The investigations also include further techniques to monitor a two-phase system under dynamic and static conditions in porous media. The results of these investigations are important in the understanding, monitoring and controlling of two-phase systems in porous media. The work is a broad study of the two-phase systems (oil/water,  $\text{scCO}_2$ /water, etc.) in porous media under various conditions.

## 1.2 Motivation for research

Understanding the two-phase system (oil/water) in the porous media is important for the improvement in secondary oil recovery process, where water is injected into the production zone to sweep oil from the reservoir. Also, mitigating the problem of global warming requires the limitation of the greenhouse gas concentration in the atmosphere. To achieve this, geological carbon sequestration has been proposed as a climate change remediation strategy. The above-mentioned processes (i.e., secondary oil recovery and the geological carbon sequestration) consist of two-phase systems, e.g.,  $\text{scCO}_2$  and brine in the saline aquifer as a result of geological carbon sequestration, and the oil/water in the reservoir in the case of the secondary oil recovery process. In the oil/water system, effective characterization is required to know the amount of each phase remaining in the reservoir. This is important to

optimise the oil recovery process. For the sequestration process, effective characterization is also necessary for the monitoring of the displacement of brine by the scCO<sub>2</sub> in the saline aquifer, and for the monitoring of the migration of CO<sub>2</sub> in the aquifer, in order to check leakage and avert dangers to potable water, humans, animals, and plants. In order to have effective control over the above systems, any factor contributing to the non-uniqueness of their characterization functions/parameters should be well understood and the degree of their contributions to the non-uniqueness of the characterization parameters should be identified. This knowledge will lead to the efficient designs of the operations and procedures for the processes. Therefore, this work is motivated by the above facts to investigate the effects of various factors on the  $P^c$ -S- $K_r$ ,  $\epsilon_b$ -S and  $\sigma_b$ -S relationships for oil/water and scCO<sub>2</sub>/brine systems in porous media. This will promote understanding of the two-phase systems and improve their predictions, control and monitoring in the porous media.

### 1.3 Research questions

In this work, a number of important research questions arising from the review of literature on the two-phase flow in porous media will be investigated. They include:

- I. What are the actual trends and the quantitative relationship of the  $\tau$ -S relationship with the domain scale of oil-water system in porous media?
- II. Can the influence of the intra-domain averaging technique be practically minimised in the upscaling of the system property for the determination of the domain-scale dependence of the dynamic capillary effect in  $P^c$ -S relationship for the oil-water system?
- III. What are the feasible techniques for *in situ* characterization of the scCO<sub>2</sub>-brine system in porous media considering the high pressure and temperature?
- IV. Does the dynamic capillary pressure effect influence the  $P^c$ -S relationship for scCO<sub>2</sub>-brine/water system?
- V. Does the dynamic capillary pressure effect affect the  $\epsilon_b$ -S and  $\sigma_b$ -S relationships for scCO<sub>2</sub>-brine/water system?
- VI. What factors influence the  $\epsilon_b$ -S and  $\sigma_b$ -S relationships in water-saturated silicate and carbonate porous media in the presence of scCO<sub>2</sub>?
- VII. How can the measurement of the geoelectrical parameters and gas permeation through membranes assist in the monitoring of the scCO<sub>2</sub>-water/brine system in the porous media?

- VIII. What useful information can be obtained from the simultaneous measurements of the geoelectrical parameters, pH and gas permeation through the membrane, in the water-saturated silicate and carbonate porous media contaminated by CO<sub>2</sub>?

## 1.4 Specific aims

The aims of this work include:

- I. To investigate the scale dependency of the dynamic capillary pressure effect in P<sup>c</sup>-S relationship for silicone oil-water system under ambient conditions.
- II. To determine the influence of non-equilibrium effect on the K<sub>r</sub>-S relationship for silicone oil-water system in porous media.
- III. To investigate the possibility of using alternative, simpler, faster and cheaper computational techniques in determining scale dependency of dynamic capillary pressure effects in two-phase flow systems in porous media.
- IV. To design and develop an experimental rig, techniques and procedures for the investigations of the P<sup>c</sup>-S, ε<sub>b</sub>-S and σ<sub>b</sub>-S relationships in scCO<sub>2</sub>-brine system in the porous media.
- V. To investigate the presence and the magnitude of the dynamic capillary pressure effect in the P<sup>c</sup>-S relationship for scCO<sub>2</sub>-water system. Also, to determine the effect of temperature and porous media permeability on the dynamic capillary pressure effect for the scCO<sub>2</sub>-water, as well as the effect of the surfactant on the displacement of the water by scCO<sub>2</sub> in the porous media.
- VI. To investigate the effects of pressure, temperature and salt concentration on ε<sub>b</sub>-S and σ<sub>b</sub>-S relationships for scCO<sub>2</sub>-brine/water system in the silicate and carbonate porous media.
- VII. To investigate the applicability of polymeric membranes in the monitoring of diffusion of CO<sub>2</sub> through water-saturated silicate and carbonate porous media.
- VIII. To perform numerical analyses of the dynamic capillary pressure effect in the scCO<sub>2</sub>-water system in porous medium using commercial simulator– STOMP (Subsurface Transport over Multiple Phases).

## 1.5 Contributions to knowledge

In general, the findings in this work contribute in many ways to the study and further understanding of two-phase flow behaviour in porous media. Particularly, the experimental and numerical investigations in this work would contribute to the advancement of two-phase study and its applications in the context of geological carbon sequestration. The main contributions to knowledge are highlighted below:

- The effects of domain scale on the dynamic capillary pressure effects in the  $P^c$ -S relationship for oil-water flow system were elucidated. This reduces the controversies in literature concerning the actual trend between the dynamic coefficient  $\tau$ , used in quantifying the dynamic capillary pressure effects, and the domain scale.
- The presence of the dynamic capillary pressure effects in the  $scCO_2$ -water system in porous media, under conditions applicable to geological carbon sequestration, was established. This is the first time the dynamic capillary pressure effect on  $P^c$ -S relationships for the  $scCO_2$ -water system in porous media was investigated. The conclusion of the investigations suggests the importance of including the dynamic coefficient,  $\tau$ , in the numerical simulator for the geological carbon sequestration
- Factors affecting the electrical parameters used in the characterization of two-phase flow were investigated in the silicate and carbonate porous media. The findings brought to light the variations in  $\epsilon_b$ -S and  $\sigma_b$ -S relationships under various conditions. The conclusions of the findings are very useful in the design of an effective monitoring system for the  $CO_2$ -water/brine migration at a geological storage site.
- The dynamics in the change of pH for water-saturated silicate and carbonate porous media contaminated by  $CO_2$  at high pressure and temperature were demonstrated. Three stages were identified in the pH change. The first stage corresponds to the formation of the carbonic acid as well as the bicarbonate. The second stage corresponds to the production of gaseous/aqueous  $CO_2$  and water in a reverse reaction. The last stage showed equilibrium in the forward and reverse reactions and was characterised with the steady value of the pH, which remained unchanged till the end of the experiments. Furthermore, the equivalence in the responses of the pH and the  $\sigma_b$  of the  $CO_2$ -contaminated system were graphically shown. The findings are very useful in the monitoring of  $CO_2$  contamination of water-saturated silicate and carbonate porous media, using pH and electrical measurement techniques
- Potentials of silicone rubber membrane coupled with a pressure sensor in the monitoring and detection of the migration of gases at different geological depths were demonstrated. The membrane-sensor system is applicable in the event of leakage of  $CO_2$  from the storage site. A mathematical criterion was derived to distinguish the presence of different gases in the subsurface using the membrane-sensor system.

## 1.6 Thesis structure

The thesis comprises of nine chapters, which are presented in the following order:

**Chapter 1** introduces the two-phase flow system in porous media and its applications in industries. Different characterization parameters for two-phase systems in porous media and their interrelationships are briefly discussed. Aims and objectives, motivation and contribution of this work to knowledge of two-phase systems in porous media are stated.

**Chapter 2** consists of a comprehensive review of literature on the geological carbon sequestration in the context of two-phase flow. Laboratory and field investigations, modelling and simulations, risks of CO<sub>2</sub> leakage from storage and other challenges are expatiated. The chapter enumerates gaps in the knowledge of geological carbon sequestration in relation to CO<sub>2</sub>-water/brine flow.

**Chapter 3** presents an experimental investigation on the scale dependent dynamic capillary pressure effect in the P<sup>c</sup>-S relationship for silicone oil-water system in the porous media. Discussions and dimensionless analysis of results are also presented.

**Chapter 4** discusses the dynamic K<sub>r</sub>-S relationship for the silicone oil-water system in the porous media. The effects of domain scale, boundary pressure, measurement locations on the domain, etc., are elucidated on the dynamic K<sub>r</sub>-S relationship.

**Chapter 5** shows the investigations of alternative, cost-effective and time-saving computational techniques for the prediction of the domain scale dependence of the dynamic coefficient using an artificial neural network (ANN). Different ANN configurations as well as linear and non-linear multivariate regression models were tested using a number of performance criteria.

**Chapter 6** contains the background to the geological carbon sequestration and the implication of the dynamic capillary pressure effects. Experimental and numerical simulation results on the dynamic capillary pressure effects in the P<sup>c</sup>-S relationship for the supercritical CO<sub>2</sub>-water system were presented and discussed. Detailed results include the P<sup>c</sup>-S and desaturation rate ( $\partial S/\partial t$ )-saturation relationships for scCO<sub>2</sub>-brine/water system. Influence of the surfactant on the displacement patterns of the water by scCO<sub>2</sub> is also shown.

**Chapter 7** presents results of geoelectrical characterization of the silicate and carbonate porous media in the presence of CO<sub>2</sub> and brine/water. Effects of pressure, temperature, chemical properties of the porous media materials and desaturation rate are discussed on the electrical parameters of the system are discussed.

**Chapter 8** is concerned with potential of silicone rubber as a membrane in the monitoring of gas movement at the different geological depths. Criteria for the detection of leakage from

geological sequestration sites are established based on the mass permeation rate of different gases, e.g., CO<sub>2</sub>, N<sub>2</sub>.

**Chapter 9** discusses the results of investigations of water contamination by CO<sub>2</sub>, at conditions equivalent to that of various geological depths. Under static conditions, the geoelectrical characteristics of the system are investigated. The results of these investigations are presented. Furthermore, the applications of silicone rubber under such conditions are presented.

**Chapter 10** presents the summary and conclusions of this work. Findings from investigations, effects of various techniques and implications of the results are also presented. Based on these findings, recommendations are made for field applications and future investigations.

## CHAPTER TWO

# GEOLOGICAL CARBON SEQUESTRATION IN THE CONTEXT OF TWO-PHASE FLOW IN POROUS MEDIA: A REVIEW\*

### Overview

*In this review, various aspects of geological carbon sequestration are discussed in relation to the principles of two-phase flow in porous media. Literature reports on geological sequestration of CO<sub>2</sub> show that the aquifer storage capacity, sealing integrity of the caprock and the in situ processes, e.g., the displacement of brine by supercritical CO<sub>2</sub> (scCO<sub>2</sub>), convection-diffusion-dissolution processes involving scCO<sub>2</sub> and brine, geochemical reactions, and mineral precipitation depend on the fluid-fluid-rock characteristics as well as the prevailing subsurface conditions. Considering the complexity of the interrelationships among various processes, experimental investigations and network of mathematical functions are required for the ideal choice of geological site with predictable fluid-fluid-rock behaviours that enhance effective monitoring. From a thorough appraisal of the existing publications, recommendations are made for improvement in the existing simulators to fully couple the entire processes involved in the sequestration operations and in situ mechanisms which include injection rate and pressure, brine displacement, simultaneous flow of free and buoyant phases of CO<sub>2</sub>, various trapping mechanisms, convection-diffusion-dissolution processes, scCO<sub>2</sub>-brine-rock reactions, precipitation of the rock minerals and the consequences on the hydraulic and hydrogeological properties in the course of time as well as the quantity of injected CO<sub>2</sub>. Suggestion is made for the inclusion of leakage parameters on site-specific basis to quantify the risks posed by the prevailing fluid-fluid-rock characteristics as well as their immediate and future tendencies. Calls are also made for thorough investigations of factors that cause non-uniqueness of the two-phase flow behaviour with suggestions for the use of appropriate experimental techniques. The review comprehensively synthesizes the available knowledge in the geological carbon sequestration in a logical sequence.*

### 2.1 Introduction

The world is currently confronted with the issue of global warming arising mainly from the anthropogenic activities, especially man's excessive use of fossil fuels for energy. This has resulted in the unhindered emissions of several climate-unfriendly gases into the atmosphere. There are significant evidence which has shown that these emissions

---

\*Abidoeye, L.K., Das, D.B., and Khudaida, K., (2014). Geological carbon sequestration in the context of two-phase flow in porous media: A review Critical Reviews in Environmental Science and Technology, DOI: 10.1080/10643389.2014.924184 (in press)

exacerbate the change in the climate by forming a blanket of gases which accumulate at the lower part of the atmosphere, trapping the reflected radiation from the earth thereby raising the surface temperature (Karl et al. 2009; Solomon et al. 2007). Owing to the increasing amount of global emission, carbon dioxide is of serious concern as it is considered to be the greatest culprit in the greenhouse effect (Metz et al. 2005; Marland and Rotty 1984). Sources of these pollutants include fossil fuels and deforestation practises (Karl et al. 2009).

In the face of increasing global energy demands, the desire to mitigate the change in climate presents a daunting and interesting challenge as ninety per cent of world's primary sources of energy still comes from fossil fuels (DOE 2010). The world population still hopes for an improvement in the standard of living, education and health care. These aspirations are directly related to energy consumption. To check the steep rise in carbon emission since the industrial revolution (200 to ~385 ppm) and preserve the planet, CO<sub>2</sub> will need to be reduced to, at most, 350 ppm (Houghton et al. 2001; Hansen et al. 2008). In tackling the challenges, various technologies have emerged while many others are under investigations and implementations to reduce the emissions of these gases into the atmosphere, utilise alternative energies, improve carbon capture, or promote storage efficiencies and so on. Figure 2.1 shows the pilot and commercial scale carbon sequestration projects being executed worldwide.

Popular sites identified as suitable for carbon storage include ocean, brine or saline aquifer, coal bed and depleted oil reservoir. However, the geological sequestration in saline aquifers is considered as the most viable option as it seems to have the largest carbon storage potential (Fujii et al. 2010; Zahid et al. 2011). Parts of the reasons for this choice include the stability, capacity and ubiquity of these aquifers. Stable sedimentary basins are necessary for dependable sequestration activities and such basins are found in most continents (Metz et al. 2005) with estimated capacities of around 1000 to 100,000 gigatonnes of carbon dioxide (Zahid et al. 2011).

Researchers have thus dedicated many studies to determine storage capacities and fluid flow mechanisms at prospective sites. The ultimate choice of a particular geological site will depend on a combination of several characteristics, which include aquifer size, porosity, permeability, depth, geology, hydrogeology, caprock integrity, petrophysical characteristics, geothermal gradient, proximity to emission sources and existing infrastructures, tectonic stability and faulting intensity (Espinoza et al. 2011). Scenarios of the injected CO<sub>2</sub> in the brine aquifer for sequestration purposes involve several *in situ* mechanisms, one of which is the displacement of the resident brine by the invading CO<sub>2</sub> plume (Zhang et al. 2011; Juanes et al. 2006). Considering this as a kind of two-phase system, multiphase flow researchers

have delved into supercritical CO<sub>2</sub>-brine (scCO<sub>2</sub>-brine) system with emphasis on capillary pressure-saturation-relative permeability relationships ( $P^c - S - K_r$ ) (Plug and Bruining 2007; Plug et al. 2006; Pentland et al. 2011; Pini et al. 2012; Tokunaga et al. 2013).

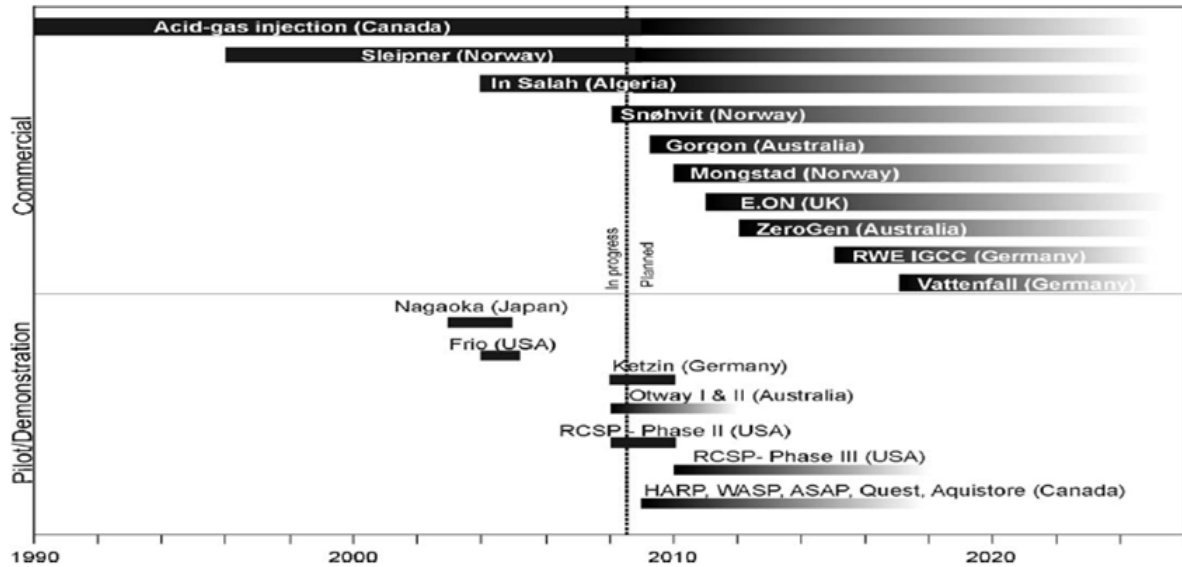


Figure 2.1: Carbon dioxide sequestration operations at pilot and commercial scales worldwide (Michael et al. 2010).

Capillary pressure and relative permeability for wetting and non-wetting phases are parameters of key importance in modelling the two-phase flow processes encountered during transport of immiscible phases in the underground (Aggelopoulos and Tsakiroglou 2008) and they constitute critical parameters used to history match and design field-scale injection projects using reservoir simulators (Doughty 2007). Many publications are available on the behaviour of  $P^c$ - $S$  relationships (Hassanizadeh and Gray 1993; Mirzaei and Das 2007; Nordbotten et al. 2008; Bottero et al. 2011a, b; Goel and O'Carroll 2011; Das et al. 2007) while several others are based on the  $K_r$ - $S$  relationship (Bennion and Bachu 2008; Water et al. 2006; Lenormand et al. 1998; Anderson 1987). Most of these publications consider the cases of oil-water and gas-water systems. So, it will be of specific importance to thoroughly understand how the  $P^c - S - K_r$  relationships behave in the scCO<sub>2</sub>-brine system.

For characterising the scCO<sub>2</sub>-brine system in geological sequestration, two approaches are most commonly considered. Firstly, it involves the use of the theories concerning convection-diffusion-dissolution processes and secondly, it relates to the use of the principles of two-phase flow in porous media. In the first case, the dissolution of the scCO<sub>2</sub> in the aquifer brine is considered and it eliminates the need for determination of capillary pressure. In this process, the carbon dioxide-brine solution is defined to be slightly denser than the

unsaturated brine causing negative buoyancy by moving to the bottom of the aquifer, enhancing safe and permanent storage, which reduces chances of leakage. The convective process promotes mixing of the brine and scCO<sub>2</sub> while enhancing further dissolution of carbon dioxide into the brine (Ozgur and Gumrah 2009). The second approach regards the supercritical carbon dioxide and brine as two immiscible fluid phases, which can be described by  $P^c - S - K_r$  relationships. This assumes that there is a limited dissolution of CO<sub>2</sub> in the brine and that displacement process dominates at least for some period after CO<sub>2</sub> injection.

To consider the scCO<sub>2</sub>-brine system as a two-phase flow system one requires the understanding of the interactions of the fluid-fluid-porous media (i.e., gas-liquid-solid or scCO<sub>2</sub>-brine-rock) in the system. Analogous to an oil-water system, the immiscible displacement of scCO<sub>2</sub>-brine/water system may be affected by the presence of heterogeneity in the media, viscosity and density ratios of the two fluids and the geophysical as well as the geochemical conditions of the domain. For example, media heterogeneities affect the  $P^c - S$  and  $K_r - S$  profiles (Das et al. 2004; Aggelopoulos and Tsakiroglou 2008; Mirzaei and Das, 2013; Khudaida and Das, 2014) while they also raise the value of the irreducible wetting phase saturation (Das et al. 2006). In addition, the heterogeneity (e.g., fractures) may create preferential flow path which increases the effective permeability of the fluid (Aggelopoulos and Tsakiroglou 2008). The permeability to fluid is also affected by the presence of micron-scale heterogeneity (e.g., lamina) where varying intrinsic permeability value the degree of heterogeneity affect the average permeability of the domain (Alabi 2011). These scenarios are important in the choice of geo-sequestration sites as they affect storage capacity of the aquifer and can influence the risks of leakage.

Recent review papers on CO<sub>2</sub> sequestration consider the alternative sequestration in limestone (Stanmore and Gilot 2005), technologies and costs (Abu-Khader 2006), health and safety issues (Zakkour and Haines 2007), analogy between traditional liquid waste disposal and carbon storage (Tsang et al. 2007), storage in marine environment (Huh et al. 2009), pilot projects (Michael et al. 2010), scCO<sub>2</sub>-brine relative permeability experiments (Müller 2011), caprock integrity (Shukla et al. 2010) and present and future challenges (Zahid et al. 2011). Shukla et al. (2010) acknowledge the influences of the fluid-fluid-media characteristics of the scCO<sub>2</sub>-brine system on trapping mechanisms, breakthrough of the injected fluid and capillary sealing of the caprock. Also, Müller (2011) notes that while there are similarities in the measurement of relative permeability for oil-water and CO<sub>2</sub>-water systems, exception exists in the reactivity of core materials with CO<sub>2</sub>, resulting in permeability, porosity and wettability alteration. These pointed to the unique characteristics of the two-phase flow

parameters in the geological sequestration processes. However, Shukla et al. (2010) are primarily concerned about caprock integrity while Müller (2011) investigates the relative permeability experimental methods.

To reliably predict CO<sub>2</sub> storage phenomena, understanding the capillary behaviour of supercritical CO<sub>2</sub> and its dependence on water saturation are essential (Tokunaga et al. 2013). Characterising a system for geological storage of CO<sub>2</sub> also comes with the challenges of dealing with high gas pressure and temperature above ambient conditions as CO<sub>2</sub> is stored at a depth of around 1 km or more from earth's surface (Rutqvist 2011). In addition to changing property of CO<sub>2</sub> at slight variation of conditions in the subsurface, these scenarios might cause non-uniqueness in the functional representation of the system such as those discussed by Das et al. (2006).

The above discussions introduce the practices of geological sequestration and the relevance of two-phase flow (scCO<sub>2</sub>-brine) parameters. It is however equally important to illustrate the challenges and trends found in the literature concerning the determination, application and interpretation of relevant two-phase flow parameters in relation to the carbon sequestration processes. In addressing these issues, this review intends to examine the research activities relating to geological sequestration of CO<sub>2</sub> together with the issues involved in the determination of two-phase relationships for scCO<sub>2</sub>-brine system from experiments, modelling and simulations.

## **2.2 Characteristics of the geological sites**

Geological sites hold the important properties that determine a successful geological CO<sub>2</sub> sequestration projects. In this regards, the geological media should meet some fundamental conditions to ensure successful storage of carbon dioxide. Three of these are capacity, injectivity and confinement (Gunter et al. 2009). Studying and modelling CO<sub>2</sub> sequestration in geological formation need a clear understanding of multi-phase flow characteristics and their behaviour in porous media. The above-mentioned parameters (i.e., aquifer capacity, injectivity and confinement) bear relation to media properties i.e., porosity, tortuosity, permeability, relative permeability, dispersion coefficient, capillarity, connectivity, adsorption and wettability as well as to two-phase flow characteristics in the medium. Some of these media properties in the context of the studies on CO<sub>2</sub> sequestration are discussed below.

### 2.2.1 Porosity and pore size distribution

In their review of characteristics of potential geological formations for CO<sub>2</sub> sequestration, Kopp et al. (2009) explain that geological formations are suitable for carbon dioxide storage if they demonstrate high values of porosity and permeability. These are crucial for storage of high amounts of carbon dioxide and allow its injection to be done economically.

Porosity is the fraction of the aquifer that is composed of voids (Bear 2013). The interconnected voids in the aquifer forms what is referred to as the effective porosity and it determines the effective storage capacity of the aquifer. Chadwick et al. (2008) suggest that the amount of CO<sub>2</sub> that can be stored in a given saline aquifer in terms of a capacity factor C is:

$$C = C^{\text{gas}} + C^{\text{liquid}} \quad (2.1)$$

$C^{\text{gas}} = \langle \phi \cdot S_g \rangle$ ,  $C^{\text{liquid}} = \langle \phi \cdot S_l X_1^{\text{CO}_2} \cdot \rho_l / \rho_g \rangle$  and C is the volume fraction of the reservoir available for storage. C is taken as the sum of the free supercritical CO<sub>2</sub> ( $C^{\text{gas}}$ ) and CO<sub>2</sub> dissolved in the brine ( $C^{\text{liquid}}$ ).  $\phi$  is the effective domain porosity and,  $S_l$  and  $S_g$  are the fractional volumes of the pore space containing liquid and scCO<sub>2</sub> phases, respectively.  $X_1^{\text{CO}_2}$  refers to the mass fraction of dissolved CO<sub>2</sub> in the brine,  $\rho_g$  and  $\rho_l$  are the densities of the scCO<sub>2</sub> and liquid phases, respectively. The angle brackets imply averaging over the spatial domain of storage. Equation (2.1) shows that the porosity,  $\phi$ , plays a very important role in determining the capacity factor of an aquifer and it can serve as a factor to check suitability of an aquifer for storage. According to Espinoza et al. (2011), the volume of CO<sub>2</sub> injected,  $V_{\text{CO}_2}$ , in an aquifer is a function of average aquifer porosity as follows:

$$V_{\text{bulk}} = \frac{V_{\text{CO}_2}}{\phi} \frac{1}{\Psi} \quad (2.2)$$

$\Psi$  is a water or brine displacement efficiency coefficient and it is a function of the media and process characteristics. In essence, the effective porosity of an aquifer is a key factor in its capacity to store CO<sub>2</sub>. According to Chadwick et al. (2008) a porosity greater than 20% is a positive indicator in a site selection while a value of less than 10% porosity calls for caution. The porosity of sediment tends to decrease with depth as the effective stress on the sediment increases. The pore size and structure of an aquifer tend to change under the same influence as the pore size is a function of porosity and specific surface. Also, due to enormous complexity of the pore structure of any porous media in terms of the number of

pores, their size, shape, orientation, and manner of interconnection of the pores, it often becomes important to consider the pore size distributions of an aquifer. The pore size distribution is defined as a fraction,  $f$ , of total pore spaces within a range of pore diameter  $\delta$  and  $\delta + d\delta$  as expressed in the following distribution function:

$$\int_0^{\infty} f(\delta) d\delta = 1 \quad (2.3)$$

Information concerning the pore size distribution of a particular aquifer can be obtained from analysis of core measurements and even geophysical logs of adjacent wells. In such sample, the  $P^c$  required to force a liquid (e.g., mercury) into the pores can be used to approximate  $\delta$ , with the following equation (Bear 2013):

$$\delta = 4\gamma \cos\theta / P^c \quad (2.4)$$

$\gamma$  is the interfacial tension between the two fluids and  $\theta$  is the contact angle. Pore size distributions are useful in the analysis of permeability reduction, e.g., as a result of clay swelling, microbial growth in pores, mineral precipitation, etc., (Tiab and Donaldson 2004). Theory for the penetration of non-wetting fluid into the pore was developed by Ritter and Drake (1945) while Burdine et al. (1950) applied it to study two-phase flow in reservoir rocks. In the absence of typical mercury injection information, pore size distribution information can be obtained from measurements made by porous semi-permeable diaphragm method (Burdine 1953). Other methods for determining pore size distribution, e.g., adsorption isotherm (Dollimore and Heal 1964; Seaton and Walton 1989) and induced polarization logging measurements (Vinegar and Waxman 1987) have been reported as well. Information on pore size distribution is important in the characterization of the displacement of brine by  $scCO_2$  in the saline aquifer as it can be used to calculate the relative permeability of the phases (Burdine 1953).

Changing porosity, mineral precipitation, dissolution and change in effective stress are some of the factors that result in the evolution of pore size distributions of a reservoir. Mineral precipitation in the porous media is often affected by pore size (Emmanuel et al. 2010) and vice versa. While the large pores permit ready precipitation of minerals, the smaller pores might inhibit the process leading to reduced bulk reaction rate, which in effect stabilises the porosity. Also, geochemical reaction with rock minerals is considered to be one of the trapping mechanisms for long-term sequestration. The pore lengths and their distribution might affect how readily the reactions occur at different parts of the sediment. Precipitation of quartz was found to be inhibited in pores smaller than 10  $\mu\text{m}$  in diameter. Also, the pore size

distribution will also affect the dissolution rate which is another mechanism identified for trapping as varying solubility is applicable (Emmanuel et al. 2010). In addition, the standard deviation of pore size distribution affects CO<sub>2</sub> breakthrough into a medium (Espinoza et al. 2011).

### 2.2.2 Intrinsic, relative and effective permeability

Permeability, as the name suggests, is an indication of how easily a fluid will pass through a porous medium. It can be defined by Darcy's law (Bear 2013; Virnovsky et al. 1995) for an incompressible fluid having viscosity,  $\mu$ , which flows through a porous medium with length,  $L$ , and cross sectional area,  $A$ , at flow rate,  $q$ , and pressure difference of  $\Delta P$  across the domain. The isotropic permeability,  $K$ , of the porous medium is defined as:

$$K = \frac{q\mu L}{A\Delta P} \quad (2.5)$$

Its value is dependent on the porous structure of the medium. Appropriate permeability needs to be maintained in the medium to ensure effective storage of CO<sub>2</sub> (Rutqvist 2012). However, the permeability of a medium is affected by the reactions, dissolution and precipitations of the rock minerals. Simulations have shown that following CO<sub>2</sub> injection, dissolution of carbonate cement initially increases the sediment porosity but subsequent reactions result in dissolution of feldspar and precipitation of carbonate minerals and clay leading to reduction in permeability and porosity (Gaus et al. 2005). This implies that the original permeability of the sediment may alter in the course of injection and will affect the prediction of the process behaviour.

Meanwhile, the flow processes (like that in geological sequestration system) can hardly occur with a single fluid. This reality leads to the concept of relative permeability that represents the two-phase relationships of scCO<sub>2</sub>-brine system in a geological media. While the permeability is the intrinsic property of the medium, relative permeability is the characteristic of the fluid-fluid-solid system and it comes to play when two or more fluids are present in the porous medium. The term describes the extent to which one fluid is hindered by the other. Though relative permeability is dependent on a number of factors, available experimental evidence indicates the concept of relative permeability that depends on only saturation is a good approximation for all practical purposes (Bear 2013). It is expressed through Darcy's law set up for individual phase  $i$  that flows in the pore space:

$$q_i = \left( \frac{KK_{ri}}{\mu_i} \right) A \frac{\Delta P_i}{\Delta x} \quad (2.6)$$

$q_i$ ,  $K_{ri}$ ,  $\mu_i$ , and  $\Delta P_i$  refer to the flow rate, relative permeability, viscosity and the pressure drop, respectively for phase  $i$ . The ratio:  $KK_{ri}/\mu_i$  denotes the "mobility" of phase  $i$ . Figure 2.2 shows the relative permeability plots of the CO<sub>2</sub>-water system. It consists of primary, secondary and tertiary drainage of the system (see, Bear (2013) for definitions of these processes). It can be seen that following the primary drainage, the residual water saturation continues to decrease in subsequent drainages. This is attributed to dissolution property of CO<sub>2</sub> in water and a contrast was shown in N<sub>2</sub>-water system which shows a fairly similar residual saturation for the subsequent drainages owing to lesser solubility of N<sub>2</sub> (Pistone et al. 2011). Water relative permeability,  $K_{rw}$  is higher for larger portion of the water saturation though the value reduces with subsequent drainages while that of CO<sub>2</sub> remains low. Relative permeability of CO<sub>2</sub>,  $K_{rg}$ , remains low owing to dissolution and diffusion into smallest pore spaces with no need to overcome the entry pressure. Evolution of CO<sub>2</sub> from this dissolution state displaces previously immobile water which further impedes CO<sub>2</sub> mobility (Pistone et al. 2011). Thus, the residual saturation of water continues to reduce following subsequent drainage.

Bickle et al. (2007) concluded that the relative permeability-residual saturation relations have a great influence on average carbon dioxide saturation as well as plume evolution velocity and as such, have a great effect on storage capacity. Hysteresis in relative permeability has the tendency to enhance residual trapping. This is defined, for a particular CO<sub>2</sub> saturation, as a reduction in relative permeability during imbibition compared to drainage (Chadwick et al. 2008). Strong hysteresis in relative permeability results in 'sticky' plumes that leave behind relatively higher amounts of CO<sub>2</sub> trapped compared to weak hysteresis leaving behind small amount. This scenario was observed in the simulation of sequestration project at Sleipner (Norway) (Chadwick et al. 2008).

On the basis of a large number of drainage experiments with various types of media, Brooks and Corey (1964) suggest the following relative permeability function:

$$k_{rw} = (S_e)^{(2+3\lambda)/\lambda} = \left(\frac{P_b}{P^c}\right)^{(2+3\lambda)} \quad P^c \geq P_b \quad (2.7)$$

$$k_{mww} = (1 - S_e)^2 (1 - S_e^{(2+\lambda)/\lambda}) = [1 - (P_b/P^c)^\lambda]^2 [1 - (P_b/P^c)^{2+\lambda}] \quad (2.8)$$

where  $\lambda$  is the pore-size distribution index,  $P_b$  is referred to as the bubbling or threshold pressure or entry pressure.  $S_e$  is the effective saturation and can be expressed as  $S_e = (P_b/P^c)^\lambda$  for  $P^c \geq P_b$ . Even though the above results are deduced for isotropic media, their validity makes them applicable to a wide range of pore-size distributions (Bear 2013).

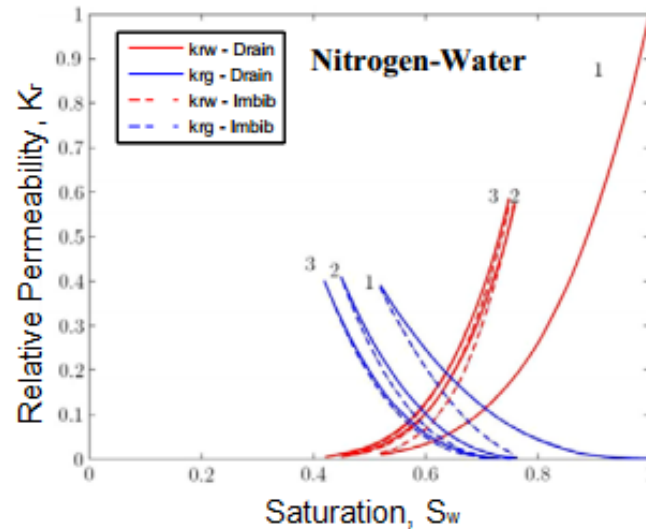


Figure 2.2: Relative permeability curves for CO<sub>2</sub> (blue) and water (red) (Pistone et al. 2011).

Several factors can affect the effective permeability of an aquifer. Pore size distributions, media heterogeneities and scale can be of considerable impact. This was corroborated by Alabi (2011) investigating the difference in the flow rate of fluid in homogeneous media and different types of heterogeneous media. The author found out that the permeabilities of heterogeneous media are lower than the permeabilities of homogeneous media and that mixed heterogeneity has higher permeability than layered type. This implies that fluid flows faster in mixed heterogeneous sample than the layered type.

### 2.2.3 Threshold pressure (bubbling pressure)

In scCO<sub>2</sub>-brine system, the pressure in the invading fluid (i.e., scCO<sub>2</sub>) at the interface between fluid-fluid and rock system is required to exceed the minimum entry pressure of the sediment. This implies a certain pressure must be reached in the non-wetting fluid before it begins to penetrate the sample, displacing the wetting fluid contained in it (Bear 2013). The minimum pressure needed to initiate this displacement is called the threshold pressure (or bubbling pressure) or non-wetting fluid entry value or breakthrough pressure. This parameter is also a pointer to injectivity of a medium and its excessive magnitude can pose serious risk to the caprock.

Understanding of the threshold pressure of a caprock saturated with water is important when a gas is to be stored in the reservoir underneath the caprock. This is also the breakthrough pressure when CO<sub>2</sub> can enter through the caprock. Its value depends on the mean pore size related to specific surface  $S_s$ , standard deviation in pore size distribution and void ratio  $e$  as well as the wettability of the minerals in the presence of water and CO<sub>2</sub> (Espinoza et al.

2011);  $e = e_{1kPa} - C_c \log(p'/1kPa)$  where  $p'$  is the *in situ* effective stress and  $e_{1kPa}$  is the critical state void ratio when the mean confining stress is 1kPa. Espinoza and Santamarina (2010) gave expression for breakthrough pressure,  $P_{thru}^*$ , by extension of Laplace's capillary pressure equation:

$$P_{thru}^* = \Psi \frac{S_s \rho \gamma \cos \theta}{e} \quad (2.9)$$

$\Psi$  is a factor that depends on the clay fabric and grain size distribution and a value of  $0.04 < \Psi < 0.08$  applies to smectite clay barriers and,  $\gamma$  is the interfacial tension. This interfacial tension is an important property of the two-phase system. Its influence depends on the prevailing conditions, e.g., temperature, pressure, salinity and cation valence. Detail discussions and the implication of these factors on  $\gamma$  will be made later in this work.

Aside the sediment where actual injection and storage occur, threshold capillary pressure is an important parameter of the caprock that gives indication about its sealing capacity or integrity of caprock. It combines with caprock permeability to determine possibility of leakage and its rate of occurrence (Fleury et al. 2010; Pusch et al. 2010). Thus, the threshold pressure for the sediment must be well below that of the caprock to avoid undue development. Also, since the injection and the *in situ* displacement processes result in pressure fluctuations within the system, the caprock entry pressure should be well in excess of any possible pressure increase for long-term safety. Practical caprock core from Sleipner (Norway) was reported to possess greater than 3.3 MPa capillary entry pressure to scCO<sub>2</sub> while that of another project from Schwarze Pumpe (Schweinrich) is predicted to be in the range 4 to 40 MPa (Chadwick et al. 2008).

#### 2.2.4 Wettability

Wettability is the ability of a liquid to adhere to a solid surface due to their intermolecular interactions. It has a significant impact on the relative permeability-saturation relationships and can be determined from the combination of cohesion forces, which cause the drop to prevent contact with the solid surface, and adhesion forces that try to spread the liquid across the solid surface in a flow system. It is among the factors that determine the entry pressure of the geological media (Espinoza et al. 2011). If the medium is CO<sub>2</sub>-wet, it becomes easier for the invading CO<sub>2</sub> to displace the resident brine. However, if the medium is water-wet, then higher entry pressure is required for the invading CO<sub>2</sub> to penetrate the medium. Publications on water-wet, CO<sub>2</sub>-wet and mixed-wet media have been reported. In relation to carbon geological sequestration, many of the representative media samples, quartz, calcite, kaolinite, microcline and illite were reported to be water-wetting (Wang et al.

2012). The possibility of the alteration in wettability based on saturation history of the medium was also reported (Plug et al. 2006).

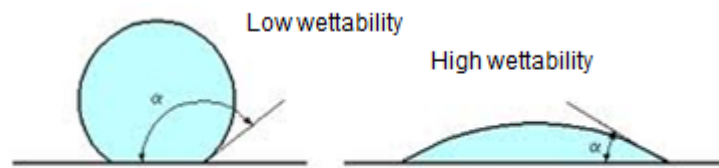


Figure 2.3: Wettability index of liquid as a function of contact angle ( $\alpha$ ):  $\alpha > 90^\circ$  (non-wetting liquid),  $\alpha < 90^\circ$  (wetting liquid). The possibility of  $\alpha=0^\circ$  (perfectly wetting) is not shown.

Wettability is related to capillary effects and occurs at different degrees according to the angle at which fluid1-fluid2 interface meets with the fluid1-solid interface. This contact angle provides an inverse measure of wettability (Shafrin and Zisman 1960). Importance of wettability in the determination of  $P^c - S - K_r$  relationships is great and the *in situ* alteration in wettability can lead to error in calculation and predictions if not considered. Wettability indices (e.g., USBM index, Ammott index and Hammervold-Longeron (HL) index) are employed in quantifying wettability and its changes for the drainage and waterflooding processes in the porous media using the  $P^c$ - $S$  curves (Pentland 2011). Table 2.1 shows the wettability indices for oil–water systems.

By implication, partial-wetting behaviour of  $\text{CO}_2$  (e.g., limestone rock under reservoir condition) results in lower capillary pressure and higher mobility for brine and can lead into lower capillary breakthrough pressure of the caprock (Chalbaud et al. 2010)

Table 2.1: Wettability indices for oil-water indices (Pentland 2011)

Index	Water-wet	Neutrally-wet	Oil-wet
Ammot (displacement by water ratio)	Positive	0	0
Hammervold-Longeron	1	0	-1
USBM	near 1	near 0	near -1

## 2.3 *In situ* trapping mechanisms of injected CO<sub>2</sub>

Trapping mechanisms come under two major categories: physical and chemical trapping mechanisms. The physical mechanism involves trapping by structural and stratigraphic patterns of the aquifer sediment and caprock while chemical mechanisms include dissolution in the brine, complex mineralisation with host rock, adsorption on coal and CO<sub>2</sub> hydrate formation (Espinoza et al. 2011). Some of these trapping mechanisms are discussed below under the broad headings of structural, dissolution, capillary and mineral trapping.

### 2.3.1 Structural trapping

Structural trapping arises from physical nature of the aquifer, e.g., anticlines or faults intercepting the upward mobile plume of CO<sub>2</sub>. Together with stratigraphic as well as hydrodynamic trappings, they constitute physical trapping mechanisms that control the initial period of CO<sub>2</sub> storage (White et al. 2001). Structural trapping occurs in the presence of a structural enclosure together with a seal forming low permeability cap-rock (Omambia and Li 2010). The injected carbon dioxide rises to the upper layer of the aquifer above the resident brine by the power of buoyancy and is immobilised under the impermeable anticline structure.

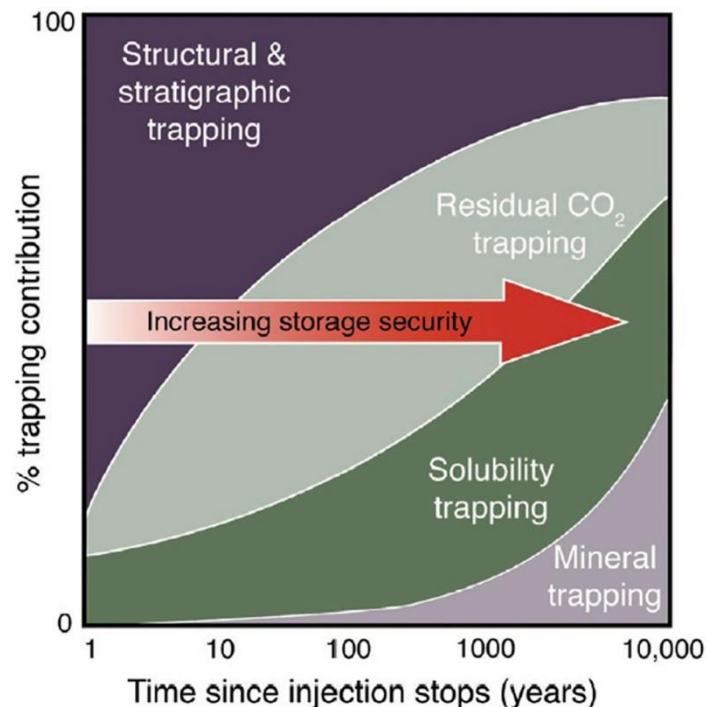


Figure 2.4: Mechanisms of CO<sub>2</sub> Trapping with time (Benson and Cole 2008).

In a sequestration project at Sleipner (Norway) structural traps are the key features focused upon prior to CO<sub>2</sub> injection as they are key to favourable geological site characterisation (Chadwick et al. 2008). From 1996, the CO<sub>2</sub> plume had reached the top of the reservoir by 1999 at Sleipner (Shukla et al. 2010). Figure 2.5 depicts this mechanism in a reservoir as CO<sub>2</sub> trapped under caprock.

### 2.3.2 Residual trapping

Residual trapping occurs as a result of the hysteresis effect in the permeability of the scCO<sub>2</sub> phase especially when the saturation direction is reversed. It is a quick process because of the tight and rigid sponge nature of the porous rock (Omambia and Li 2010). As the scCO<sub>2</sub> is injected into the deep aquifer formation, it displaces the resident fluid. When the scCO<sub>2</sub> continues to move, the previous brine takes its place trapping some of the scCO<sub>2</sub> adhered to the pore surface and stay behind trapped in the pore spaces as residual droplets rendered immobile like water in a sponge (Taku Ide et al. 2007). Mechanisms of CO<sub>2</sub> trapping in the reservoir are depicted in Figure 2.5.

The trapping of a phase in this manner can be characterised by the relationship between initial and residual saturation, known as the capillary trapping curve.

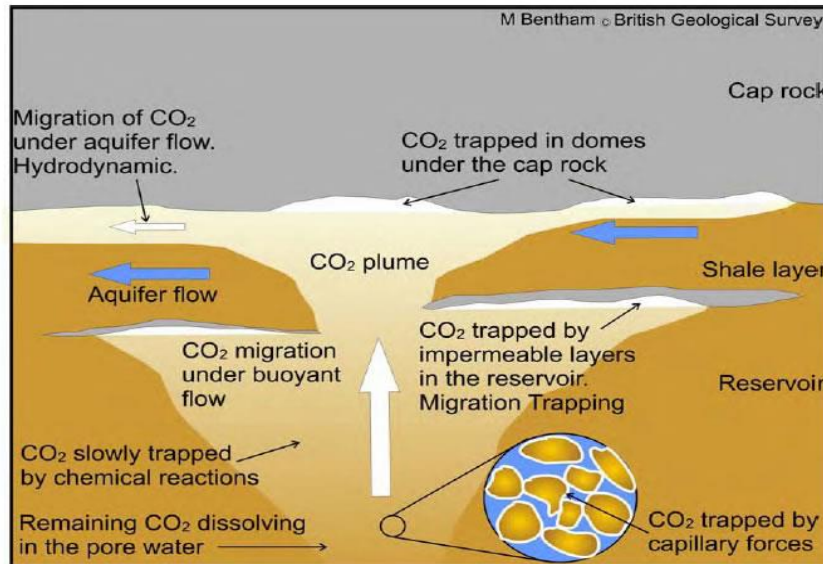
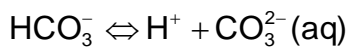
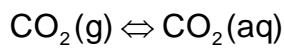


Figure 2.5: Various mechanisms of CO<sub>2</sub> trapping in the reservoir (Bentham 2006)

This phenomenon can be characterised by maximum trapped saturation and the form of the capillary trapping curve as these depict the physics of this phenomenon and also give an important indication of system wettability.

### 2.3.3 Solubility trapping

It is envisaged that the long-term sequestration of CO<sub>2</sub> in deep saline aquifers will occur via dissolution in the brine and/or chemical complexation with the formation (White et al. 2003). Solubility trapping occurs when CO<sub>2</sub> in gaseous or supercritical state dissolves in the aquifer brine at the prevalent conditions of temperature, salinity and pressure (Omambia and Li 2010). This results in the increase of the solution density and lowered pH as shown in Figure 2.6. As the CO<sub>2</sub> dissolves in water, part of this mixes with the water and forms carbonic acid which goes on to produce bicarbonate with hydrogen ions. This reduces the pH of the system at reservoir conditions to approximately 3. The following steps represent the ionization process:



Being heavier than other surrounding fluids as a result of the dissolved CO<sub>2</sub>, convective currents are created causing the denser solution to settle at the bottom of the aquifer trapping the CO<sub>2</sub> more securely. The lighter brine with less dissolved CO<sub>2</sub> then rises to the top of the rock formation (Silin et al. 2008). The mass density of brine-CO<sub>2</sub> solution,  $\rho_{sol}$  (kg/m<sup>3</sup>), can be estimated from equation (2.11) (Espinoza et al. 2011):

$$\rho_{sol} = \rho_w + m_{\text{CO}_2} \chi_{\text{CO}_2} - \chi_{\text{CO}_2} \rho_w V_{\phi} \quad (2.11)$$

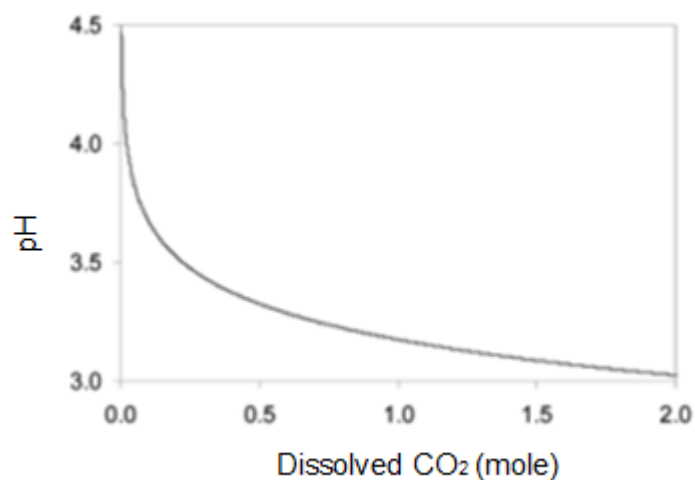


Figure 2.6: Solution pH as a function of solubility of CO<sub>2</sub> in brine (Espinoza et al. 2011).

$\rho_w$  (kg/m<sup>3</sup>) is the density of pure water,  $\chi_{CO_2}$  (mol/m<sup>3</sup>) is the CO<sub>2</sub> concentration in water,  $m_{CO_2}$  (kg/mol) is the molecular weight of CO<sub>2</sub>,  $V_\phi$  (m<sup>3</sup>/mol) is the apparent molar volume of CO<sub>2</sub> as a function of temperature, T(C) expressed by Garcia (2001) as.

$$V_\phi = 37.51 \cdot 10^{-6} - 9.585 \cdot 10^{-8} T + 8.740 \cdot 10^{-10} T^2 - 5.044 \cdot 10^{-13} T^3 \quad (2.12)$$

Densification of the brine-CO<sub>2</sub> solution promotes the convective mixing in the aquifer, which improves the effectiveness of this trapping mechanism. This continues until the system reaches equilibrium condition.

Solubility is affected by the temperature and pressure of the system, and the pore size distribution. So, the choice of basins with higher density of large pores will aid this mechanism (Emmanuel et al. 2010). The dissolution increases with pressure and decreases with temperature as shown in the chart presented by Dodds et al. (1956) with different patterns of dissolution below and above critical conditions. Also, salt concentration of the brine has been shown to affect the solubility of CO<sub>2</sub>. There appears to be an indirect linear relationship between CO<sub>2</sub> solubility and salt concentration as shown in Figure 2.7. This implies that aquifer with lower brine concentration favors this dissolution mechanism.

A dimensionless number, namely, Rayleigh number (Ra) is important in the dissolution-convection processes involved in the solubility trapping. Ra is particularly associated with buoyancy-driven flow. It is dependent on the fluid property and the characteristic length of the system expressed as (Farajzadeh 2009):

$$Ra = \frac{\beta_c g \Delta c R^3}{\nu D} \quad (2.13)$$

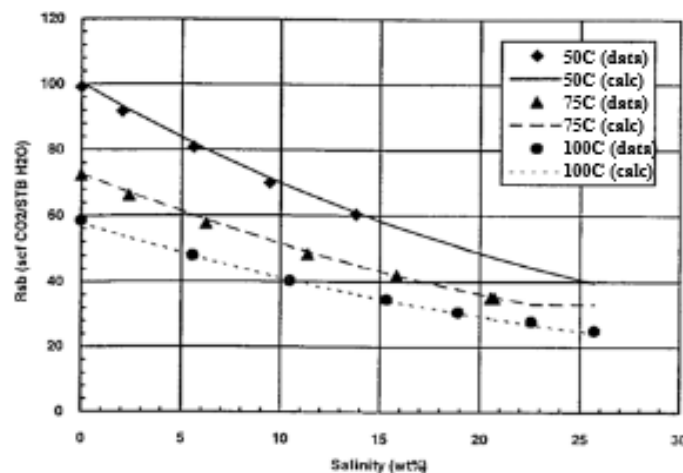


Figure 2.7: CO<sub>2</sub> solubility as a function of salinity (Chang et al. 1998)

$\beta_c$  is the volumetric expansion coefficient ( $\text{m}^3/\text{mol}$ ),  $g$  is the acceleration due to gravity ( $\text{m/s}^2$ ),  $c$  is the gas concentration ( $\text{mol/m}^3$ ),  $R$  is the characteristic length of the system ( $\text{m}$ ),  $\nu$  is the kinematic viscosity ( $\text{m}^2/\text{s}$ ) and  $D$  is the diffusion coefficient ( $\text{m}^2/\text{s}$ ). As  $Ra$  increases mass transfer of  $\text{CO}_2$  into the brine-saturated porous medium increases and the concentration front moves faster (Farajzadeh 2009). Low  $Ra$  results into the steady-state concentration while its high value leads to the system instability (Ouakad 2013).

### 2.3.4 Mineral trapping

When carbon dioxide is dissolved in brine, it decreases the pH of the solution leading to acidification as expressed in equation (2.10). This acidified solution in contact with host rock results in mineral dissolution, precipitation and reactions, which are the processes that induce mineral trapping. With time, the reactions of the acid with dissolved ions and rock minerals in the aquifer lead to chemical complexes such as magnesite, dolomite, calcite, drawsonite and siderite. These occur as products of dissolution and complexing, resulting in chemical precipitation of solid carbonate minerals (secondary carbonates). It is regarded as a permanent sequestration process. However, it is a slow process with significant contribution occurring only in the geological time scale.

Reaction between  $\text{CO}_2$  and alkali aluminosilicate minerals will generate a soluble alkali bicarbonate as well as carbonates promoting the mechanism of solubility trapping. In this line of series, parallel and complex reactions and processes, pH of the system changes dramatically as the dissolution of carbonate ions raises it up to 5 while aluminosilicates can take the pH up to 8 (Espinoza et al. 2011).

Beni et al. (2012) evaluated the potential of mineral trapping on  $\text{CO}_2$  sequestration in the sandstone formation near Minden in Germany. They found that after about 200 years, this mechanism contributes significantly in the storage and the prospect increases even more with time. The typical reaction of  $\text{CO}_2$ -acidified water with silicate minerals is represented in equation (2.14) (Drever and Stillings 1997):



Equation (2.14) has a reaction rate of  $1.26 \times 10^{-14} \text{ mol.m}^{-2}.\text{s}^{-1}$  (White et al. 2004) and the reaction is not affected by dissolution of  $\text{CO}_2$ . But the reaction with aluminosilicates (including

feldspars, micas, clays) turns the system alkaline with pH up to 8 (Li et al. 2006) while faster carbonate reactions raise the pH up to 5 (Algive et al. 2009).

## 2.4 Modelling and simulations of scCO<sub>2</sub>-brine-rock system

Modelling and simulations of geological sequestration processes are highly required to assess the feasibility of CO<sub>2</sub> sequestration into a particular aquifer or reservoir. Modelling the sequestration entails considerations for the technicalities of the storage systems and the economics. This ranges from capture, transport and storage together with the associated costs brought together in discounted cash flow calculations (Chadwick et al. 2008). However, the interest of this section is to discuss the basics of modelling and simulations involved in geological sequestration.

Generally, the geological sequestration systems can be described using multiphase and multi-component processes with consideration for non-isothermal conditions occurring near the injection region owing to CO<sub>2</sub> expansion with Joule-Thompson effects (Class et al. 2009). Basic multiphase equations are built upon mass and momentum conservations as well as various constitutive equations. For the simultaneous flow of CO<sub>2</sub> and water, the governing equation can be expressed as:

$$\phi \frac{\partial S_i}{\partial t} + \nabla \cdot q_i = 0 \quad (2.15)$$

'i' stands for the phases; CO<sub>2</sub> (g) or brine/water (w). S is the phase saturation, q the velocity and  $\phi$ , the porosity. The velocity q is given by the extended version of Darcy's law;

$$q_i = -K_r K / \mu_i [\nabla P_i + \rho_i g \nabla z] \quad (2.16)$$

For radial injection in the aquifer (Saripalli et al. 2001);

$$q_{r,i} = Q_i f_i(S_i) / 2\pi r h \quad (2.17)$$

$K_r$  represents the relative permeability for phase i and K is the medium intrinsic permeability. P is the phase pressure,  $\rho$  the density and g is the acceleration due to gravity,  $\nabla_z$  is the gradient of upward unit vector. Q is the injection rate and f is the phase fractional flow. For the injected phase, substituting for radial velocity in equation (2.15) results into two-phase displacement theory based on the Buckley-Leverette theory (Saripalli et al. 2001):

$$\frac{Q_g f_g}{2\pi r h \phi} \frac{\partial S_g}{\partial r} + \frac{\partial S_g}{\partial t} = 0 \quad (2.18)$$

In addition to the above, a detailed description of the constitutive equations for the sequestration system requires several mathematical expressions which include the CO<sub>2</sub>

saturation in the expanding radial plume and its derivative, equation of state for the phase partitioning behaviour of CO<sub>2</sub>-H<sub>2</sub>O mixture, models for dissolution of CO<sub>2</sub> in brine and vice versa with their derivatives along the horizontal and vertical regions and pressure distribution in the region of the plume. While the radial flow of the injected phase is inserted as velocity in equation (2.18) (Saripalli et al. 2001), the buoyant flow of the process needs a separate velocity expression as a function of radius. Furthermore, incorporating expressions for leaks is desired for robust modelling and analysis of injection and sequestration processes.

For CO<sub>2</sub> leaks scenarios, two significant processes are of concern: vertical migration as a free phase through fractures and buoyancy driven flow through permeable zones of a water-saturated caprock were identified (Huo and Gong 2010; Saripalli et al. 2001). The Young-Laplace relation for capillary pressure provides a handy expression for determining the entry capillary pressure from the values of two-phase interfacial tension and pore size obtained for the caprock (Singh et al. 2010). Thickness of the CO<sub>2</sub> bubble layer near the caprock will provide the needed parameter for the exerted pressure on the confinement and expression for free phase flow of CO<sub>2</sub> through the aperture is required for the complete description of the leak scenario. In the very robust case, incorporating chemical reactions from dissolution, mineral precipitations, various trapping mechanisms are highly desired. The above scheme can be simplified for easy solution depending on the level of analysis desired but the more processes that are incorporated into the model the better the simulation and the more robust and better its application. This calls for the assessment of the currently available simulators. Though, it is recognised that the solution methods become complicated with complex multi-process models.

Popular approaches to the solution of mathematical modelling are analytical, semi analytical and numerical techniques. For example, Woods and Comer (1962) obtained an analytical solution to equation (2.18) for radial injection of gases into an initially water-saturated reservoir. Similarly, Nordbotten et al. (2005) provide an analytical solution to the space-time evolution of a CO<sub>2</sub> plume. However, for very complex problems, non-linearity in constitutive relations often defies analytical solution. As such, numerical solution is often applied. Numerical solution allows simulations that incorporate diverse injection wells with varying injection rates, heterogeneous geologic formations, and simultaneous chemical reactions as well as mass transfer processes. If sufficient data are available, achievable CO<sub>2</sub> saturation, local or regional pressure constraints, dissolution as well as residual saturation can be assessed with numerical simulation as they are dependent mainly on the reservoir and fluid properties as well as injection strategies (Chadwick et al. 2008).

Software designed for hydrocarbon systems in the oil industries are easily adaptable to CO<sub>2</sub> storage as evident by code inter-comparison study (Pruess et al. 2004). However, currently many numerical simulators have emerged in the field of sequestration processes with function-specific as well as general applications. They include NUFT-SYNEF (Morris et al. 2011a; Morris et al. 2011b), STOMP (White 2002), FEMH (Bower and Zyvoloski 1997), ECLIPSE-VISAGE (Ouellet et al. 2011), OpenGeoSys (Wang and Kolditz 2007), TOUGH2 (Pruess et al. 1999), TOUGHREACT (Xu et al. 2006), TOUGH-FLAC (Rutqvist 2011; Rutqvist et al. 2002), CODE-BRIGHT (Olivella et al. 1994; Vilarrasa et al. 2010), DYNAFLOW (Preisig and Prévost 2011), STARS (Bissell et al. 2011). Also, COORES, DuMux, GPRS, MUFTE, MoReS, ROCKFLOW and ELSA are some of the models with capability for simulating different carbon sequestration scenarios and are involved in the benchmark study for the inter comparison of mathematical and numerical models in the context of geological carbon sequestration (Class et al. 2009). In some (e.g., TOUGHREACT) fluids and heat flows are coupled with reactive geochemistry to enhance applications in geological carbon sequestration.

The simulation code, 'subsurface transport over multiple phases (STOMP)' developed using advance computational tools by Pacific Northwest National Laboratory (PNNL, Washington) has the ability for simulating fully coupled mass and heat transport with kinetic and/or equilibrium controlled chemical reactions, temporal and spatial responses to injection, injectivity, hydrogeological and fluid properties change (White and McGrail 2005). Class et al. (2009) emphasised the investigation of influence of gridding, model concepts and mechanisms to ensure quality control and assessment of numerical simulators. However, further developments are required in the ability of the simulators to quantify and relate leak factors on a site-specific basis. This should establish the threshold values that may compromise the reservoir integrity. For example, one needs to determine what quantity of CO<sub>2</sub>, in conjunction with gas-brine-rock interactions and time will result in leakage. Ability to easily predict this scenario will afford the researchers the opportunity to establish site-specific limit of injection. For example, the work of Schwartz (2014) using TOUGHREACT presented a leakage factor: transmissibility. This was established for a potential leak zone as a product of width and permeability with a threshold value of  $1.7 \times 10^{-3} \text{ m}^3$ . This is established based on the media property. However, such threshold established on gas-brine-media and time factors together with associated geophysical and geochemical processes will serve a caution on the limit of sequestration for site-specific assessments.

## 2.5 $P^c$ - $S$ - $K_r$ relationships and phase characteristics in $scCO_2$ -brine system

Some properties of  $CO_2$ -water systems have been discussed in the previous sections and are shown to be temperature and pressure dependent. Among them, the interfacial tension of  $CO_2$ -water had been shown to decrease with increasing pressure and attains a plateau in the supercritical state (Espinoza and Santamarina 2010; Kvamme et al. 2007). In contrast, contact angle of the system also changes with pressure relative to the wettability of the medium. It increases with pressure on oil-wet surfaces and decreases slightly on water-wet surfaces (Chiquet et al. 2007; Espinoza et al. 2011). The implication of this behaviour on two-phase flow characteristics can be discerned based on Young-Laplace relation:

$$P^c = 2\gamma^{wn} \cos\theta / r \quad (2.19)$$

where  $P^c$  decreases with decrease in interfacial tension,  $\gamma^{wn}$ , and increase in contact angle.

Researchers of multiphase flow have reported patterns of  $P^c - S - K_r$  relationships for multiphase flow and expatiated on number of factors affecting these relationships. Most of the works are published for oil-water systems but of the recent ones, some studies relating to carbon sequestration can be found. Changes in the interfacial tension as well as the contact angle will have impact on capillary pressure, residual saturation, evolution of flooding, capillary effects and relative permeabilities (Espinoza et al. 2011). Below, the reports presented and the approaches adopted are examined.

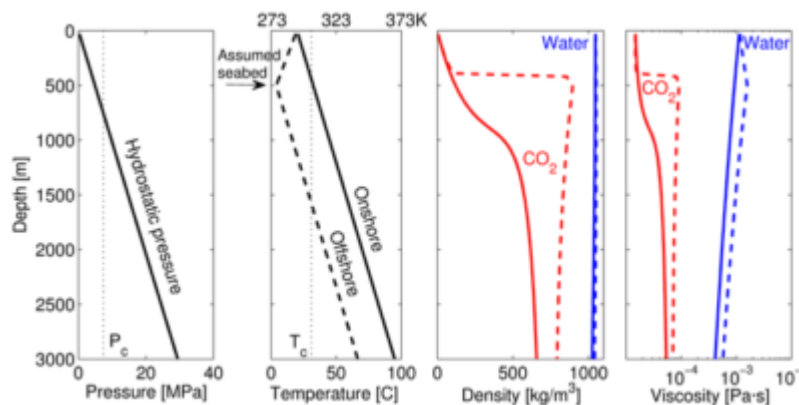


Figure 2.8: Density and viscosity of water and  $CO_2$  with depth (Espinoza et al. 2011)

### 2.5.1 Effects of viscosity and density ratios of $CO_2$ on $P^c$ - $S$ - $K_r$ relationships

The density and viscosity of the CO<sub>2</sub> have been shown to vary under different conditions of pressure and temperature. In Figure 2.8, the density of CO<sub>2</sub> can be seen following nonlinear rise from the surface to the injection bed about 1 km below ground and then follow a fairly straight line into a deeper injection field about 3 km down for the onshore sequestration. For the offshore operation this pattern changes as the density rises rapidly around the sea bed and then remains almost constant henceforth and larger at the same depth compared to onshore. In another part of Figure 2.8, the viscosity of CO<sub>2</sub> in offshore and onshore sequestration follows similar, though with slight variation, values. On the other hand, Figure 2.8 shows that the density of water remains constant with depth while there is slight variation in its viscosity with depth. Implication of the above properties behaviour is that at different depths of injection of CO<sub>2</sub> for sequestration, the ratios of viscosity and density of CO<sub>2</sub> to that of brine will vary. Viscosity and density ratios are some of the parameters identified to affect two-phase flow in porous media (Das et al. 2007; Goel and O'Carroll 2011). In the context of carbon sequestration, viscosity ratio refers to the ratio of the viscosity of the non-wetting phase i.e., scCO<sub>2</sub> ( $\mu_{CO_2}$ ) to that of the wetting phase i.e., water or brine ( $\mu_w$ ). This ratio is mathematically expressed for viscosity as:  $\mu_r = \mu_{CO_2} / \mu_w$  and density as:  $\rho_r = \rho_{CO_2} / \rho_w$ , respectively. While discussing the rate dependency of the  $P^c - S - K_r$  relationships for the oil-water system, Joekar-Niasar and Hassanizadeh (2011) stated that the invading front in a two-phase system becomes unstable if the viscosity ratio is less than one under drainage or if greater than unity under imbibition while the front becomes stable if the ratio is higher than one in drainage and lower than one in imbibition. This implies that the displacement of brine by scCO<sub>2</sub> may face instability and the lower the viscosity ratio at shallower depth, the higher the instability at the displacement front.

Das et al. (2007) pointed out that density ratio effect on  $P^c - S - K_r$  relationships is dependent on the flow direction. The saturation-rate dependency of the relationships also known as dynamic effect increases as density ratio increases if the flow is in the downward direction while the trend is still on the increase for decreasing density ratio if the flow is in the upward direction (Das et al. 2006). Implication of the above discussion in the characterisation of  $P^c - S - K_r$  relationships for the scCO<sub>2</sub>-brine system in different geological media will require applicable mathematical functions, which in no doubt will be complex. Otherwise, the relationship will be determined for individual sites.

### 2.5.2 Instability in the displacement of fluid/fluid interface in scCO<sub>2</sub>-brine-porous media system

In a two-phase system in porous media, instability at the displacement front can occur because of the higher mobility phase displacing a lower mobility phase as in the case of the scCO<sub>2</sub>-brine system leading to fingering of the displacing phase (Berg and Ott 2012). This can be observed in both miscible and immiscible displacement conditions (Van Meurs 1957; Saffman and Taylor 1958). Analytical model by Van Wunnik and Wit (1989) had earlier shown the source of this condition to be as a result of viscous pressure gradient leading to a steeper pressure gradient of the lower-mobility phase letting the finger grow. Among the factors controlling this condition, mobility is defined as the ratio of the relative permeability ( $K_r$ ) of the phase to its viscosity ( $\mu$ ) and mobility ratio ( $m$ ) as the ratio of the mobility of the displacing phase to that of the displaced. For CO<sub>2</sub> displacing brine,  $m$  is expressed in equation (2.20):

$$m = \frac{K_m/\mu_n}{K_{rw}/\mu_w} \quad (2.20)$$

$K_m$  and  $\mu_n$  are the relative permeability and viscosity of CO<sub>2</sub>, respectively while the  $K_{rw}$  and  $\mu_w$  are the respective relative permeability and viscosity of water. It determines the stability and the efficiency of the displacement (Berg and Ott 2012) which becomes unstable at high  $m$  resulting in viscous fingering (Salimi et al. 2012). This is enhanced by the much lower viscosity of the CO<sub>2</sub>.

Furthermore, capillarity was identified as another factor of importance affecting instability growth rate (Yortsos and Hickernell 1989; Babchin et al. 2008) causing 'capillary dispersion' (Riaz and Tchelepi 2004) by which a sharp front becomes transformed into a diffused zone with elongated tail (Berg and Ott 2012). This dispersion effect acts to suppress finger (Homsy 1987). In addition, the scale of consideration determines the influence of this capillarity as the dispersion occurs at the same length scale as the shock front. Capillary number,  $Ca$ , is used to quantify the influence of this force and it is defined as the ratio of the viscous to capillary forces expressed as:

$$Ca = \mu V/\gamma \quad (2.21)$$

$\mu$  is the viscosity of the displacing fluid,  $V$  the characteristic velocity and  $\gamma$  is the interfacial tension between the two-phases. Change in  $Ca$  has been shown to affect the stability of the two-phase displacement patterns at different values of  $m$ . Numerical simulation results by Lenormand et al. (1988) showed that at high  $m$  and low  $Ca$  ( $-8 < \log Ca < -6$ ), capillary fingering dominates the displacement which becomes stable at high  $Ca$  (Figure 2.9a). At low

m (Figure 2.9b), there exists a crossover region as the Ca increases. At this region the displacement mechanisms switches from the capillary to viscous fingering. Noticeable from Figure 2.9, at high m, is the improved saturation of the displacing phase as the displacement transitioned to stable displacement at appropriate Ca. Also, Figure 2.9 showed the possibility of inefficient storage that may result from operating under viscous fingering at low m. Wang et al. (2013) demonstrated the influence of the Ca and the significance of crossover on the displacement of water by scCO<sub>2</sub>. They found an increase in scCO<sub>2</sub> saturation as the logCa increases from -7.61 to -6.61 where capillary fingering dominates. At higher injection rates, viscous fingering dominates, and the scCO<sub>2</sub> saturation remains nearly constant.

Furthermore, equation (2.21) indicates the importance of the interfacial tension in the two-phase flow system. This also reveals some information about the stability of the system. For example, in the numerical simulation by Berg and Ott (2012), low interfacial tension in the range of 0-0.05 mN/m generally leads to unstable displacement while marginal stability is recorded at 0.1 mN/m. For interfacial energy that is greater than 1 mN/m, it becomes stable at an experimental scale.

Various factors have been reported to affect the  $\gamma$  between CO<sub>2</sub>/water or CO<sub>2</sub>/brine systems. These include the temperature, pressure, salt concentrations and type of ions in the system. Under similar conditions,  $\gamma$  for CO<sub>2</sub>/water and CO<sub>2</sub>/brine show similar evolution with respect to temperature and pressure (Chun and Wilkinson 1995; Chalbaud et al. 2010). It decreases with pressure at constant temperature and this is more significant at lower pressure near the critical region (Nielsen et al. 2012; Shojai Kaveh et al. 2011) especially at low temperature (Chalbaud et al. 2010). At higher pressure, a plateau is reached at the value of  $\gamma$  for the system that slight increases with salt concentration at constant temperature (Chalbaud et al. 2010). This behaviour has been attributed to the solubility effects of CO<sub>2</sub>, which increases with pressure at low pressure and remains nearly unchanged at higher pressure when the difference in densities between CO<sub>2</sub> and brine remains constant. The dissolution effect on the density difference ( $\Delta\rho$ ) becomes more important at high pressure since  $\gamma$  calculation is a linear function of  $\Delta\rho$  (Chalbaud et al. 2010; Chiquet et al. 2007). For a given height of stored CO<sub>2</sub>, underestimating the  $\gamma$  between CO<sub>2</sub>/water will lead to overestimating the displacement efficiency making it seem like there is more space for storage than in reality (Chalbaud et al. 2010). The valence of the cations present in the gas-brine-rock system has been shown to be important in the value of the  $\gamma$ . For CO<sub>2</sub>-water system,  $\gamma$  is more than twice higher for the divalent cation (e.g., Ca<sup>+2</sup>) than the monovalent type e.g., Na<sup>+</sup> (Aggelopoulos et al. 2010).

In addition, the viscosity ratio and the non-wetting phase saturation have relation to the Ca and the stability of the two-phase system. Zhang et al. (2011) observe higher incident of viscous fingers in the two-phase flow at high Ca. For very low viscosity ratio, unstable displacement dominates with the viscous fingers for all Ca. For moderately low viscosity ratio, there exists a value in Ca at which there is a crossover from unstable to stable displacement. This condition corresponds to  $\log \mu_r > 0$  (Zhang et al. 2011). Based on Figure 2.8, at moderate depths of the aquifers (between 500 to 1000m), stable displacement is enhanced at offshore sites where CO<sub>2</sub> viscosity is higher.

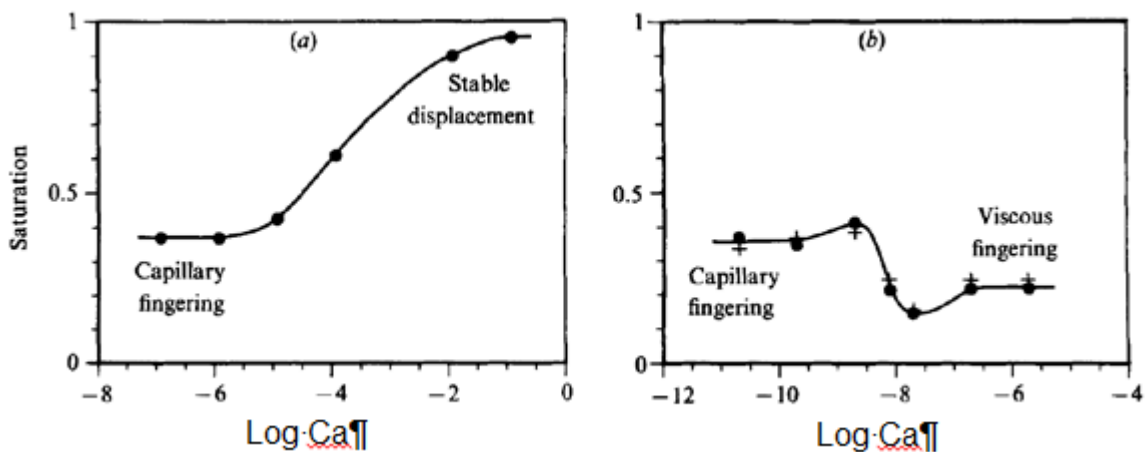


Figure 2.9: Capillary number and the displacement in the two-phase system (a) high viscosity ratio ( $\log m = 1.9$ ), (b) low viscosity ratio ( $\log m = -4.7$ ). Vertical axis represents the saturation of the displacing phase (Lenormand et al. 1988).

Authors like Plug and Bruining (2007) and Plug et al. (2006) acknowledge that the supercritical CO<sub>2</sub> state is prone to phase transition together with property fluctuation. These behaviours may not be unexpected to affect the stability and the  $P^c - S - K_r$  relationships for the system. Plug and Bruining (2007) observed irregular  $P^c - S$  relationships for supercritical CO<sub>2</sub> (at 40°C and 85 bar) under drainage while the usual  $P^c - S$  curve pattern was obtained for liquid CO<sub>2</sub> (27°C and 85 bar). This was attributed to CO<sub>2</sub>-wetting behaviour or occasional imbibition of water during the process. This behaviour can also be viewed as part of the manifestation of the above-described instability in the displacement. The scCO<sub>2</sub> phase undergoes irregular transition in properties and characteristics at slight change of temperature, pressure and velocity, which are difficult to maintain constant in the system. The fact that this is absent in the liquid case points to the fact that reduced interfacial tension in scCO<sub>2</sub> (Nielsen et al. 2012; Espinoza and Santamarina 2010) may be responsible judging from the report of Berg and Ott (2012). Both authors (Nielsen et al. 2012; Espinoza and Santamarina 2010) reported that the interfacial tension of CO<sub>2</sub>-water systems reduces with pressures but levels off above the CO<sub>2</sub> critical condition (~7 MPa) at fixed temperature

(Nielsen et al. 2012). However, the work of Kaveh et al. (2013) show that the decrease continues up to 100 bar. Furthermore, the sharp deviation in contact angle from the subcritical to supercritical regions of CO<sub>2</sub> (Saraji et al. 2013) show that phase transition holds important information about the phenomena in the scCO<sub>2</sub>-brine system. Considering these cases, phase transition in the geological media in conjunction with numerous subsurface processes associated with scCO<sub>2</sub>-brine and porous media systems may be complex and point the finger at the system stability and reliability. This calls for more understanding of the fluid-fluid-media system and characteristics, e.g., P<sup>c</sup>-S-K<sub>r</sub> relationships under the varying conditions. K<sub>r</sub>-S functions are essential for accurate analyses of the CO<sub>2</sub>-water displacement process (Berg and Ott 2012).

### 2.5.3 Influence of pressure, dissolution and wettability on P<sup>c</sup>-S-K<sub>r</sub>

The comparisons made between N<sub>2</sub> and CO<sub>2</sub> experiments by Plug and Bruining (2007) showed that CO<sub>2</sub> dissolution in water results in lower residual gas saturation. This is similar to the findings of Pistone et al. (2011). Also, the capillary pressure of scCO<sub>2</sub> was found to be lower if compared to gas and liquid CO<sub>2</sub> at every corresponding saturation. Several authors (Tokunaga et al. 2013; Plug and Bruining 2007) are unanimous in their observations that the P<sup>c</sup> – S relationships decrease as pressure increases owing to decreasing interfacial tension (Chun and Wilkinson 1995; Espinoza et al. 2011) while for secondary imbibition the negative P<sup>c</sup> at around high water saturation was attributed to alteration in wetting behaviour (Plug and Bruining 2007). Though the effects of dissolution were more pronounced for the CO<sub>2</sub> injection compared to N<sub>2</sub>, the capillary pressure was said not to be affected by the dissolution since the P<sup>c</sup> curves in both cases appear in the same range. But, it is well known that the dissolution effects act to reduce the surface tension of a two-phase system as earlier pointed out by Bennion and Bachu (2008) for CO<sub>2</sub>-brine and H<sub>2</sub>S-brine systems. Therefore, it is difficult to rule out the effect of dissolution on the observed differences in P<sup>c</sup>-S at higher pressures. For scCO<sub>2</sub>, small perturbations in the system dynamics cause sudden events resulting in the spontaneous imbibition of water into the system during drainage (Plug and Bruining 2007). This results in a decreasing capillary pressure and an irregular drainage curve. Also, the wettability effect showed that the sand remains water-wet going by the positive drainage capillary pressure measured for all temperature and pressure conditions considered. Plug et al. (2006) showed that a coal bed was water-wet in primary drainage but increasing pressure changes this to CO<sub>2</sub>-wet conditions in medium rank coal. They found that the effects of adsorption were not very pronounced with the significant CO<sub>2</sub>-wet condition re-occurring for the imbibition processes conducted. Their reports concluded that imbibition experiments provide good qualitative information regarding the wettability of coal.

#### 2.5.4 $P^c$ - $S$ - $K_r$ relationships in consolidated porous rocks

The work of Pini et al. (2012) reported  $P^c - S$  for consolidated media, namely, the Berea and Arqov sandstone samples. Discussing the relation in reference to temperature, the  $P^c - S$  curves for the Berea sandstone showed that capillary pressure decreases as temperature reduces and this behaviour was attributed to an increase in  $CO_2$  dissolution as the temperature decreases reducing the interfacial tension. By implication, the supercritical  $CO_2$  will have a higher  $P^c$  than liquid  $CO_2$ . But this will contradict the conclusion of other authors that the liquid  $CO_2$  has a higher  $P^c$  than  $scCO_2$  (Plug and Bruining 2007). Also, the  $P^c - S$  profile in Berea sandstone, described as a well sorted and homogenous sample, was consistently low for a wide range of saturation with a sharp rise in  $P^c - S$  values close to irreducible saturation. In comparison, the Arqov sample described as heterogeneous in nature displays a sharper rise and broader distribution in  $P^c - S$  while the profile remains considerably higher than in Berea sandstone for most of the saturation values. This brings to mind the influence of heterogeneities in the  $P^c - S$  relation as earlier reported for oil-water systems (Mirzaei and Das 2007) as the micro-heterogeneities are abundant in oil reservoirs (Van Lingen et al. 1996; Pickup et al. 2005). A list of experimental methods, fluid and media characteristics and various equipment applications by various authors in connection with  $P^c - S - K_r$  determination for  $scCO_2$ -brine system in the context of geological sequestration is shown in Table 2.2

## 2.6 Leakage risks and monitoring

Risks of leakage of stored carbon dioxide portend serious dangers to the potable water aquifers that may lie along the escape paths. Also, on the earth's surface, living species are susceptible to  $CO_2$  inhalation while leakage through the ocean with consequent acidification poses harm to marine life. Technically, leaks could occur as results of gravity override together with viscous instability causing the carbon dioxide to move to the top of the injection layer bypassing large quantities of brine (Gasda 2008; Saripalli et al. 2001; Metz et al. 2005). If the caprock however has favourable pathways, the carbon dioxide could escape vertically compromising the intention of the process. The vertical buoyant pressure applied on the caprock by the carbon dioxide is as a result of difference in density between the formation waters and the carbon dioxide, and the thickness of the carbon dioxide plume accumulation. Monitoring technologies are widely discussed in the literature. They are built upon the physico-chemical properties of the  $CO_2$ -brine-rock system or the detection of the reaction by-products or even the coupled process effects such as micro-seismicity (Espinoza et al.

2011). Methods like electrical resistivity and wave propagation are most often employed in deep reservoir applications (Nakatsuka et al. 2010) while application of tracers like SF<sub>6</sub> aid the monitoring of fluid movement.

The monitoring methods should extend several hundred meters beyond the injection region to safely check the advancing plume of CO<sub>2</sub>. In addition, monitoring the deep region around the aquifers should be coupled with near surface and surface monitoring.

To this end, available technologies should be adequately utilised. These include: electromagnetic techniques (Nakatsuka et al. 2010), temperature signals (Bielinski et al. 2008) and infrared monitoring (Charpentier et al. 2009) that have been demonstrated either in the laboratory or pilot applications for subsurface monitoring. Methods like electromagnetic techniques utilise the wide gap between the dielectric permittivities of CO<sub>2</sub> and water to create contrast with reference to the CO<sub>2</sub> saturation in the domain. Non-isothermal effects such as CO<sub>2</sub> dissolution and change of phase are made use of in the temperature signal method while the characteristic infrared wave absorption property of CO<sub>2</sub> is harnessed in the infrared monitoring technique. Near surface monitoring is also essential as stated before and this involves the analysis of near surface water, air and soil samples on a regular basis as CO<sub>2</sub> leaks can acidify the water and create conspicuous contrast between the original and current soil and air compositions. On the surface, the use of the gravity method (Alnes et al. 2008) as CO<sub>2</sub> is heavier than air and lighter than water, remote sensing of air composition (Leuning et al. 2008) and surface analysis of carbon content by Inelastic Neutron Scattering (INS) (Wielopolski and Mitra 2010) have been reported. Overall, monitoring protocols are essential for effectiveness of success of geological sequestration of CO<sub>2</sub>.

Table 2.2: Typical P<sup>c</sup>-S-K<sub>r</sub> experiments for scCO<sub>2</sub>-brine/water system in the literature (d: diameter L: Length)

Author(s)	Porous Materials	Fluid	Permeability (m <sup>2</sup> )	Porosity	Process Condition(s)	Equipment Type	P <sup>c</sup> Measurement Method	Sample Dimensions (cm)
Plug and Bruining (2007)	Unconsolidated sand	scCO <sub>2</sub> -water	2 x 10 <sup>-10</sup>	0.36	21-40 (°C), 1-85 (bar)	Porous plate and micropore technique	Pressure difference across domain	8.4 (d) 2.5 (L)
Plug et al. (2006)	Unconsolidated sand, coal		–	0.36-0.38 (sand), 0.42-0.45 (coal)	21-40 (°C), 1-85 (bar)	Porous plate and micropore technique	Pressure difference across domain	8.4 (d) 2.5 (L)
Tokunaga et al. (2013)	Unconsolidated sand		3.9 x 10 <sup>-11</sup>	0.381	45 (°C) 85-120 (bar)	Porous plate	Externally controlled fluid-fluid interface adjustment in relation to reference plane	8.2 (d) 3 (L)
Pentland et al. (2011)	Consolidated sandstone	scCO <sub>2</sub> -brine	4.6 x 10 <sup>-13</sup>	0.22	70 (°C) 90 (bar)	Porous plate	Pressure difference across domain	3.85 (d) 7.53 (L)
Pini et al. (2012)			2.7 x 10 <sup>-13</sup>	19.5	25-50 (°C) 90 (bar)	Modified porous plate		5 (D) 9 (L)

## 2.7 Summary

To address the issues of climate change and the problems of global warming requires meticulous scientific and engineering approaches. The current opinions favour the geological sequestration option. Therefore, scCO<sub>2</sub>-brine-rock interactions together with the *in situ* processes and trapping mechanisms should be quantified accurately as they play significant roles in determining the efficiency and safety of these processes. . Out of many candidate sites, choosing an appropriate geological site requires optimizing the process functions relating to the media, fluid and operational characteristics. This is more so as these characteristics directly or indirectly affect the processes, which determine safe CO<sub>2</sub> storage, e.g., dissolution and structural trapping, reaction and mineral precipitation, etc. CO<sub>2</sub> solubility is influenced by the porosity and pore size distribution (Emmanuel et al. 2010). So, developing the optimization protocols will aid the general practices in this regard. In relation to this, mathematical modelling and simulation tools have played significant roles, providing insightful predictions of the fate of the stored carbon and various processes including the trapping mechanisms. But, the site-specific indicators of CO<sub>2</sub> leakage, and predictable compromise of reservoir integrity with the quantity and dynamics of CO<sub>2</sub> in the reservoir are desired to be integrated in the system software with fully-coupled geochemical, fluid-fluid-solid, hydrogeological, physical and chemo-physical conditions. Such an indicator or factor should consider the impact of man-made leakage zones (see, e.g., (Humez et al. 2011; Tao and Bryant 2014)) as well as natural-leakage zones (see, e.g., (Schwartz 2014)). Affordable and commercial availability of the software products will drive research and field developments.

As a special kind of two-phase flow system,  $P^c - S - K_r$  relationships for scCO<sub>2</sub>-brine-rock systems are important in the modelling and analysis of the sequestration operations. But, the list of available experimental publications is far from sufficient especially when viewed from possible factors that can affect  $P^c - S - K_r$  relationships from closely related process as encountered in the studies of oil recovery, oil spill remediation, contaminant transport and so on. Wettability of the medium is shown to be responsible for the irregularity in the pattern of  $P^c - S - K_r$  relationships (Plug and Bruining 2007) with the possibility of *in situ* alteration in media wettability. This needs further investigation in order to keep the function applicable in the modelling and prediction of sequestration process and storage safety.

Most of the  $P^c - S - K_r$  relationships reported are related to quasi-static or equilibrium conditions. The dynamic behaviour of the system particularly at the immediate time following

injection prior to the attainment of equilibrium needs to be better understood. In this regard, the difference in the quasi-static or dynamically measured  $P^c - S - K_r$  relationships will be of interest. Researchers of multiphase flow had dedicated past decades to the study of various dynamic effects in system properties of multiphase flow. Part of the investigations dwelled largely on the saturation-rate dependency of the system properties and a number of publications had resulted (Hassanizadeh and Gray 1993; Das et al. 2007; Mirzaei and Das 2007; Hanspal and Das 2012; Dahle et al. 2005; Goel and O'Carroll 2011; Das and Mirzaei 2013). Particularly, for  $P^c - S$  relationships, the dynamic coefficient,  $\tau$ , used in quantifying this phenomenon has been said to be dependent on media permeability (Mirzaei and Das 2007; Tian et al. 2012; Hanspal and Das 2012; Dahle et al. 2005), microheterogeneity (Mirzaei and Das 2007), fluid properties (Das et al. 2007; Goel and O'Carroll 2011), scale of observation (Dahle et al. 2005; Bottero et al. 2006; Bottero et al. 2011a; Nordbotten et al. 2007), etc. Though, the observations and reports were made largely in relation to oil-water system, investigating the same effects for the rock-scCO<sub>2</sub>-brine system will broaden the present state of study while improving the applicability and integrity of  $P^c - S - K_r$  relationships as a modelling function for the rock-scCO<sub>2</sub>-brine system.

For example, different media permeabilities are encountered and hardly can two porous media share the same permeability even at contiguous sediment. A look at Table 2.2 reveals this reality as each experiment has different media permeability unique to it. Even within an aquifer or reservoir, media anisotropy may be assumed but the reality dictates otherwise (Pickup et al. 2005; Nordbotten et al. 2007; Aggelopoulos and Tsakiroglou 2008). Microheterogeneities are another closely related property of the porous media. These are abundant in the reservoir (van Lingen et al. 1996; Pickup et al. 2005) and they affect the micro and macro scale quantity of the system variables while  $\tau$  is said to increase with its intensity (Mirzaei and Das 2007). Aquifer or reservoir exhibits these properties or characteristics with few exceptions and are worth investigating in the context of carbon sequestration, especially the way they affect the  $P^c - S - K_r$  relationships.

To determine  $P^c - S$  relationships for two-phase flow in any aquifer or reservoir, pressures in both phases need to be measured separately and saturation simultaneously determined. From the literature discussed in this review, it seems that the common laboratory measurement methods used for determining the  $P^c - S$  parameters for scCO<sub>2</sub>-brine/water system can be better described as pressure drop across the domain to get the  $P^c$  and the measurement of the outflow water or brine for the saturation. An advanced *in situ* saturation measurement method was presented by Pini et al. (2012) using a medical X-ray CT scanning

instrument with good resolution. This has the additional ability to determine the sample porosity. But the cost of this instrument and technicalities may pose challenges to many promising investigations. To overcome this, instruments like time domain reflectometer (TDR) can be recommended. They had been variously used to obtain *in situ* saturation measurement for decades (Das and Mirzaei 2013; Goel and O'Carroll 2011; Camps-Roach et al. 2010; Topp et al. 1984). Most of these experiments were conducted for oil-water and air-water systems mostly at near ambient condition but the instrument is still easily adaptable to the supercritical condition of carbon sequestration. The TDR probe has the capacity to determine the bulk electrical conductivity of the system in addition to the relative permittivity used in determining water saturation.

It has been argued that external measurement of capillary pressure loses significance near residual saturation (Morrow and Harris 1965; Bottero 2009) as the non-wetting phase pressure dominates at this period when the wetting phase experiences disconnectivity and thus making the measured wetting phase pressure appear larger. This makes the  $P^c$  smaller than supposed. But, the challenges of *in situ* phase pressure measurement are not simple, considering the high pressure and above ambient temperature of the supercritical  $CO_2$ . At this state, most of the semi permeable membranes used by many authors (Das and Mirzaei 2012; Bottero et al. 2011; Hou et al. 2012) or porous ceramic discs (Camps-Roach et al. 2010; Goel and O'Carroll 2011) employed in oil-water or air-water systems will fail to distinguish any phase under supercritical conditions as they were designed to operate under ambient conditions. However, there is hope in some of the metallic materials recently used by some authors under similar conditions even though they were not used to measure phase pressures. For example, C276 Hastelloy porous plates used by Tokunaga et al. (2013) and aluminium silicate by Pentland (2011) were described as semi permeable hydrophobic and hydrophilic discs, respectively under the supercritical conditions. Many other materials may still be available from membrane manufacturers to achieve this aim.

The effect of scale on dynamic effect in  $P^c - S - K_r$  relationships is also well reported (Dahle et al. 2005; Bottero et al. 2011; Camps-Roach et al. 2010). Most of the experiments available for the  $scCO_2$ -brine-rock system are, at most, at the core scale size. How these relationships vary with size of the aquifer or field scale will be of great importance in the complete assessment of the factors affecting the  $P^c - S - K_r$  functions and will improve the versatility of their applications. The following bullet points will help to emphasis some suggestions based on this review:

- There are needs for experimental investigations of the effects of media characteristics e.g., domain scale, on the  $P^c - S - K_r$  relationships for scCO<sub>2</sub>-brine system at conditions applicable to geological carbon sequestration.
- To promote understanding of caprock integrity, investigations of the pore size distribution on relative permeability of CO<sub>2</sub> needs to be made clearer in conjunction with interfacial tension of the scCO<sub>2</sub>-brine system. For example, one may ask, 'how does the combination affect the entry pressure of the caprock?' Such investigations need to be conducted in the context of pressure, temperature, salt concentration, cation valence that are known to influence the interfacial tension. Contributions of the long-time mineral precipitation to change in salinity, combinations of cation valences and their effects on the above parameters will be very enlightening.
- Use of surfactants to curtail migration of scCO<sub>2</sub> in saline aquifer and promote residual trapping will deserve future investigations, e.g., can surfactants check viscous and capillary fingerings in scCO<sub>2</sub>-brine-rock systems? There are many works on the use of surfactant and CO<sub>2</sub> in the literature, which are related to enhanced oil recovery (EOR).
- Inclusion of leakage parameters on a site-specific basis in the modelling and simulation of the system should be encouraged.
- The dynamic capillary pressure effects for the  $P^c - S - K_r$  relationships should be investigated in relation to scCO<sub>2</sub>-brine-rock system and these relationships should be incorporated in the relevant simulators for the geological carbon sequestration.
- The wettability alteration and the caprock integrity from the perspective of the alternation of the scCO<sub>2</sub>-brine-rock system conditions from neutrality to acidity and alkalinity as a result chemical complexation and mineral dissolution deserve more investigations. As different cationic valences change the interfacial tensions, how do similar changes in the subsurface conditions affect the wettability? This will be an important question to answer in future investigations.
- How continuous or intermittent injection and its rates influence residual trapping of injected CO<sub>2</sub> will be a subject of interesting investigations.
- Cheap and simple CO<sub>2</sub> leakage detection systems should be developed for the common household to be used for the independent assessment of CO<sub>2</sub> gas accumulation, especially for residents closer to transport pipeline or geo-sequestration sites.

## CHAPTER THREE

# SCALE DEPENDENT DYNAMIC CAPILLARY PRESSURE EFFECT FOR TWO-PHASE FLOW IN POROUS MEDIA IN RELATION TO FLUID VISCOSITY RATIO\*

### Overview

*Causes and effects of non-uniqueness in capillary pressure and saturation ( $P^c$ - $S$ ) relationship in porous media are of considerable concern to researchers of two-phase flow. In particular, a significant amounts of discussion has been generated regarding a parameter termed as dynamic coefficient ( $\tau$ ) which has been proposed for inclusion in the functional dependence of the  $P^c$ - $S$  relationship to quantify dynamic  $P^c$  and its relation with time derivative of saturation. While the dependence of the coefficient on fluid and porous media properties is less controversial, its relation to domain scale appears to be dependent on artefacts of experiments, mathematical models and the intra-domain averaging techniques. In an attempt to establish the reality of the scale dependency of the  $\tau$ - $S$  relationships, a series of well-defined laboratory experiments was carried out to determine  $\tau$ - $S$  relationships using three different sizes of cylindrical porous domains of silica sand. This chapter presents , findings on the scale dependence of  $\tau$  and its relation to high viscosity ratio ( $\mu_r$ ) silicone oil-water system, where  $\mu_r$  is defined as the viscosity of non-wetting phase over that of the wetting phase. An order of magnitude increase in the value of  $\tau$  was observed across various  $\mu_r$  and domain scales. Also, an order of magnitude increase in  $\tau$  is observed when  $\tau$  at the top and the bottom sections in a domain are compared. Viscosity ratio and domain scales are found to have similar effects on the trend in  $\tau$ - $S$  relationship. Dimensional analysis of  $\tau$  was carried out and the result shows how different variables, e.g., dimensionless  $\tau$  and dimensionless domain volume (scale), may be correlated and provides a means to determine the influences of relevant variables on  $\tau$ . A scaling relationship for  $\tau$  was derived from the dimensionless analysis which was then validated against independent literature data. This showed that the  $\tau$ - $S$  relationships obtained from the literature and the scaling relationship match reasonably well.*

### 3.1 Introduction

A capillary pressure ( $P^c$ ) and saturation ( $S$ ) relationship is vital in the characterization of immiscible two-phase flow phenomena in porous media (e.g., Bear 2013; Das and Hassanizadeh 2005; Das et al. 2014). This relationship is non-linear in nature and it depends

---

\*Abidoye, L.K. and Das, D.B., (2014). Scale-dependent dynamic capillary pressure effect for two-phase flow in porous media. *Advances in Water Resources*, 74, pp. 212–230, DOI: 10.1016/j.advwatres.2014.09.009.

on several factors, e.g., flow dynamics (steady or dynamic), fluid and porous material properties, contact angles, medium heterogeneities (e.g., permeability heterogeneity, non-uniformity in particle size), scales of observation, etc. (Bear 2013; Das et al. 2007; Bottero et al. 2011; Hanspal et al. 2013; Mirzaei and Das 2013; Khudaida and Das 2014). In general, the forces which influence dynamic immiscible flow in porous media act in a manner so as to drive the fluids to a state of static equilibrium, i.e., when the rate of change of saturation ( $\partial S/\partial t$ ) is zero. During this process, the fluid/fluid interfaces in the porous medium move to re-establish a new state of equilibrium (Mariotti et al. 2010; Dahle et al. 2005; Gielen et al. 2005; Blunt et al. 2002). In practice, a state of stability in the system is utilised to obtain the equilibrium  $P^c$ -S relationship for the system. In pore-scale modelling, the pressure in one of the phases is allowed to increase and a succession of equilibrium fluid configurations is computed in the pore network to obtain the  $P^c$ -S relationship (Blunt et al. 2002). These are then applied to non-equilibrium conditions with fluids sometimes flowing at high flow rates. The implicit assumption in such an approach is that the disturbances to interfacial properties are rapidly dissipated (Hassanizadeh et al. 2002).

At the equilibrium or quasi-static condition, the approach for the characterisation of the  $P^c$ -S relationship is typically coupled with an extended version (i.e., an equation of two-phase flow in porous medium) of Darcy's law for single phase flow in porous medium (Bear 2013; Das et al. 2005). In this case, the capillary pressure is defined as a function of saturation as expressed in equation (3.1):

$$P_{nw} - P_w = P^{c, \text{equ}}(S) = f(S) \quad (3.1)$$

where,

$P_{nw}$  = average pressure for non – wetting phase ( $\text{ML}^{-1}\text{T}^{-2}$ )

$P_w$  = average pressure for wetting phase ( $\text{ML}^{-1}\text{T}^{-2}$ )

$P^{c, \text{equ}}$  = equilibrium (steady state) capillary pressure ( $\text{ML}^{-1}\text{T}^{-2}$ )

$S$  = wetting phase saturation (-)

In the last decade, it has been argued by a number of authors that the application of equation (3.1) to non-equilibrium condition will be inappropriate as the equation lacks the requisite parameters to address the dynamic characteristics of the flow prior to the attainment of flow equilibrium when the rate of change of saturation ( $\partial S/\partial t$ ) may be high. The need for a modification of the traditional relation (i.e., equation (3.1)) was the conclusion of some authors (e.g., Kalaydjian 1992; Hassanizadeh and Gray 1990; Hassanizadeh and Gray 1993) with a view to accommodating a more complete description of the system under non-equilibrium conditions. Ever since its proposition, a phenomenal factor in the description of dynamic two-phase flow, namely a dynamic coefficient ( $\tau$ ), has been the subject of several

publications (Das and Mirzaei 2012; Hanspal and Das 2012; Bottero et al. 2011a; Bottero et al. 2011b; Camps-Roach et al. 2010; Das et al. 2007; Mirzaei and Das 2007; Hassanizadeh et al. 2002). The modification is mathematically expressed as in equation (3.2):

$$(P^{c,dyn} - P^{c,eq})|_S = -\tau \partial S / \partial t|_S \quad (3.2)$$

where,

$P^{c,dyn}$  = dynamic capillary pressure [ $ML^{-1}T^{-2}$ ]

$\partial S / \partial t$  = time derivative of saturation [ $T^{-1}$ ]

While the interpretation of  $\tau$  in terms of its physical meaning seems to be well understood, some of the factors influencing its values are not uniquely characterised, i.e., the significance of the dependence of  $\tau$  on these factors seems to vary from one case to another. According to previous authors (e.g., Das et al. 2007; Hassanizadeh et al. 2002), the dynamic effect is related to the dependence of capillary pressure-saturation relationship on the time derivative of saturation resulting from finite time needed by the fluid to neutralise the effect of the internal and external forces in order to establish flow equilibrium. Other reports have indicated that the length of time needed to attain flow equilibrium and, hence, the dynamic effect, is larger in less permeable medium than in more permeable sample. The same is true for porous medium with higher degrees of micro-heterogeneity. Thus, larger values of  $\tau$  have been reported in the literature for fine grained or low permeability medium (Das et al. 2007; Camps Roach et. al, 2010; Hanspal and Das 2012; Tian et al. 2012) and domains with micro-heterogeneities (Das and Mirzaei 2013; Mirzaei and Das 2007; Mantney et al. 2005). Among the other factors that affect the magnitude of  $\tau$ , strong impacts of fluid properties are well acknowledged (Das et al. 2007; Goel and O'Carroll 2011; Joekar-Niasar and Hassanizadeh 2011; Hou et al. 2014).

The effect of scale/size of the domain has been linked to the  $\tau$  values as well. It seems that these effects are quantified more commonly in reference to numerical models of pore/core scales and application of different averaging techniques therein. However, these are rarely characterised through experimental studies. Dahle et al. (2005) observe a scale dependency in the value of  $\tau$  in their numerical investigation of dynamic effects in  $P^c$ -S relationship using a bundle-of-tubes model. Their model leads to a similar relationship as in equation (3.2) but with the inclusion of an intercept term,  $\beta$ . By determining a dimensionless grouping containing  $\tau$  and  $\beta$ , respectively, they report that the dimensionless grouping shows a dependency on saturation and that  $\tau$  increases as the square of the averaging volume length,  $L$ . This suggests a geometrical increase in  $\tau$  with the length scale of the domain and that its magnitude may become arbitrarily large as the domain size rises from core to the field scale. This square of length relationship (Dahle et al. 2005) was however controverted by

Bottero et al. (2011a) in their investigation of non-equilibrium effects at different averaging windows in a porous medium domain of 21cm height. Bottero et al. (2011a) determined  $\tau$  experimentally and obtained averages at different windows of observation, namely, 11 and 18cm sections, within the same porous domain of 21cm height. An order of magnitude increase in  $\tau$  was found at an averaging window of 11cm as compared to the local values. A similar order of increase was obtained in  $\tau$  at an averaging window of 18cm as compared to the values at 11cm averaging window. Thus, it can be inferred from the work of Dahle et al. (2005) and Bottero et al. (2011a) that  $\tau$  generally increases with the scale of observation. The proportion of this trend to domain scale is however difficult to affirm from the current studies and there are clear inconsistencies in this regard. Das and Mirzaei (2012, 2013) and, Mirzaei and Das (2013) found that the functional  $\tau-S$  relation follows non-linear trends at different locations within the same domain using a saturation-weighted technique for averaging domain scale  $\tau$  where local  $\tau$  increases with decrease in  $S$ . However, these authors did not find a clear relationship between the averaged and local values of  $\tau$ . Furthermore, insignificant differences were observed between the local and average (domain scale) values of  $\tau$ , which are in contrast to other findings where  $\tau$  is viewed as a parameter that increases with the scale of domain (e.g., Dahle et al. 2005; Bottero et al. 2011a). Similarly, in the work of Camps-Roach et al. (2010), an up-scaling procedure showed little or no change in  $\tau$  as its values remained almost identical for column scale as it was for the local measurements. (Bottero et al. (2011a), who used averaging techniques such as those discussed by Nordbotten et al. (2007, 2008, 2010) for averaging capillary pressure and relative permeability, found that the average values of  $\tau$  showed no dependency on water saturation within a water saturation range of 50 to 85%. This trend is contrary, within the similar saturation range, to what Das and Mirzaei (2012, 2013) have observed on values of  $\tau$  and many other papers such as that by Dahle et al. (2005). Besides the above literature, there are a number of other relevant papers. For example, Bourgeat and Panfilov (1998) reported a homogenisation method by which the dynamic capillary pressure effects were studied for oil-water flow in a heterogeneous porous domain. Cuesta et al. (2000) reported a travelling wave solution for dynamic two-phase flow in porous media.

It is evident from the literature that a significant amount of discussion has been made to discuss the dynamic capillary pressure equation (equation (3.2)). From these discussions it can be concluded that the existing publications on the determination of  $\tau$  use both experiments and numerical simulations at pore or/and core scale (Bottero et al. 2011a; Das and Mirzaei, 2012, 2013; Camps-Roach et al. 2010; Dahle et al. 2005). They use various types of averaging techniques to determine averaged  $\tau$  at domain/larger scale and relate the

local and averaged  $\tau$  values. While it is acknowledged that the exact values of the coefficient may be different for specific two-phase systems, the inconsistencies in the general trend in the results in the literature however raise many questions, e.g., are the observed behaviours of  $\tau$  an artefact of the averaging methods? Similarly, would the extent of the scale dependencies of  $\tau$  be any different if they were measured at different and separate domain scales and not averaging windows within the same domain? Considering the above arguments, one may opine that the scale dependency of a parameter, such as  $\tau$  in this case, should be determined using separate domains for the same conditions, e.g., material properties, boundary conditions, etc. At the moment in the open literature, there is no experimental evidence to demonstrate the scale dependency of  $\tau$  in this fashion.

To address these issues, the work in this chapter aims to carry out a series of controlled laboratory experiments with separate and different sizes of porous medium with the aim of finding the trend in the magnitude of  $\tau$  depending on the scale. This work is designed to ensure that the procedure is less-dependent of mathematical averaging method for calculating the coefficient as far as possible. This approach has the advantages of assigning  $\tau$  to independent domain sizes, and reducing any ambiguity, which may arise from intra-domain system averaging. The experiments in this work rely on determining average quantities at the local scale (e.g., measurement sensors for water saturation, pressure). The scales of these measurement points are significantly small as compared to the size of the porous domains at which averaged quantities at the domain scale are calculated. In other words, the processes that govern the  $\tau$  values at the local and domain scale are likely to be different. This point is discussed further in this work by relating the local and domain scale  $\tau$  values with the help of a  $\tau$  scaling factor.

In the context of this work, fluid property effects are important as well. Stauffer (1978) emphasises the importance of fluid properties on  $\tau$  according to the following equation:

$$\tau = \frac{\alpha \phi \mu}{\lambda K} \left( \frac{P^d}{\rho g} \right)^2 \quad (3.3)$$

where  $\tau$  is the relaxation parameter for unsaturated porous domain,  $\alpha$  is a dimensionless parameter (defined to be 0.1),  $\phi$  is the porosity,  $K$  is the permeability,  $P^d$  and  $\lambda$  are the Brooks and Corey parameters related to the pore and entry pressure, and particle size distributions of the materials, respectively,  $\mu$  is the viscosity of the wetting phase,  $g$  is the gravity constant,  $\rho$ , the fluid density of the wetting phase. However, the relation does not account for the effects of the non-wetting phase viscosity and density. In the light of recent publications (see, e.g., Hou et al. 2014; Goel and O'Carroll, 2011; Joekar-Niasar et al. 2011; Das et al. 2007;

Gielen et al. 2005), it is strongly established that the properties of the non-wetting fluid play significant influence on the displacement process and the magnitude of  $\tau$ . Also, the non-inclusion of the wetting phase saturation in equation (3.3) means that the equation cannot possibly be applied in quantifying the  $\tau$ -S relationship. Without exception, recent publications cited above expressed some dependence of  $\tau$  with saturation. Nevertheless, the equation (3.3) draws the attention to the importance of fluid properties, particularly viscosity, as  $\tau$  has direct relation to it.

Recently, Joekar-Niasar et al. (2010) emphasised the dependence of  $\tau$  on viscosity ratio as well as an effective viscosity which depends on the values of fluid viscosities of the wetting and non-wetting phases. It was pointed out that if this ratio is less than one under drainage or greater than one in imbibition, invading front can become unstable. Conversely, the ratio that is far higher than unity in drainage or far less in imbibition results into a stable front. Viscous fingering is also said to result into less dynamic effect while stable front regime does otherwise (Joekar-Niasar et al. 2011). It is later shown in this work how the stable fronts arising from high viscosity ratios of the silicone oil-water system, used in our experiments for drainage process, results in higher dynamic effect as the viscosity ratio increases. The effect of viscosity was further explained by Joekar-Niasar et al. (2010) and Joekar-Niasar and Hassanizadeh (2011) in terms of the redistribution time needed by the fluid-fluid interface to reach equilibrium, which takes longer in larger viscosity. In the same vein, higher density ratio is found to result into higher dynamic capillary pressure effect (Das et al. 2007). It has been observed in the literature that this promotes instability of fluid/fluid interfaces leading to the formation of fingers (e.g., DiCarlo 2004; Van Duijn and Floris 1992). The occurrences of instabilities and overshoots during two-phase flow in porous media have been shown theoretically by means of travelling wave analysis by Van Duijn et al. (2013). Fingering is also discussed in detail by Kissling and Rohde (2010) and DiCarlo (2013).

In the current work, the non-wetting fluids have significantly different viscosities but approximately the same densities. Thus, the effect of the density ratio will not be considered in the discussion. The experimental work of Goel and O'Carroll (2011) reported the influence of viscosity ratio on the magnitude of  $\tau$  which increases with increasing viscosity of the non-wetting phase. This work utilised low viscosity non-wetting fluids, namely, 5 and 0.65cSt silicone fluids. The authors show that the  $\tau$  values at various viscosity ratios collapse when normalised with effective viscosity especially for effective water saturations larger than 50%.

While the above discussion points to the importance of domain scales and fluid properties (especially, viscosity ratio) to determine the magnitude of  $\tau$  and its relationship to other

process and system parameters (e.g., permeability), the relationship of the scale dependency of  $\tau$  with viscosity ratio needs further studies. This is the main aim of this work. In particular, it is aimed to determine these relationships by a set of well-defined experiments with different domain scales and high-viscosity non-wetting phase fluids so as to increase the range of viscosity effects (200, 500 and 1000 cSt) studied so far. Indeed, this work complements other published works on dynamic capillary pressure effects in relation to domain scales and fluid property. However, it is expected that this work would provide a better understanding of the behaviour of the dynamic capillary pressure effect.

## **3.2 Materials and methods**

### **3.2.1 Porous medium, domain size and fluid property**

The porous medium used in this work was prepared using sand particles (CH30) obtained commercially from the Minerals Marketing Company (Cheshire, UK). The particles were compacted to prepare the porous samples following the same method of preparation and characterisation detailed in Das and Mirzaei (2012). The porous sample has an average porosity of 0.38. The intrinsic permeability of the sample is  $5.66 \times 10^{-11} \text{ m}^2$  which was measured using a constant head permeameter (Bear 2013). Silicone oil of different viscosities, namely, 200, 500 and 1000cSt (Basildon Chemicals, Abingdon, UK) were used as the non-wetting phase while distilled water was used as the wetting phase. Silicone oil is a good non-wetting model fluid. Although their viscosities may be different, their densities are almost the same. Therefore, any effect of the fluid properties on the results can be mainly attributed to viscosity difference. Table 3.1 shows the properties of the fluids and the porous materials. Sample holders of different sizes were utilised to investigate the variation of  $\tau$  with domain size. These domains were cylindrical in shape, 10.2cm in diameter and had varying heights, namely, 4, 8 and 12cm. Configurations of the domains are illustrated in Figure 3.1.

### **3.2.2 Experimental methods**

Depending on the size of the domain, varying numbers of pressure transducers (PTs), which were bought from WIKA Instruments Ltd (Redhill, UK), were positioned at different levels of the three domains chosen for this work. At each level, one pair of PTs were inserted, where one PT is aimed at measuring the wetting phase pressure while the second PT measures the pressure of the non-wetting phase pressure. The PTs installed in the experimental cells included one pair of PTs at the centre of the 4cm cell, two pairs at the 2cm (top) and 6cm (bottom) points of the 8cm cell and, 3 pairs at the 2cm (top), 6cm (middle) and 10cm (bottom)

points of the 12cm cell, respectively, where all distances are measured from the top boundary of the porous domains.

Table 3.1: Fluid and material properties used in the experiments in this work

Properties	Porous Material	Silicone Oil			Water
		1	2	3	
Permeability, $K$ ( $m^2$ )	$5.66 \times 10^{-11}$				
Porosity, $\phi$ (-)	0.38				
Particle Density, ( $kg/m^3$ )	2660				
Average Particle Diameter, $D_p$ ( $\mu m$ )	482.4				
Particle Size Range ( $\mu m$ )	$100 < D_p < 900$				
Viscosity, $\mu$ (cSt)		200	500	1000 <sup>a</sup>	1 <sup>c</sup>
Surface Tension, $\sigma$ (N/m) @ 25°C		0.0210	0.0211	0.0211 <sup>a</sup>	72 <sup>b</sup>
Specific Gravity <sup>a</sup> , 25°C		0.972	0.973	0.974	1
Entry Pressure (kPa)		0.9	1.5	1.5	-
Pore size distribution index	3.5				

<sup>a</sup> [www.baschem.co.uk](http://www.baschem.co.uk) (Silicone oil -water system)

<sup>b</sup> Adamson and Gast, 1997 (water-air system)

<sup>c</sup> [www.machinerylubrication.com](http://www.machinerylubrication.com)

Figure 3.1 is a schematic diagram of the experimental set up. Figure 3.1 illustrates the domain sizes, the configurations of the PTs as well as the TDR probes at different levels of the domain. The PTs are distinguished using hydrophilic nylon (pore size:  $0.1\mu m$ ) and hydrophobic polytetrafluoroethylene, PTFE (pore size:  $1\mu m$ ) membranes which were purchased from Porvair Filtration Group Ltd (Hampshire, UK) on the faces of the PTs to measure water and silicone oil pressures, respectively. They were held in place by capped fitting with a rubber seal. As the membranes are thin, they were supported by thicker Vyon filters approximately 5mm thick (Porvair Filtration Group Ltd, Hampshire, UK). Prior to this, the membranes and filters were immersed in their respective fluid (water or silicone oil) and vacuumed for at least 24hrs to remove any entrapped air. The assembly of the PTs was also made within the respective fluid to avoid any air trap. The PTs were calibrated using a portable pressure calibrator, DPI 610 (Druck Limited, Leicester, UK). Good linearity was obtained in pressure-output voltage relationship and the linear equations of the fits obtained from Microsoft Excel (2010) were employed in the programming of the sensors. The PTs were connected to a data logger via a multiplexer (Campbell Scientific Ltd, Shepshed, UK).

Water saturation in the porous medium was determined using time domain reflectometry (TDR) probe (Campbell Scientific Ltd, Shepshed, UK). A TDR probe is positioned at the same level as with a pair of PTs. The TDR probes were earlier calibrated in a 4cm cell and the results fitted with a polynomial function for *in situ* measurement of local water saturation corresponding to a level in a cell.

Transient average domain saturation is also determined using a graduated glass cylinder placed on a high precision weighing balance ( $\pm 0.1$  mg) which was connected to the computer and data logged in real time by the weighing balance software (A&D Company Limited, San Jose, USA). This method was adopted to determine average domain scale saturation as it represents the true saturation in the domain at any particular time from a material balance point of view. A similar approach was adopted by Bottero et al. (2011a) to determine the average (column-scale) fluid saturation over the whole sand column from the change of volumes of fluids in inflow and outflow burette. Having determined the porosity and the total amount of water in the porous domain with the dead volume of the system subtracted, the transient domain saturation was determined.

The sample holder was set on a metal base with wire gauze and hydrophilic filter at the base of the column. The fine wire gauze was used to prevent fine sand particles from slipping into the outflow line, which might affect desaturation rate value while the hydrophilic membrane acts to prevent oil outflow. A predetermined amount of water was then poured into the cell to a certain position followed by pouring of sand through a metal sieve of appropriate size to ensure uniform sand deposition and prevent air trap. The cell was vibrated simultaneously to promote uniformity in the deposition of the sand particles. After the deposition of the sand particles was complete, the excess water was drained through the outflow valve. This gave an indication of the amount of water in the saturated domain. A hydrophobic filter was then placed over the sand to prevent water flow out through the top of the domain boundary. Finally, the column was sealed with a metal cap, which provided the connection to silicone oil supply.

The silicone oil was supplied from a Marriotte bottle, which maintained a constant pressure on the fluid column irrespective of fluid volume. The Marriote bottle was directly connected to an air compressor (R.E.P. Air Services, Loughborough, UK) which provided the requisite pressure for injecting silicone oil in the experimental cells (also discussed in the next section).

### **3.2.3 Dynamic and equilibrium experiments on two-phase flow**

As mentioned earlier, the two-phase flow experiments were conducted on 4, 8 and 12 cm cells. Pressure was supplied using an air compressor, which imposed a set air pressure on a column of silicone oil in a Marriote bottle (see, Figure 3.1). The bottle ensures that the oil invades the porous medium at a constant pressure throughout the experiment.

For the dynamic drainage, a set pressure was imposed on the oil, which pushed it to the top of the domain through the inlet valve. When the outlet valve remains closed, the pressure simply transmits through the fluid phases without infiltration of oil into the sand domain. This was indicated by the readings of the PTs, which rose gradually till it attained approximately the same magnitude as the imposed pressure at different levels in the domain.

For the dynamic drainage processes, 10, 15 and 20kPa pressures were imposed on top of the domains. These processes provide results for two scenarios. Firstly, the  $\tau$  values can be calculated using a number of the pressure conditions (three values in this case) as has been done in a number of papers (e.g., Bottero et al. 2011a; Das and Mirzaei, 2012; Hanspal and Das, 2012; Das and Mirzaei, 2013). Secondly, the chosen pressure boundary conditions provide the possibility of obtaining  $\tau$  values for selected cases where the pressure gradient is the same in two domains of different size. For example, the pressure gradients are the same in 4cm and 8cm cells when pressures of 10 and 20kPa are imposed, respectively. Similarly, the pressure gradients in 8 cm and 12 cm cells are the same when 10 and 15 kPa are imposed. These issues are discussed again in a latter section (section 3.2).

When the outflow valve was released in the experiments, drainage of the porous domain began and it gave noticeably different  $P^c$ -S profiles for different boundary conditions. Replicate runs of some of the experiments were conducted to check repeatability of the experiments. The ambient laboratory temperature was at approximately 20°C.

The experiments in the cells were repeated for 200, 500 and 1000cSt silicone oil. The equilibrium or quasi-static experiments were conducted by gradual increase in air pressure imposed on the silicone oil in the Mariote bottle at less than 500Pa in a single step. Sufficient time was allowed for the fluids to attain equilibration before the pressure was further raised. This was continued until the porous medium saturation could not be reduced anymore which was adopted as the final measured saturation. This approach was adopted so as to avoid any confusion of the final measured saturation with the typical definition of irreducible saturation in porous media. In this work, the final measured saturation is not necessarily the irreducible saturation and it simply reflects what final saturation has been obtained for the experimental conditions (e.g., pressure drop).

For each silicone oil and domain scale chosen, dynamic and equilibrium or quasi-static drainage experiments were conducted. As stated earlier, the local saturation was determined using the TDR probe for the local level while an average domain saturation was determined from a graduated cylinder placed on a weighing balance whose software program was set at the same output rate (15s) as the data-logger for sensors to ensure corresponding relation of

generated data. The rate of change of saturation in this cylinder is taken to represent the whole domain desaturation rate while the capillary pressure for the whole domain was derived from saturation-weighting of the capillary pressures at different local levels in the system. Thus, at a particular output time, the domain saturation is determined from the balance measurement while the domain capillary pressure is determined from saturation-weighting of the TDR and PTs measurements at the local levels.

### 3.2.4 Calculation of dynamic coefficient ( $\tau$ )

The dynamic coefficients were determined for the different cases using equation (3.2). To do this, the equilibrium and dynamic drainage pressures of each phase were interpolated at selected saturations using the 'Forecast' function in Microsoft Excel (2010). The function calculates, or predicts, an unknown parameter by using known values on the basis of a linear regression. The predicted values are y-values for given x-values and the results can be plotted easily as a typical x-y graph in Excel. This readily provides the corresponding points for the parameters in the equation (3.2), i.e.  $P_{nw}$  and  $P_w$  at a particular saturation,  $S$ , for both the dynamic and equilibrium drainage experiments. The differences in the equilibrium and dynamic  $P^c$  data, which are required for equation (3.2) were obtained at arbitrarily chosen saturation values but covering the entire saturation range, i.e., 0-1. Similarly, the desaturation rate data were interpolated using the same function. The plots of the differences between the dynamic and equilibrium capillary pressures against the desaturation rates at the respective water saturation for different imposed conditions were fitted with a straight line using Microsoft Excel (2010). The slope of this line gives the  $\tau$  values. Most papers in the literature have used linear interpolation to determine the dynamic pressure difference at a specific saturation (e.g., Bottero et al. 2011a). Also, from the saturation and time data, desaturation rate ( $\partial S/\partial t$ ) was determined using the central differencing scheme. This is the most popular approach in the literature (e.g., Das et al. 2007; Bottero et al. 2011a; Mirzaei and Das, 2013). The capillary number,  $\mu v/\gamma$ , determined for the system at viscosity ratio of 200 was  $1.14 \times 10^{-6}$  at the highest superficial velocity, which was determined from the highest flow rate recorded at the outflow volume collected in the bottle on the weighing balance.  $\mu$  is the viscosity of the oil,  $v$  is the superficial velocity and the  $\gamma$  is the interfacial tension between the oil and water.

As described earlier, while the saturation at local levels was determined from calibrated TDR probe readings, that of the whole domain was determined from water outflow measured on a weighing balance. Taking density of water at ambient condition as  $1 \text{gcm}^{-3}$  the volume collected was readily determined and the domain saturation was calculated based on

difference in the initial volume of water in the porous medium and the outflow. The saturation-weighting of the local levels  $P^c$  provides the domain level  $P^c$  at every count of time,  $t_n$  [s] (see equation (3.4)). Similar to the  $\tau$  determination at the local levels, equation (3.2) was used to determine  $\tau$  for the domain.

The numerical simulations by Hanspal and Das (2012) have reported the effects of temperature on dynamic capillary pressure. At the moment, there are little experimental studies on the role of temperature on dynamic capillary pressure effects and in particular, the temperature effects on the scale dependent  $\tau$ -S relationships. This work does not consider the effects of temperature and therefore  $\tau$  is only measured at ambient conditions. But the temperature dependency of the dynamic capillary pressure effects is an interesting topic and should be explored in detail in the future.

### 3.2.5 Averaging approach

The averaging technique to determine  $\tau$  for the whole domain utilised the following saturation weighted relation for capillary pressure:

$$P_{\text{domain}}^c \Big|_{t_n} = \left( \frac{\sum_{j=1}^m (1-S_j)(P_{nwj}) - \sum_{j=1}^m S_j(P_{wj})}{\sum_{j=1}^m (1-S_j) - \sum_{j=1}^m S_j} \right) \Big|_{t_n} \quad (3.4)$$

where  $P_{\text{domain}}^c \Big|_{t_n}$  represents the domain representative capillary pressure at a particular saturation and the corresponding experimental time,  $t_n$  [s] referring to the time at nth count of data generated,  $P_{nw}$  [Pa] and  $P_w$  [Pa] are the non-wetting and wetting phase pressures at the nth count of the generated data.  $S$  [-] refers to the wetting phase saturation and  $j = 1, 2, m$ , with  $m$  being the total number of measurement levels in the domain, i.e., 1 for 4cm, 2 for 8cm and 3 for 12cm cells. Although the the fluid-fluid interfaces was not tracked within the experimental domain, in principle the higher viscosity of the non-wetting phase may result in sharper saturation front of the interfaces. To take care of this possible situation in the calculation of domain averaged  $P^c$  the following approach was taken. Prior to the arrival of the oil phase at the lower measurement points in 8 and 12cm high columns, the first term of equation (3.4) is set to zero. At these points, the calculated  $P^c$  values are negative and are discarded.

In general, a sharper fluid-fluid interface is thought to have greater influence on when the interface reaches the measurement points and, hence, it may affect the calculated  $P^c$ . However, this was not a concern in this study. As evident from equation (3.4), the domain

scale  $P_c$  is calculated using the local water saturation in the porous medium determined from the TDR probes and not the saturation determined from outflows. Furthermore, the average  $P^c$  is only determined when the oil phase reaches all the measurement points. In this way, any discrepancy that may arise in the equilibrium  $P^c$ - $S$  data at the domain and local levels was avoided. Such an approach has been adopted in a number of earlier studies (e.g., Bottero et al. 2011a; Das and Mirzaei, 2013) and the same tradition was continued in this work.

In addition, the following central difference scheme was used to obtain the desaturation rate for the entire domain based on the outflow volume collected in the cylinder placed on the balance:

$$\left. \frac{\partial S}{\partial t} \right|_{t_n} = \frac{S|_{t_{n+1}} - S|_{t_{n-1}}}{t_{n+1} - t_{n-1}} \quad (3.5)$$

This is a well-accepted method and is frequently used in the literature (Bottero et al. 2011a; Das and Mirzaei, 2012).

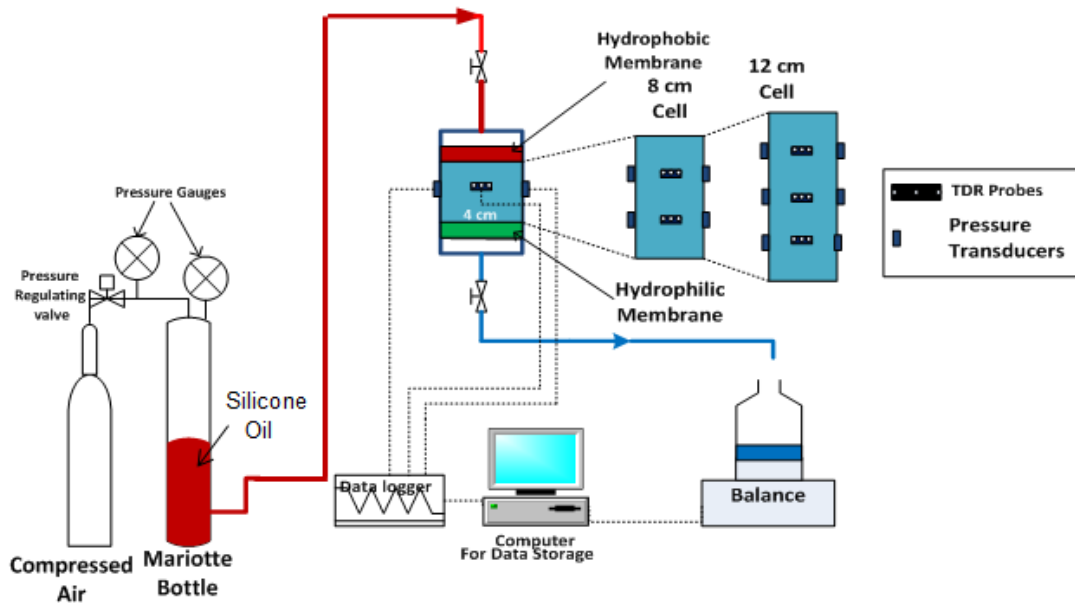


Figure 3.1: A schematic diagram of experimental set up showing different core scale domains (i.e., 4cm, 8cm and 12cm) used in this work. Only primary drainage experiment is conducted in this study.

### 3.3 Results and discussions

It has earlier been emphasised that the non-uniqueness in the characterization parameters affect the monitoring and control of two-phase systems in porous media. Results of the

investigations of the domain scale contributions to the dynamic effects in  $P^c$ -S relationship for silicone oil-water system are presented in a logical order leading to the experimental and model results on  $\tau$ -S relationship for the silicone oil-water system at various domain scales and viscosity ratios.

Determination of  $\tau$ -S relationship for two-phase flow requires prior determination of  $P^c$ -S and  $\partial S/\partial t$ -S relationships for the system of interest. Therefore, the discussion will begin with the findings on  $P^c$ -S and  $\partial S/\partial t$ -S relationships for different domain scales and viscosity ratios. In addition, imposition of the same boundary pressure on dissimilar domain scales leads to different impacts of pressure gradient ( $\Delta P$ ) across different domain scales with decreasing magnitude of  $\Delta P$  as the domain length increases. The impacts of these effects on the  $P^c$ -S and  $\partial S/\partial t$ -S relationships and the eventual  $\tau$ -S relationships are given due prominence in the discussion in this section. At the end, the parameters of importance identified in this work and from relevant papers from the literature form the basis for the development of a dimensionless correlation for  $\tau$  using Buckingham  $\Pi$ -theorem.

In order to assess the repeatability of the experiments, replicate experiments were conducted which showed reproducibility under similar conditions for both the  $P^c$ -S relationship as well as the desaturation rate.

Figure 3.2 shows a typical replicate  $\partial S/\partial t$  - S curves for the 4cm cell and 200 viscosity ratio oil at 20kPa imposed pressure. The repeatability indicates consistent packing of the porous medium in the cell. Viscosity ratio ( $\mu_r$ ) was earlier defined as the ratio of the viscosity of the non-wetting phase to that of the wetting phase. In this work, viscosity ratio and viscosity can be used interchangeably since the kinematic viscosity of water is taken to be 1cSt. Thus, the viscosity ratio has the same magnitude as the viscosity of the non-wetting phase. From Figure 3.2, it can be seen that the desaturation rate rises fast to a high value (in the absolute sense) and declines steadily until the saturation approaches the irreducible saturation point. Under dynamic drainage, as the outflow from the domain continues, the desaturation rate rises to the highest value at a high saturation. This is followed by declination as the rate decreases henceforth towards irreducible saturation. Similarly, other equilibrium and dynamic drainage experiments conducted in duplicates showed good reproducibility. All of the results show that the dynamic  $P^c$ -S curves lie above the equilibrium or quasi-static curves and it is uppermost for the largest imposed pressure i.e. 20kPa. This goes to affirm the presence of dynamic capillary pressure effects and that it is consistent with the findings from other authors (Topp et al. 1967; Chen et al. 2007; Das et al. 2007; Sakaki et al. 2010; Das and Mirzaei 2012).

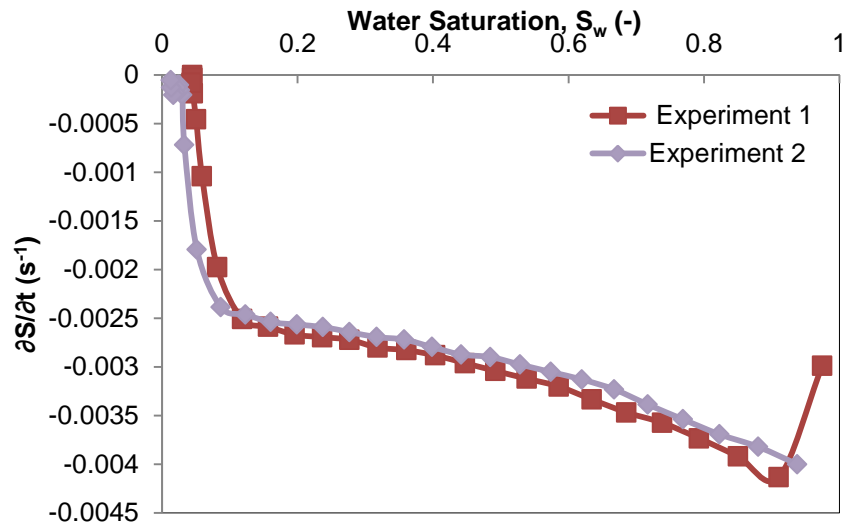


Figure 3.2: Replicate desaturation rate as a function of average domain saturation at 20 kPa imposed pressure in a 4cm cell for viscosity ratio of 200.

### 3.3.1 $P^c$ -S and $\partial S/\partial t - S$ relationships for different fluid viscosity ratios

#### 3.3.1.1 $P^c$ -S relationships

The trends/patterns of the  $P^c$ -S relationships in this work are consistent with what have been reported by other authors (Bear 2013; Das et al. 2007) and therefore, they are not discussed in length. As an example of the  $P^c$ -S curves obtained in this work, Figure 3.3 provides a graphical picture of the relationships for different viscosity ratios with the 4cm high porous domain. In consistence with other studies, the capillary pressure rises as the water saturation reduces and it becomes almost upright as the saturation approaches the irreducible condition. Also, the dynamic drainage  $P^c$ -S curves for 10, 15 and 20kPa lie above the quasi-static drainage curve. This is the reflection of dynamic effect and is in line with the desaturation patterns. Also, worthy of note is the increase in the  $P^c$  with viscosity increase. The required entry pressure is seen to similarly increase with  $\mu_r$ . This is owing to the resistance of the porous domain to flow which increases with  $\mu_r$ . Thus, a  $\mu_r$  of 200 has the least resistance to enter the medium while 1000  $\mu_r$  has the highest.

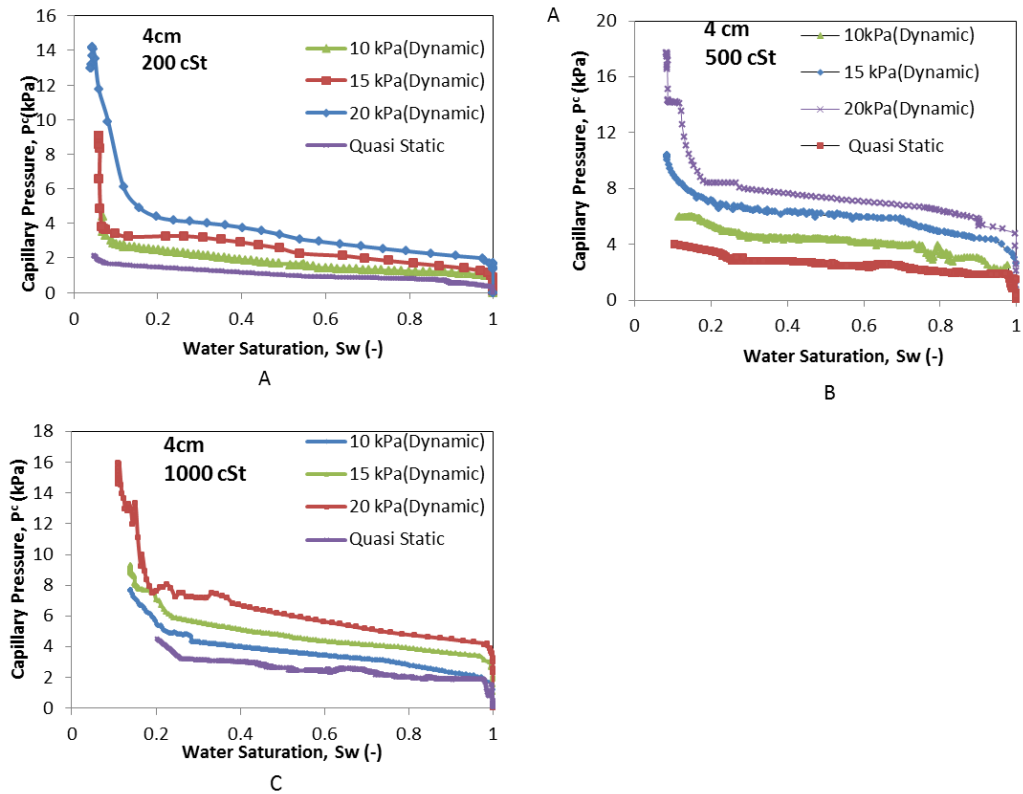


Figure 3.3: Capillary pressure and saturation relationship for quasi-static and dynamic conditions in 4cm cell for silicone oil of different viscosity ratios: (A) 200 (B) 500 (C) 1000.

At comparable saturation, 200 $\mu_r$  silicone oil-water system has a capillary pressure that is less than the 500cSt system while the 1000cSt has the highest  $P^c$ . Similar patterns are observed for the bigger domains.

### 3.3.1.2 $\partial S/\partial t$ -S relationships: Influences of fluid properties and porous domain characteristics

The desaturation rate ( $\partial S/\partial t$ ) of the aqueous phase is one of the important factors, which determines the magnitude of  $\tau$ . Therefore, a good understanding of the desaturation rate and its relationship with the saturation is crucial in quantifying the scale dependency of  $\tau$ . As expected, it is found that  $\partial S/\partial t$  decreases as the domain size increases with a visible effect of the imposed pressure on it along the depth of the domain. This is depicted in Figure 3.4(A-F) for  $\mu_r$  of 200. Starting from 8cm cell in Figure 3.4(A), it is found that the top section of the domain has the highest desaturation rate. The bottom section has a lower desaturation rate in comparison while the whole domain scale has the least rate of desaturation. This is attributed to the influence of pressure gradient, which reduces as the depth to injection point increases thereby lowering  $\partial S/\partial t$  values and raising the value of  $\tau$ . It would be recalled that

the 8cm cell is subdivided into two sections of 4cm each. Each has the TDR probe for *in situ* measurement of water saturation. Similar patterns are seen in Figure 3.5(A) and Figure 3.6(A) for 500 and 1000  $\mu_r$ , respectively.

It is noticed that the  $\partial S/\partial t$ -S relationship for the bottom section is closer to that of the whole domain scale. This can be explained in terms of the general effect of pressure gradient which reduces the  $\partial S/\partial t$  at the bottom section and domain scale, respectively. Figure 3.4(B) presents the  $\partial S/\partial t$ -S relationship in the 12cm cell for 200  $\mu_r$ . Similar to the pattern in 8cm cell,  $\partial S/\partial t$ -S decreases along the depth of the domain. The top section has the highest desaturation rate followed by the middle section. The  $\partial S/\partial t$  is least at the bottom section and remains the closest to that of the whole domain. Furthermore, the pattern remains similar in Figure 3.5(B) and Figure 3.6(B) for 500 and 1000  $\mu_r$ , respectively. It is noticeable that the  $\partial S/\partial t$ -S profiles at the middle and bottom sections are closer, which indicate higher influence of pressure gradient as the fluid leaves the top section of the domain and infiltrates into the lower section.

However, the variations in the desaturation rates in different cell sizes seem to reduce as the viscosity ratio increases. The effect of pressure gradient can still be noticed if one considers the comparisons of results from the top compartments of all the cell sizes, i.e., 4, 8, and 12cm shown in Figure 3.4(C) for 200  $\mu_r$ . Obviously, the 4cm cell does not have more than one compartment; 8cm cell has top and bottom sections of 4 cm each and the 12cm cell has top, middle and bottom compartments of sections of 4cm each. The closeness of the desaturation profiles, which almost overlies, for the same imposed boundary pressure is an indication of similar pressure gradient effects at these portions of the domains. The flow patterns at the start have much similarity until the irreducible saturation was approached where they followed different desaturation paths owing to the amount of irreducible saturation based on the domain sizes. It is visible that in the 4cm cell irreducible saturation was the least and the value increases with size of the domain. For 500 and 1000  $\mu_r$ , Figure 3.5(C) and Figure 3.6(C), respectively, similar patterns were obtained with that of 4cm cell for 500  $\mu_r$  having slightly higher rate of desaturation than the other cell sizes. At 1000  $\mu_r$ , the pattern is not much different with minor rearrangement of positions for the different cell sizes.

Other comparable sections of different cell sizes can be further discussed with a thorough look at the bottom and middle sections of the 8 and 12cm cells. Comparing the bottom sections of the 8 and 12 cm cells shown Figure 3.4(D) for 200  $\mu_r$  indicates partly overlapping profiles. Further comparison of the bottom section of 8cm cell to the middle section of 12cm

cell in Figure 3.4(E) depicts similar patterns. For 500 and 1000  $\mu_r$  (Figure 3.5(E) and Figure 3.6(E)), the middle section of the 12cm cell almost completely overlapped the profiles of the bottom section of the 8cm cell. This is not surprising as the two sections of different domain sizes are at the same distance from the injection point of their respective domains.

Finally, comparison was made of the  $\partial S/\partial t - S$  patterns at the domain scales for the different cell sizes-4, 8 and 12cm (Figure 3.4(F)) for 200  $\mu_r$ . The rate is the highest in the smallest (4cm) cell and the least in the largest (12cm) cell (absolute values) under similar conditions. Worthy of note is the pattern of the desaturation that includes a sudden jump at the start of the drainage followed by linear decline till around irreducible saturation. It is clear from Figure 3.4(F) that the desaturation rates scarcely exhibit rising trend. Largely, it declines following the initial quick rise at the start of the drainage. The short initial rise in the desaturation rate can be explained in the light of the divisions of fluid-fluid regions: the upstream invaded region, the front zone with a pressure jump associated with threshold capillary pressure ( $P^c$ ) and the virgin region, i.e. the region further into the domain which is still fully saturated with the wetting phase (Egermann et al. 2006). It was stated that the flow of the wetting fluid in the medium prior to non-wetting phase contacting the inlet face of the porous medium follows Darcy's law with the overall pressure drop and absolute permeability value. As the non-wetting phase starts to flow in the porous medium there is a reduction in the desaturation rate owing to the threshold pressure jump at the displacement front. This position corresponds to the turning point or start of declination shown in Figure 3.4F.

Furthermore, higher impact of pressure gradient at lower measurement points results in lower desaturation rates (absolute value) at different domain scales. Thus, the flow in the 4cm cell felt a lesser effect of pressure drop per unit length compared to the similar imposed pressure in larger domains, i.e., 8 and 12cm. Similar scenarios are depicted in Figure 3.5(F) and Figure 3.6(F) for 500 and 1000  $\mu_r$ , respectively.

### **3.3.2 Scale Dependency of $\tau$ -S relationships for Different Fluid Viscosity Ratios**

As earlier stated, the forecast function in Microsoft Excel (2010) was utilised for linear interpolation in order to establish corresponding points of saturation and capillary pressure at different pressures. This was done for both the quasi-static and dynamic drainage conditions as well as to determine the desaturation rate.

The estimated differences in the dynamic and equilibrium capillary pressures ( $P^{c,dyn} - P^{c,eq}$ ) were fitted to a straight line against the desaturation rate ( $\partial S/\partial t$ ) at chosen saturation values for different imposed boundary conditions. Two possible curve-fitting approaches were tried. First, a direct fit of the data points, which may generate an intercept on the y-axis, was used. Secondly, an approach which forces the fit through the origin by assuming an additional point at 100% saturation when  $\partial S/\partial t = 0$  is chosen. Slopes of these straight lines represent the dynamic coefficient. The first approach is commonly used in the literature (Mirzaei and Das 2013; Das and Mirzaei 2012; Dahle et al. 2005; Manthey et al. 2005).  $\tau$  results from the first approach (intercept fit) are presented in this work and the comparison of the two approaches is shown in Figure 3.7.

It can be seen that the two approaches produced similar trends that only differ at some middle saturation range. In other words, the fitting method might not influence the calculated dynamic coefficient at high and low water saturation values. In any case, the first approach was used in this work to calculate the dynamic coefficient values which is inconsistent with most studies.

Figure 3.8 presents the results for the dynamic coefficient as a function of saturation at different domain scales for different viscosity. The results in Figure 3.8(A-C) show that the coefficient follows a rising trend as the saturation decreases. Also, it increases in magnitude as the viscosity ratio ( $\mu_r$ ) increases. The dynamic coefficients are found to be in the range of  $1.72 \times 10^5$  and  $4.77 \times 10^5$  Pa s for the saturation values of 0.2 and 0.9 in the 4cm cell for the viscosity ratio ( $\mu_r$ ) of 200. For the same domain scale,  $\mu_r$  of 500 results in the dynamic coefficients in the range of  $1.26 \times 10^6$  to  $7.40 \times 10^6$  Pa s while the  $\mu_r$  of 1000 results in the coefficient in the range of  $5.00 \times 10^6$  to  $9.08 \times 10^6$  Pa s. As evident, the results show a general rising trend in the magnitude of the dynamic coefficients as the viscosity ratio increases. This increase in the dynamic coefficients is a result of the decrease in the desaturation rate as  $\mu_r$  increases. Also, the dynamic coefficient increases exponentially as the saturation decreases. A graphical comparison of the results at different viscosities in 4cm cell is shown in Figure 3.8(D). As evident, the results show an order increase in  $\tau$  as the  $\mu_r$  increases from 200 to 500 and 1000 at the same domain scale. However,  $\tau$  remains within the same order of magnitude at  $\mu_r$  of 500 and 1000.

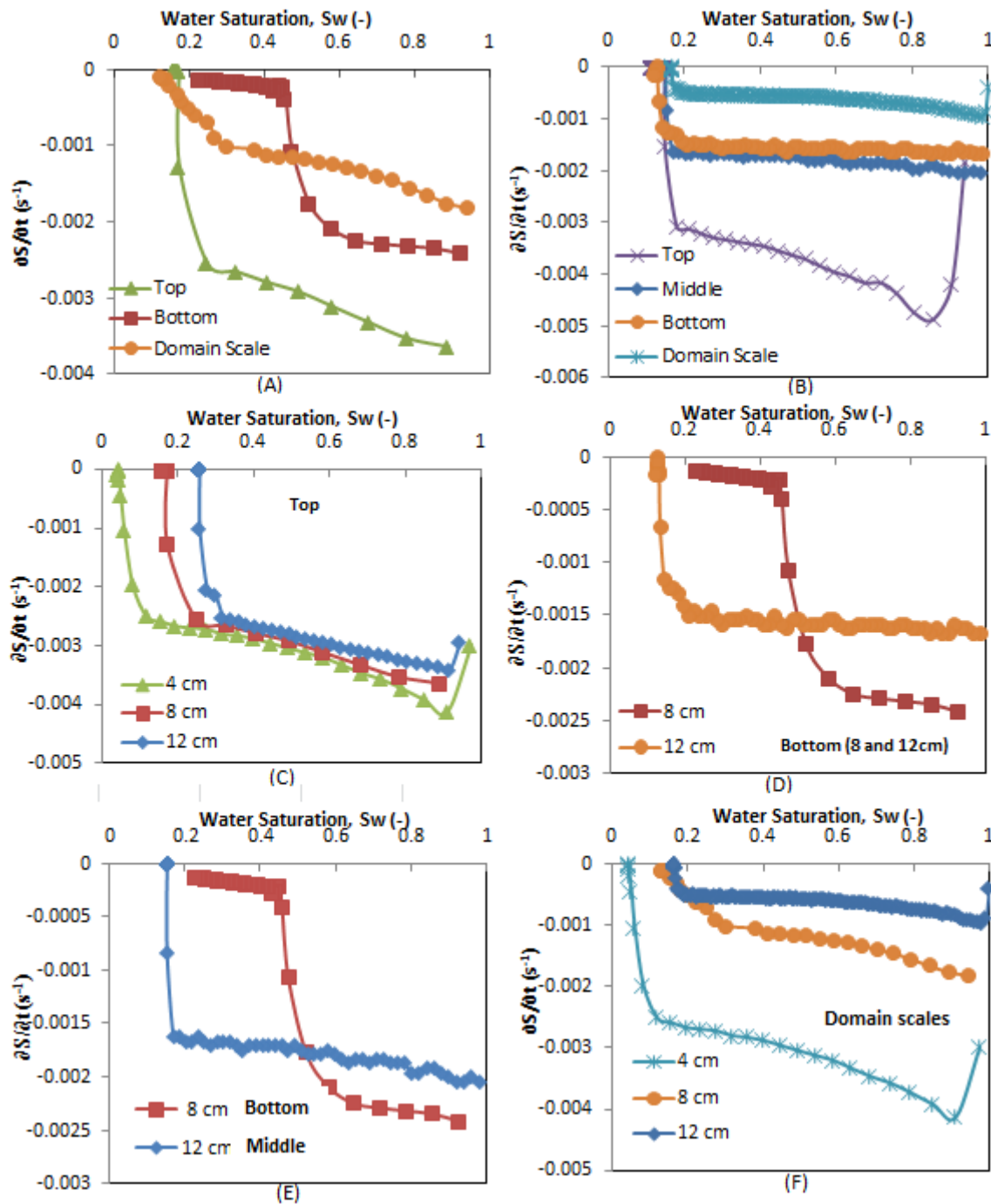


Figure 3.4: Desaturation patterns at different sections and domain scales for viscosity ratio of 200 at 20kPa imposed pressure: (A) 8cm cell (B) 12cm cell (C) Top sections in each of 4, 8 and 12cm cells (D) Bottom sections in each of 8 and 12cm cells (E) Bottom of 8cm cell compared to the middle of 12cm cell (F) Domain scales of 4, 8 and 12cm cells.

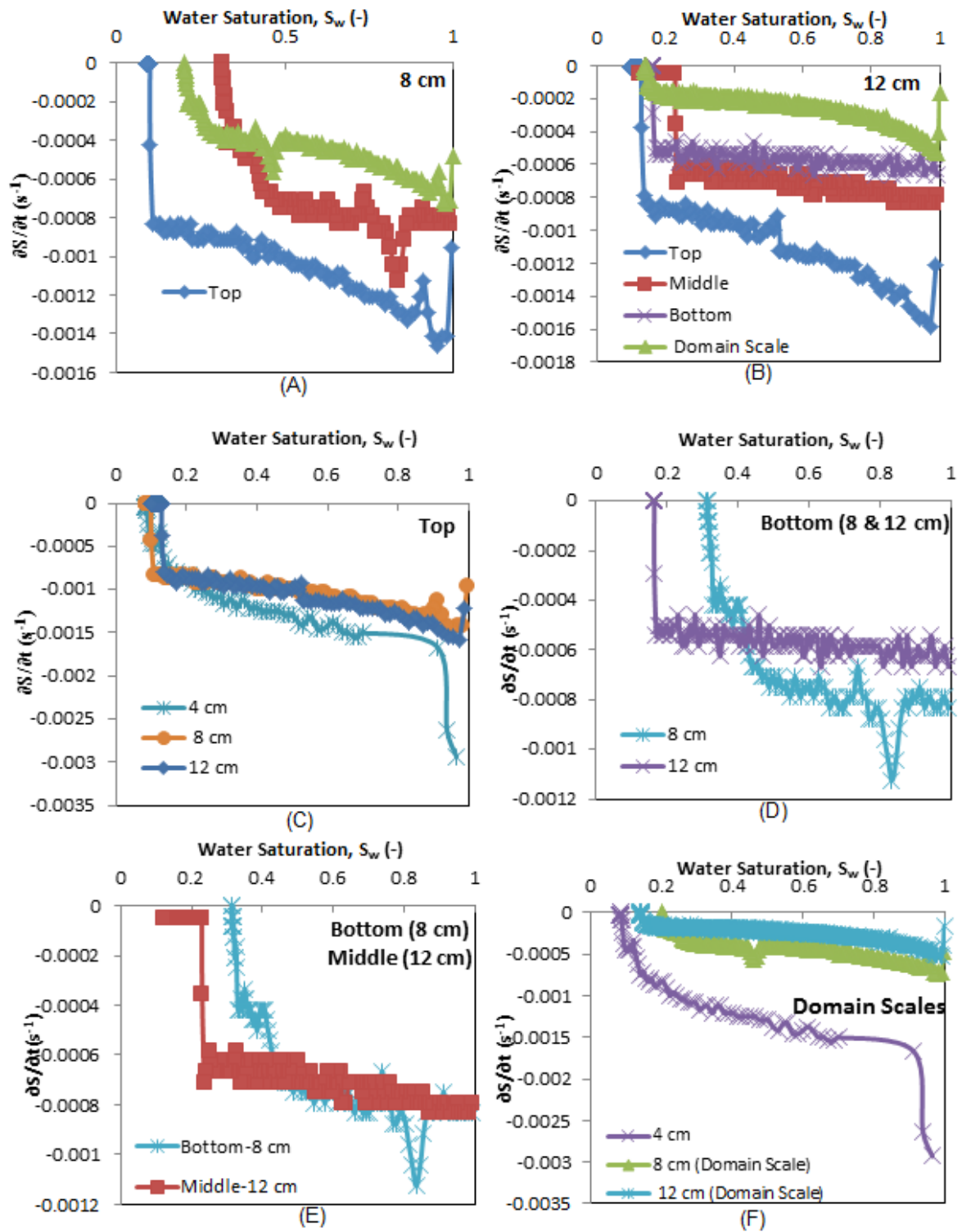


Figure 3.5: Desaturation patterns at different sections and domain scales for 500 viscosity ratio at 20kPa imposed pressure: (A) 8cm cell (B) 12cm Cell (C) Top sections in each of 4, 8 and 12cm cells (D) Bottom sections in each of 8 and 12cm cells (E) Bottom of 8cm cell compared to the middle of 12cm cell (F) Domain scales of 4, 8 and 12cm cells.

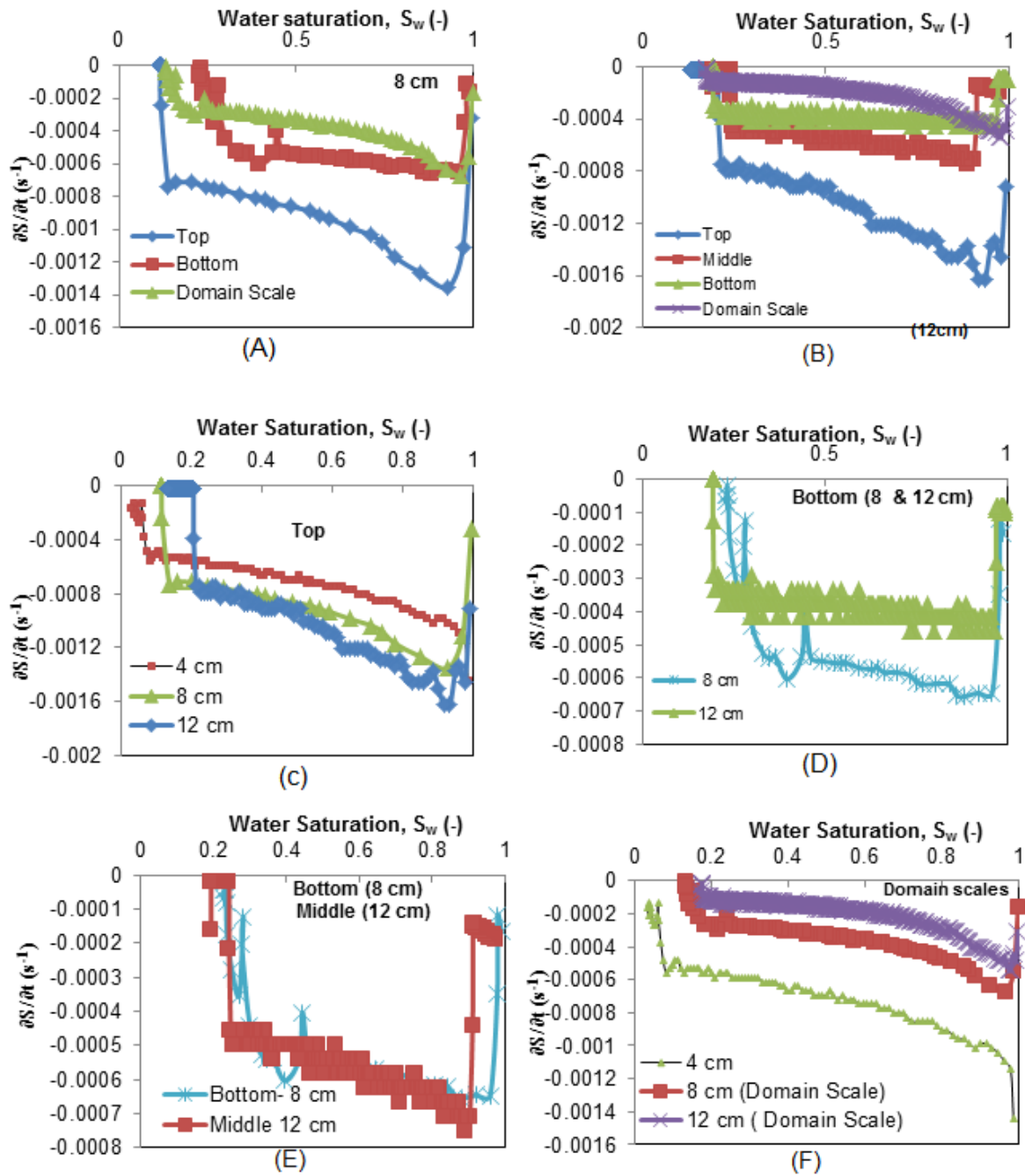


Figure 3.6: Desaturation patterns at different sections and domain scales for 1000 viscosity ratio at 20 kPa imposed pressure: (A) 8cm cell (B) 12cm Cell (C) Top sections in each of 4, 8 and 12cm cells (D) Bottom sections in each of 8 and 12cm cells (E) Bottom of 8cm cell compared to the middle of 12cm cell (F) Domain scales 4, 8 and 12cm cells.

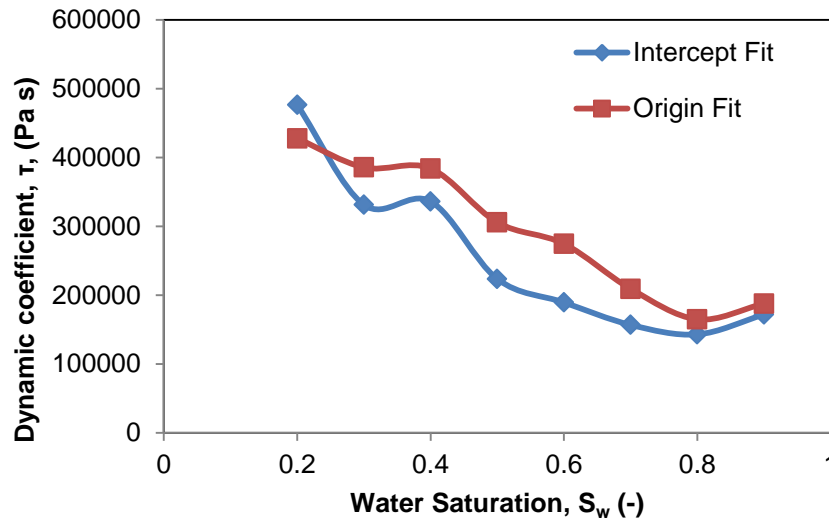


Figure 3.7 :Comparison of Intercept and Origin fitting approaches on magnitude of dynamic coefficient for a viscosity ratio of 200 in a 4cm cell.

For the larger porous domains (8cm and 12cm) similar trends are observed with additional effect of the domain depth as the fluid front moves from the top of the domain during the drainage process. For example, Figure 3.8(A) shows that in the 8cm cell and  $200 \mu_r$ , there are variations in the trends of  $\tau$  values at the top and bottom compartments of the cell. As explained in subsection 3.2.2, bigger cells of heights 8cm and 12cm are subdivided into multiple compartments of 4cm with each compartment having a TDR probe and a pair of pressure transducers. These are hypothetical compartments but their size corresponds to the typical averaging volumes over which a TDR probe carries out the measurements for water saturation.

For the same applied pressure on all cell sizes, the effect of pressure gradients across the domain becomes more apparent, as the domain size increases, especially at lower measuring points i.e. further away from the top injection point. For the same reason, the desaturation rate changes down the domain. From the local measurement points to domain scale, there is an increasing magnitude of dynamic coefficient. While there is similar magnitude of  $\tau$  at the top of the domain in 8cm cell compared to 4cm cell, the bottom has  $\tau$  magnitude close to the domain scale. Thus, for the 8cm scale,  $\tau$  at the bottom measurement point and domain scale have an order increase in magnitude close to irreducible saturation.  $\tau$  values ranging from  $4.01 \times 10^5$  to  $1.31 \times 10^6$  Pa s were obtained for  $200 \mu_r$  in the 8cm cell at the domain scale between 0.9 and 0.3 saturation. The desaturation rate for the entire domain was calculated based on the outflow collected in the cylinder on the balance while the top and bottom desaturation rate was determined from TDR probe readings. The capillary

pressure for the domain scale was determined from saturation-weighted average of the local level capillary pressure in the cells.

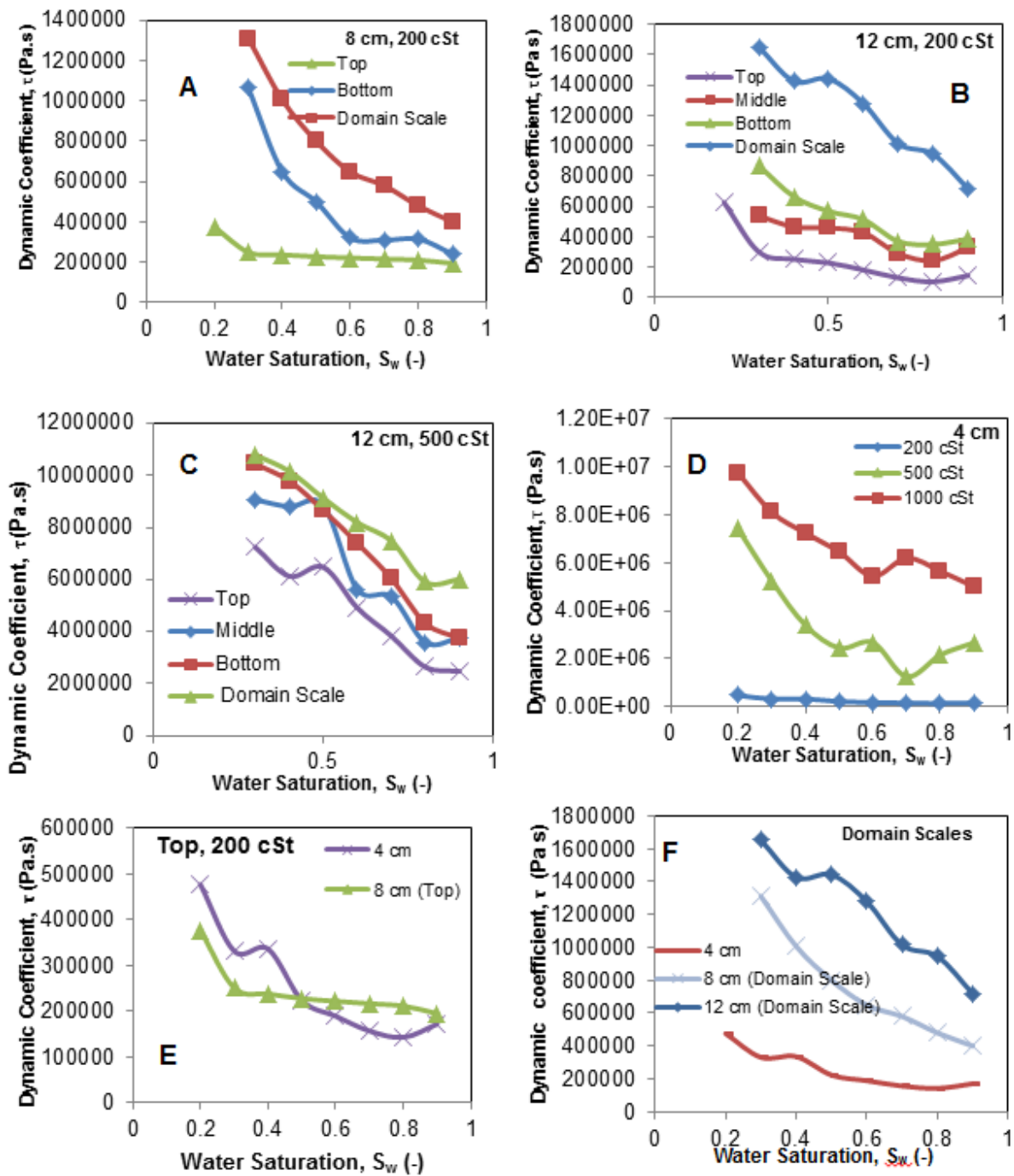


Figure 3.8: Dynamic coefficients and saturation relationship for the silicone oil-water system: (A) 8cm cell, 200 viscosity ratio (B) 12cm cell, 200 viscosity ratio (C) 12 cm cell, 500 viscosity ratio (D) 200, 500 and 1000 viscosity ratio silicone oil in 4 cm cell (E) Top sections of 4 and 8 cm cells for 200 viscosity ratio (F) Domain scales for 4, 8 and 12 cm cells, 200 viscosity ratio. Domain scale  $\partial S/\partial t$  obtained from balance readings.

Figure 3.8(E) compares  $\tau$  at the top section of the 8cm cell with the domain scale values obtained at 4cm scale. It can be seen that the two share similarities in the trend of  $\tau$ -S curves. Similarly, for the 12cm cell and 200  $\mu_r$ , in comparison with 4cm cell for the same viscosity ratio, a higher value of  $\tau$  ( $1.653 \times 10^6$  Pa s) having an order of magnitude increase was obtained at saturation of 0.3 for the domain scale. Figure 3.8(B) shows this trend as well as the other sections of the 12cm cell.  $\tau$  values of  $1.08 \times 10^7$  and  $1.25 \times 10^7$  Pa s representing an order increase in the values of  $\tau$  were obtained in the 12cm high cell for 500 and 1000  $\mu_r$  in comparison with the respective  $\tau$  values in the 4cm scale for the respective viscosities at 0.3 saturation. Figure 3.8(C) shows the relationship at 12cm scale for 500 $\mu_r$ . The effect of pressure gradient is present but it seems to be lesser in impact than that for 200 $\mu_r$  as the domain scale values of  $\tau$  lie close to the values at the bottom level. Similar effect of scale had earlier been expressed by Bottero et al. (2011a, b), where they affirmed an order of magnitude increase from local to upscaled or domain scale.

Figure 3.8(D) compares the values and trends of  $\tau$  for 200, 500 and 1000 $\mu_r$  at the 4cm scale.  $\tau$  values continue to increase as the viscosity ratio increases and it is the highest at 1000 $\mu_r$ . Also, Figure 3.8(F) compares the domain scale values of  $\tau$  for different scales, namely, - 4, 8 and 12cm cells where the highest  $\tau$  values are found for the 12cm scale.  $\tau$ -S relationships at different layers appear closer for 500 $\mu_r$  in Figure 3.8(C) as compared to 200 $\mu_r$  in Figure 3.8(A). This might be owing to the decreasing desaturation rate at the different layers of the domain for higher viscosity oil (500 $\mu_r$ ).

To further bring to light some of the trends seen in this work, the results are discussed in the context of what have been shown in the literature. Effect of viscosity ratio on  $\tau$  was earlier reported by Goel and O'Carroll (2011) for the viscosity ratios of 0.442 and 4.098 and it was reported that  $\tau$  increases with viscosity ratio as obtained in this work. In their results, average  $\tau$  ranges from  $1.2 \times 10^6$  to  $2.74 \times 10^6$  Pa s for the 4.098 viscosity ratio while for 0.442 viscosity ratio  $\tau$  values range between  $4.85 \times 10^5$  to  $2.16 \times 10^6$  Pa s. In comparison, the results in this work show that the reported  $\tau$  values are in a similar range as in 200 $\mu_r$  in the 12cm cell with the average  $\tau$  ranging between  $7.18 \times 10^5$  to  $1.65 \times 10^6$  Pa s at the domain scale. Even though the difference in the viscosity ratios is quite large (200 in this work by assuming water has 1cSt viscosity at ambient condition), the closeness of the results can be explained in the context of the domain size used. Goel and O'Carroll (2011) used a pressure cell of 10cm diameter similar to the cell with 10.2cm diameter but the length of their cell was 20cm compared to the cells in this work with maximum height of 12cm. This shows that the effect of height can be very significant on the results. Furthermore, intrinsic permeability of

their medium ( $1.53 \times 10^{-11} \text{ m}^2$ ) is lower than that of this work and this is known to influence the magnitude of  $\tau$  (Das et al. 2007). In addition, the influence of  $\partial S/\partial t$  can still be found in the reported values. For example, Goel and O'Carroll (2011) reported  $9.8 \times 10^{-4}$  and  $2.9 \times 10^{-3} \text{ s}^{-1}$  as the highest  $\partial S/\partial t$  values for the 4.098 and 0.442 viscosity ratios, respectively, as compared to  $4.1 \times 10^{-3}$  and  $3.4 \times 10^{-3} \text{ s}^{-1}$  at 4 and 12 cm domain scale, respectively, for  $200\mu_r$  in this work. While the values are closely of the same order, the gradient in the  $\partial S/\partial t$  values, which might result from the pressure gradient effect discussed above, will be much higher in their work considering the length of the domain used in the work (20cm). Thus, higher values of  $\tau$  might be reported than expected.

Also, Camps-Roach et al. (2010) reported  $\tau$  in the range  $3.7 \times 10^5$  to  $10^6 \text{ Pa s}$  for the air-water system for a cell of 10cm diameter and 20cm height. This can be compared with the results found in this work and the same reason can be adduced for the closeness of  $\tau$  despite a large difference in viscosity values. In addition, Das and Mirzaei (2012) utilised a similar viscosity ratio (200) as in this work and the same 12cm height cell, their results for  $\tau$  range between  $10^3$  to  $10^6 \text{ Pa s}$ . This is lower than the corresponding viscosity ratio and scale in this work but the difference can be explained in the light of higher permeability medium used by Das and Mirzaei (2012) which was  $8.7 \times 10^{-10} \text{ m}^2$ . By and large, the results in this work are comparable to other studies although they are for different fluids pair and domain sizes.

In the light of the above discussion, the effects of scale and viscosity ratio on the trend in the magnitude of  $\tau$  can be discerned. Also, the effect of pressure drop on the domain scale magnitude of  $\tau$  is apparent. Addressing these observations one after the other, the rise in the value of  $\tau$  with viscosity can be largely attributed to decrease in desaturation rate with increased viscosity of the non-wetting phase. As equation (3.2) shows,  $\tau$  value is inversely affected by the desaturation rate ( $\partial S/\partial t$ ), i.e., the lower the desaturation rate, the higher the  $\tau$ . Thus, the value of  $\tau$  rises as the  $\mu_r$  increases from 200 to 500 and 1000. An order increase in the magnitude of  $\tau$  from 200 to 500 and 1000  $\mu_r$  at the 4cm scale is observed. This trend repeats itself for viscosity values at 12cm scale with  $\tau$  at 200, 500 and 1000  $\mu_r$  having an order increase in magnitude compared to their respective values at the 4cm scale. Considering different domain sizes,  $\tau$  showed an order increase in magnitude from the 4cm scale to 12cm scale for all viscosities which goes on to say that there is a direct relationship between  $\tau$  and domain scale. Also, a decrease in the desaturation rate with depth may be strongly connected to the pressure drop across the domain. This has the implication of raising  $\tau$  values considering the relation in equation (3.2). This is in contrast to the findings

of Camps-Roach et al. (2010) that  $\tau$  does not change with the averaging window considered in their work. However, the observation in this work is similar to the report by Bottero et al. (2011a) with respect to the domain scale. Bottero et al. (2011a) reported an order increase in upscaled values of  $\tau$  for their experimental domain in comparison to the local level. Similarly, they observed that magnitude of pressure difference at the local scale (0.7cm) was close to that at the averaging window of 11cm while the desaturation rates were more apart with  $4 \times 10^{-2} \text{ s}^{-1}$  and  $4 \times 10^{-3} \text{ s}^{-1}$  for the respective scales in their experiment. Thus, they concluded that the scale dependency of the dynamic coefficient is mainly because of the rate of change of saturation, whose magnitude decreases with the increase of the length scale. To explain this, equation (3.2) can be used, where  $\tau$  is related to both the pressure difference and the desaturation rate. While the pressure difference can be fairly similar under different conditions the  $\partial S/\partial t$  can become drastically low under many conditions, e.g., viscosity ratios of the two-phase system, distance from injection point, porous media properties and so on. In contrast to the observation of Dahle et al. (2005),  $\tau$  may not become arbitrarily large as the averaging length increases as observed in the above discussion.

### 3.3.3 Influence of the similar pressure gradient on domain scale dependence of $\tau$ -S

The results discussed in this work used different pressure gradient ( $\Delta P$ ) across domain sizes. To know whether the results obtained in this study will be different under the influence of similar  $\Delta P$  across the different domain scales, the results of the investigations with similar  $\Delta P$  are shown in Figures 3.9 and 3.10 for the domain scale  $\tau$ -S relationships in different domain sizes and viscosity ratios. The approach for calculating the dynamic coefficient for this investigation was described under the methodology.

Figure 3.9(A) shows that there is slight increase of  $\tau$  from the 4cm to 8cm high domain scales. The increase becomes more significant at the irreducible saturation. Figure 3.9(B) shows clearly that  $\tau$ -S increases significantly with domain scales. Figure 3.9B shows result for the silicone oil-water system at 200 viscosity ratio. Figure 3.10 shows the results for the 500 viscosity ratio. Figure 3.10(A) shows that there is clear dependence of  $\tau$ -S relationship on the domain scale, increasing from the 4 to 8cm high domain scales. Similarly, there is evidence of domain dependence on  $\tau$ -S from 8cm to 12cm high domain scales for 500 viscosity ratio. This is shown in Figure 3.10(B).

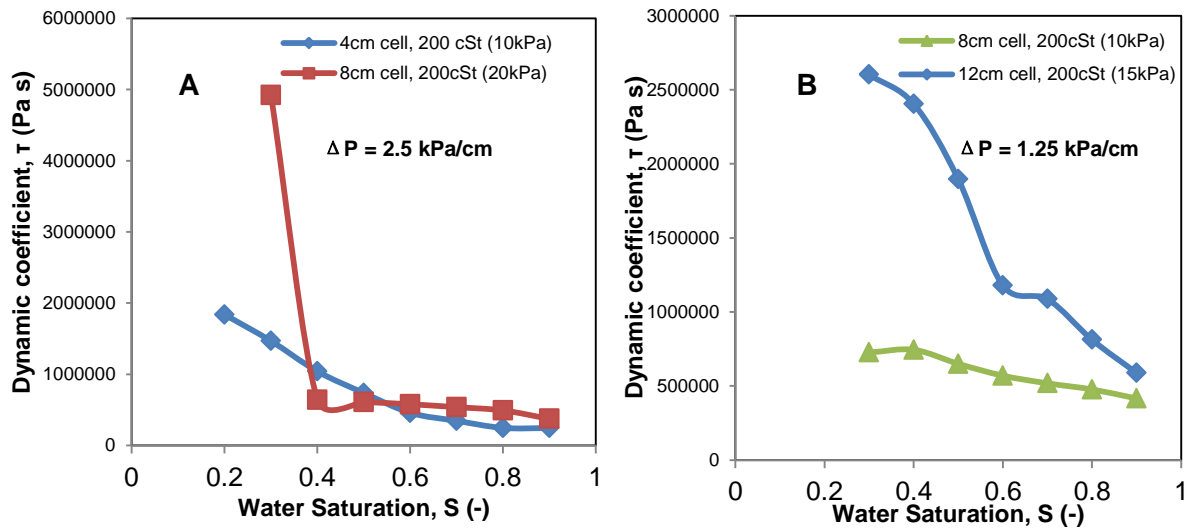


Figure 3.9: Influence of similar pressure gradient ( $\Delta P$ ) on domain scale dependence of  $\tau$ - $S$  curves at the viscosity ratio of 200

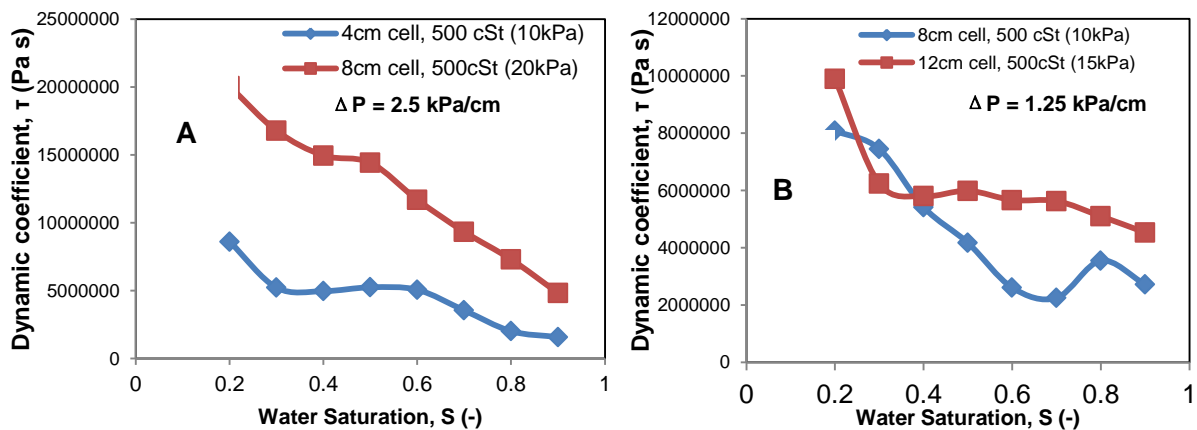


Figure 3.10: Influence of similar pressure gradient ( $\Delta P$ ) on domain scale dependence of  $\tau$ - $S$  curves at the viscosity ratio of 500.

### 3.3.4 $\tau$ scaling factor ( $\tau_r$ )

So far, the results on  $\tau$  are discussed in terms of specific fluid properties. However, the ratio of  $\tau$  at a measurement point to the  $\tau$  value for the whole domain scale seems to provide interesting general insights into the scaling dependency of  $\tau$  and therefore it is discussed briefly in this section. Physically, the ratio of  $\tau$  means the ratio of  $(P^{c,dyn} - P^{c,eq})|_s / \partial S / \partial t|_s$  at two different averaging scales and any term that affects  $(P^{c,dyn} - P^{c,eq})|_s / \partial S / \partial t|_s$  should also affect the ratio. As said before, the local  $\tau$  value depends on the measurement point in the

domain and increases with the depth away from the injection point. Further, it is the highest for the domain scale. Thus, this ratio should be equal to or smaller than unity at all saturation. To indicate the above ratio,  $\tau$  scaling factor,  $\tau_r$  is defined as the ratio of  $\tau$  at a particular measurement point to that at the domain scale, both measured for the same porous domain, fluid pair and medium permeability.  $\tau_r$  is then plotted as a function of  $S$ . This is expected to provide a more general trend on the scaling dependency of  $\tau$  in relation to the viscosity ratio.

For the 4cm high cell, there is only one measurement point at the centre of the domain, thus this scale is excluded from this discussion. For the 8cm high cell with two pairs of measurement points,  $\tau_r$  is higher at the bottom, than the top measurement point for 200  $\mu_r$ . This is illustrated in Figure 3.11(A). The difference between  $\tau_r$  at these two points appears to be nearly constant at higher water saturation but it becomes more pronounced as the saturation decreases. Also, the relationship of  $\tau_r$  with saturation at the bottom of the domain becomes increasingly non-linear in nature. The relation of  $\tau_r$  for 500  $\mu_r$  for the same domain scale is shown in Figure 3.11(B). It shows some alternation of higher and lower values of  $\tau_r$  between the bottom and the top measurement points. However, by and large,  $\tau_r$  at the bottom measurement points show higher values indicating that  $\tau$  at the bottom of the domain is closer to the values for the whole domain. Similar to the behaviour at 200  $\mu_r$ , the trend in  $\tau_r$  at the 1000  $\mu_r$  maintains clearly higher values for the bottom measurement points. The relationship is illustrated in Figure 3.11(C).

The  $\tau_r$  trend in the 12cm high domain follows similar pattern as above. This therefore confirms the general trend of  $\tau_r$ . In addition to the top and bottom measurement sections, the 12cm cell has a middle measurement point. Figure 3.12(A) shows that  $\tau_r$  remains highest at the bottom section for 200  $\mu_r$ . This is where the pressure gradient is least, resulting in the lowest  $\partial S/\partial t$ . This trend is further affirmed in Figure 3.12(B) and Figure 3.12(C) for 500 and 1000  $\mu_r$  respectively. However, it can be seen that the ratio is the highest for 500  $\mu_r$ . This is connected to the fact that  $\tau$  values at the measurement points for 500  $\mu_r$  in the 12cm high cell are closer in value to the  $\tau$  at the domain scale than other viscosity ratios for the same 12cm high cell. Since  $\tau$  is related to how far or close to equilibrium is the two-phase system (Das et al. 2007), above behaviours can be explained in terms of the equilibration times, which becomes longer as the depth of the domain from the injection point increases. Since  $\tau$  is higher at the bottom, it implies higher equilibration time is required at this point while the highest equilibration time will be found at the domain scale. Thus, the equilibration

time increases with depth from the injection point. This implies a higher scaling factor is needed with increasing distance away from the injection point.

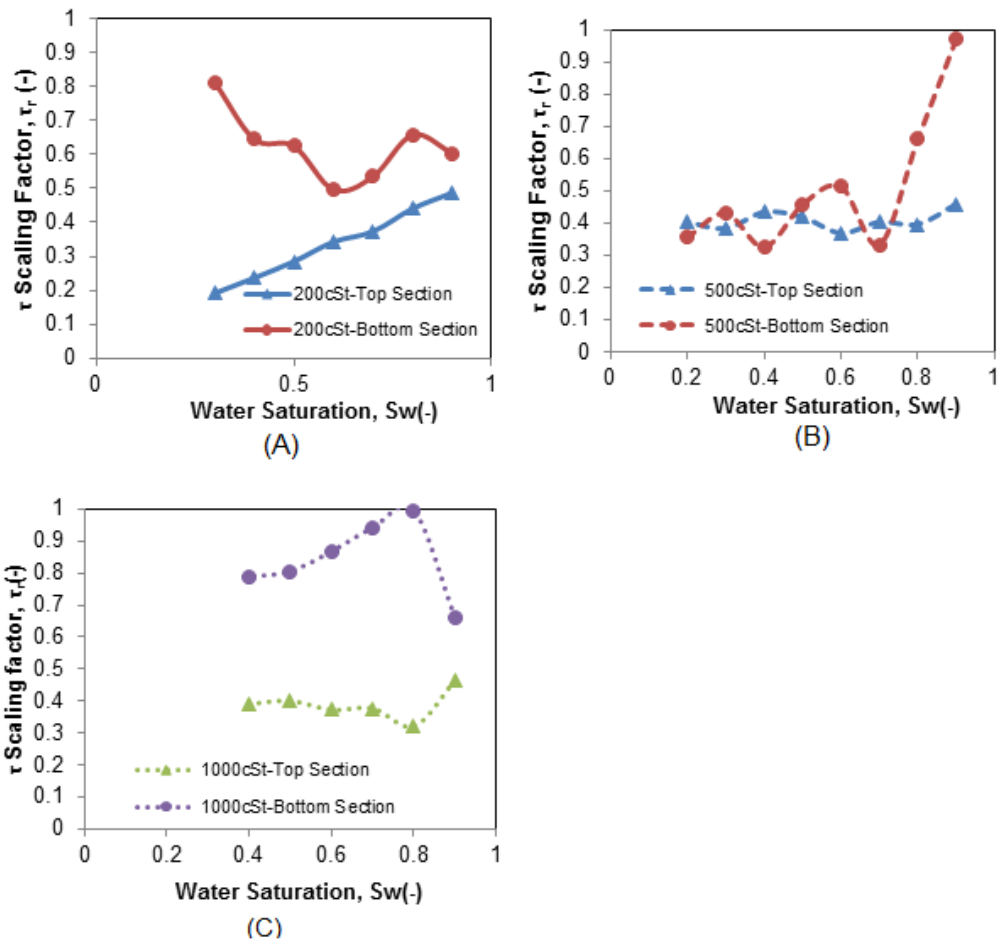


Figure 3.11:  $\tau$  scaling factor in 8cm high cell for different viscosity ratios (A) viscosity ratio of 200 (B) viscosity ratio of 500 (C) viscosity ratio of 1000.

### 3.3.5 Non-dimensional analysis of dynamic coefficient using the Buckingham's II theorem

As discussed in a number of other publications and this work, many factors are attributed to the presence of dynamic capillary pressure effect in two-phase flow in porous media. In the light of the results in this work, the influence of domain scales is elucidated while the effects of viscosity ratio are emphasised. Overall, it can be safely stated that it is a combined effect of these effects that determines the magnitude of  $\tau$  and not simply the scale of the domain or the viscosity ratio or the medium permeability. Therefore, relating these variables through a functional form provides the advantage of applying this relation to directly estimate  $\tau$  and in particular to quantify the interplay of variables in determining the  $\tau$  value in systems varying in scales or other properties.

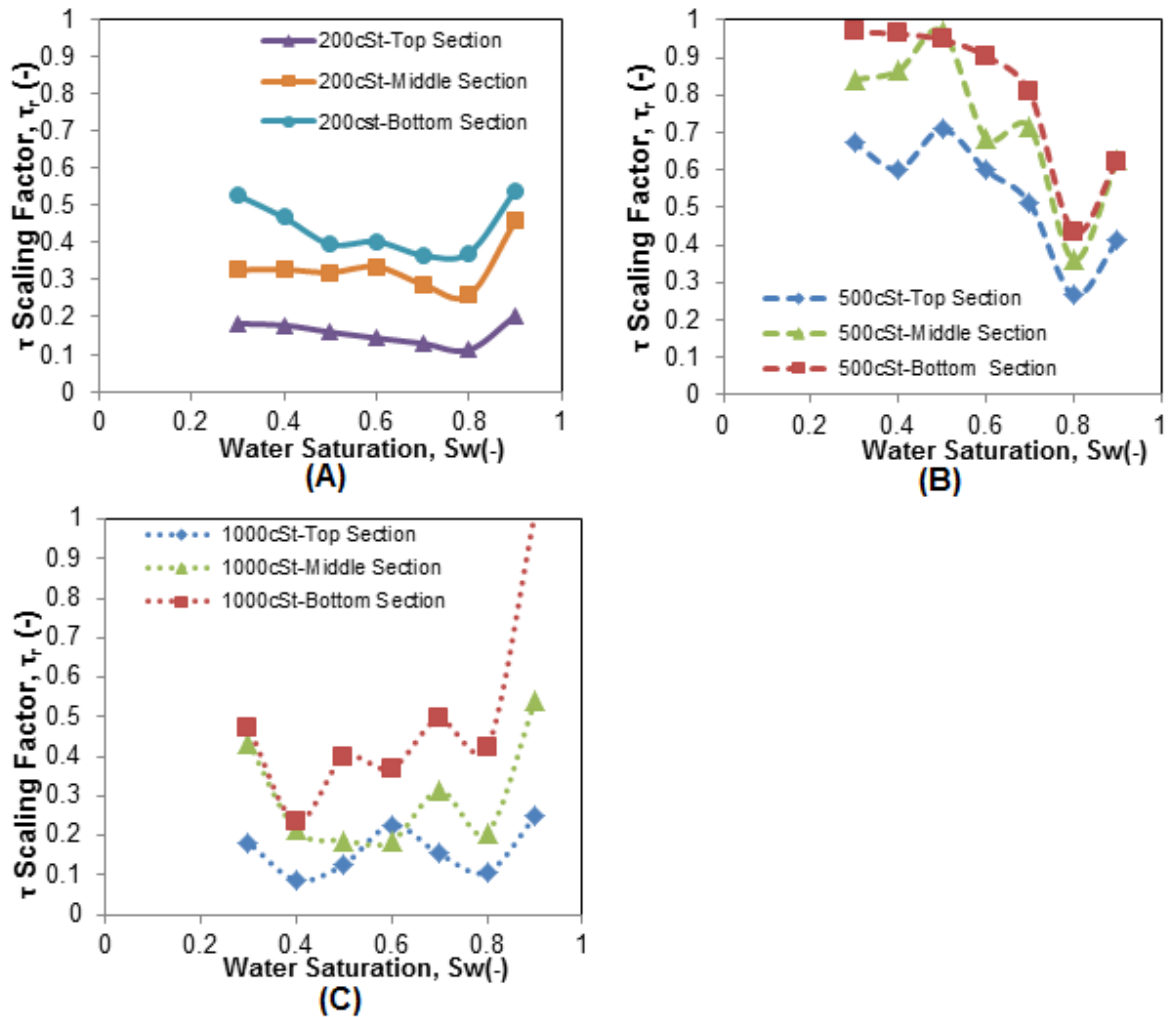


Figure 3.12:  $\tau$  scaling factor in 12cm high cell for different viscosity ratios: (A) viscosity ratio of 200 (B) viscosity ratio of 500 (C) viscosity ratio of 1000.

Such a functional relationship can be derived from a non-dimensional analysis of  $\tau$  and the relevant variables highlighted above. This can derive from the fact that all variables in the equation should have zero dimensions. By constructing non-dimensional groups of variables expressing a relationship among different variables, it is then possible to express empirical data in the form of a function. More importantly, the lumped behaviour of a parameter (i.e.,  $\tau$  in this case) in domains of different size can be understood. When a dimensional analysis is applied, if the relevant dimensionless groups are the same on two systems, e.g., a smaller and a bigger porous domain, the result of the smaller system would be applicable to the larger system or vice versa. Therefore, conceptually a non-dimensional analysis of the dynamic coefficient provides an attractive way to correlate the experimental results in this work and determine further how it behaves in combination with other variables.

To carry out the non-dimensional analysis of  $\tau$ , the well-known Buckingham's  $\Pi$ -theorem was employed owing to its usefulness in determining sets of dimensionless parameters from chosen variables. In principle, the theorem reduces a dimensionally homogenous relationship (i.e. every independent, additive term has the same dimension) involving  $n$  variables in  $m$  fundamental dimensions to a single relationship among  $n-m$  independent dimensionless products (Ghosal and Datta 1993). Thus, using the  $\Pi$ 's notation to represent the dimensionless term, the theorem can be expressed as:

$$\Pi_1 = \Phi(\Pi_2, \Pi_3, \dots, \Pi_{n-m}) \quad (3.6)$$

Where  $\Pi$  represents dimensionless term. In this work, a common method was applied, namely the 'method of repeating variables' to determine the  $\Pi$  terms, where the following variables have been used based on the knowledge on the dynamic coefficient.

$$f(\tau; g, K, P^d, V, \lambda, \rho_r, \mu_r, S, \phi) = 0 \quad (3.7)$$

Here  $\tau$  is the dependent variable and  $g, K, P^d, V, \lambda, \rho_r, \mu_r, S, \phi$  are the independent variables. In equation (3.7),  $g$  is the gravity,  $K$ , the isotropic intrinsic permeability,  $P^d$ , the entry pressure,  $\phi$ , the porosity,  $\lambda$ , the pore size distribution index,  $V$ , the domain volume representing domain scales,  $\rho_r$  and  $\mu_r$  are the fluid density and viscosity ratios, respectively, while  $S$  is the water saturation. The variables are chosen based on the most significant variables that have been reported to be important in determining the  $\tau$ . It is defined that the effects that boundary conditions or any other parameters (e.g., pressure gradient) have on the results are directly captured by the values of  $\tau$  and  $S$ .

In the analysis, it is necessary to use the dimensional terms for forming the dimensionless groups. Therefore, the analysis begins by choosing the five dimensional variables in equation (3.7), namely,  $\tau$ ,  $g$ ,  $K$ ,  $P^d$  and  $V$ . The dimensionless variables (e.g.,  $\phi$ ,  $S$ ) can be incorporated in the derived functional form as convenient but based on the knowledge of how a particular variable affect the  $\tau$ .

Using the standard theorem procedures, it can be shown that two dimensionless groups of variables are needed to form a functional relationship between the above variables, which are as follows:

$$\Pi_1 = \frac{\tau \sqrt{g}}{K^{1/4} P^d} \quad (3.8)$$

$$\Pi_2 = VK^{\frac{-3}{2}} \quad (3.9)$$

$\Pi_1$  contains the dynamic coefficient,  $\tau$ , and it can be interpreted as the dimensionless group of  $\tau$ .  $\Pi_2$  can be viewed as the non-dimensional volume of the domain (scale) which is made dimensionless with respect to the permeability of the porous domain.  $\Pi_2$  can be modified to include the non-dimensional parameters in equation (3.7) without affecting the dimensionality of the group. This requires some user's experience and knowledge of the relevant process. However, there is significant understanding of how the dynamic coefficient generally depends on these variables, i.e.,  $\tau$  is directly proportional to viscosity and density ratios while it is inversely related to saturation, porosity and pore size distribution index. Using these general understanding, equation (3.9) is modified to include the non-dimensional independent parameters as follows:

$$\Pi_3 = \frac{VK^{\frac{-3}{2}} \rho_r \mu_r}{\phi \lambda S} \quad (3.10)$$

$\Pi_3$  can still be viewed as a term that represents the non-dimensional form of the volume (scale) of the domain. Further, it can now be stated that;

$$\Pi_1 = f(\Pi_3) \quad (3.11)$$

$$\Pi_1 = f(\Pi_3)$$

Expressing this in a non-linear form:  $\Pi_1 = a[\Pi_3]^b$

Or

$$\frac{\tau \sqrt{g}}{K^{1/4} P^d} = a \left[ \frac{VK^{\frac{-3}{2}} \rho_r \mu_r}{\phi \lambda S} \right]^b \quad (3.12)$$

Where  $a$  and  $b$  are the correlation coefficients to be determined from experiments for specific case. Equation (3.12) shows the dimensionless groupings, which describe an interplay of variables that affects  $\tau$ . Furthermore, equation (3.12) shows a dependence of dimensionless  $\tau$  on a term representing the dimensionless volume of the domain. Plots of the relationship in equation (3.12) using the data in this work are shown in Figure 3.13 for the whole domain scales. To obtain the  $\tau$  values for this section, all three pressures (i.e., 10, 15, 20 kPa) were employed as they have been used to obtain the results in Figure 3.8. Figure 3.13(A) shows the  $\Pi_1 - \Pi_3$  relationship for all the viscosity ratios. It shows a rising trend in this relationship for 200  $\mu_r$ , which is almost linear for some of the  $\tau$  values. It should be pointed out that the position of the saturation is reversed owing to its inverse relation in  $\Pi_3$ . So, instead of

increasing saturation along the  $\Pi_3$  axis, it reduces in value. Similarly, the relationship in 500  $\mu_r$  in the same Figure 3.13(A) follows a similar pattern though with less-aligned scatter points resulting in a lower  $R^2$  value (0.7781). 1000  $\mu_r$  exhibits similar trend. Large magnitude of  $\tau$  obtained in higher viscosity silicone oil-water systems (500 and 1000  $\mu_r$ ) results in large values of  $\Pi_1$  that dwarfs the  $\Pi_1 - \Pi_3$  relationships for 200  $\mu_r$ .

The influences of saturation and domain scale are not clearly discernible in Figure 3.13(A) as each viscosity attains its final saturation, expressed in  $\Pi_3$ , differently, irrespective of other terms. However, the impact of viscosity is visible as  $\Pi_1$  increases with increasing viscosity ratio for the same value of  $\Pi_3$ . It is also visible at some points that  $\Pi_1$  for 500  $\mu_r$  lies higher than for 1000  $\mu_r$  at the same  $\Pi_3$ . This may appear contrary to expectation, but its explanation lies in the fact that at the same  $\Pi_3$  the values of the two variables,  $V$  and  $S$ , are not the same for each of the viscosities. At this same saturation point, the  $\tau$  value in 500  $\mu_r$  corresponds to a certain  $V$  and  $S$  while in 1000  $\mu_r$ ,  $\tau$  at this point correspond to lower  $V$  and higher  $S$ , thus giving  $\Pi_1$  a lower value in 1000  $\mu_r$ .

In order to calibrate the general scaling relationship between  $\Pi_1$  and  $\Pi_3$  (equation (3.12)) the data points for all viscosities and scales in this work are combined with  $\Pi_1$  and  $\Pi_3$  calculated from some typical literature data, namely, the data from Das and Mirzaei (2012). All of these data points are grouped together in Figure 3.13(B). The best fitted curve through these points provides a scaling relationship as shown in equation (3.13):

$$\frac{\tau\sqrt{g}}{K^{1/4}P^d} = 9e - 14 \left[ \frac{VK^{-3/2} \rho_r \mu_r}{\phi\lambda S} \right]^{1.31} \quad (3.13)$$

Equation (3.13) shows a power law correlation among different system variables, e.g., dimensionless  $\tau$ , dimensionless domain volume (scale) and the viscosity ratio for the system considered. It is appreciable that a scaling relationship such as the one shown in equation (3.13) may be derived using different forms (i.e., both power and non-power law behaviour). However, observations on the data presented in Figure 3.13 suggest the existence of an exponent and proportionality constant between the two dimensionless groups ( $\Pi_1, \Pi_3$ ) in consistent with what one would expect in a power law function. Power law functions are well understood as they occur in most studies in some form and they are useful to interpret data easily, e.g., these functions can be plotted as straight lines using logarithmic scales. Keeping these points in mind, a power-law function was used to determine the scaling relationship for the non-dimensional form of dynamic coefficient (equations (3.12) and (3.13))

To demonstrate the validity and applicability of the scaling relationship (equation (3.13)), a set of independent data from Bottero (2009) were tested. Figure 3.13(C) shows a plot of the dimensionless groups ( $\Pi_1$  and  $\Pi_3$ ) calculated from the data of Bottero (2009). As evident in Figure 3.13(C) these data are reasonably well predicted by the scaling relationship for the same parameters used by Bottero (2009). In Figure 3.13 (C), only one significant outlier could be found in comparison of the  $\Pi_1$ - $\Pi_3$  curve from Bottero (2009) and the predicted  $\Pi_1$ - $\Pi_3$  relationship using equation (3.13).

An attempt was also made to predict the  $\tau$ -S relationship for the experimental data of Bottero (2009) using equation (3.13). The comparison of the original (Bottero, 2009) and predicted  $\tau$ -S relationships are shown in Figure 3.13(D) which shows a similar trend in the data. Again, only one significant outlier occurs at the saturation value of 0.8. These results seem to show that a scaling relationship such as the one in equation (3.13) has useful general application in the prediction of dynamic capillary pressure effect in terms of the dynamic coefficient.

This chapter has demonstrated that the dynamic coefficient depends on a number of parameters (e.g., domain size, viscosity ratio). The work further shows that by constructing non-dimensional groups of quantities expressing a relationship among these different variables (i.e.,  $\Pi_1$  and  $\Pi_3$ ), it is possible to summarise experimental results and determine their functional relationship. This approach has an advantage that it is possible to find out how many dimensionless groups are required to replace the variables that affect the dynamic coefficient. The empirical data obtained in this work along with the scaling relationship involving the two dimensionless groups suggest that it is possible to determine how significant the dynamic capillary pressure effect is in a particular situation in terms of the dynamic coefficient.

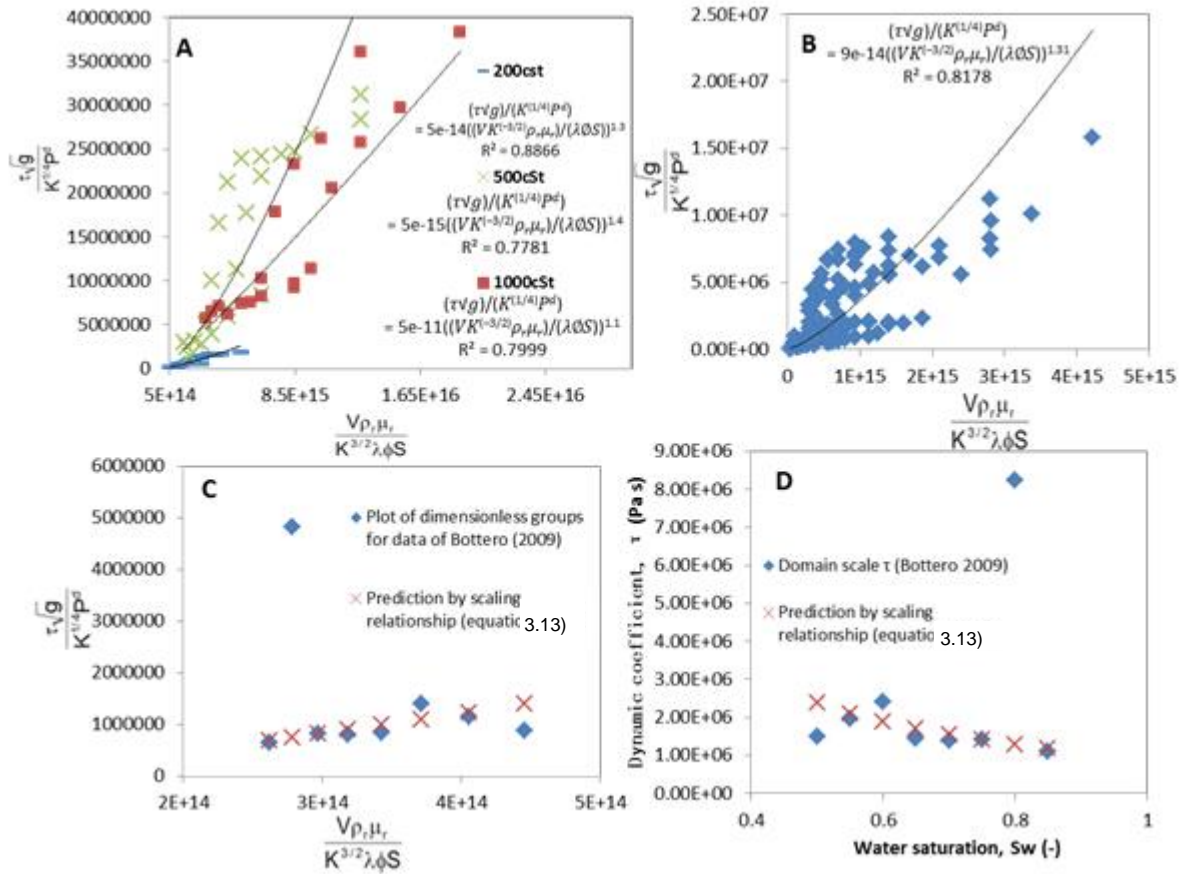


Figure 3.13: Derivation and validation of a scaling relationship obtained from dimensional analysis (A) relationship between the dimensionless groups for 200, 500 and 1000 viscosity ratio (B) calibration of the scaling relationship using data in this work for all viscosity ratios and additional literature data reported by Das and Mirzaei (2012) (C) comparison of the relationship between the dimensionless groups for the parameters used by Bottero (2009) and predictions by equation (3.13) for the same parameters (D) comparison of  $\tau$ -S data from Bottero (2009) and predictions by equation (3.13) for the same parameters.

### 3.4 Summary

In this work, the effects of fluid viscosity ratio and scale of observation on the magnitude of dynamic capillary pressure (indicated by dynamic coefficients) have been elucidated. Two types of scale dependencies of the  $\tau$ -S relationships were analysed in this work, which relate to (i) the scale dependencies between small and larger domain and, (ii) the scale dependencies between the local measurement point and domain scale. It is confirmed that  $\tau$  increases with the scale of observation and the viscosity ratio of the fluid-fluid system. It was also found that its value is inversely affected by  $\partial S/\partial t$ , which is connected to the degree of resistance to the fluid motion, namely, viscosity. In almost all cases,  $\tau$  is found to decrease monotonically with increase in S although there are some instances where the  $\tau$ -S relationship is non-monotonic.

An order increase in magnitude of  $\tau$  was observed as the domain scale changes from the 4cm scale to a region of low saturation in the 8cm domain scale. A similar order of increase with higher magnitude was recorded in the 12cm domain scale. The results showed that the relationship between  $\tau$  and domain scale depends further on viscosity ratio. Also, difference in pressure gradients in different domain sizes acts to reduce the desaturation rate, which in effect causes a rise in the magnitude of  $\tau$ .

In addition, the fluid viscosity ratio together with the experimental scale results in an order increase in the value of  $\tau$  as the scale increases from the smaller to larger domain for the same viscosity. While a higher order increase is found with increase in viscosity ratio from 200 to 500, the change in  $\tau$  while  $\mu_r$  changes from 500 to 1000 is found to be of the same order. It can be reasonably inferred that the scale dependency of the dynamic coefficient is mainly because of the rate of change of saturation, whose magnitude decreases with the increase in depth of the domain from the injection point. This can also be said of  $\tau$  dependency on viscosity ratios of the two-phase fluids. As the viscosity ratio increases, the desaturation rate reduces and hence  $\tau$  increases.

The dimensionless correlations developed for the system showed the applicability of the power law for the system and can be found useful in the first hand estimation of dynamic coefficients for the system of interest provided the system parameters are available. In short, the magnitude of  $\tau$  is similarly affected by the coupled effects of viscosity and domain scales and  $\tau$  may not become arbitrarily large as the averaging length increases.

## CHAPTER FOUR

# SCALE DEPENDENCY OF DYNAMIC RELATIVE PERMEABILITY CURVES IN RELATION WITH FLUID VISCOSITY AND DYNAMIC CAPILLARY PRESSURE EFFECT\*

### Overview

Capillary pressure-saturation-relative permeability relationships ( $P_c$ - $S_w$ - $K_r$ ) are functions of importance in modeling and simulations of two-phase flow in porous media. These relationships are found to be affected by porous medium and fluid properties but the manner in which they are affected is a topic of intense discussion. For example, the reported trend in fluid viscosity and boundary conditions effects have been found to be contrary to each other in different studies. In this work, the dependency of dynamic  $K_r$ - $S_w$  relationships (averaged data) on domain scale was determined in addition to investigating the effect of fluid viscosity and boundary pressure using silicone oil (i.e. 200 and 1000 cSt) and water as the respective non-wetting and wetting fluids with a view to eliminating some of the uncertainties reported in the literature. Water relative permeability,  $K_{rw}$ , was found to increase with increasing wetting phase saturation but decreases with the increase in viscosity ratio. On the other hand, the oil relative permeability,  $K_{rnw}$ , was found to increase with the increasing non-wetting phase saturation in addition to the increase in viscosity ratio. Also, it was found that with the increasing boundary pressure  $K_{rw}$  decreases while  $K_{rnw}$  increases. The influence of scale on relative permeability was slightly indicated in the non-wetting phase with  $K_{rnw}$  decreasing as domain size increases. Effect of measurement location on dynamic relative permeability was explored which are rarely found in the literature. Comparison was also made between  $K_r$ - $S_w$  relationship obtained under static and dynamic condition. Finally, mobility ratio ( $m$ ) and dynamic coefficient ( $\tau$ ) were plotted as a function of water saturation ( $S_w$ ), which showed that  $m$  decreases as  $\tau$  increases at a given saturation, or vice versa.

### 4.1 Introduction

The characteristics of two-phase flow in porous media in terms of capillary pressure-saturation-relative permeability relationships ( $P^c$ - $S$ - $K_r$ ) have been extensively investigated under the influence of porous media, fluid properties and flow conditions. Such studies are conducted in the context of a number of engineering problems, e.g., contaminants remediation, oil recovery, etc. Relative permeability-saturation ( $K_r$ - $S$ ) and capillary pressure-saturation ( $P^c$ - $S$ ) relationships are used to describe the complex interplay of capillary,

---

\* Goel, G., Abidoeye, L.K., Das, D.B., and Chahar, B.R. Scale dependency of dynamic relative permeability curves in relation with fluid viscosity and dynamic capillary pressure effect. Environmental Fluid Mechanics (submitted).

gravitational and viscous forces which affect the two-phase flow in porous media (Miller et al. 1998; Manthey, 2006). But, the non-uniqueness in these relationships is well acknowledged. For example, for the  $P^c$ -S relationships and their saturation-rate dependency, reported factors such as fluid properties like viscosity and density ratios (Gielen et al. 2005; Das et al. 2007; Goel and O'Carroll, 2011; Joekar-Niasar and Hassanizadeh, 2011; Hou et al. 2014), domain scale (Dahle et al. 2005; Camps-Roach et al. 2010; Bottero et al. 2011a; Das and Mirzaei, 2012; Mirzaei and Das, 2013), media permeability (Das et al. 2004; Camps-Roach et al. 2010; Tian et al. 2012; Hanspal et al. 2013), micro-heterogeneities (Das et al. 2006; Manthey, 2006; Mirzaei and Das, 2013), among others. Hou et al. (2012) explored the influence of measurement sensor's response on the magnitude of the dynamic capillary effects at scale of representative elementary volume and argue that the effect may be due to the experimental measurement artefacts. However, their acknowledgement of the impact of the micro-heterogeneities on the dynamic capillary effect, at larger scales, is in agreement with the earlier submission of Das et al. (2006) and Mirzaei and Das (2007).

This saturation-rate dependency of the system properties observed during non-steady state two-phase flow is referred to as the dynamic capillary pressure effect (Hassanizadeh et al. 2002) and a large body of literature involving experimental, modelling and theoretical studies has emerged concerning these phenomenon (Topp et al. 1967; Smiles et al. 1971; Stauffer, 1978; Kalaydjian, 1992; Wildenschild et al. 2001; Hassanizadeh et al. 2002; O'Carroll et al. 2005a; O'Carroll et al. 2005b; Oung et al. 2005; Camps-Roach et al. 2010; Sakaki et al. 2010; Goel and O'Carroll, 2011; Das and Mirzaei, 2012; Diamantopoulos and Durner, 2012; Hou et al. 2012; Hou et al. 2014; Zhang et al. 2014). Studies by Stauffer (1978), Kalaydjian (1992), Hassanizadeh and Gary (1993) suggest that an extension of the  $P^c$ -S function should include a saturation rate dependent term. This modification is already expressed in equation (3.2).

Determining the  $P^c$ -S and  $K_r$ -S relationships experimentally for both the quasi-static and dynamic conditions in the laboratory is time consuming and researchers often resort to indirect estimation of the  $K_r$ -S relationship using  $P^c$ -S curve with the aid of the relative permeability models like Burdine (1953) and Mualem (1976). These are most frequently used to simulate two-phase flow though there exist other categories of  $K_r$ -S constitutive models, e.g., empirical and analogy based models (Gerhard and Kueper 2003). By estimating the  $K_r$ -S relationships from experimental  $P^c$ -S curves, the transfer of above-mentioned inherent non-uniqueness in the  $P^c$ -S relationships becomes inevitable. Corroborating this assertion, Gao, et al. (2013) observed that dynamic effects on relative permeability become more important as the pore size increases. Thus, investigating the relationships of the  $K_r$ -S curve with some

of the above-mentioned factors including the dynamic capillary pressure effect is an effort in the right direction.

Even though some of the factors above were reported to have influences on the  $K_r$ - $S$  relationships, the consistencies of the trend cannot be affirmed. For example, the effects of viscosity on  $K_r$ - $S$  relationships have been controversial in the literature (Leverett, 1939; Odeh, 1959; Downie and Crane, 1961; Amaefule and Handy, 1982; Demond and Roberts, 1987; Avraam and Payatakes, 1995; Wang et al. 2006; Yiotis et al. 2007; Nejad et al. 2011; Ahmadiouydarab et al. 2012; Dou and Zhou, 2013). Few experimental studies (Amaefule and Handy, 1982; Nejad et al. 2011) show that relative permeability decreases with increasing viscosity ratio,  $\mu^n/\mu^w$ , where  $\mu^n$  and  $\mu^w$  are the viscosities of the non-wetting and wetting phases, respectively. Another experimental study (Avraam and Payatakes, 1995) shows that both oil (non-wetting) and water (wetting) relative permeability increase with increasing viscosity ratio. On the other hand, numerical and modelling studies (Ehrlich, 1993; Yiotis et al. 2007; Ahmadiouydarab et al. 2012; Dou and Zhou, 2013) demonstrate that water relative permeability decreases while oil relative permeability increases with increasing viscosity ratio. These are obvious inconsistencies, which need further investigations.

Also, the porous medium property effects on the relative permeability had been shown to be significant. Das et al. (2004; 2006) investigated the effects of grain size, amount and distribution of micro-heterogeneities on the  $K_r$ - $S$  relationship and found that water relative permeability was higher in coarse grain sand, while oil relative permeability was higher in fine grain sand. The effects of gravity were neglected in earlier work (Das et al. 2004) but these were included in the latter work (Das et al. 2006). Das et al. (2006) further showed that larger intensity of heterogeneity led to higher irreducible water saturation in addition to having a significant effect on the  $K_r$ - $S$  relationship. Petersen et al. (2011) mentioned the significance of pore geometry and flow behaviour on the  $K_r$ - $S$  relationship. Recently, Dou and Zhou (2013) reported that in the case of large capillary number, presence of heterogeneity would result in a decrease of oil relative permeability while it would be opposite in case of homogeneous media.

As discussed earlier, many recent studies have considered non-uniqueness of  $P^c$ - $S$  curves in terms of dynamic effects in capillary pressure. For example, the experimental results by Goel and O'Carroll (2011) and Das and Mirzaei (2013) on dynamic capillary pressure effect, namely the dynamic coefficient-saturation ( $\tau$ - $S$ ) relationships, provide some highlights on these factors as shown in Figure 4.1. Both of the studies were conducted for primary drainage (PD) under quasi-static and dynamic conditions, i.e., in the cases when  $\partial S/\partial t$

values are near and far from zero, respectively. Goel and O'Carroll (2011) used F70 silica sand as the porous media having a mean permeability of  $1.42 \times 10^{-11} \text{ m}^2$ . Water and silicone oil with two differing viscosities (i.e. 0.65 and 5 cSt) were used as the respective wetting and non-wetting fluids. Pressures of both phases and water saturation were measured using tensiometers and EC-5 probes at three levels inside the domain. Das and Mirzaei (2013) used two different sands with mean permeabilities of  $8.7 \times 10^{-10} \text{ m}^2$  and  $3.1 \times 10^{-10} \text{ m}^2$  along with water and silicone oil of viscosity 200 cSt which is higher than that used by Goel and O'Carroll (2011) used. The results obtained in the two studies are different owing to not only porous medium properties (e.g., permeability, particle size) and fluid properties but also the domain size. While the domain in one study (Goel and O'Carroll, 2011) comprised of a cylindrical column 20 cm long and 10 cm inner diameter, in the other study (Das and Mirzaei, 2013) the domain was a cylindrical column 12 cm long and 10.2 cm inner diameter. Therefore, it can be understood that domain size is an important factor influencing dynamic effects in capillary pressure. It also implies that these factors must have profound impact on the dynamic  $K_r$ -S relationship.

It is indeed a matter of great interest how the dynamic  $K_r$ -S relationship will be affected by porous medium properties, fluid viscosity and domain size. This is because different pressure gradients and saturation distributions are created in the domain as the viscosity of the fluids, porous medium permeability and domain size change which also affect the dynamic coefficient. Joekar-Niasar and Hassanizadeh (2011) explained that  $\tau$  (see, equation (3.2)) depends on both the viscosity ratio as well as an effective viscosity which rely on the fluid viscosities of the wetting and non-wetting phases. The authors argue that if the viscosity ratio is less than one under drainage the invading front can become unstable. Such instability of fluid/fluid interfaces leading to the formation of fingers have also been observed by a number of other authors (e.g., van Duijn and Floris, 1992; DiCarlo, 2004). The appearances and disappearances of instabilities and overshoots during two-phase flow in porous media are shown theoretically by means of travelling wave analysis by van Duijn et al. (2013). Fingering is also discussed in detail by Rohde and Kissling (2010), Kissling et al. (2012) and DiCarlo (2013). As the dynamic saturation front in a porous domain could vary within the domain and  $K_r$  relationships are primarily point relationships, it becomes important to know the location dependent  $K_r$ -S relationship. When the  $K_r$  data are averaged over a domain, the average  $K_r$  data are likely to be different from the location dependent  $K_r$  data because the  $K_r$ -S relationships are non-linear relationships. However, the significance of this difference is not very well understood for dynamic two-phase flow conditions. Finally, there is little known about the relationship between the dynamic relative permeability and dynamic capillary pressure effect.

Indeed the scale dependency and methods for upscaling of  $P^c$ -S,  $K_r$ -S and  $\tau$ -S relationships have been the subjects of intense study in the literature (Barker and Thibeau, 1997; Renard and De Marsily, 1997; Gasda and Celia, 2005; Manthey et al. 2005; Camps-Roach et al. 2010; Nick and Matthäi, 2011; Yang et al. 2013; Sharifi and Kelkar, 2013). Barker and Thibeau (1997) and Renard and De Marsily (1997) suggested that the constitutive relationship should be used at the same scale as that of a predictive model but the practicality would only be attained with upscaling. In this regard, Gasda and Celia (2005) proposed correction for the coarse grid simulation so that it could match better with the fine grid simulations. Just like the  $P^c$ -S relationships, Sharifi and Kelkar (2013) showed that upscaled relative permeability was time dependent and large scale constitutive relationships were mainly controlled by permeability variation of the porous media (Yang et al. 2013).

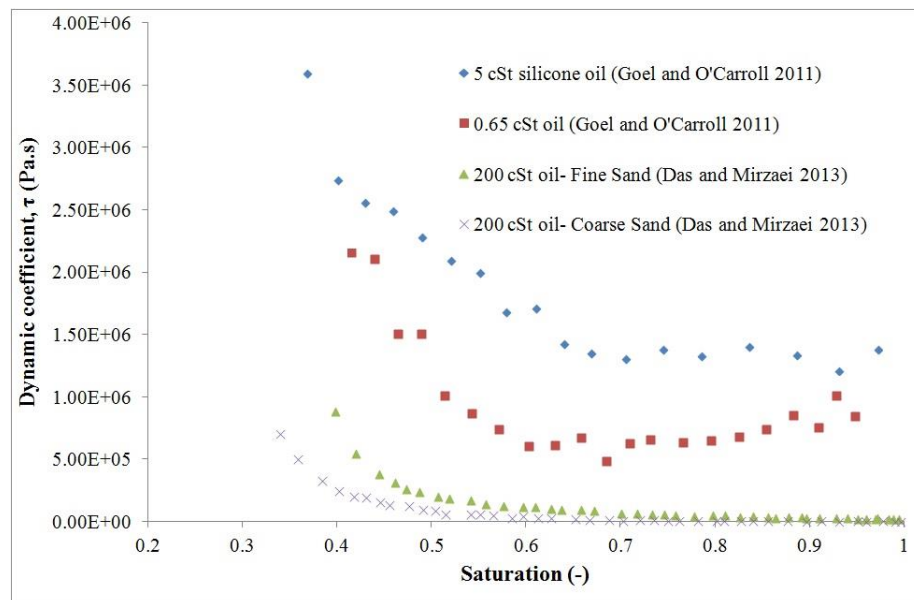


Figure 4.1: Comparison of dynamic coefficient - water saturation curves for water and silicone oil with three differing silicone viscosities (0.65, 5 and 200 cSt respectively). Data for silicone oil with 0.65 and 5 cSt are taken from Goel and O'Carroll (2011) and the remaining data for 200 cSt are from Das and Mirzaei (2013). Goel and O'Carroll (2011) used sand having a mean permeability of  $1.42 \times 10^{-11} \text{ m}^2$ . Das and Mirzaei (2013) used two different sands with mean permeabilities of  $8.7 \times 10^{-10} \text{ m}^2$  (coarse sand) and  $3.1 \times 10^{-10} \text{ m}^2$  (fine sand).

The above discussions present the factors that affect the properties of the two-phase system. It was further explained the inconsistencies in reports regarding the trends of the effects of these factors on  $K_r$ -S relationships. However, one is confronted with the obvious challenge of identifying the true situation of these relationships with regards to the scale of the domain. In particular, it is believed that there is little discussion on the scale dependency of the dynamic relative permeability-saturation ( $K_r$ -S) curves in relation to  $\tau$ -S relationships in the open literature. In this work, it is intended to elucidate the effects of scale and fluid properties on  $K_r$ -S relationships in order to ascertain the trend that exists between them. The high values of

viscosity ratios (200 and 1000) in this work are intended to eliminate further ambiguity in this relationship. Furthermore, to avoid the influence of intra-domain averaging technique as employed in most of the literature reports, Separate and different domain sizes (8 and 12cm high cylindrical cells) were used as experimental domains. Effects of measurement locations within the domain in relation to the domain boundary on the results are also determined.

## 4.2 Materials and methods

### 4.2.1 Porous medium, domain size and fluid properties

In this work,  $K_r$ - $S$  relationships for different viscosity ratios and domain scales of two-phase flow in porous media were determined from the  $P^c$ - $S$  experiments, described in subsection 3.2. For the purpose of this work, 8 and 12cm high porous domain sizes were considered. Henceforth, the former shall be referred to as 8cm domain and the latter as 12cm domain. Details are shown in the experimental set up diagram in Figure 3.1. Also, only two viscosity ratios were considered, namely, 200 and 1000. Since the aim of this work is to investigate the dynamic  $K_r$ - $S$  relationship,  $P^c$ - $S$  results from two dynamic conditions of the experiments, described in subsection 3.3, were used in the relative permeability model, i.e.,  $P^c$ - $S$  results at the dynamic boundary conditions of 10 and 20 kPa.

### 4.2.2 Methods of averaging and parameters calculation

To upscale the local values of measured quantities to the domain level, an appropriate averaging technique is needed. This applies to the local pressures of both phases in order to determine capillary pressure for the entire domain at specific wetting phase saturation. The mathematical technique for the averaging of  $P^c$  is expressed in equation (3.4).

A central difference method was applied to determine the desaturation rate ( $\partial S/\partial t$ ) in the two-phase system. This was performed using the mathematical relation in equation (3.5).

### 4.2.3 Relative permeability calculation

This work estimates the  $K_r$ - $S$  relationship for entire saturation range as follows. The  $P^c$ - $S$  model given by van Genuchten (1980) combined with the Mualem (1976) model yields the following relative permeability function:

$$K_{rw} = S^{eff} \left[ 1 - \left( 1 - S^{eff} \left( \frac{1}{m} \right) \right)^m \right]^2 \quad (4.1)$$

$$K_{r_{mw}} = (1 - S^{\text{eff}})^{\frac{1}{2}} \left( 1 - S^{\text{eff} \left( \frac{1}{m} \right)} \right)^{2m} \quad (4.2)$$

where,  $K_{rw}$  and  $K_{r_{mw}}$  (-) are the relative permeability of wetting (water) and non-wetting phase (silicone oil), respectively.  $m$  (-) is a parameter which is related to van Genuchten pore size distribution coefficient ( $n$ ), and  $S^{\text{eff}}$  (-) is the effective water saturation given by  $S^{\text{eff}} = (S - S_{rw}) / (1 - S_{rw})$ , wherein  $S_{rw}$  (-) is residual water saturation, and  $S$  (-) is water saturation. For the purpose of this work, effective saturation was calculated from the experimentally measured saturation values. Then  $n$  and  $m$  were determined using the fitted van Genuchten (1980) model. Using these values of effective saturation,  $n$  and  $m$ , values of  $K_{rw}$  and  $K_{r_{mw}}$  were determined. It is appreciate that van Genuchten-Mualem equations are derived under specific assumptions (van Genuchten, 1980; Mualem, 1976). These assumptions were accepted and defined that they can be applied to the system under consideration in this work.

#### 4.2.4 Dynamic coefficient ( $\tau$ ) calculation

This work is primarily concerned with elucidating the trends in dynamic  $K_r$ - $S$ . However, interrelationship of  $K_r$ - $S$  with  $\tau$  is expatiated in the discussion of results. Details of the  $\tau$  calculation can be found in the subsection 3.2.4.

### 4.3 Results and discussions

This work is focussed on finding the influence of different factors, which affect the  $K_r$ - $S$  relationship under dynamic conditions. The work presented here is focussed on especially the effect of fluid viscosity and scale dependency for the two-phase flow involving silicone oil and water for homogeneous porous domain.

#### 4.3.1 $P^c$ - $S$ and $\partial S / \partial t$ - $S$ relationships for different domain scales

To understand the behaviour of the system, the behaviour of the  $P^c$ - $S$  curves and desaturation rate ( $\partial S / \partial t$ ) under dynamic conditions at 10kPa boundary pressure is shown with 200 cSt silicone oil as the non-wetting phase (Figure 4.2). It will be recalled that the 12cm-high cell has three measurement points labelled as top, middle and bottom where all points are equally spaced around the domain geometry. Similarly, the 8cm-high cell has two measurement points labelled as top and bottom (see, explanation at subsection 3.2).

Figure 4.2 shows that the  $P^c$ -S curves are fairly similar at different depths of the domains except at the top of the domain of the 12cm high cell where the  $P^c$ -S profiles which is higher than at the other lower positions of the domain. Noticeable from Figure 4.2 is that the final measured saturations obtained at different measurement points differ. Combinations of factors might be responsible for this. It could be attributed to the effect of pressure gradient across the height of the domain. As the distance from the injection point increases, influence of pressure drop increases. This seems to manifest in the decrease in  $\partial S/\partial t$  values (absolute value) with increasing distance from the injection point (i.e. the lower the measurement point, the lower the  $\partial S/\partial t$ ). This also leads to the  $P^c$ -S relationships terminating at different saturation points at different depths of each domain. While the  $P^c$ -S curves at the top of each domain attain lower final measured saturation, the profile at further depths away from the injection points terminate at higher final measured saturation values. This behaviour is shown in Figures 4.2 (A) and (B) for the 12 and 8cm high cells, respectively. The impact of pressure gradient becomes more conspicuous in  $\partial S/\partial t$  at different depths of each domain as shown in Figures 4.2(C) and (D) for the 12 and 8cm high cells, respectively. Wide gap exists between the  $\partial S/\partial t$ -S profile at the top of the domain compare to the other lower measurement points. In the 12cm high cell, this trend continues at lower measurement points with  $\partial S/\partial t$  - S curve remaining higher at the middle measurement positions than at the bottom position.

Also, the high viscosity of the silicone oil used in the work may be a contributing factor. However, the gap between the  $\partial S/\partial t$  - S profiles at lower measurement positions (middle and bottom) is much lower compared to the gap existing between the  $\partial S/\partial t$ -S profiles at the top of the domain and the middle measurement position. Bottero *et al.* (2011b) earlier showed that the difference in  $P^c$ -S profiles at different averaging windows remains quite small while the difference in  $\partial S/\partial t$ -S profiles at the different averaging windows appear considerable. This had been seen as the major contribution to the magnitude of the upscaled dynamic coefficient ( $\tau$ ). Hence,  $\tau$  increases as the size of domain scale or averaging window increases (Dahle *et al.* 2005; Bottero *et al.* 2011b).

Similar behaviour was encountered in the  $P^c$ -S and  $\partial S/\partial t$ -S profiles for the two-phase system with 1000cSt silicone oil as the non-wetting phase. However, the aim of this work is to show the effects of fluid properties, domain scale and the dynamic flow conditions on the relative permeability.

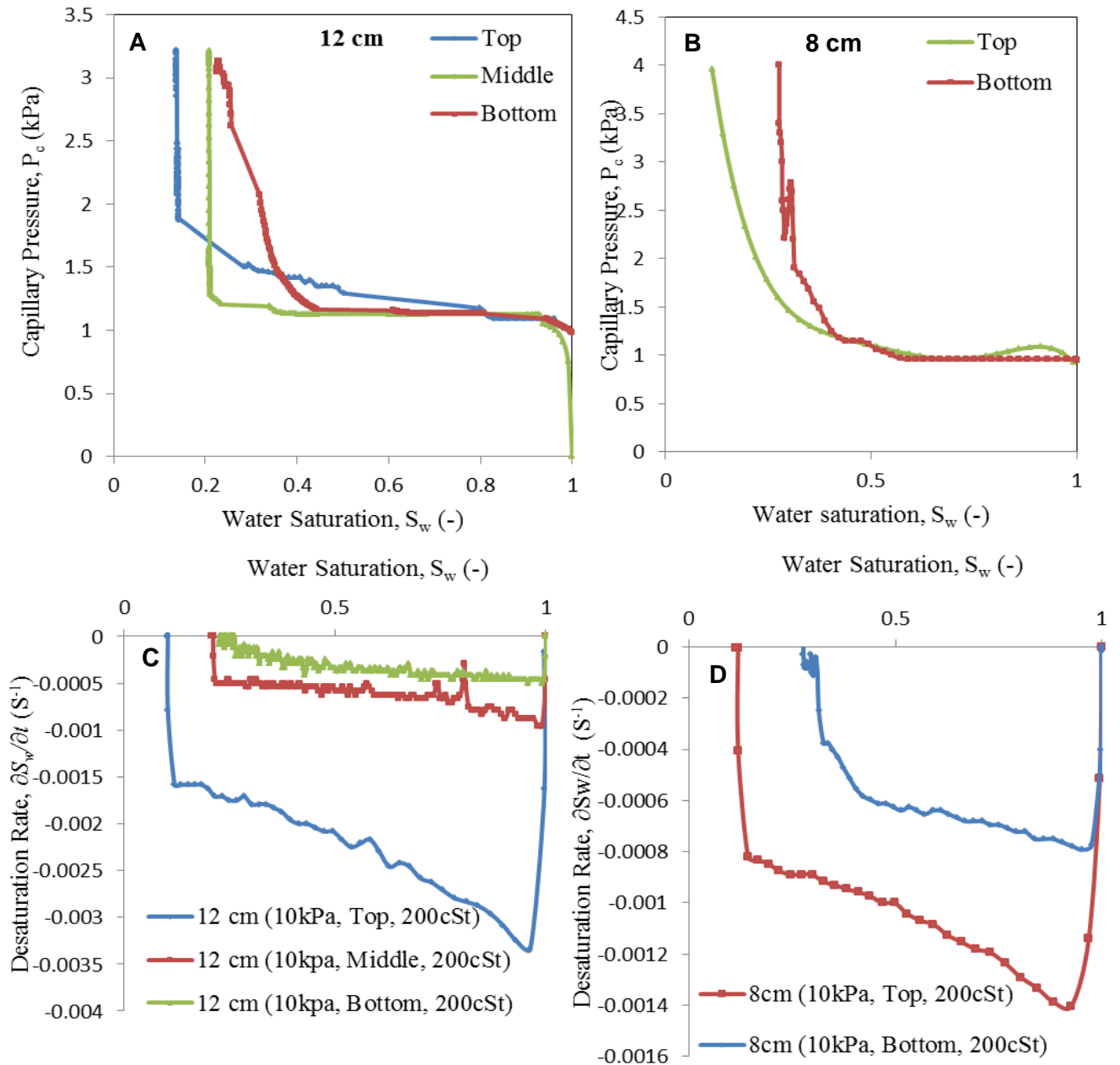


Figure 4.2:  $P^c$ - $S$  and  $\partial S/\partial t$ - $S$  patterns in the 8 and 12 cm high domains with 200 cSt silicone oil at 10 kPa boundary pressure.

### 4.3.2 Effects of viscosity ratio on relative permeability–saturation relationship

To determine the effects of viscosity ratio, experiments were performed using water and silicone oil with two differing viscosities (200 and 1000 cSt respectively). It corresponds to viscosity ratio of 200 and 1000 respectively if viscosity of water is taken as 1 cSt. The results are shown in Figure 4.3. It can be easily noticed that irrespective of the fluid pair, relative permeability of the fluid increases with the increasing saturation of the respective fluid. This

trend conforms to the previous literature studies. Further, it can be observed that water relative permeability decreases with increasing viscosity ratio while oil relative permeability increases with increasing viscosity ratio, which is in line with experimental, numerical and modelling studies (Ehrlich, 1993; Mohanty, 2002; Yiotis et al. 2007; Ahmadlouydarab et al. 2012). This behaviour can be explained using the lubrication effect (Odeh, 1959; Amaefule and Handy, 1982; Dou and Zhou, 2013). As the oil displaces water (drainage), a layer of water is trapped between oil and walls of the capillary. This layer of water acts as lubricant to the movement of oil. The oil moves through the larger capillaries and the smaller capillaries filled with water are bypassed.

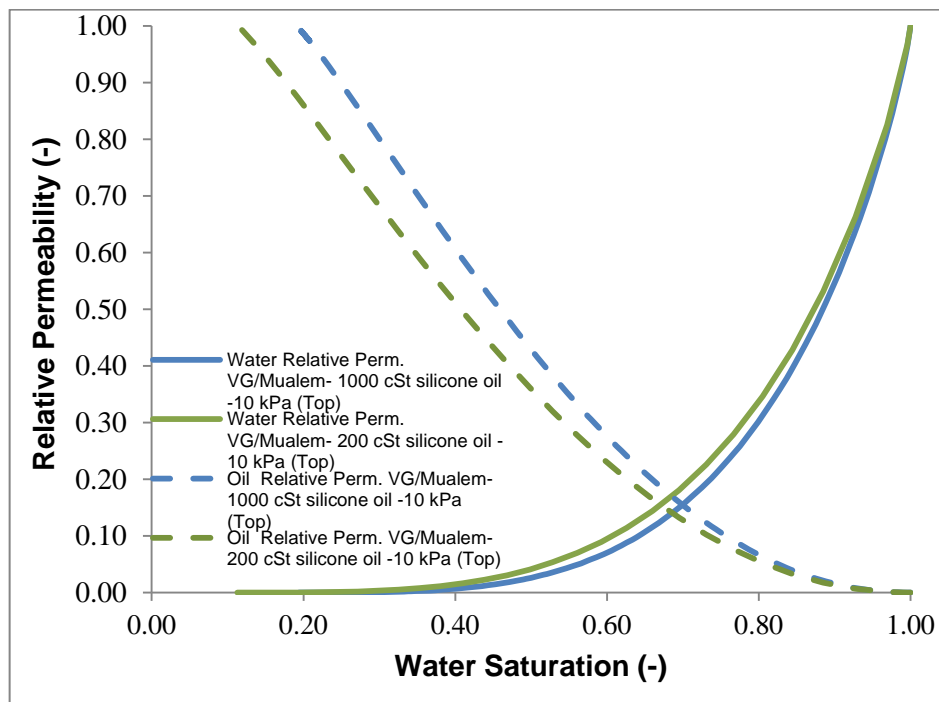


Figure 4.3: Relative permeability-water saturation curves for water and silicone oil with two different viscosities (200 and 1000 cSt respectively) for 8 cm high domain and boundary pressure of 10 kPa.

At higher viscosity ratio water flows in the form of bubbles which results in lower relative permeability for water. The minimum residual water contents for the 200 and 1000 cSt silicone oil-water were 11% and 19%, respectively. Therefore, more water remains as residual for higher viscosity ratios. This was also observed by others (Abrams, 1975; Nejad et al. 2011).

The maximum capillary numbers for 200 cSt and 1000 cSt oil (for the 10 kPa boundary pressure and 8 cm domain) were  $6.57 \times 10^{-5}$  and  $1.56 \times 10^{-5}$ , respectively. It can be understood that water relative permeability increases whereas oil relative permeability decreases with increasing capillary number. This trend was confirmed by another research (Mohanty, 2002).

### 4.3.3 Effects of boundary pressure on dynamic relative permeability–saturation relationship

Some of the typical results are plotted in Figure 4.4 for water and silicone oil (200 cSt) in the 12 cm domain. It can be observed that with increasing boundary pressure water relative permeability decreases while oil relative permeability increases. This can be explained by the relative speed of flow under the different injection pressures. At the 10 kPa injection pressure, the invading oil penetrates more slowly and the water phase that wets the sand surface gets gently displaced. As the injection pressure increases to 20 kPa, the oil invades at faster speed while the response of the wetting phase may be described as sluggish owing its wettability characteristics. Also, at 10 kPa, the pressure in the water decreases and reaches static state gradually while that of the oil increases gradually. As the injection pressure increases (20 kPa) the oil pressure rises fast while the water pressure decreases faster than before. This manifests in the  $K_{rw}$  becoming higher with pressure and  $K_{rw}$  becoming lesser with pressure.

Earlier research by Ataie-Ashtiani et al. (2002) showed that pressure gradient could significantly influence  $K_r$ - $S$  relationship. In comparisons, Gao et al. (2013) showed that the relative permeability increased with increasing injection for both wetting and non-wetting phases and observed inconsistencies in this trend. However, both of these (Ataie-Ashtiani et al. 2002; Gao et al. 2013) were modelling studies on heterogeneous systems. Gawish and Al-Homadh (2008) earlier found that the oil relative permeability decreased with increasing boundary pressure. Their investigations were conducted under steady state unlike the dynamic condition in the present study. So, it can be inferred that the relative permeability of the non-wetting phase generally increases with boundary pressure, while the trend in the wetting phase cannot be conclusively inferred.

The maximum capillary number for 10 kPa and 20 kPa boundary pressure (for 200 cSt oil and 12 cm domain) were found to be  $5.68 \times 10^{-5}$  and  $1.79 \times 10^{-4}$  respectively. It suggests that the oil relative permeability increases whereas the water relative permeability decreases with increase in the capillary number.

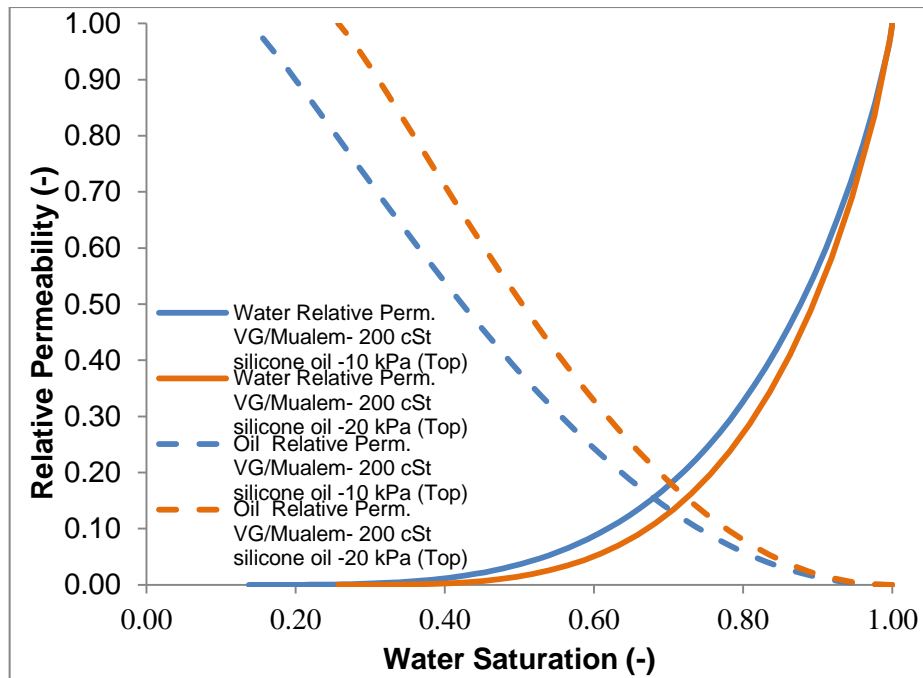


Figure 4.4: Relative permeability-water saturation curves for water and silicone oil (200 cSt) for the 12 cm high domain and boundary pressures of 10 and 20 kPa.

#### 4.3.4 Effects of domain size on dynamic relative permeability–saturation relationship

Investigations of domain size effects on  $K_r$ - $S$  relationship were performed, using the 8 and 12cm-high domain cells. The results are plotted in Figure 4.5 for water and silicone oil (200 cSt) in the 8 and 12 cm domain. Domain scale average values are used for plotting Figure 4.5. Averaging is done as per the standard procedure. The values  $K_{r_{nw}}$  obtained at the scales of 8 cm and 12 cm are almost similar while  $K_{r_{nw}}$  values differ slightly at the low water saturation values. The similarity in these curves was expected as the permeability is the same. The difference in the non-wetting phase relative permeability at low water saturation may be due to the presence of micro scale heterogeneities (Ataie-Ashtiani *et al.* 2002; Das *et al.* 2004; Das and Mirzaei, 2013).

#### 4.3.5 Effects of location on relative permeability–saturation relationship

Depth of the measurement in a porous domain was also shown to affect the  $K_r$ - $S$  curve. The results of the investigations are plotted in Figure 4.6 for water and silicone oil (200 cSt) in the 8 cm domain. It can be observed that at the top of the column, relative permeability of water is higher than that of the bottom if the saturation is uniform throughout the column. This trend is opposite for the oil relative permeability. But, in reality because of the saturation gradients,

water relative permeability is less at the top and more at the bottom. An average of the top and bottom relative permeability is also plotted which lies in between of the top and bottom relative permeability.

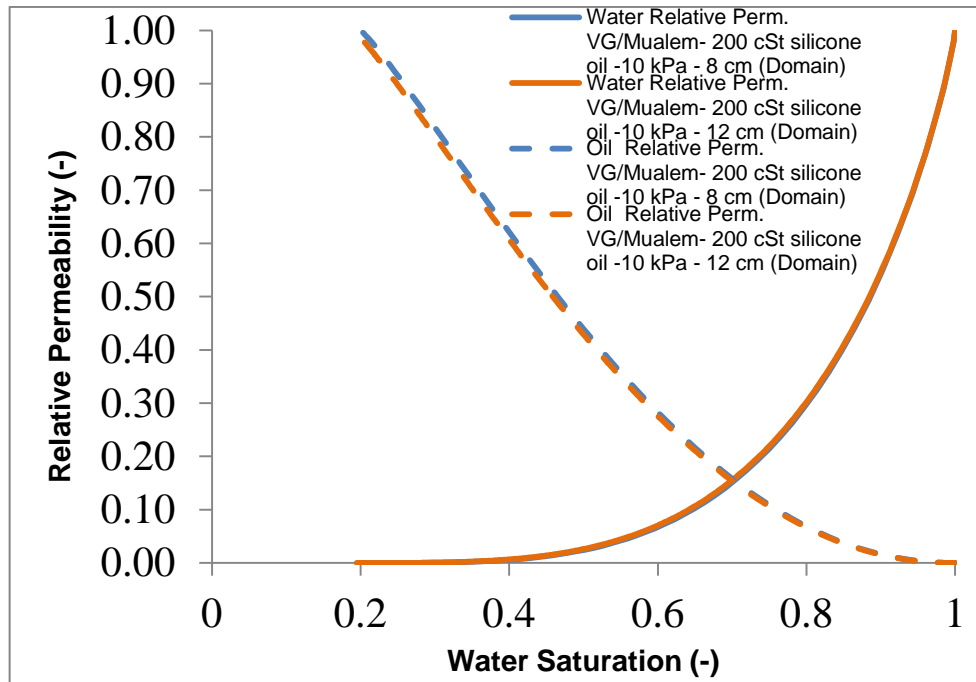


Figure 4.5: Relative permeability-water saturation curves for water and silicone oil (200 cSt) for boundary pressure of 10 kPa in the 8 and 12 cm domains.

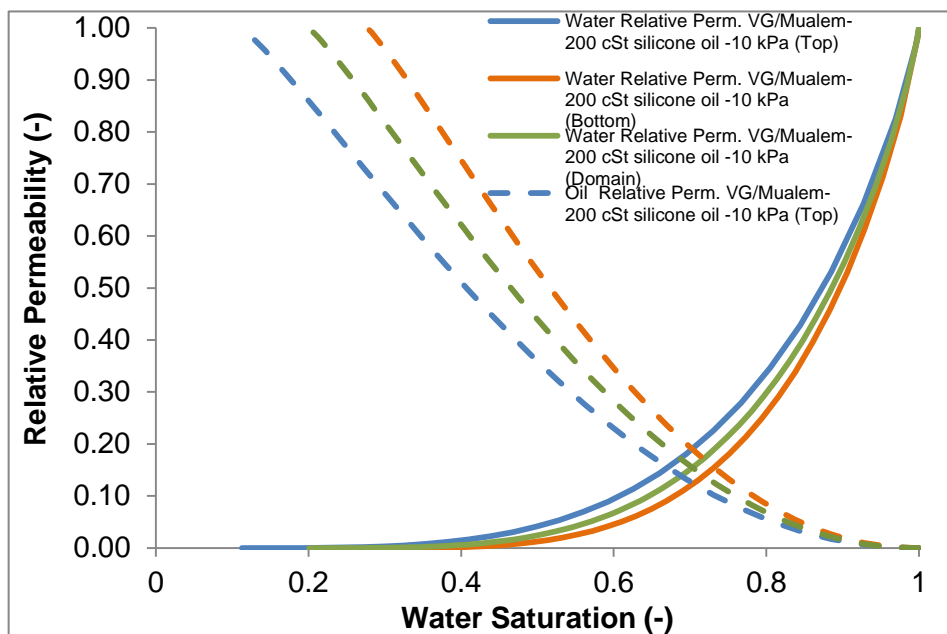


Figure 4.6: Relative permeability-water saturation curves for water and silicone oil (200 cSt) for boundary pressure of 10 kPa in the 8 cm high domain.

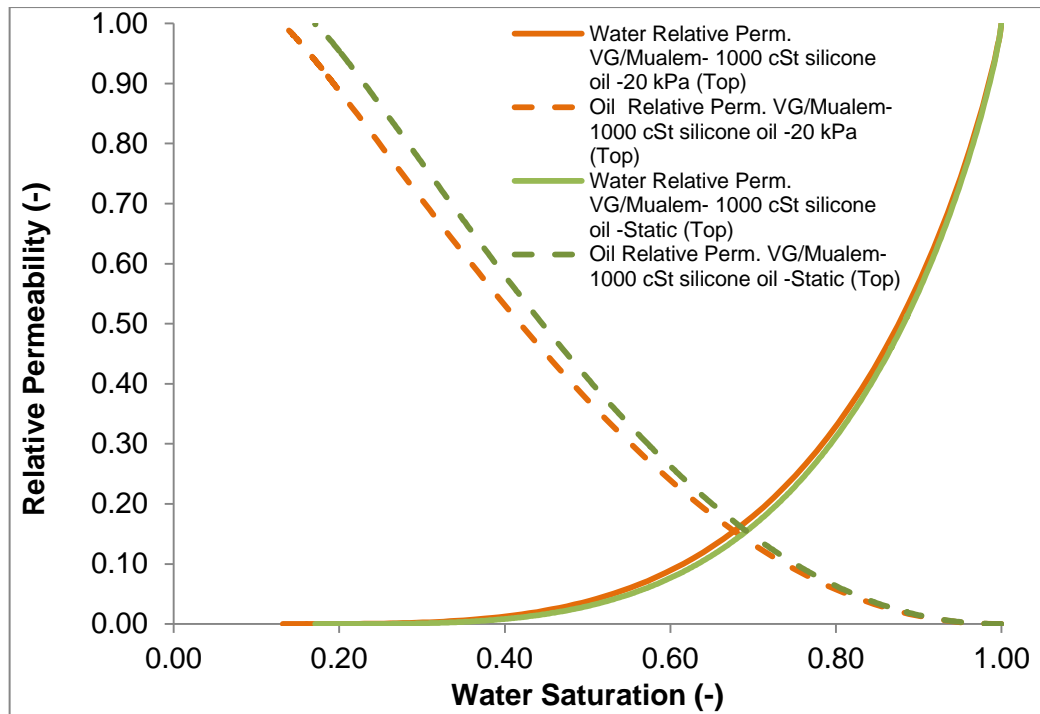


Figure 4.7: Comparison of static and dynamic relative permeability vs. water saturation curves for water and silicone oil (1000 cSt) for the 12 cm high domain.

#### 4.3.6 Comparison of static and dynamic relative permeability–saturation relationships

The dynamic and quasi-static  $K_r$ - $S$  curves were compared in order to understand the effects flow conditions on the  $K_r$ - $S$  relationship. The results are plotted in Figure 4.7 for water and silicone oil (1000cSt) in the 12cm domain. It can be observed that at the top of the column dynamic relative permeability of water is higher than that of the static relative permeability of water. This trend is opposite for the oil relative permeability. Similar results were obtained at other levels and in the other domain size (8cm). These results are qualitatively similar as obtained in previous experimental and modelling studies (Tsakiroglou et al. 2007; Joekar-Niasar and Hassanizadeh, 2011).

#### 4.3.7 Comparison of mobility ratio ( $m$ ) and dynamic coefficient ( $\tau$ )

In order to quantify effects of the stability of fluid fronts, mobility ratio ( $m$ ) (Das et al. 2007) was computed using equation (4.3) and the results are plotted to include comparison with dynamic coefficient. These are shown in Figure 4.8 and Figure 4.9.

$$m = \left( \frac{K_{rw} \mu^n}{K_{rnw} \mu^w} \right) \quad (4.3)$$

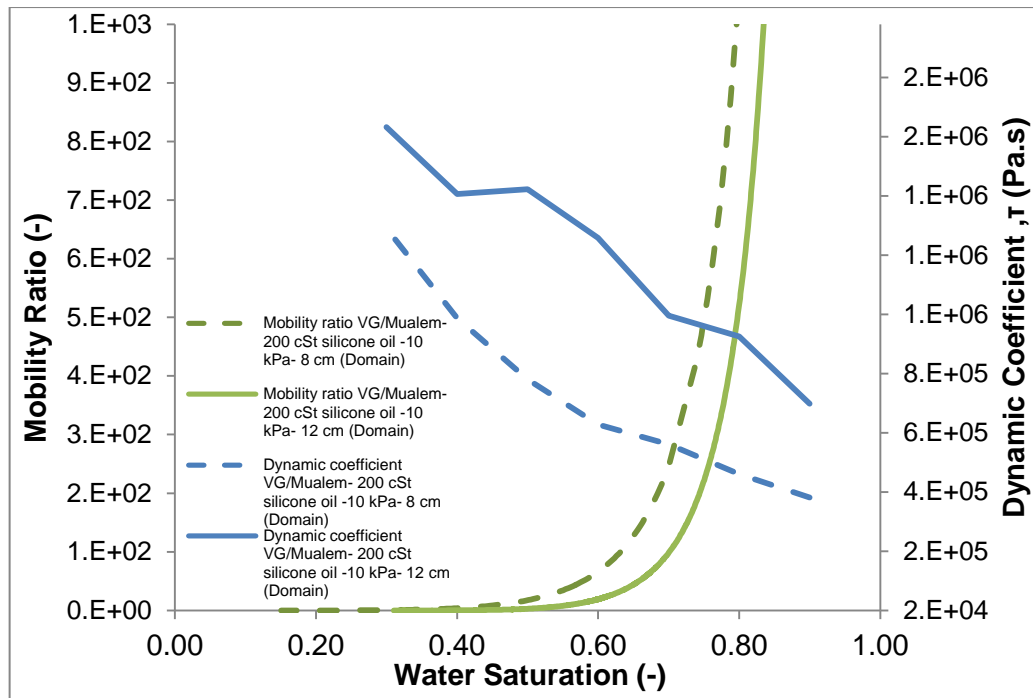


Figure 4.8: Plots of mobility ratio ( $m$ ) and dynamic coefficient ( $\tau$ ) as a function of water saturation with 200cSt silicone oil at the top boundary pressure of 10kPa for the 8 and 12cm high domains.

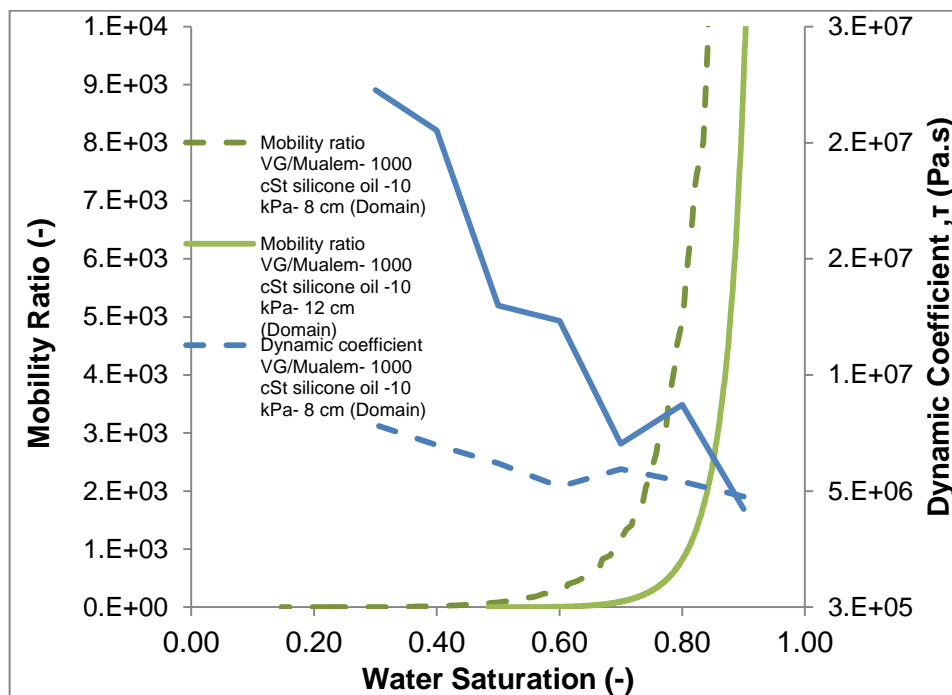


Figure 4.9: Plots of mobility ratio ( $m$ ) and dynamic coefficient ( $\tau$ ) as a function of water saturation with 1000cSt silicone oil at the boundary pressure of 10kPa for the 8 and 12cm high domains.

For the 200 cSt oil (Figure 4.8), it was observed that the mobility ratio decreased with an increase in domain size while the dynamic coefficient was found to be increasing. A similar

trend was noticed in 1000 cSt oil (Figure 4.9). It was observed that for a saturation of 50%, the value of mobility ratio is more than 1. The fluid fronts are considered to be stable. The trend observed here are similar to that observed by Das et al. (2007) and Hou et al. (2012), i.e., as  $m$  decreases  $\tau$  increases at a given saturation.

#### 4.4 Summary

Relative permeability models were employed to investigate the effect of dynamic flow conditions, porous media domain scales and boundary conditions on the  $K_r$ - $S$  relationship for silicone oil-water flow in porous media. Results show that the  $K_r$ - $S$  relationship is susceptible to the influence of fluid properties (i.e. viscosity) and porous media characteristics.  $K_{rw}$  increases with increasing wetting phase saturation and decreases with the increase in viscosity ratio. On the other hand,  $K_{rnw}$  increases with increasing non-wetting phase saturation as well as with the increase in viscosity ratio. Also, the  $K_{rw}$  decreases while the  $K_{rnw}$  increases with the increasing boundary pressure. The boundary pressure effect is significant in comparison to fluid viscosity ratio and scale dependency. At 40% water saturation and for the 8cm high domain, the  $K_{rnw}$  increased by 24.5% when viscosity ratio was increased from 200 to 1000. The same is true for the 12cm high domain. The boundary pressure, location of sensors and fluid viscosity play a significant role in the  $K_r$ - $S$  relationship. The dynamic relative permeability curves are different from the static relative permeability curves, which is in line with previous studies. This study shows that  $K_r$ - $S$  is affected by dynamic effects and therefore provisions should be made in models to include these dynamic  $K_r$ - $S$  relationships.

## CHAPTER FIVE

# ARTIFICIAL NEURAL NETWORK (ANN) MODELLING OF SCALE DEPENDENT DYNAMIC CAPILLARY PRESSURE EFFECTS IN TWO-PHASE FLOW IN POROUS MEDIA\*

### Overview

*A number of numerical simulations and experimental investigations have reported the impact of specific domain size on the dynamic capillary pressure which is one of the forces that govern two-phase flow in porous media. These investigations are often achieved with time-consuming experiments and/or costly/complex computational methods. In view of this, a computationally efficient and simple alternative platform for the prediction of the domain scale dependence of the dynamic capillary pressure effects, defined in terms of a coefficient named as dynamic coefficient ( $\tau$ ), is developed using artificial neural network (ANN). The input parameters consist of the phase saturation, media permeability, capillary entry pressure, viscosity ratio, density ratio, temperature, pore size distribution index, porosity and domain volume with corresponding output  $\tau$  obtained at different domain scales. Good generalization of the model was achieved by acquiring data from independent sources comprising experiments and numerical simulations. Different ANN configurations as well as linear and non-linear multivariate regression models were tested using a number of performance criteria. Findings in this work showed that the ANN structures with two hidden layers perform better than those with a single hidden layer. In particular, the ANN configuration with 13 and 15 neurons in the first and second hidden layers, respectively, performed the best. Using this best-performing ANN, effects of increased domain size were predicted for three separate experimental results obtained from literature and from the in-house laboratory investigations with different domain scales. Results showed increased magnitude of  $\tau$  as the domain size increases for all the independent experimental data considered. This work shows the applicability and techniques of using ANN in the prediction of scale dependence of two-phase flow parameters.*

### 5.1 Introduction

Characterising single and two-phase flow in porous media is of particular interest in issues relating to remediation of immiscible , oil recovery, flow in pulp and paper systems, and others (Bear 2013; Ingham and Pop 2005). The two-phase flow behaviour in porous medium can be macroscopically

---

\*Abidoeye, L.K. and Das, D.B. Artificial Neural Network (ANN) Modelling of Scale Dependent Dynamic Capillary Pressure Effects in Two-Phase Flow in Porous Media, Journal of Hydroinformatics (Accepted)

described by the equations for conservations of fluids' mass and momentum (Kalaydjian 1987), however, these should be coupled with constitutive relationships among capillary pressure, ( $P^c$ ), saturation ( $S$ ) and relative permeability ( $K_r$ ) (Mirzaei and Das 2007; Khudaida and Das, 2014).

The traditional approaches for determining  $P^c$ - $S$ - $K_r$  relationships assume that the flow parameters are functions of steady-state saturation (i.e.,  $dS/dt = 0$ ) only. For example, the definition of  $P^c$  according to the Laplace law (shown in equation (5.1)) is valid under static conditions (Kalaydjian 1992), where  $\gamma$  is the interfacial tension between the two fluids and  $\theta$  is the contact angle.

$$P^c = \frac{2\gamma \cos \theta}{r} \quad (5.1)$$

The Laplace law defines  $P^c$  to be a function of contact angle ( $\theta$ ) which, in turn, depends on the physical properties of the fluids and the porous medium (e.g., wettability (Dullien et al. 1990) and viscosity ratio (Danish and Jacquin 1983)) that are in contact with one another. Despite these notions, the saturation-rate dependency of  $P^c$ - $S$  relationships has been observed in many studies during dynamic two-phase flow in porous media which is referred to as the dynamic capillary pressure effect (Hassanizadeh et al. 2002; Mirzaei and Das, 2007). To this end, a large number of papers involving numerical simulations and experiments concerning the dynamic  $P^c$ - $S$  relationship have been published (see e.g., Topp et al. 1967; Smiles et al. 1971; Stauffer 1978; Kalaydjian 1992; Wildenschild et al. 2001; Hassanizadeh et al. 2002; O'Carroll et al. 2005a; O'Carroll et al. 2005b; Oung et al. 2005; Camps-Roach et al. 2010; Sakaki et al. 2010; Goel and O'Carroll 2011; Das and Mirzaei 2012; Diamantopoulos and Durner 2012; Das and Mirzaei 2013). Particularly, the studies by Kalaydjian (1992) and Hassanizadeh and Gray (1993) identified the dependence of the  $P^c$  on saturation ( $S$ ) and the rate of change of saturation  $\left(\frac{\partial S}{\partial t}\right)$ . This is defined as 'dynamic

capillary pressure effect' and it is quantitatively described with the proportionality constant term,  $\tau$ , known as the dynamic coefficient. In the last couple of decades, this term has been incorporated in a traditional mathematical definition for the two-phase systems. This is expressed in equation (3.2), which is reproduced as equation (5.2) in this chapter.  $\tau$  accounts for the difference between the  $P^c$ - $S$  relationships, under the dynamic and static flow conditions.

$$P^{c,dyn} - P^{c,static} = -\tau \left( \frac{\partial S}{\partial t} \right) \quad (5.2)$$

where,  $P^{c,dyn}$  ( $\text{kg}\cdot\text{m}^{-1}\cdot\text{s}^{-2}$ ) is the phase pressure difference ( $P_{nw}-P_w$ ) measured under dynamic or non-equilibrium condition,  $P^{c,static}$  ( $\text{kg}\cdot\text{m}^{-1}\cdot\text{s}^{-2}$ ) is the capillary pressure measured under equilibrium condition,  $\frac{\partial S}{\partial t}$  ( $\text{s}^{-1}$ ) is the rate of saturation change, and  $\tau$  ( $\text{kg}\cdot\text{m}^{-1}\cdot\text{s}^{-1}$ ) is called the dynamic coefficient.  $P_w$  and  $P_{nw}$  are the pressures of the wetting and non-wetting phases, respectively.

As explained by Das et al. (2007), the magnitude of  $\tau$  relates to how close or far from capillary equilibrium ( $\frac{\partial S}{\partial t}=0$ ) is the two-phase flow system. However, its magnitude is reported to be dependent on the size of the domain (Dahle et al. 2005; Camps-Roach et al. 2010; Bottero et al. 2011a, b; Das and Mirzaei 2012; Das and Mirzaei 2013) apart from other factors, e.g., fluid viscosity and density ratios (Gielen et al. 2005; Das et al. 2007; Goel and O'Carroll 2011; Joekar-Niasar and Hassanizadeh 2011), permeability of the medium (Camps-Roach et al. 2010; Tian et al. 2012; Hanspal et al. 2013) and heterogeneities (Das et al. 2006; Manthey et al. 2005; Das and Mirzaei 2013; Mirzaei and Das, 2013). This work is specifically concerned with the domain scale effects on the dynamic coefficient ( $\tau$ ).

Understanding the influence of domain scale on the magnitude of  $\tau$  is important as the two-phase flow can occur in porous domains at pore, core and/or larger field scales. Previous experimental (Bottero et al. 2011b) and numerical (Dahle et al. 2005) studies showed an increasing magnitude of  $\tau$  as the domain size increases. However, some authors have expressed different conclusions about the effect of domain size on  $\tau$ . Camps-Roach et al. (2010) and Das and Mirzaei (2012, 2013) do not find significant difference between the locally measured and the upscaled value of  $\tau$ . This indicates the possible inconsistency surrounding the exact trend of the magnitude of  $\tau$  with the domain scale.

Meanwhile, investigating the dynamic capillary pressure effects on two-phase flow systems in the porous media often requires time-consuming experiments and/or cost-intensive modelling and simulations, which generally involve complex procedures to set up and run the simulations (Hanspal et al. 2013; Spalding 1981; Khudaida and Das, 2014). Furthermore, determining the effects of domain scale on  $\tau$  also imposes further challenges with various averaging techniques proposed and applied in the literature. For example, Bottero et al. (2011a) proposed a centroid-corrected averaging method as the most appropriate for two-phase system while authors such as Das and Mirzaei (2012, 2013), Camps-Roach et al. (2010) and Manthey et al. (2005) employed different averaging techniques to determine the scale dependency of  $\tau$ . While the scale dependency of  $\tau$  continues to be a topic of discussion, there is an obvious lack of industrially relevant, easy-to-use tools that can determine these behaviour. To address these challenges/issues, it is desirable to investigate the domain scale effect on  $\tau$  using alternative platforms offering less complex and fast implementation procedures to achieve the same end. In this work, a computationally economical and simpler platform for investigating the effects of domain scale on  $\tau$  is presented using artificial neural network (ANN).

Indeed, ANN is a powerful modelling tool with the ability to learn and generalize functions from rounds of training as well as extract essential information from data (Khashei and Bijari 2013; Wang and Fu 2008). It provides a novel, elegant and valuable class of computational tools for data

analysis and prediction (White, 1989). Its building blocks or the elements are the 'neurons' which are grouped into input, hidden and output layers with respective biases, weights and transfer functions (Yurdakul and Akdas 2013; Mueller and Hemond 2013). The network manipulates the values of the biases and weights in a sequence of training processes and uses the transfer functions to establish the relationships between the inputs and the outputs. It has found applications in wide areas of science and engineering problems including medical fields to illustrate medical diagnosis (Amato et al. 2013), renewable energy systems, economics, psychology and many more (Kalogirou 2013).

Although, the modelling parameters involved in the two-phase flow in porous media are interrelated in a complex manner, it has been shown that ANN can approximate the relevant functions to the desired accuracy (Zhang et al. 1998; Hanspal et al. 2013). This quality of ANN can, thus, be harnessed to investigate the complex behaviour of two-phase flow in porous media. For example, please see the works on the application of ANN to study two-phase flow pattern (Mehta et al. 2013), oil flow rate (Ahmadi et al. 2013), groundwater contamination and pollutant infiltration forecasting (El Tabach et al. 2007), optimization of groundwater remediation problems (Rogers and Dowla 1994; Johnson and Rogers 2000), large-scale water resource management (Yan and Minsker 2006), and permeability modelling in petroleum reservoir management (Karimpouli et al. 2010). Recently, Hanspal et al. (2013) demonstrated the effectiveness of ANN in the determination of dynamic effects in two-phase flow system, though they did not investigate the effect of domain scale on  $\tau$ . They concluded that a well-trained and validated ANN structure can give reliable prediction of  $\tau$  in two-phase flow systems. In addition to being inexpensive, ANN offers a faster alternative to modelling of complex system with the freedom from excessive imposition of constraints on the complex relationships between the input and output variables. Thus, this work explores the above qualities of ANN to investigate the domain scale dependency of  $\tau$  in the two-phase flow system in porous media.

## 5.2 Modelling approaches

ANN and multivariate regression (MVR) techniques were used to investigate the domain scale dependency of the  $\tau$  in the two-phase flow system. The MVR was chosen because of the ease of implementation and to provide an alternative approach to compare different ANN configurations against.

### 5.2.1 ANN

For successful modelling of dynamic two-phase flow behaviour using ANN, the impacts of the network configuration, training and evaluation procedures cannot be overemphasised. In this work, different network configurations were investigated using a feed forward network. This is the commonest network in engineering applications (Kalogirou 2013). For the purpose of training, a

back-propagation algorithm was employed. Details of the configurations, training and data processing are discussed further.

### 5.2.1.1 Data sources and pre-processing

In this work, the literature data were obtained from the results by Das and Mirzaei (2012), Hanspal and Das (2012), Goel and O'Carroll (2011), Das et al. (2007), Mirzaei and Das (2007) and the in-house laboratory experiments (Abidoeye and Das, 2014). Nine independent variables that have been identified as important in the literature were used as input variables in the simulations. These include, water saturation ( $S$ ), media permeability ( $k$ ), capillary entry pressure ( $P_d$ ), fluid viscosity ratio ( $\mu_r$ ) defined as the ratio of the non-wetting phase viscosity ( $\mu_{nw}$ ) to that of the wetting phase viscosity ( $\mu_w$ ), fluid density ratio ( $D_r$ ) defined as the ratio of the non-wetting phase density ( $D_{nw}$ ) to that of the wetting phase density ( $D_w$ ), temperature ( $T$ ), pore size distribution index ( $\lambda$ ), porosity ( $\phi$ ), and domain volume ( $V$ ). The output variable is the corresponding  $\tau$ . The number of data points under each variable is 307. In selecting these data sources, efforts were made to ensure that the data contain varying experimental or simulation parameters and conditions needed to fulfil the objective of this work. For example, the works of Das and Mirzaei (2012), Goel and O'Carroll (2011), Mirzaei and Das (2007) and, Hanspal and Das (2012) were conducted using different domain volumes. Furthermore, the in-house laboratory experiments were conducted for different heights of domain (4, 8 and 12 cm height) but with the same diameter for 500 cSt viscosity ratio of silicone-oil water system. These features enhance the training of the ANN network to easily capture the non-linear relationships between the domain size and  $\tau$ . Important statistics of the variables are listed in Table 5.1.

Compared to the number of data points commonly required to plot a complete  $\tau$ - $S$  curve (typically less than 10 data points, see, e.g., Bottero et al. (2011b)), the amount of data used in this work (>300 data points) is over 30 times more than what is typically required. Also, this work employs a simple ANN structure. These features ensure that artificial over-fitting of the data is avoided. Complex ANN structures and few data can lead to artificial over-fitting in ANN modelling (Hanspal et al. 2013).

### 5.2.1.2 ANN development

Various configurations of ANN were developed and tested to determine the most suitable network. The configuration approach followed that demonstrated in Hanspal et al. (2013) as proposed by Srinivasulu and Jain (2006). The ANNs include single and double hidden layers. The program file with lines of code was written and implemented in MATLAB to create, train, validate and test the networks as well as to generate the goodness of fit of the parameters e.g. correlation coefficients and slope for the predicted output ( $\tau$ ). The developed networks consist of different layers comprising the input, hidden and the output layers. The input layer is occupied by the independent

variables while the output layer is for the dependent variable. The hidden layer is occupied by the neurons, which are the constitutive units that receive the input and operate on them to produce the output. The code divides the dataset randomly into 60, 20 and 20% corresponding to the data for training, validation and testing. As stated before, the training was performed with the Levenberg-Marquardt function (Marquardt 1963) using the back-propagation algorithm. The Levenberg-Marquardt function is a curve-fitting function applied in non-linear least squares problems. It optimises the parameter of the model curve by minimising the sum of the squares of the deviation from the empirical dependent variable. The back-propagation learning algorithm operates by iterative adjustment of the weights and biases in response to the error value between the predicted and the desired outputs. 'Tansig' and 'Purelin' transfer functions were used in this work. These transfer functions calculate a layer's output from its net input. While 'Tansig' is nonlinear, 'Purelin' is linear. For a network with single hidden layer, 'Tansig' was used between the input and the hidden layers while 'Purelin' was used between the hidden and the output layer. For a network with double hidden layer, 'Tansig' was used between the input and the hidden layers as well as between the first to the second hidden layers while 'Purelin' was used between the second hidden layer and the output.

Mean square error (MSE) was employed as the network default performance criterion relating the calculated outputs from the ANN to the actual target (dependent variable) in the training, validation and testing processes. In the simulation, pre-processing was performed using lines of code in the script with function "mapminmax". This function scales the inputs so that they fall into the range of -1 to 1. In the training process, the epochs and goals serve as the stopping criteria of the number of iterations and the error tolerance, respectively. Epoch is the maximum number of times all of the training sets presented to the network, while goal refers to the maximum error tolerance to be met by the developed network. Thus, the training stops if the error goal is met or the maximum number of epochs is attained. In this work, an epoch of 200 and a goal of zero were used. Different network configurations were constructed and each configuration differs in the number of hidden layers or neurons. The number of neurons was gradually increased for either single or two-hidden layers. In this work, the representation of the layers in the ANN configurations is ANN [X-H1-Y] and ANN [X-H1-H2-Y] for single and double hidden layers, respectively. "X" represents the input layer and its number refers to the number of independent variables, "H1" and "H2" represent the first and the second hidden layers, respectively and their number represent the number of neurons in that layer. "Y" is the output layer and its number represents the number of the dependent variable.

## 5.2.2 Linear (LR) and non-linear (NLR) regression models

For the purpose of comparisons with the performances of the different ANN configurations, multiple linear (LR) and non-linear (NLR) regression models were investigated with the aid of MATLAB. Both regression models utilised the entire dataset.

The LR was formulated for the nine independent variables against the dependent variable,  $\tau$  as shown in equation (5.3):

$$\tau = b_0 + b_1(\chi_1) + b_2(\chi_2) + b_3(\chi_3) + b_4(\chi_4) + b_5(\chi_5) + b_6(\chi_6) + b_7(\chi_7) + b_8(\chi_8) + b_9(\chi_9) \quad (5.3)$$

$b_0, \dots, b_9$  are the regression coefficients,  $\chi_1, \dots, \chi_9$  represent the independent variables. The regression coefficients for the LR were determined using the left division method (Gauss elimination and least square techniques) (Hanspal et al. 2013).

For the non-linear regression of the independent variables, polynomials of various orders (Jain and Indurthy 2003) were used. The regression was implemented using non-linear fitting function (nlfitt) in MATLAB to determine the vector of fit coefficients ( $b_0, \dots, b_9$ ) in the models listed below:

$$\tau = b_0 + b_1(\chi_1)^{0.05} + b_2(\chi_2)^{0.05} + b_3(\chi_3)^{0.05} + b_4(\chi_4)^{0.05} + b_5(\chi_5)^{0.05} + b_6(\chi_6)^{0.05} + b_7(\chi_7)^{0.05} + b_8(\chi_8)^{0.05} + b_9(\chi_9)^{0.05} \quad (5.4)$$

$$\tau = b_0 + b_1(\chi_1)^2 + b_2(\chi_2)^2 + b_3(\chi_3)^2 + b_4(\chi_4)^2 + b_5(\chi_5)^2 + b_6(\chi_6)^2 + b_7(\chi_7)^2 + b_8(\chi_8)^2 + b_9(\chi_9)^2 \quad (5.5)$$

$$\tau = b_0 + b_1(\chi_1)^3 + b_2(\chi_2)^3 + b_3(\chi_3)^3 + b_4(\chi_4)^3 + b_5(\chi_5)^3 + b_6(\chi_6)^3 + b_7(\chi_7)^3 + b_8(\chi_8)^3 + b_9(\chi_9)^3 \quad (5.6)$$

$$\tau = b_0 + b_1(\chi_1)^4 + b_2(\chi_2)^4 + b_3(\chi_3)^4 + b_4(\chi_4)^4 + b_5(\chi_5)^4 + b_6(\chi_6)^4 + b_7(\chi_7)^4 + b_8(\chi_8)^4 + b_9(\chi_9)^4 \quad (5.7)$$

Table 5.1: Statistics of the input and output variables

	Water saturation, S (-)	Permeability, k (m <sup>2</sup> )	Entry pressure, P <sub>d</sub> (Pa)	Domain volume, V (m <sup>3</sup> )	Pore size distribution, λ (-)	Viscosity ratio, μ <sub>r</sub> (-)	Porosity, φ (-)	Density ratio, D <sub>r</sub> (-)	Temperature, T (°C)	Dynamic coefficient, τ (Pa.s)
Maximum	9.96x10 <sup>-1</sup>	5.00x10 <sup>-9</sup>	1.50x10 <sup>3</sup>	1.57x10 <sup>-3</sup>	8.84	1.00 x10 <sup>3</sup>	0.400	2.00	80.00	1.05 x10 <sup>11</sup>
Minimum	1.05x10 <sup>-1</sup>	1.50 x10 <sup>-11</sup>	3.75x10 <sup>2</sup>	3.27 x10 <sup>-4</sup>	2.07	5.00 x10 <sup>-1</sup>	0.32	0.50	20.00	1.18 x10 <sup>3</sup>
Arithmetic Average	4.78x10 <sup>-1</sup>	1.70 x10 <sup>-9</sup>	7.78x10 <sup>2</sup>	9.41 x10 <sup>-4</sup>	3.44	1.77 x10 <sup>2</sup>	0.373	1.15	22.4	5.57 x10 <sup>9</sup>
Standard deviation	2.57x10 <sup>-1</sup>	2.19 x10 <sup>-9</sup>	4.29x10 <sup>2</sup>	2.42 x10 <sup>-4</sup>	1.49	2.66 x10 <sup>2</sup>	0.0311	0.374	9.43	1.89 x10 <sup>10</sup>

### 5.2.3 Models performance testing criteria

The performances of all models were weighed with different statistical evaluations as demonstrated in Hanspal et al. (2013) using the following statistical analyses:

#### A. Sum square error (SSE)

This describes the total deviation of the predicted values ( $S_{cal}$ ) from the target values ( $S_{obs}$ ):

$$SSE = \sum_{i=1}^N (S_{obs} - S_{cal})^2 \quad (5.8)$$

where  $N$  = Total number of data points predicted,  $S_{obs}$  = observed or target values of dynamic coefficient,  $\tau$  and  $S_{cal}$  = predicted or calculated value of dynamic coefficient,  $\tau$ . SSE and mean square error (MSE) are related by equation (5.9):

$$MSE = \frac{SSE}{N-k} \quad (5.9)$$

where,  $k$  is the number of variables.

#### B. Average absolute relative error (AARE)

This is the average of the relative errors in the prediction of a particular variable and it is expressed as a percentage. Lower value of AARE indicates better model performance. It can be computed as follows:

$$AARE = \frac{1}{N} \sum_{i=1}^N \left| \frac{S_{cal} - S_{obs}}{S_{obs}} \right| \times 100 \quad (5.10)$$

#### C. Nash-Sutcliffe efficiency coefficient (E)

The Nash-Sutcliffe efficiency coefficient is used to describe the accuracy of model outputs in relation to observed data. A value of  $E$  equal to 1 depicts a perfect match between observed data and outputs therefore the closer the model efficiency is to unity the more accurate the model.  $E$  is computed as follows:

$$E = 1 - \frac{\sum (S_{cal} - S_{obs})^2}{\sum (S_{obs} - \bar{S}_{obs})^2} \quad (5.11)$$

where  $\bar{S}_{obs}$  = average observed dynamic coefficient,  $\tau$ , in this work.

#### D. Threshold statistics (TS)

The threshold statistic for a level of absolute relative error of  $x\%$  from a particular model is a measure of consistency in the prediction errors (Jain and Ormsbee, 2002). The threshold statistic can be computed as follows:

$$TS = \frac{N_x}{N} \quad (5.12)$$

where  $N_x$  = number of data points predicted for which the average relative error (ARE) is less than  $x\%$ . Larger value of threshold statistics indicates better model performance.

#### 5.2.4 Prediction of domain scale dependency of $\tau$ -S relationships

Following the rigorous statistical evaluation of the models described earlier, prediction of the effect of domain size on the  $\tau$ -S relationships was performed using the best-performing model. Separate data from independent experiments are predicted separately. To do this, the actual domain volume (V) of the experiment was increased by 10 or 20% and the corresponding  $\tau$  was predicted as a function of saturation using the best-performing ANN.

### 5.3 Results and discussions

A computationally cost-effective and reliable ANN structure that predicts the domain scale dependency of  $\tau$ -S relationships will serve a useful purpose in determining the significance of dynamic capillary pressure for two-phase flow systems. The results in this work are aimed at demonstrating this possibility. So, the results of training, validation and testing of the ANNs are discussed below. Also, the performances of the different ANN configurations together with the MVR models are compared on the bases of the different performance criteria. Scale dependency of  $\tau$ -S relationships were then predicted for the two-phase flow system using the best-performing configuration.

#### 5.3.1 ANN configurations

The training, validation and testing as well as the post-training regression analyses for different ANN configurations are shown in Figure 5.1 and Figure 5.2 for ANN [9-13-15-1] and ANN [9-15-17-1], respectively. Figure 5.1(A) shows how the mean square error (MSE) reduces during training, validation and testing as the number of epoch increases. This eventually culminates in the optimal performance during validation at 108 epochs having approximately zero MSE value, i.e., 0.0023. This behaviour shows that the network learns well as the number of epochs increase. The testing session shows acceptable MSE that is very close to zero as well. The post-training regression analysis (Figure 5.1(B)) shows the

linear regression line fit the data points. This regression line has a correlation coefficient ( $c$ ) and slope ( $m$ ) of 0.99 and 0.97, respectively, which are very close to 1. These show the reliability of the fit. In the Figure 5.1, it can be observed that the target data cluster around the regression line in a way that shows reliable prediction. Similarly, the behaviour of the network for ANN [9-15-17-1] is shown in Figure 5.2. The network exhibits similar behaviour as discussed above. The learning improves with the number of epochs for the training, validation and testing (Figure 5.2(A)). This is indicated by the reduction in the MSE values and the optimal MSE with validation occurs before the number of epochs reaches 51. In comparison to the behaviour of ANN [9-13-15-1], shown in Figure 1(A), the testing and validation errors are larger in Figure 2(A), under corresponding condition. . The regression line for the ANN structure [9-15-17-1] is shown in Figure 5.2(B). The fit shows good  $c$  and  $m$  values of approximately 0.95 and 1.00, respectively. The regression analysis in Figure 5.2(B) shows that the cluster of the target data around the regression fit line is more scattered unlike that shown for ANN [9-13-15-1] (Figure 5.2(B)). This gives an indication that ANN [9-13-15-1] may be more reliable than ANN [9-15-17-1].

The performances of various ANN configurations, in terms of the values of  $c$  and  $m$  of the regression line of fits to the target data  $\tau$  are listed in Table 5.2. As is well known, values of the slope,  $m$  and correlation coefficient,  $c$ , closer to 1 indicate reliable prediction. From the table, it can be observed that majority of the ANN configurations perform well as indicated by the high values of the  $c$  and  $m$ . However, the two-hidden-layer models perform better than the single-hidden-layer models as they have the slope and correlation coefficient closer to 1 than the single-hidden-layer structure. In all, ANN [9-13-15-1] and ANN [9-15-17-1] appear to be leading in performance. However, the criteria listed in subsection 2.3 are further employed in weighing the performances of all the models including the MVR models. In Table 5.2, the slope of the regression line obtained from ANN [9-15-17-1] is shown to be slightly greater than 1 (i.e., 1.02). This can be explained to mean slight over prediction of the target data by the model. This is also visible in the Figure 5.2(B) where the line of fit is slightly above the best line of fit (i.e.,  $Y=T$ ). In contrast, Figure 5.1 shows that the regression line obtained from ANN [9-13-15-1] lies slightly below the best line of fit (i.e.,  $Y=T$ ) and hence, the slope is slightly below 1 (i.e., 0.97).

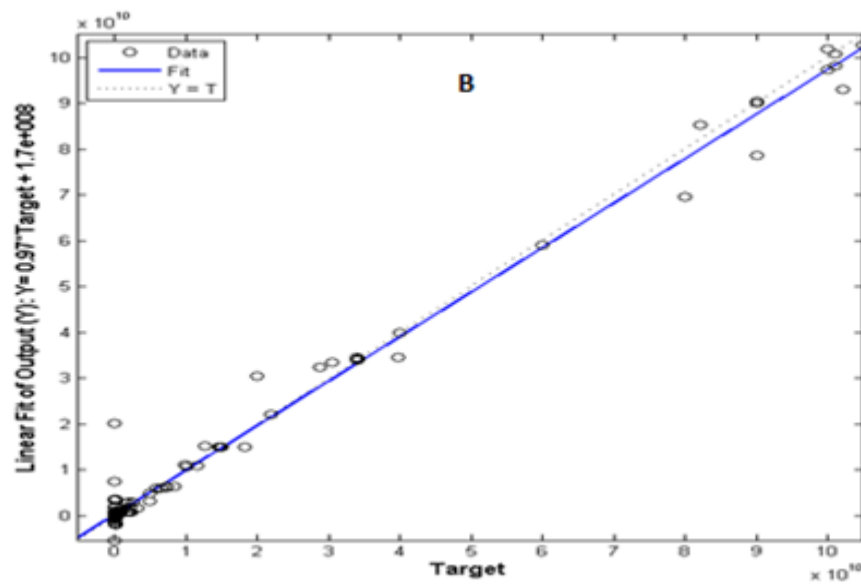
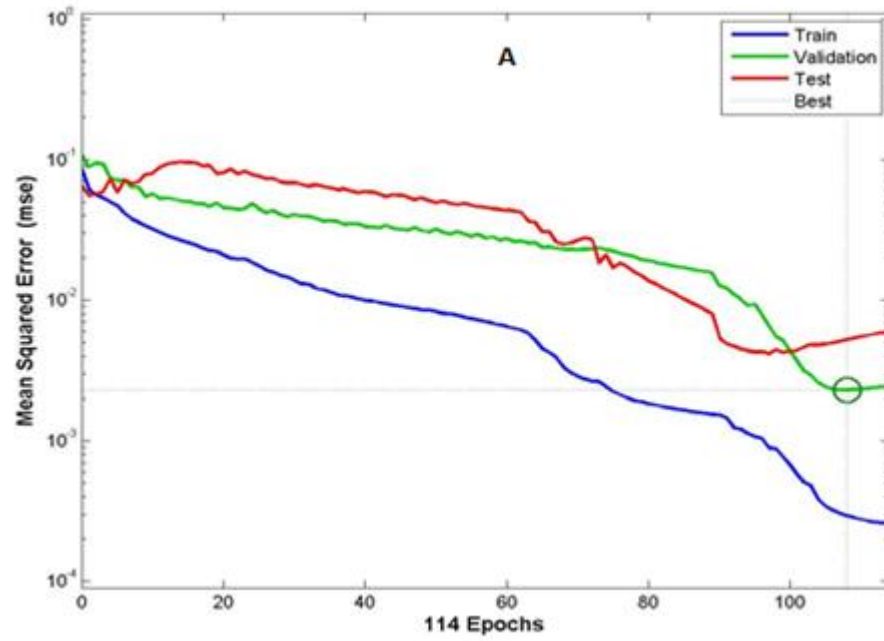


Figure 5.1: (A) Training and (B) post-training regression analysis using ANN [9-13-15-1]

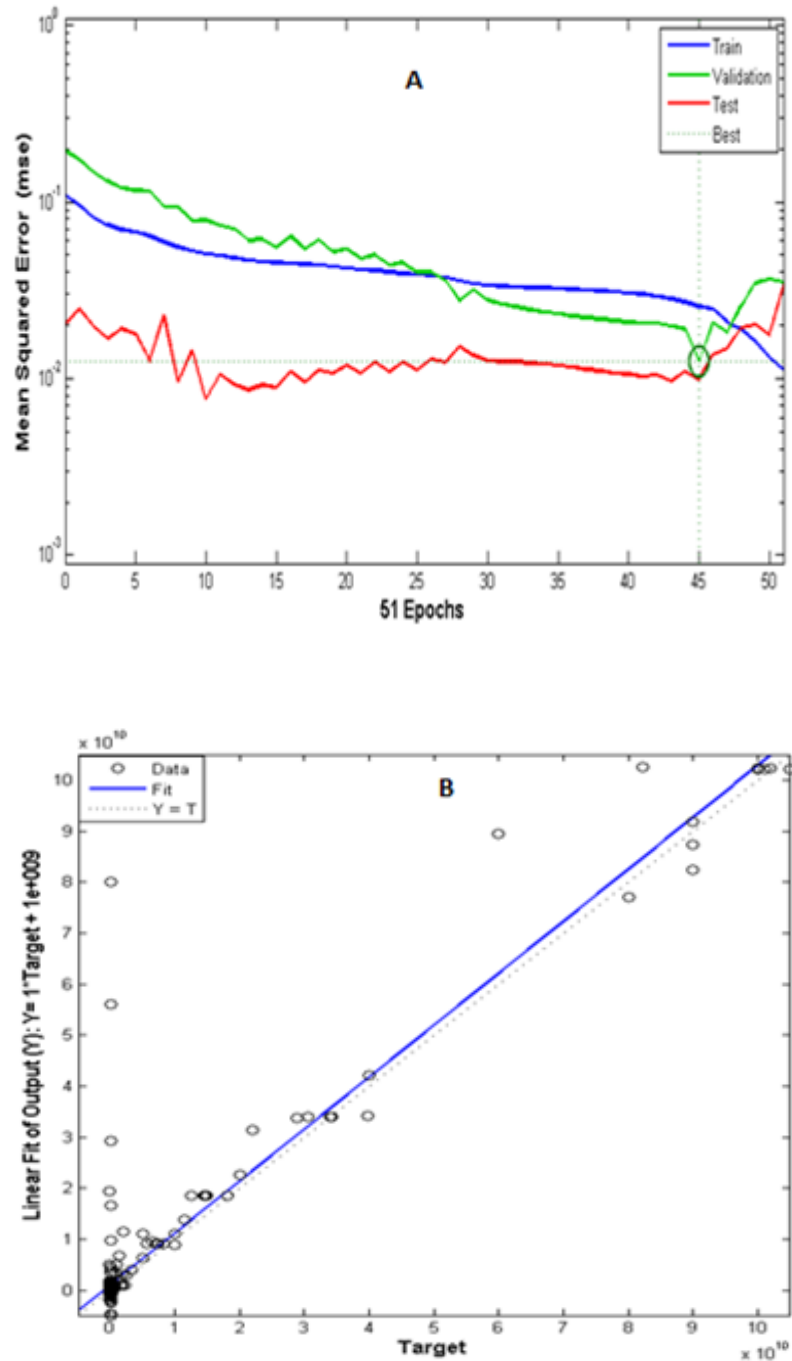


Figure 5.2: (A) Training and (B) post-training regression analysis using ANN [9-15-17-1]

Figure 5.3 shows the plots of average absolute relative error (AARE) for all ANN configurations, linear regression (LR) and non-linear regression (NLR) models. In comparison, AARE is generally low for the different ANN configurations while the LR and NLR generally have high AARE.

Table 5.2: Slope and correlation coefficient for different ANN configurations (single and double hidden layered ANN structures)

<b>S/N</b>	<b>ANN Configurations</b>	<b>Slope (m)</b>	<b>Correlation Coefficient (c)</b>
1	9-2-1	0.7986	0.7986
2	9-3-1	0.8557	0.8557
3	9-4-1	0.925	0.925
4	9-5-1	0.8819	0.8819
5	9-7-1	0.8459	0.8459
6	9-9-1	0.9218	0.9218
7	9-10-1	0.8976	0.8976
8	9-2-2-1	0.881	0.881
9	9-3-2-1	0.8345	0.8345
10	9-2-3-1	0.8962	0.8962
11	9-5-3-1	0.9191	0.9191
12	9-7-5-1	0.9406	0.9406
13	9-9-7-1	0.9262	0.9262
14	9-10-8-1	0.9529	0.9529
15	9-10-10-1	0.9631	0.9631
16	9-11-13-1	0.9865	0.9865
17	9-13-15-1	0.9723	0.9949
18	9-15-17-1	1.0185	0.9468

The lower the AARE the better the performance (Hanspal et al. 2013). Thus, it seems that the ANNs perform better than the LR and NLR models. Among the ANN configurations, ANN [9-13-15-1] has the least AARE followed by ANN [9-11-13-1].

In Figure 5.4, the plots of the sum squared error (SSE) similarly show that the SSE is generally higher for LR and NLR models. For the ANN structures, the ANN [9-13-15-1] configuration has the least SSE followed by ANN [9-11-13-1]. Comparison of the model output in relation to the target is described in terms of the Nash-Sutcliffe efficiency coefficient (E) depicted in Figure 5.5 for all the models. Again, it is visible that ANN [9-13-15-1] has the highest efficiency followed by ANN [9-11-13-1]. Also, threshold statistics (TS) for all the models show that ANN [9-13-15-1], ANN [9-11-13-1] and ANN [9-15-17-1] have the leading percentages. The plots are shown in Figure 5.6 for TS 5, TS 10, TS 25, TS 50 and TS 100. High value of TS implies good model performance.

From the above discussions, the performance criteria show that ANN structures have better reliability in predicting the two-phase flow parameters than MVR models (both linear and non-linear). From the results, ANN [9-13-15-1] has shown the best performance.

### 5.3.2 Prediction of $\tau$ -S relationships

Results of the statistical analyses discussed in section 3.1 compare the predicted output of the models to the actual target output ( $\tau$ ). The discussions in this section focus on the comparison of the actual  $\tau$ -S relationships (target) to that predicted by some selected ANN, which include the best-performing model: ANN [9-13-15-1]. Figure 5.7 shows the plot of  $\tau$ -S relationships using the entire dataset in comparison with the prediction by ANN [9-13-15-1]. It can be observed that the ANN structure has a good predictive ability of the  $\tau$ -S relationships at both low and high saturation. Almost the entire  $\tau$ -S dataset are overlaid by the predicted values. In Figure 5.7,  $\tau$  is shown to increase as the saturation reduces. From the start of the displacement of the wetting phase by the non-wetting phase, there exists only minimal change in  $\tau$  as the saturation reduces. The trend, however, changes around the irreducible saturation where the  $\tau$  value rises very steeply. This trend is widely reported in the literature (Das and Mirzaei 2013; Goel and O'Carroll 2011; Camps-Roach et al. 2010; Sakaki et al. 2010). According to Das et al. (2007), increase in the magnitude of  $\tau$  indicates increased deviation of the  $P^c$ -S relationships from equilibrium condition. Since the magnitude of  $\tau$  becomes spectacularly large towards irreducible saturation, one can infer that the system properties at this region exhibit wider deviations from equilibrium.

Predictions of the  $\tau$ -S relationships by ANN [9-15-17-1], ANN [9-10-10-1] and ANN [9-11-13-1] are shown in Figures 5.8 to 5.10, respectively. While these plots show good prediction of the  $\tau$ -S relationships for the entire dataset, they show more mismatches in comparison with Figure 5.7, especially at low water saturation or at high values of  $\tau$ . However, ANN [9-11-13-1] and ANN [9-10-10-1] appear to predict better than ANN [9-15-17-1], having a lower number of mismatches especially at low water saturation.

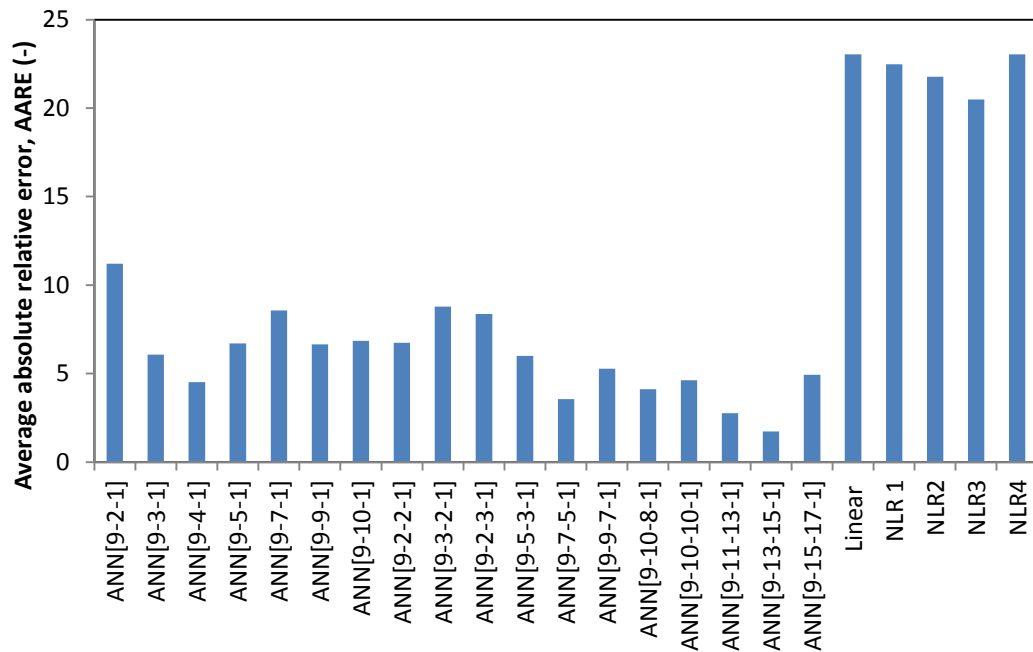


Figure 5.3: Average absolute relative error (AARE) for ANN, linear (LR) and non-linear (NLR) regression models.

Plots of the predictions of  $\tau$ -S relationships by linear and non-linear regression models are shown in Figure 5.11 and Figure 5.12. The predictions by these models are less reliable, especially at low water saturation where the  $\tau$  values are higher. Even the performances of these regression models are much less-satisfactory in comparison to any of the ANN configurations with plots shown in Figures 5.7 to 5.10. This reveals the limitations of the regression models in the prediction of  $\tau$ -S relationships for two-phase flow systems.

Judging from the results of the statistical analyses on the prediction of  $\tau$  as well as the above models performances on the prediction of  $\tau$ -S relationships, it can be concluded that ANN [9-13-15-1] is the best structure among the models tested in this work. This conclusion is similar to that of Hanspal et al. (2013).

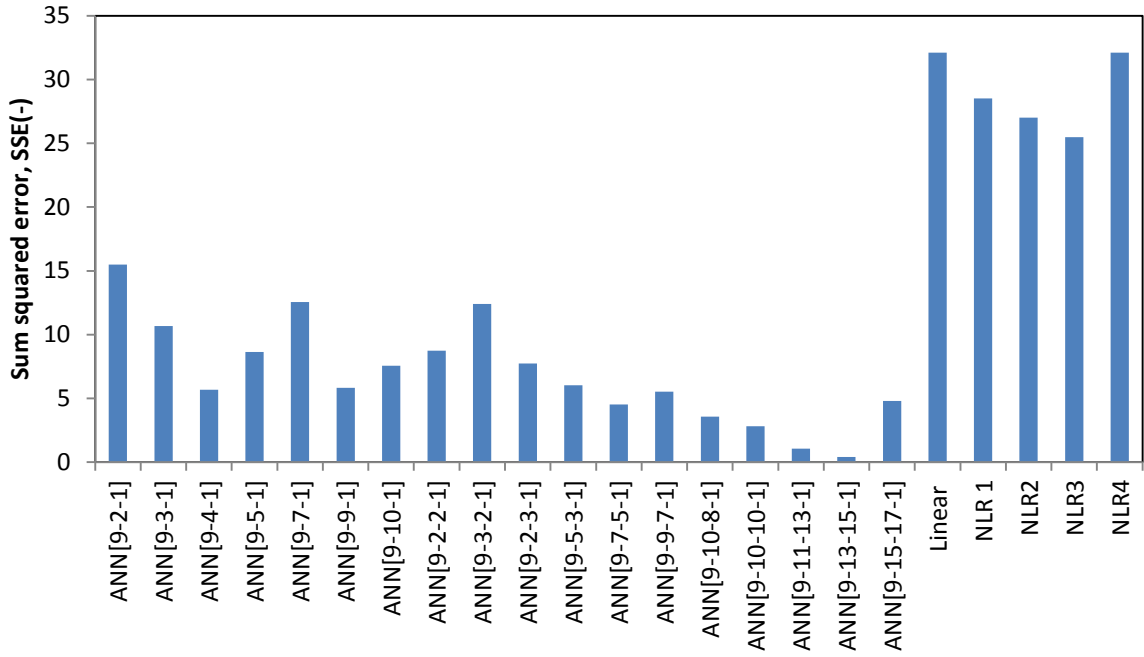


Figure 5.4: Sum squared error (SSE) for ANN, linear (LR) and non-linear (NLR) regression models.

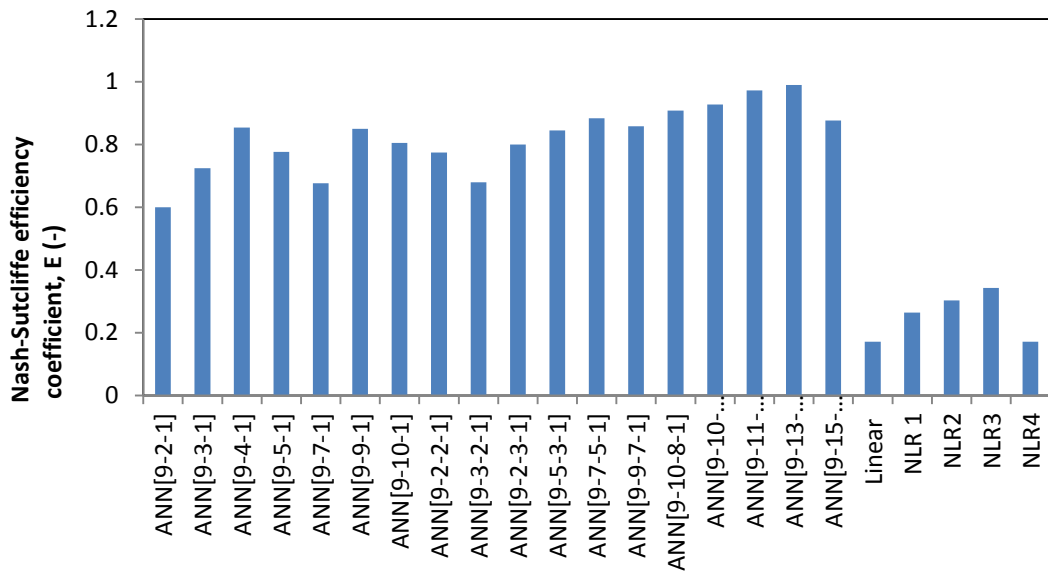


Figure 5.5 Model output efficiency for ANN, linear (LR) and non-linear (NLR) regression models.

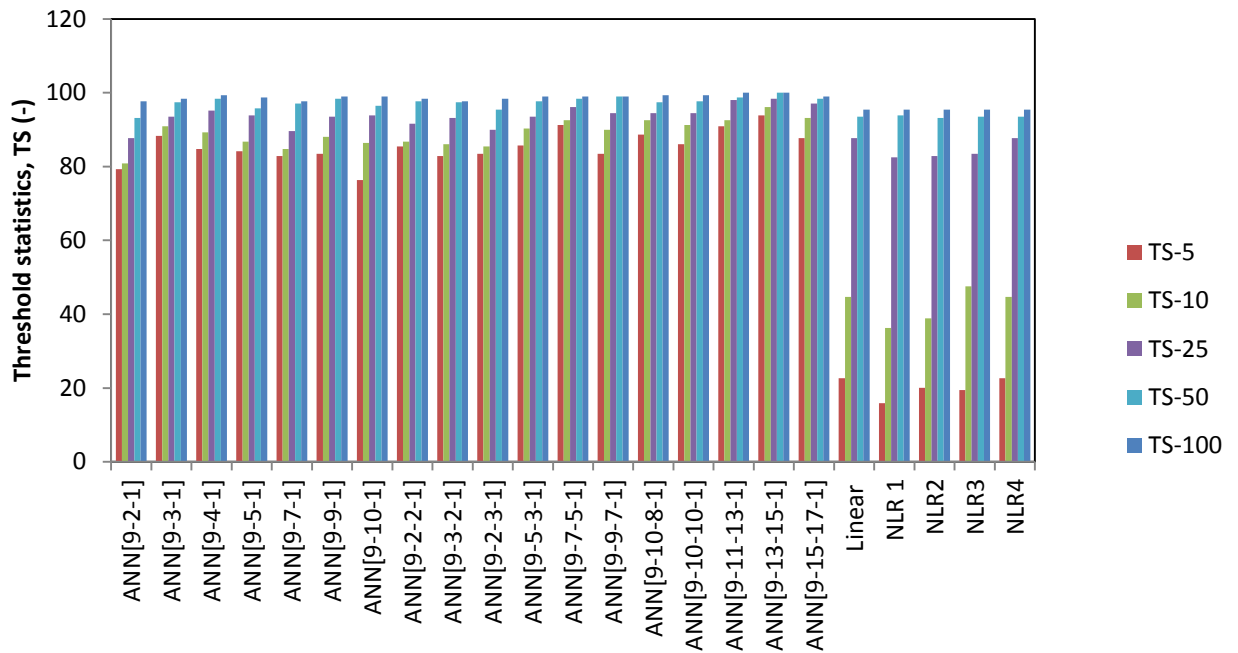


Figure 5.6: Threshold statistics (TS) for ANN, linear (LR) and non-linear (NLR) regression models.

They found that the regression models performed poorly in the prediction of the  $\tau$ -S relationships and concluded that generally the regression models are much less in predictive ability than ANN structures for two-phase flow system characteristics. In their work, the display of non-linear regression models seem better than shown in Figure 5.12 of this work even though similar functions were used. This can be explained by the fact that they utilise only five independent variables in their work as different from nine used in this work. Therefore, it can be inferred that the performances of the regression models become less reliable as the number of independent variables increases for two-phase flow system.

### 5.3.3 Domain scale dependency of $\tau$ -s relationships

In the previous analyses and discussions, the ANN [9-13-15-1] structure is shown to be the best-performing network in the context of this work. In this section, the network is used to predict the domain scale dependency of  $\tau$ -S relationships on the basis that the network is trained and validated. Separate data from different experiments are independently predicted. These include data from literature as well as the in-house laboratory experiments (Abidoye and Das, 2014). Figures 5.13 to 5.15 display the results of the predictions. In the Figures 5.13 to 5.15,  $\tau$  for the original domain size is represented by two plots. One plot was obtained from the experimental data and the other was obtained from the ANN prediction of the original experimental data at the original domain scale (volume). These are labelled original volume (experiment) and the original volume (ANN) for the actual experimental data and the ANN prediction, respectively. The other two plots in each of Figure 5.13 and 5.14 are

obtained when the domain scale (volume) is increased by 10 and 20%, respectively, and the corresponding  $\tau$ -S relationships are predicted using ANN [9-13-15-1]. The results show that increasing the volume of the domain increases the magnitude of  $\tau$ . In Figure 5.13, at a 10% increase in original domain volume, a  $\tau$ -S curve lies higher than at the original domain size. This effect becomes greater at 20% increase in domain volume.

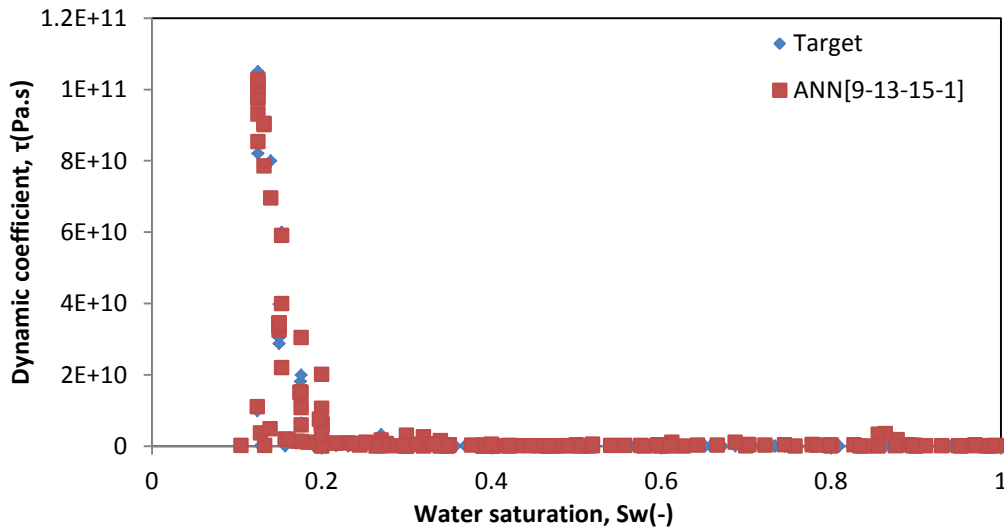


Figure 5.7: The dynamic coefficient values from ANN structures output and target data against water saturation using ANN [9-13-15-1].

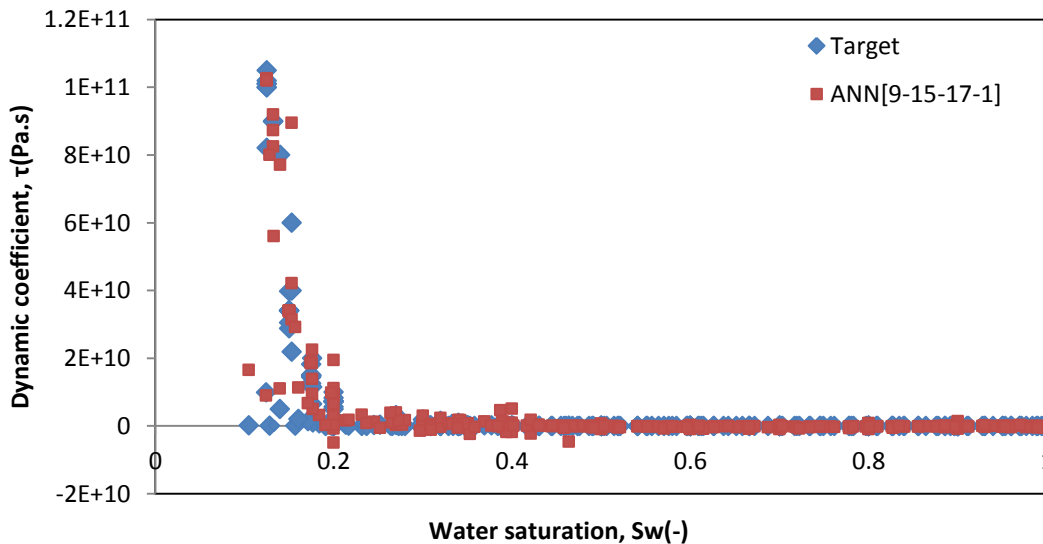


Figure 5.8: The dynamic coefficient values from ANN structures output and target data against water saturation using ANN [9-15-17-1].

This trend points to an important observation in the literature about the dependency of  $\tau$ -S curves on domain scale. A number of authors have reported the same phenomenon (Bottero et al. 2011a; Dahle et al. 2005). Bottero et al. (2011a) found that there is a shift to higher values in the  $\tau$ -S relationships as the scale goes from local measurements to higher

averaging windows. Also, Dahle et al. (2005) using a bundle of tubes model reports this phenomenon with a greater effect of scale on  $\tau$ -S relationships which is said to be proportional to the square of the length of the domain.

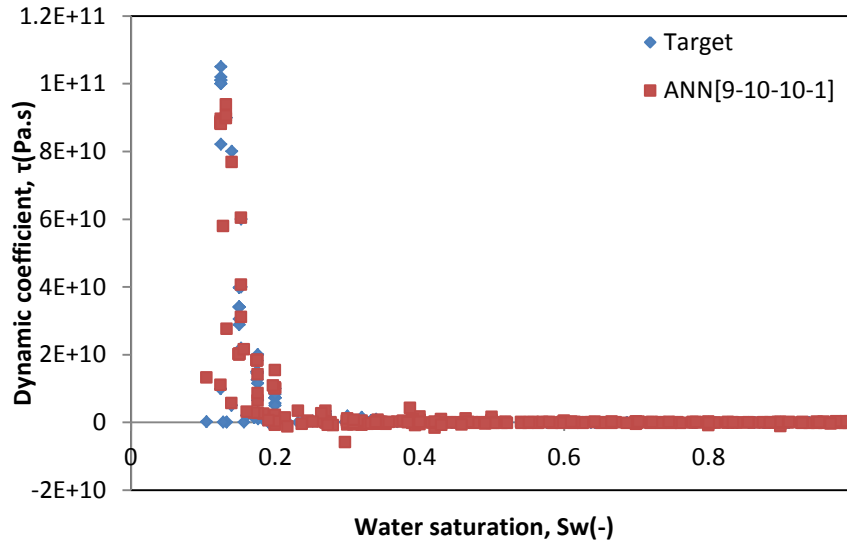


Figure 5.9: The dynamic coefficient values from ANN structures output and target data against water saturation using ANN [9-10-10-1].

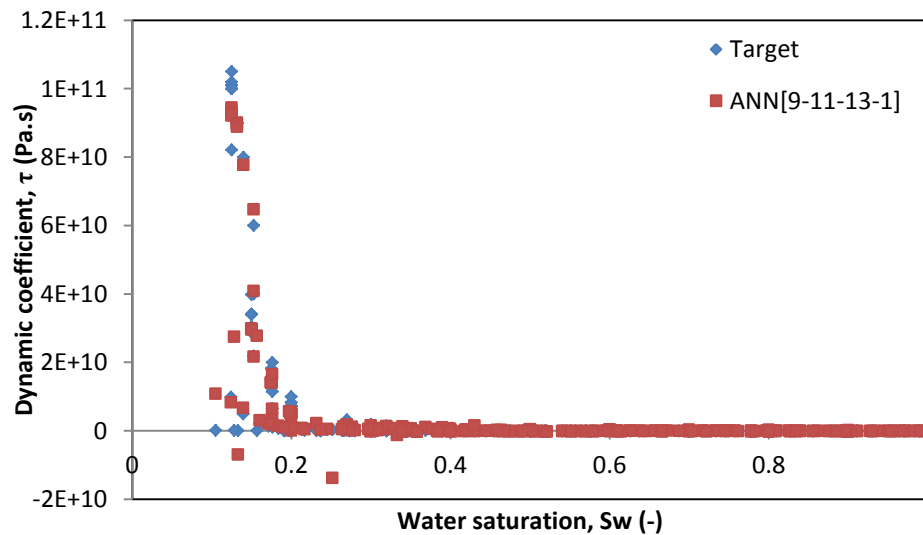


Figure 5.10: The dynamic coefficient values from ANN structures output and target data against water saturation using ANN [9-11-13-1].

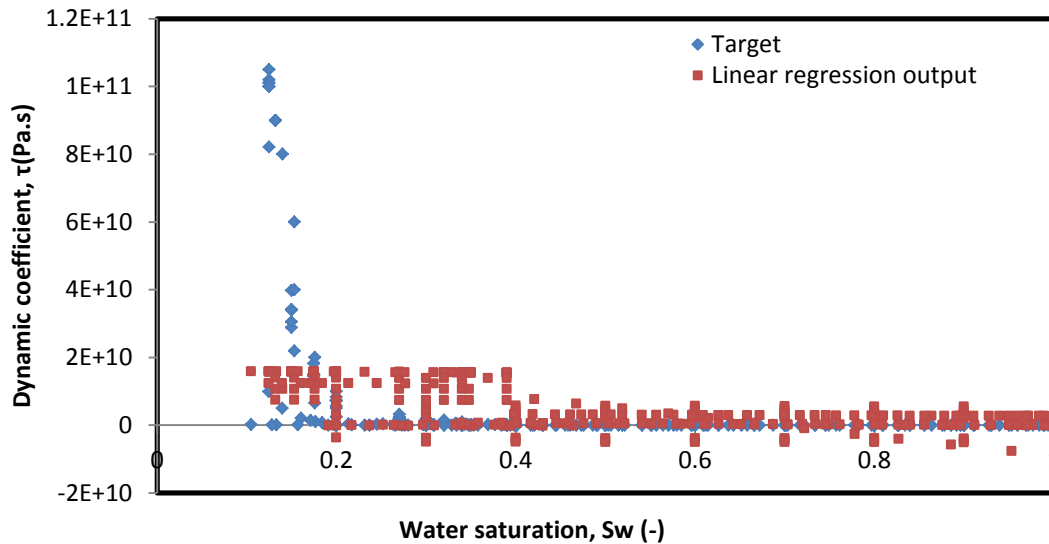


Figure 5.11: The dynamic coefficient against the water saturation values for the entire dataset and the predictions by linear regressions structure.

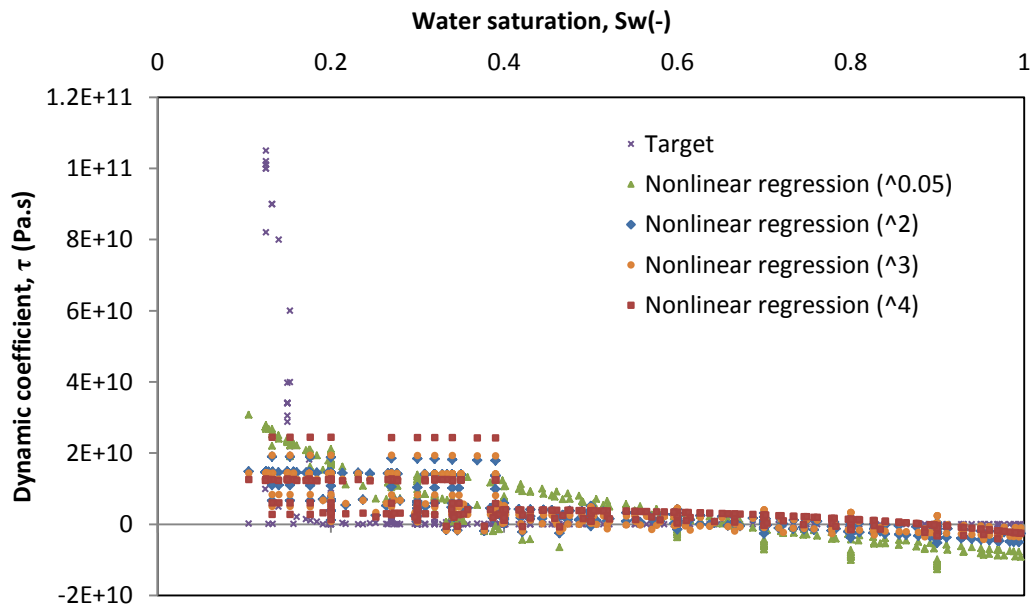


Figure 5.12: The dynamic coefficient against the water saturation values for the entire dataset and the predictions by non-linear regression structures

Furthermore, using the experimental results by Goel and O'Carroll (2011), increasing the domain volume shows an increase in the  $\tau$ -S relationships. This is shown in Figure 5.14. The relationship for 10% increase in the domain size lies above the  $\tau$ -S curve from the original experimental domain size. 20% increase in the domain size also shows a further rise in the  $\tau$ -S relationships. Finally, results from the in-house laboratory experiments for higher viscosity ratio silicone oil-water system (500) were also tested using the ANN [9-13-15-1]. This is shown in Figure 5.15.

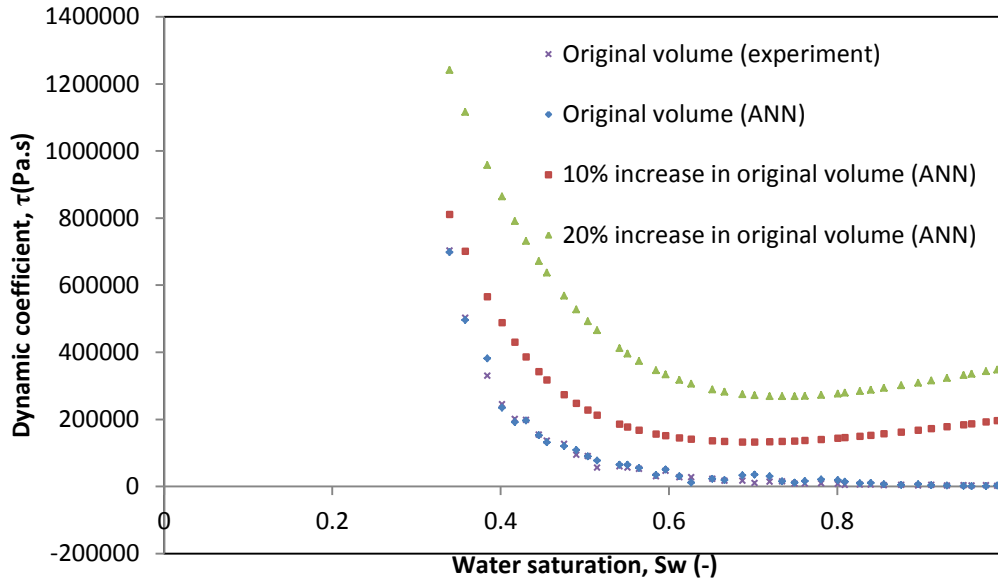


Figure 5.13: Prediction of dynamic coefficient values against water saturation for the original, 10%, and 20% increase in domain size using the ANN [9-13-15-1]. Data for the original domain size were obtained from Das and Mirzaei (2012) where the oil viscosity is 200 cSt.

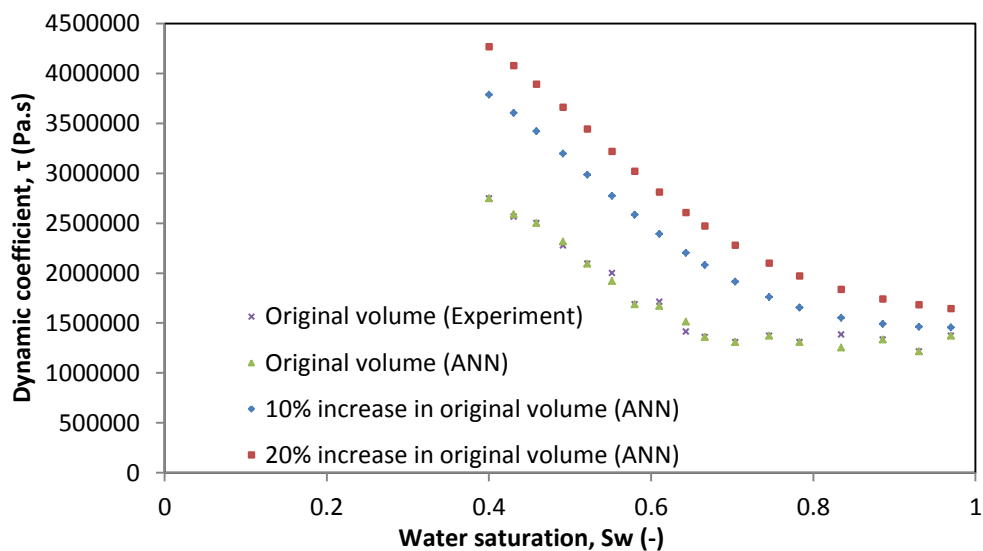


Figure 5.14: Prediction of dynamic coefficient values against water saturation for the original, 10%, and 20% increase in domain size using ANN [9-13-15-1]. Data for original domain size were obtained from Goel and O'Carroll (2011) where the oil viscosity is 5 cSt.

It can be seen from the Figure 5.15 that the  $\tau$ - $S$  curve rises as the domain size increases. But the rise in this case is rather sluggish, especially at higher water saturation. This can be attributed to high viscosity ratio (500) in this case. The original  $\tau$ - $S$  curve of Das and Mirzaei (2013) shown in Figure 5.13 uses a viscosity ratio of 200 and the work of Goel and O'Carroll (2011) uses viscosity ratio of 5. Viscosity ratio refers to the ratio of the viscosity of the oil to that of the water.

As demonstrated, the trend in  $\tau$ -S as the domain size increases indicates the dependency of the dynamic effects in the system properties of the two-phase flow system on the media characteristics. Since increase in  $\tau$  indicates increased deviation from equilibrium (Das et al. 2007), the domain size certainly impacts the dynamic  $P^c$ -S relationships in two-phase flow in the porous media. Judging from equation (5.2), increasing the magnitude of  $\tau$  implies two things. Provided the value of  $P^{c,static}$  remains unaffected by domain scale, then the increase in the value of  $\tau$  is influenced by increasing the value of  $P^{c,dyn}$  and/or decreasing the value of the  $\frac{\partial S}{\partial t}$ . Thus, it may be rightly considered that  $P^{c,dyn}$  increases as the domain scale increases. Similarly, it is plausible to consider that  $\frac{\partial S}{\partial t}$  decreases as the domain scale increases, which may be caused by decreasing pressure gradient as the domain height, or size increases. While the simultaneous impact of the changes can cause the observed effects on  $\tau$ , the ratio of their contribution may differ. Bottero et al. (2011a) observe that the marginal change in pressure difference ( $P^{c,dyn} - P^{c,static}$ ) with upscaled windows of observation is less significant. They attribute the change of  $\tau$  with domain scale to the  $\frac{\partial S}{\partial t}$ , which decreases significantly as the domain size or length increases. Thus,  $\frac{\partial S}{\partial t}$  plays a significant role in the domain scale dependency of  $\tau$ .

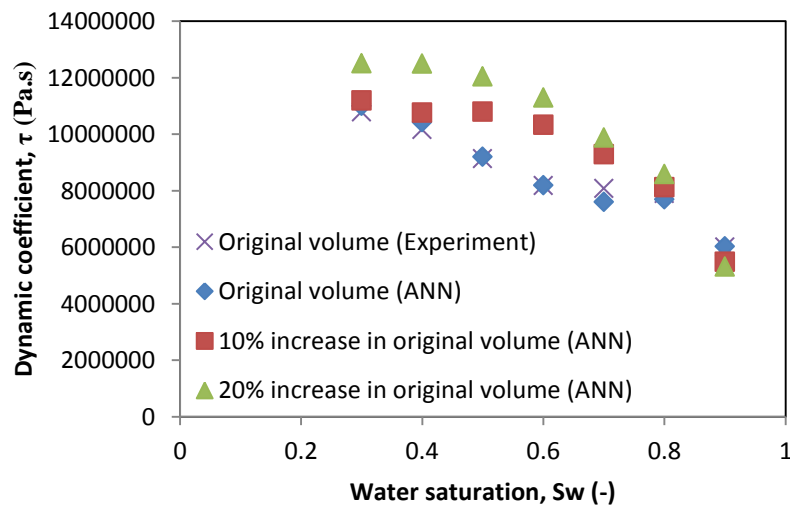


Figure 5.15: Dynamic coefficient values against water saturation for the original, 10% and 20% increase in domain size using ANN [9-13-15-1]. Data for original domain size were obtained from the in-house laboratory experiments (Abidoeye and Das 2014) where the oil viscosity is 500 cSt.

## 5.4 Summary

Application of ANN for the prediction of the scale dependence of the dynamic capillary pressure effects in two-phase flow in porous media has been elaborately demonstrated.

Statistical analyses of the models tested showed that ANN configurations with two-hidden layers outperformed those with single layers. Further comparison of the ANNs with linear and non-linear regression models showed that ANNs have better prediction ability of the two-phase flow system characteristics.

Using the best-performing ANN structure (ANN [9-13-15-1]) in this work, the prediction of the domain size dependency for  $\tau$ -S relationships reveals that the  $\tau$ -S curve rises as the domain size increases in all the viscosity ratios tested. It was pointed out that the rate of change of saturation plays a more significant role in the domain scale dependency of  $\tau$ .

Findings showed the reliability and applicability of the ANN in characterizing and predicting the complex relationships for two-phase flow in porous media. Since the ANN system can be readily accessed and conveniently set up, it offers savings in cost and computational time in comparison to the flow-physics based simulators.

## CHAPTER SIX

# DYNAMIC CAPILLARY PRESSURE EFFECTS IN SUPERCRITICAL CO<sub>2</sub>-WATER FLOW SYSTEM: EXPERIMENTS AND NUMERICAL SIMULATIONS\*

### Overview

*In the context of geological carbon sequestration, flow of supercritical CO<sub>2</sub>-water (scCO<sub>2</sub>-water) can be considered as a two-phase system. Characterising the flow in this case involves the use of capillary pressure–saturation–relative permeability relationships ( $P^c$ - $S$ - $K_r$ ). However, the saturation rate dependencies of this relationship, known as dynamic capillary pressure effect, are not very well understood for scCO<sub>2</sub>-water system, although they are reported for other two-phase flow systems. In this work, a series of controlled experimental measurements and numerical simulations of the dynamic capillary pressure effect and its magnitude ( $\tau$ ) for the scCO<sub>2</sub>-water system in unconsolidated silica sand of different permeability was reported. It is shown that the  $P^c$ - $S$  relationship for scCO<sub>2</sub>-water system undergoes dynamic capillary pressure effect with the dynamic  $P^c$ - $S$  curve lying higher than the  $P^c$ - $S$  curve under the quasi static condition. Drainage of water by scCO<sub>2</sub> shows a unique displacement pattern in which desaturation rate remains largely uniform for a wide range of wetting phase saturation except under the influence of surfactant where the desaturation rate declines linearly. It is also shown that  $\tau$  increases with the decrease in wetting phase saturation, increase in temperature and decrease in sample permeability. Numerical results compare well with the corresponding experimental results for a wide range of water saturation. Differences/errors in the calculation for two-phase system variables as a result of dynamic capillary pressure effects are discussed in relation to geological carbon sequestration system. As a result of the dynamic capillary pressure effect alone, the porous domain water saturation could be more than 28% overestimated. With increased temperature, the error in the estimation of the domain water saturation increases to above 37%. With the decrease in sample permeability, more than 41% overestimation was found.*

### 6.1 Introduction

Geological sequestration of CO<sub>2</sub> is a subject of rigorous activities, investment and research at the moment (Petvipusit et al. 2014; Stephens 2006). The primary objective of these efforts is to mitigate global warming by minimising the amount of anthropogenic CO<sub>2</sub> in the atmosphere. Following the injection of supercritical CO<sub>2</sub> (scCO<sub>2</sub>) into a geological formation, subsequent displacement of the resident brine or groundwater by the invading fluid (scCO<sub>2</sub>)

---

\*Abidoeye, L.K. and Das, D.B. . Dynamic capillary pressure effects in supercritical CO<sub>2</sub>-Water flow system: Experiments and numerical Simulations, AIChE Journal (submitted).

occurs as a two-phase flow system (Abidoye et al. 2014; Das et al. 2014). Similar two-phase flow behaviour is regularly encountered in the studies of oil recovery, immiscible contaminant remediation, and so on. A case in point is the subsurface contamination by non-aqueous phase liquids, i.e., NAPLs (e.g., oils, perchloroethylene (PCE), etc.), which are produced, and may be accidentally spilt, by various chemical process industries (CPIs). These NAPLs may remain in the subsurface for hundreds of years and pose environmental threats worldwide (Das et al. 2007; Chandrappa and Das 2014).

Like the above two-phase flow systems, studying and understanding the flow of scCO<sub>2</sub>-brine/water in the subsurface involve experiments, modelling and simulation of the system and processes (Abidoye et al. 2014; Khudaida and Das 2014; Das et al. 2014). Doing this requires the determination and analysis of capillary pressure ( $P^c$ ) and relative permeability ( $K_r$ ) as functions of saturation of wetting ( $S$ ) or non-wetting ( $S_{nw}$ ) phases.  $P^c$ ,  $S$  and  $K_r$  are parameters of key importance in modelling the two-phase flow processes taking place in the subsurface (Aggelopoulos and Tsakiroglou 2008).

As explained in section 3.1, the  $P^c$ - $S$  relationships of the two-phase systems are traditionally studied under the equilibrium or quasi-static condition (see, e.g., Jennings 1987; Donaldson et al. 1969; Donaldson et al. 1991). However, many factors have been identified to affect the above relationship. This has led to a modification of the  $P^c$ - $S$  function to account for dynamic  $P^c$  effect in two-phase flow systems prior to the attainment of equilibrium or quasi static condition. The modification is already shown in equation (3.2) with the introduction of the parameter named dynamic coefficient,  $\tau$ . As said before, the magnitude of  $\tau$  has been related to how close or far the two-phase system is from equilibrium (Das et al. 2007). Most of the works available on these relationships are related to oil-water systems in application to oil recovery. However, recent development in climate change and the subsequent practice of the geological carbon sequestration has brought scCO<sub>2</sub> and brine/water into focus as an important two-phase system in porous media (Abidoye et al 2014; Chandrappa et al. 2011). Geological storage of supercritical CO<sub>2</sub> generally utilises brine aquifers where it is hoped that the CO<sub>2</sub> will remain trapped for geological time-scales (Elenius and Gasda 2012). However, since the displacement of brine and migration of CO<sub>2</sub> occur in the subsurface, reliable predictions and monitoring of the fate of CO<sub>2</sub> require understanding of the capillary behaviour of supercritical CO<sub>2</sub> and its dependence on water saturation (Tokunaga et al. 2013).

It is known that the  $P^c$  for scCO<sub>2</sub>-water-rock system increases with injection pressure (Alkan et al. 2010). However, the saturation rate dependence of the  $P^c$ -S relationship for scCO<sub>2</sub>-water system has not been well understood. Currently, no experimental investigations have been reported for the  $\tau$ -S behaviour in relation to geological sequestration of CO<sub>2</sub>. Furthermore, no experimental reports are available on the temperature dependency of  $\tau$ -S relationship for scCO<sub>2</sub>-water-porous media system. In reality, prior to the attainment of equilibrium, the unsteady state or dynamic condition resulting from the injection of the scCO<sub>2</sub> into the host media cannot be described by the traditional  $P^c$ -S relation. Thus, it is imperative to investigate the presence of the dynamic effect in the  $P^c$ -S relationship for scCO<sub>2</sub>-water system, using the new relation in equation (3.2). Authors of a number of recent works on dynamic  $P^c$  effect (see, e.g., Juanes 2008; Camps-Roach et al. 2010; Goel and O'Carroll 2011) called for an inclusion of the  $\tau$  in the modelling and simulation of geological sequestration systems. Using numerical simulations, Khudaida and Das (2014) and Das et al. (2014) report the presence of the dynamic  $P^c$  effect in the  $P^c$ -S relationship for the scCO<sub>2</sub>-water system. However, no direct experimental study to confirm the presence of dynamic  $P^c$  effect, and if so an estimation of  $\tau$  for supercritical CO<sub>2</sub>-Water flow system, had been previously reported for the scCO<sub>2</sub>-water system. Thus, it is hoped that this work will fill the gap in knowledge and enhance the study on the geological carbon sequestration.

This work has used experimental techniques to study the dynamic  $P^c$  effect in the scCO<sub>2</sub>-water system in a silica porous domain where the effects of temperature and media permeability are also investigated. Effects of surfactant on the desaturation rate of water by injected CO<sub>2</sub> and, hence, the dynamic  $P^c$ , are investigated. In this work, only drainage of water-saturated porous media by scCO<sub>2</sub> is considered. Furthermore, numerical simulation of the dynamic  $P^c$  effect in scCO<sub>2</sub>-water system is conducted and the results compared with that of the experiments. Finally, this work aims to expatiate the errors in the estimation of porous domain water saturation from using equilibrium  $P^c$ -S relationship as a result of dynamic  $P^c$  effects.

## 6.2 Methodology

### 6.2.1 Fluids and porous Materials

High purity (99%) CO<sub>2</sub> was used in this work to displace the water from the water-saturated porous media domain. The porous media domain used in this work was composed of silica sand categorised as fine-grained (CH30) or coarse-grained (DA 14/25) sand samples. They were obtained from Minerals Marketing Limited (Buxton, UK). Physical and chemical properties of the samples are listed in Table 6.1. Before use, they were pre-treated by

washing in deionised water and dried for at least 24 hours. To ensure uniform packing of the porous domain in every experiment, the sand was poured through a sieve into the experimental cell, which initially contains water. The surfactant used was alkylpolyglucosides obtained from BASF (Ludwigshafen, Germany).

### 6.2.2 Sample holder for porous domains and instruments

The sample holder is a steel cell domain designed to hold pressure transducer ports at its centre. The domain has the dimension of 4 cm height by 10 cm diameter. The domain has ports at its centre, where the phase pressures were measured with the aid of pressure transducers (PTs). The PTs' cables were connected to a datalogger (Compact DAQ chassis, National Instrument, Newbury, UK), which collects the data readings from the PTs for onward processing in the computer. The data from the PTs were processed in the computer using LABVIEW (National Instruments, Newbury, UK). For measuring water phase pressure, the pressure transducers are housed in a fabricated steel holder with sintered metal at the inner face. The sintered metal was overlaid with a hydrophilic nylon membrane with a pore size of  $0.1\mu\text{m}$  (Porvair Filtration Group Ltd, Hampshire, UK). On top of the hydrophilic membrane was placed a 5mm thick Vyon hydrophilic filter (Porvair Filtration Group Ltd, Hampshire, UK) previously soaked in a beaker of water and vacuumed for at least 24 hours. An open steel cap was then corked on top of the holder to hold the filter and the membrane in tight contact with the sintered metal disc and also seal off any unwanted tiny sideways, where fluid might preferentially follow. The open space in the steel cap was filled with cotton wool previously soaked in water in order to avoid pooling of fluid in the small hollow space. Similarly, to measure the  $\text{scCO}_2$  phase pressure,  $1\mu\text{m}$  hydrophobic polytetrafluoroethylene, PTFE membranes (Porvair Filtration Group Ltd., Hampshire, UK) was used together with the thick hydrophobic filter (Porex Technologies, GmbH, Germany) and cotton wool. In this case, the cotton wool and the filter were soaked in silicone oil and vacuumed for at least 24 hrs.

The assembly was done in the same way as for the water phase pressure measurement.  $\text{CO}_2$  is reported to be soluble in silicone oil (Wedlake and Robinson, 1979) and can thus be used to distinguish the phases as water is known to be insoluble in the oil. To ensure quick response of the pressure transducer, the gap between the sintered metal disc and the face of the pressure transducer at the base of the holder was made as small as possible.

*In situ* wetting phase saturation (S) measurement was done with three-pin time domain reflectometry probes (TDR). The pins were locally fabricated to perform under high temperature and pressure applicable to this work. They were insulated in the region of contact with the steel domain to avoid interference with the signal. The TDR probe cable was

plugged into the multiplexer (Campbell Scientific Ltd, Shepshed, UK). This was connected to the time-domain reflectometer-TDR100 (Campbell Scientific Ltd, Shepshed, UK) where the impulses were generated. This was then connected to a CR10X datalogger (Campbell Scientific Ltd, Shepshed, UK) for automatic recording of the data generated. At the start of the experiment, the TDR probes were calibrated to generate the offset and multiplier following the Campbell Scientific Instruction manual for such. Similarly, the PTs were calibrated using a Druck 610 Calibrator (Druck Limited, Leicester, UK). To sync the readings from the LABVIEW with readings from the Loggernet of the CR10X datalogger, same interval of 10s was set for data acquisition in both devices.

The calibration results were fitted with polynomial functions and applied in programming the respective software. Further readings of water saturation were obtained from water outflow collected in a graduated glass cylinder placed on an accurate weighing balance which was connected to the computer and data logged in real time by the weighing balance software (A&D Company Limited, San Jose, USA). For accuracy of outflow volume readings, the dead volume in the steel tube upstream of the sample holder was subtracted from the actual weighing balance reading. Figure 6.1 is a schematic diagram of the experimental set up. Figure 6.1 illustrates the domain size, the configurations of the PTs as well as the TDR probes.

Observations of the responses of the sensors - TDRs and the PTs, to change in system conditions (e.g., change in water saturation, in the case of TDR, and the change in pressure, in the case of PTs) did not reveal any significant lag. The sensors responded well to changing conditions during the calibration as well as the actual experiments. The experimental rig was located in a heating cabinet having electric heaters. The system temperature was regulated using PID temperature controller (West Control Solutions, Brighton, UK).

The sample holder has stainless steel end-pieces at the top and bottom. The top end piece of the sample holder was connected to the supercritical fluid pump via a steel tube. Similarly, the bottom end piece was connected to the outflow bottle on an electronic weighing balance via backpressure regulator (BPR) (see, Figure 6.1). . The  $\text{scCO}_2$  is injected via the upstream tube and the downstream tube serves as the outlet for water. The inner part of the bottom end piece was laid with hydrophilic membrane to minimise outflow of  $\text{scCO}_2$  while hydrophobic membrane was fitted to the top end piece to prevent escape of water. For fine control of outflow, a metering valve (Swagelok, Kings Langley, UK) was located at the outflow line. Following the metering valve is a precision back pressure regulator, BPR

(Equilibar, Fletcher, NC, USA) that keeps the system at the minimum set pressure. The back pressure regulator is a dome loaded type, using PTFE-glass materials as diaphragm and was loaded with nitrogen gas (BOC Industrial Gases, Loughborough, UK) from a cylinder with appropriate single-stage regulator (Gas-Arc Group Ltd, Norfolk, UK).

### 6.2.3 Dynamic and equilibrium experiments

At the start of the experiment, the experimental rig was set up from bottom upward. After placing the sample holder on the bottom end piece (base cover), a small amount of water was poured into the cell to a certain position followed by pouring of sand through a metal sieve of appropriate size to ensure uniform sand packing and minimise air trap. Equal amounts of sand (500g) was used in all cases. Then, the top end piece with the hydrophobic membrane was put in position. At this stage, all valves remained closed except V-4 (see, Figure 6.1) via which deionised water was passed into the sample holder and pressurised from the water tank using the hand pump up to the experimental set pressure (monitored from the pressure gauge located next to the hand pump). At high pressure, all air present in the tubing and in the sand was considered dissolved (Plug and Bruining, 2007). After the supply of water into the sand-filled sample holder, valve, V-4, was then closed leaving the sample holder and water at set pressure. CO<sub>2</sub> used in this work was obtained from BOC industrial gases (Loughborough, UK) at 99.9% purity. The supercritical fluid pump 260D model (Teledyne Isco, Lincoln, USA) was filled with liquid CO<sub>2</sub> from the CO<sub>2</sub> cylinder by opening of the valve, V-1 and setting the pump on the refill mode. After filling the pump volume, the valve, V-1, was closed and the supercritical fluid pump was set at the experimental pressure.

Table 6.1: Fluid and Material Properties

Properties \ Materials	Fine silica sand (CH30)	Coarse silica sand (DA14/25)	Fluids Properties			
			Pressure: 80.5bar Temperature: 40°C		Pressure: 80.5bar Temperature: 50°C	
	-	-	CO <sub>2</sub> <sup>a</sup>	Water <sup>b</sup>	CO <sub>2</sub> <sup>a</sup>	Water <sup>b</sup>
Permeability, K (m <sup>2</sup> )	5.66 x 10 <sup>-11</sup>	3.65 x 10 <sup>-10</sup>	-	-	-	-
Porosity, $\phi$ (-)	0.37	0.38	-	-	-	-
Density (kg/m <sup>3</sup> )	2660	2740	288	996	223	992
Average particle diameter, D <sub>p</sub> (μm)	482.4	946.1	-	-	-	-
Viscosity, $\mu$ (Pa s)	-	-	23 x 10 <sup>-6</sup>	654 x 10 <sup>-6</sup>	21 x 10 <sup>-6</sup>	548 x 10 <sup>-6</sup>
SiO <sub>2</sub> (%) <sup>c</sup>	99 <sup>b</sup>	99 <sup>b</sup>	-	-	-	-
Entry pressure, P <sup>d</sup> (Nm <sup>-1</sup> )	660	431	-	-	-	-
Pore size distribution index, $\lambda$ (-)	3.86	3.50	-	-	-	-
Residual water saturation, S <sub>rw</sub> (-)	0.11	0.09	-	-	-	-

<sup>a</sup> [http://www.peacesoftware.de/einigewerte/CO2\\_e.html](http://www.peacesoftware.de/einigewerte/CO2_e.html) (accessed September, 2014)

<sup>b</sup> [http://www.peacesoftware.de/einigewerte/wasser\\_dampf\\_e.html](http://www.peacesoftware.de/einigewerte/wasser_dampf_e.html) (accessed September, 2014)

<sup>c</sup> [www.sibelco.co.uk](http://www.sibelco.co.uk) (accessed September, 2014)

While the TDR probes give the readings of change in the in-situ water saturation, additional readings were recorded by the weighing balance from the water outflow. There was good agreement between these two readings while the dead volume was subtracted. Some sets of experiments were repeated two or three times to allow for statistical analysis. The equilibrium or quasi-static experiments were conducted by using single-pump gradient program of the supercritical fluid pump 260D model (Teledyne Isco, Lincoln, USA). This program allows stepwise, time-controlled pressurisation of the supercritical fluid. To achieve this, the supercritical fluid pump and the back pressure regulator were set at the same constant pressure, i.e., 80bar, following similar arrangements as described above. Then, the supercritical fluid pump was put in gradient program mode and raised at 0.5 kPa every hour. This is considered as quasi static or equilibrium displacement since the flow proceeded slowly at each step. This continued until there was no appreciable change in the water outflow measured on the balance or when continuous gas breakthrough occurred.

#### 6.2.4 Numerical Simulation

In order to further understand dynamic  $P^c$  effects for  $scCO_2$ /water flow in porous domain, numerical simulation was conducted using the simulator, *Subsurface Transport Over Multiple Phases* (STOMP). The code is developed by the Pacific Northwest National Laboratory, US ([www.pnl.gov](http://www.pnl.gov)). The simulator is capable of simulating different modes of multiphase flow and multi-component transport in porous media. In this work, the  $CO_2$ -Water operational mode (STOMP- $CO_2$ ) is used to simulate the dynamic and quasi-static two-phase flow behaviour. STOMP- $CO_2$  solves the conservation equations (partial differential) for component mass (i.e., water,  $CO_2$ ) on a structured orthogonal grid (White et al. 2012). The partial differential equations were solved numerically. To solve these conservation equations, they are first converted to algebraic form using the integral finite difference approach applied to structured orthogonal grids and Euler- backward time differences (Versteeg and Malalasekera 1995; Patankar 1980).

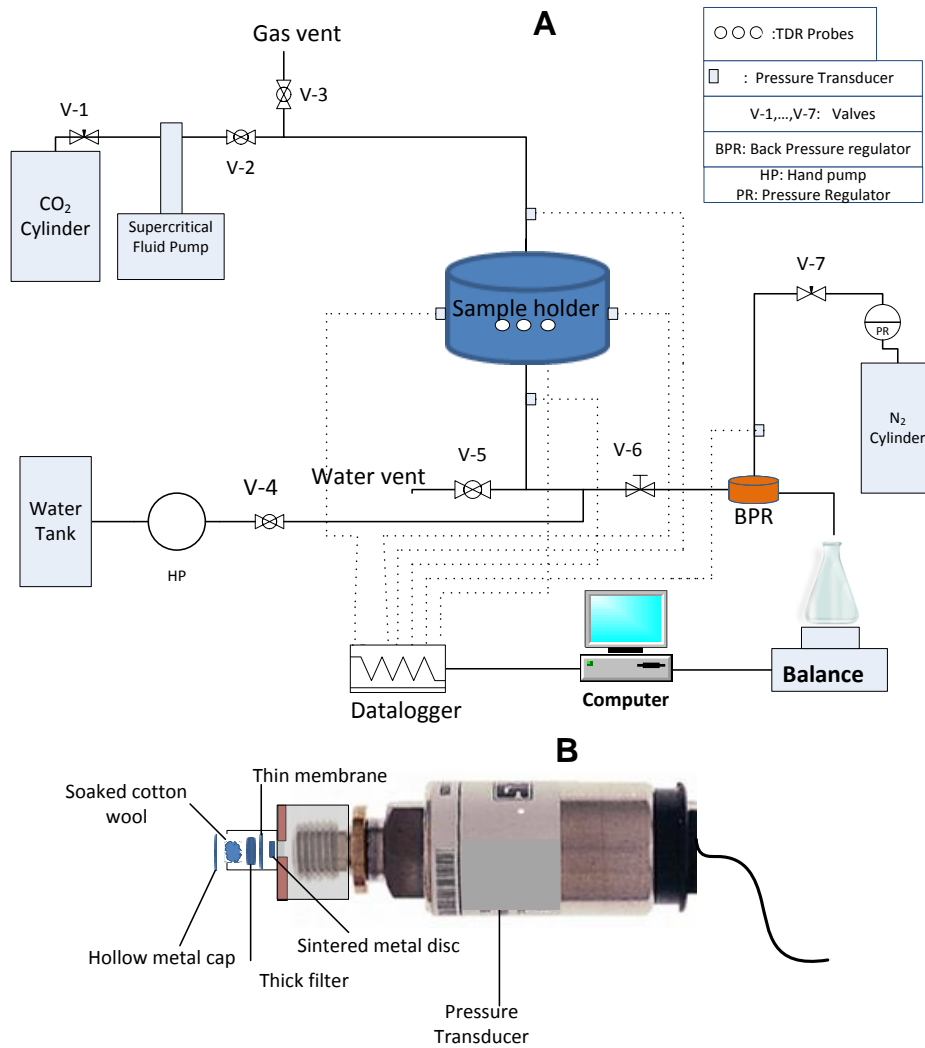


Figure 6.1: (A) High pressure experimental set-up for the scCO<sub>2</sub>-water system (B) Configuration of the phase pressure measurement system.

The resulting algebraic equations are closed through a series of constitutive equations. Newton-Raphson iteration is used to resolve the nonlinearities in the system of conservation equations and constitutive equations (White et al. 2012). Many authors have successfully used STOMP to simulate CO<sub>2</sub>-Water (see, e.g., Das et al. 2014; Khudaida and Das 2014) and Oil-Water (e.g., Das et al. 2007; Das and Mirzaei 2012; Ataie-Ashtiani et al. 2001) flow in porous media.

The results from the simulations also serve as comparison to the experimental results. Two-phase flow in coarse and fine silica sand samples were modelled under quasi-static and dynamic conditions. The boundary conditions, model governing equations, and the nodal configurations of domain geometry for the simulation are expressed in Table 6.2, Table 6.3 Table 6.4, respectively. The porous media properties used for the simulation remained as listed in Table 6.1. The simulations of the dynamic and quasi static displacements follow

similar procedures as described in Das et al. (2014) and Mirzaei and Das (2007). The CO<sub>2</sub> property data table is stored in a data file that was included in the simulation file. It enables interpolation of CO<sub>2</sub> property during the initialization stage of the simulation (White et al. 2012). To obtain the property of the CO<sub>2</sub> at a particular condition, the temperature and pressure of interest are specified in the simulation file. Two different temperatures - 40 and 50°C, but the same pressure (see, Table 6.2) were used for the simulations.

Table 6.2: Boundary conditions for different displacement cases used in the simulation

		<b>Top Boundary</b>		<b>Bottom Boundary</b>	
Displacement case	Time Duration (hr.)	Dirichlet CO <sub>2</sub> Pressure (Bar)	Zero Flux Water	Dirichlet Water Pressure (Bar)	Zero Flux CO <sub>2</sub>
Dynamic	3	80.5		80	
Quasi static	>40	Base pressure=80 (0.005bar/step)		80	

Table 6.3: Equations used for the simulation

Equation no	Description	Equations	Definition of parameters
6.1	Conservation of fluid mass in the two-phase flow system	$\frac{\partial}{\partial t}(\phi \rho_\gamma S_\gamma) + \nabla \cdot (\rho_\gamma \mathbf{q}_\gamma) = 0 \quad (6.1)$ for $\gamma \equiv w, nw$	'w': the wetting phase (water); 'nw': the nonwetting phase (CO <sub>2</sub> ); $\phi$ [-]: porosity; $S$ [-]: average fluid saturation in the porous medium; $\rho$ [ML <sup>-3</sup> ]: the fluid density; and $q$ [LT <sup>-1</sup> ]: the fluid flux
6.2	Multiphase version of Darcy's law for conservation momentum	$\mathbf{q}_i = -K_r K / \mu_i [\nabla P_i + \rho_i g \nabla z] \quad (6.2)$	K [L <sup>2</sup> ]: the intrinsic porous media permeability; $\mu$ [ML <sup>-1</sup> T <sup>-1</sup> ]: the fluid viscosity; $K_r$ [-]: the relative permeability; $P$ [ML <sup>-1</sup> T <sup>-2</sup> ]: the phase pressure; $z$ [L]: upward unit vector; $g$ [LT <sup>-2</sup> ]: acceleration due to gravity
6.3	Brooks-Corey relationships for $P^c$ (Brooks and Corey 1964)	$S_{ew} = \left( \frac{P^c}{P^d} \right)^{-\lambda} \text{ for } P^c \geq P^d \quad (6.3)$	$S_{ew}$ [-]: effective saturation of the wetting phase; $P^d$ [ML <sup>-1</sup> T <sup>-2</sup> ]: entry pressure of the medium; $\lambda$ [-]: pore size distribution index; $S_{rw}$ [-]: irreducible wetting phase saturation
6.4		$S_{ew} = 1 \text{ for } P^c \leq P^d \quad (6.4)$	
6.5		$S_{ew} = \left( \frac{S_w - S_{rw}}{1 - S_{rw}} \right) \text{ for } 0 \leq S_{ew} \leq 1 \quad (6.5)$	
6.6		Brooks-Corey-Burdine relationships for relative permeability (Brooks and Corey 1964; Burdine 1953)	
6.7		$k_{rnw} = (1 - S_{ew})^2 (1 - S_{ew}^{(2+\lambda)/\lambda}) \quad (6.7)$	

Table 6.4: Number of nodes and nodal spacing for the domain used for numerical simulation

Geometry	Number of Nodes and Nodal Spacing		
	N x ΔR (cm)	N x ΔΘ (°)	N x ΔZ (cm)
3D Cylindrical	4 x 1.25	4 x 90	1 x 0.05, 24 x 0.1625, 1 x 0.05

Note: R, Θ and Z are the dimensions related to radii, angle and height of the porous domain. N is the number of nodes or subdivisions in each dimension.

### 6.2.5 Averaging Method

The solution procedure to model fluid flow in porous media starts at the sub-sample scale where the conservation equations for momentum and mass are assumed known. The simulations give the P<sup>c</sup>-S relationships at these sub units. Then, averaging technique is applied to derive the average P<sup>c</sup>-S curves at larger scale that take into account the complexity of the domain together with the sub-unit scale processes.

In this work, the following mathematical averaging technique was used to obtain the domain scale P<sup>c</sup>-S relationship. This is because the measurement takes place only at the centre of the domain.

At nth time step, t<sub>n</sub>, the average P<sup>c</sup> is calculated as:

$$P^c|_{t_n} = \frac{1}{n} \sum_{i=1}^n P_{nwi} - \frac{1}{n} \sum_{i=1}^n P_{wi} \quad (6.8)$$

At each node of the numerical grid, the saturation and volume of the wetting and non-wetting fluids are related as follows,

$$V_{wj} + V_{nwj} = \phi \times V_j \quad (6.9)$$

$$S_{w\gamma} = \frac{V_{\gamma j}}{V_j \times \phi} \quad \gamma \equiv w, nw \quad (6.10)$$

$$S_{wj} + S_{nwj} = 1 \quad (6.11)$$

where, V<sub>wj</sub> and V<sub>nwj</sub> are the volumes of the wetting and non-wetting phases in the 3D cell centred around the arbitrary node j, respectively. V<sub>j</sub> is the volume of node j. S<sub>nwj</sub> is the saturation of the non-wetting phase at node j.

Average water saturation in the domain is calculated using an averaging of saturation of individual node in the whole domain,

$$S_w|_{t_n} = \frac{\sum_{j=1}^m S_{wj} V_j|_{t_n}}{\sum_{j=1}^m V_j} \quad (6.12)$$

Based on the averaged water saturations at different time steps,  $\partial S/\partial t$  is then calculated as the slope at any point, given by the average water saturation and time level on the S-t curve. It is approximated based on a central differencing scheme, as shown in equation (6.13):

$$\left. \frac{\partial S_w}{\partial t} \right|_{t_n} = \frac{S_w|_{t_{n+1}} - S_w|_{t_{n-1}}}{t_{n+1} - t_{n-1}} \quad (6.13)$$

$S_w|_{t_n}$ ,  $S_w|_{t_{n+1}}$ , and  $S_w|_{t_{n-1}}$  are the average wetting phase saturation at the time steps  $t_n$ ,  $t_{n+1}$ , and  $t_{n-1}$ , respectively.

### 6.2.6 Calculation of dynamic coefficient ( $\tau$ )

Similar to the approach employed by Goel and O'Carroll (2011), Camps-Roach et al. (2010), and Sakaki et al. (2010), only one pressure, namely, 50kPa head (80.5bar from CO<sub>2</sub> pump, and 80bar from BPR) was applied in all the dynamic experiments. The dynamic coefficient determination was based on the P<sup>c</sup>-S data obtained under the dynamic and quasi-static conditions. The same pressure head was applied in the numerical simulation of the dynamic flow condition.

The dynamic coefficients were determined using equation (3.2). To use equation (3.2), there is a need for P<sup>c</sup> data for the dynamic and quasi static conditions at the same water saturation (S). From the experimental and simulation data, the phase pressures (i.e., pressures for water and scCO<sub>2</sub>) from the equilibrium and dynamic experiments were fitted with between 5<sup>th</sup> to 10<sup>th</sup> degree polynomials depending on the one with least residuals using MATLAB. The fitting equation was then used to generate capillary pressures at selected saturation within the experimental data saturation range. This procedure provides the corresponding points for the parameters in equation (3.1), i.e., P<sub>nw</sub> and P<sub>w</sub>, at a particular saturation, S, for both the dynamic and equilibrium conditions in order to get the P<sup>c</sup> at that particular saturation. These results were then used in equation (3.2) to obtain P<sup>c,dyn</sup>, and P<sup>c,equ</sup>. Similarly, the desaturation rate data were fitted with similar order of polynomials that give the least residuals and the desaturation data were generated for saturation values corresponding to the ones obtained for the capillary pressures. From equation (3.2), the division of P<sup>c,dyn</sup>-P<sup>c,equ</sup> at a particular saturation by the corresponding desaturation rate gives the dynamic coefficient,  $\tau$ , at that particular saturation.

## 6.3 Results and discussions

The results of various experimental investigations and numerical simulations of the dynamic effects in  $P^c$ -S relationship for the  $scCO_2$ -water system in porous media, with different physical characteristics, are presented and discussed. Note that, this work only considers the drainage of water-saturated porous media by  $scCO_2$ .

### 6.3.1 Experimental results

Dynamic effect refers to the saturation-rate dependency of  $P^c$  for two-phase flow system in porous medium. The presence of the dynamic  $P^c$  effect is demonstrated with the difference in  $P^c$ -S profiles under the dynamic and equilibrium conditions for a particular two-phase flow system in porous medium. This phenomenon has been identified in a number of two-phase systems especially oil-water system in porous media (Mirzaei and Das 2013; Goel and O'Carroll 2011; Bottero et al. 2011a). The current work is concerned with the phenomenon of dynamic  $P^c$  effect in a  $scCO_2$ -water system in porous medium. In this work, the expression "dynamic  $P^c$  effects" is used interchangeably with "dynamic effects".

### 6.3.2 Dynamic effects in $P^c$ -S relationship for supercritical $CO_2$ -water system

Plots in Figure 6.2 show the difference between the dynamic  $P^c$ -S curve and that of the quasi static curve in a silica sand sample with higher permeability (i.e., coarse sand, DA14/25), at different temperatures. The  $P^c$ -S curves help to determine entry pressures under different experimental conditions. The entry pressure signifies the pressure at which the invading phase ( $scCO_2$ ) enters into the medium after the start of the displacement of the resident phase (water). For the  $P^c$ -S curve for  $scCO_2$ -water in coarse silica sand at  $40^\circ C$ , shown in Figure 6.2(A), after the entry of  $CO_2$  into the domain, the quasi static  $P^c$ -S profile appeared constant for most part of the water saturation values until the irreducible saturation ( $S_r$ ) is approached. Close to the irreducible saturation, the  $P^c$ -S curve starts to rise steeply. For the case of dynamic curve, there is a gentle rise in the  $P^c$ -S profile with decrease in the water saturation value, even after the entry of supercritical  $CO_2$  ( $scCO_2$ ) into the domain. However, both categories of  $P^c$ -S curves (i.e., quasi static and dynamic) show steep rise in the values as they approach the irreducible water saturation. The quasi-static  $P^c$ -S curve consistently remains lower in profile compared with the dynamic  $P^c$ -S curve. The results affirm the presence of the dynamic  $P^c$  effect in the  $P^c$ -S relationship for the  $scCO_2$ -water system in porous media. Detailed explanations of dynamic capillary pressure effects for other fluids in

porous media have been previously demonstrated (see e.g., Kalaydjian 1992; Hassanizadeh and Gray 1990; Hassanizadeh and Gray 1993; Das et al. 2007; Das and Mirzaei 2013). In Figure 6.2(A), the  $P^c$ - $S$  curves for the  $scCO_2$ -water system in coarse sand at  $40^\circ C$  are shown with the error bars. The error bars were obtained from the statistics of three different experimental measurements, using standard deviation around the mean values of the  $P^c$ , at a particular saturation. It could be seen that the deviation from the mean value is small for the large part of the water saturation values making the error bars hardly visible. The error bars become conspicuous near the irreducible water saturation. Thus, the reliability of the measurements is high for a wide range of water saturation values, prior to the region of irreducible saturation.

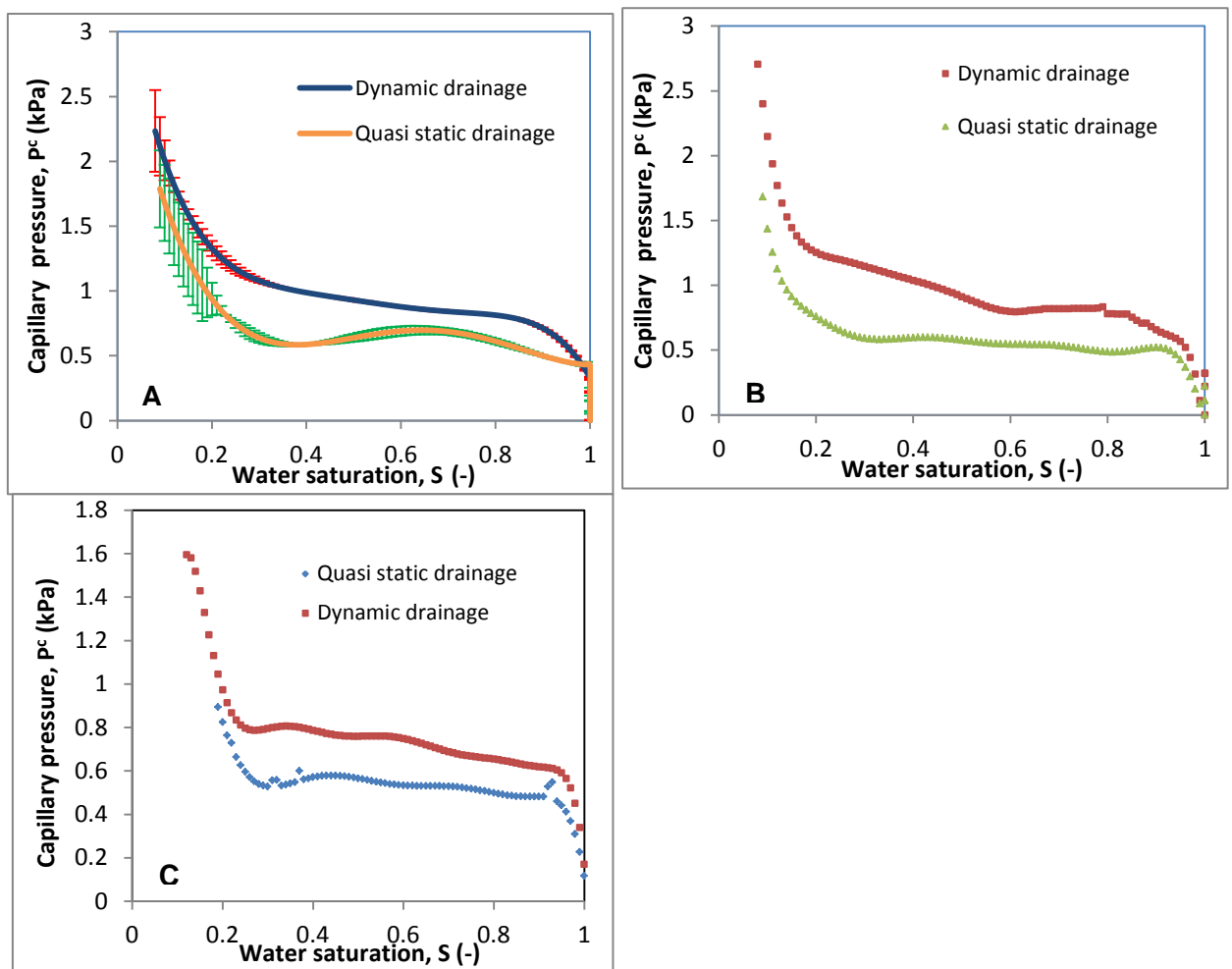


Figure 6.2:  $P^c$ - $S$  relationship under dynamic and quasi static conditions in (A) coarse sand at  $40^\circ C$ , (B) coarse sand at  $50^\circ C$ , (C) coarse sand at  $40^\circ C$  with 0.1% surfactant. All dynamic experiments are conducted at 80.5 bar.

Figure 6.2 further shows some variations in the  $P^c$ - $S$  curves under dynamic and quasi static conditions for coarse sand at a higher temperature ( $50^\circ C$ ) (Figure 6.2(B)), and for coarse sand saturated with 0.1% surfactant solution (Figure 6.2(C)). Figure 6.2(B) shows the  $P^c$ - $S$

curves for both dynamic and quasi static conditions at 50°C in coarse sand samples while Figure 6.2(C) shows the P<sup>c</sup>-S curves in coarse sand samples for scCO<sub>2</sub> displacing 0.1% surfactant (alkylpolyglucosides) solution (BASF, Ludwigshafen, Germany) at 40°C.

### 6.3.3 Displacement pattern in supercritical CO<sub>2</sub> –water system in porous media

Data on the desaturation rate ( $\partial S/\partial t$ ) of the scCO<sub>2</sub>-water system in porous media reflects *in situ* displacement characteristics of the two-phase system under various conditions. For example, the stability of the displacement front in the CO<sub>2</sub>-water system in porous media can determine the extent of the displacement without fingering, which in turn can lead to more storage space (Abidoye et al. 2014; Berg and Ott 2012). On the other hand, unstable displacement can lead to viscous fingering and minimize storage potential of the geological sequestration site.

The desaturation rate of the water phase in the domain as the scCO<sub>2</sub> is injected is shown in Figure 6.3 for the coarse sand samples under the same conditions, as in Figure 6.2. Figure 6.3 shows the desaturation rate in coarse sand at 40°C, 50°C, and in a coarse sand sample saturated with 0.1% surfactant solution at 40°C. In the coarse sand saturated with water at 40°C, Figure 6.3 shows that after a short rise (considering absolute value of  $\partial S/\partial t$ ) in the desaturation rate at the start of the fluid displacement, the  $\partial S/\partial t$  becomes virtually constant for wide range of water saturation (between 0.9 and 0.3) until irreducible saturation is approached where the decline in desaturation rate begins. The peak value of  $\partial S/\partial t$  (absolute value) in coarse sand at 40°C is found to be around  $6.75 \times 10^{-4} \text{ s}^{-1}$ . Similar trend as above is exhibited by  $\partial S/\partial t$ -S relationship in coarse sand at 50°C. The peak of the  $\partial S/\partial t$  value occurs around  $4.8 \times 10^{-4} \text{ s}^{-1}$ , which is lower than in coarse sand at 40°C.

The presence of surfactant in the solution is shown to affect the trend in the  $\partial S/\partial t$ -S profile, as shown in Figure 6.3. There is obvious departure from the usual patterns under the influence of surfactant. After the initial short rise, the  $\partial S/\partial t$  declines at a fairly constant gradient till irreducible saturation value is attained. The presence of surfactant indeed raises the viscosity of the water and increases its resistance to flow. Thus, the viscosity ratio of the two-phase system (scCO<sub>2</sub>-water) is reduced by the addition of surfactant. The contact of scCO<sub>2</sub> with water/surfactant will also lead to foam production (Ma et al. 2013) and, hence, reduce the mobility of the CO<sub>2</sub> phase (Rafati et al. 2012).

The  $\partial S/\partial t$  values reported in this work are comparable to those reported by Goel and O'Carroll (2011). In silicone oil-water drainage experiments, they reported the highest  $\partial S/\partial t$

values of  $9.8 \times 10^{-4}$  and  $2.9 \times 10^{-3} \text{ s}^{-1}$  for silicone oil viscosities of 5cSt and 0.65cSt, respectively. In this work, the  $\partial S/\partial t$  values range from  $4.8 \times 10^{-4} \text{ s}^{-1}$  to  $6.75 \times 10^{-4} \text{ s}^{-1}$  for the coarse sand sample at 50 and 40°C, respectively. The closeness in values of the above results with that of Goel and O'Carroll (2011) can be attributed to the low-viscosity silicone oil used in their experiments. Also, the large portion of the  $\partial S/\partial t$ -S curve that appears constant for wide range of water saturation can be attributed to the low viscosity ratio between scCO<sub>2</sub> and water (i.e., ratio of viscosity of CO<sub>2</sub> to that of water), as well as the high pressure at which the experiments were conducted.

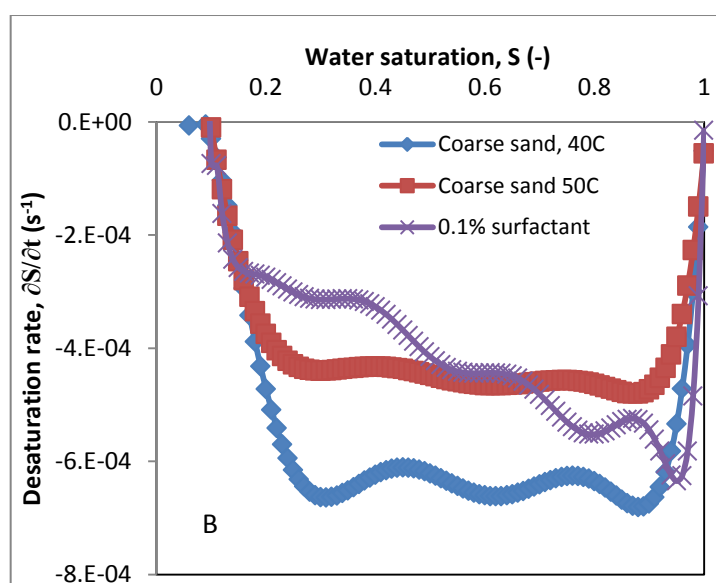


Figure 6.3: Desaturation rate in coarse sand at 40°C and 50°C, and coarse sand at 40°C saturated with 0.1% surfactant. All dynamic experiments conducted at 80.5 bar.

#### 6.3.4 Dynamic coefficient ( $\tau$ ) for supercritical CO<sub>2</sub>-water system in coarse sand sample: Influence of temperature

Dynamic coefficient,  $\tau$ , have been used to quantify the magnitude of dynamic effects in two-phase flow systems (see, e.g., Hassanizadeh and Gray 1990; Hassanizadeh and Gray 1993; Das et al. 2007; Bottero et al. 2011a). According to some authors (see, e.g., Hassanizadeh et al. 2002; Das et al. 2007), the dynamic effect is related to the dependence of  $P^c$ -S on the time derivative of saturation resulting from finite time needed by the fluid to neutralise the effect of the internal and external forces in order to establish flow equilibrium.  $\tau$  establishes the speed at which fluid–fluid interfaces reach equilibrium positions (Das et al. 2007). Thus, a large value of  $\tau$  indicates a large amount of time for the system to reach equilibrium, while its

lower value does otherwise. In this section, the results of the calculated dynamic coefficients in scCO<sub>2</sub>-water system in coarse silica sand sample, using equation (3.2) are presented.

The dynamic coefficient,  $\tau$ , was determined using the data obtained from plots in Figure 6.2 and Figure 6.3. The  $\tau$ -S plots for various conditions in coarse silica sand sample are shown in Figure 6.4, using a semi-log plot. The  $\tau$ -S curve rises as the water saturation decreases. The magnitudes of  $\tau$  under different conditions start with high values at high water saturation. This can be attributed to the low values of  $\partial S/\partial t$  that is recorded from the start of the desaturation. It is clear from equation (3.2) that a low value of  $\partial S/\partial t$  leads to a high value of  $\tau$ . In Figure 6.4, the magnitude of  $\tau$  ranges from  $2.7 \times 10^5$  Pa s at high water saturation to  $7.9 \times 10^6$  Pa s at a saturation close to the irreducible saturation. For low viscosity silicone oil (5cSt) and water system, Goel and O'Carroll (2011) report a  $\tau$  value above  $1 \times 10^6$  Pa s around the start of drainage. In lower viscosity silicone oil (0.65cSt) and water systems, a value of  $\tau$  close to  $1 \times 10^6$  Pa s was reported in the region of high water saturation values. These values of  $\tau$  from Goel and O'Carroll (2011) are one order of magnitude higher than  $2.7 \times 10^5$  Pa s recorded close to the beginning of displacement in this work (Figure 6.4). Reasons for this may be explained to be due to the lower viscosity ratio of the scCO<sub>2</sub>-water system used in this work compared to the silicone oil-water system used by Goel and O'Carroll (2011). Also, the size of the domain used in their work was higher than the one in this work. It is known that the magnitude of  $\tau$  increases with an increase in viscosity ratio and domain scale (Bottero et al. 2011a; Dahle et al. 2005; Goel and O'Carroll 2011; Joekar-Niasar and Hassanizadeh 2011). Similarly, Camps-Roach et al. (2010), use a higher domain scale than the one in this work, and report values up to  $2 \times 10^6$  Pa s at the start of displacement of water by air in air-water system. However, a lower value of  $\tau$  (less than  $5 \times 10^3$  Pa s) is reported around the start of drainage by Das and Mirzaei (2012) for high viscosity silicone oil (200cSt) and water system. In Figure 6.4, the values of  $\tau$ , at low values of water saturation appear in the range of  $1.3 \times 10^6$  to  $8 \times 10^6$  Pa s. This seems to be in agreement with values reported by the above authors. For example, at low water saturation and close to irreducible saturation, Goel and O'Carroll (2011) report values in the range  $1 \times 10^6$  Pa s for an air-water system,  $2 \times 10^6$  and  $3 \times 10^6$  Pa s for 0.65 and 5cSt silicone oil, respectively, in silicone oil-water system drainage experiments. Similarly, Das and Mirzaei (2012) report values close to  $1 \times 10^6$  Pa s around irreducible saturation. In Figure 6.4, the  $\tau$ -S relationship in the same coarse sand samples are shown for conditions at 40°C, 50°C as well as  $\tau$ -S relationship in coarse sand saturated with 0.1% surfactant solution at 40°C. The influence of temperature is visible from the  $\tau$ -S relationship for coarse sand at 50°C, which lies higher than at 40°C. This shows that  $\tau$  increases with temperature. This finding is in

conformity with the conclusion of Hanspal and Das (2012). The influence of surfactant on  $\tau$ -S relationship is not very discernible in the figure as the curve seems to overlies the  $\tau$ -S curve in coarse sand at 40°C.

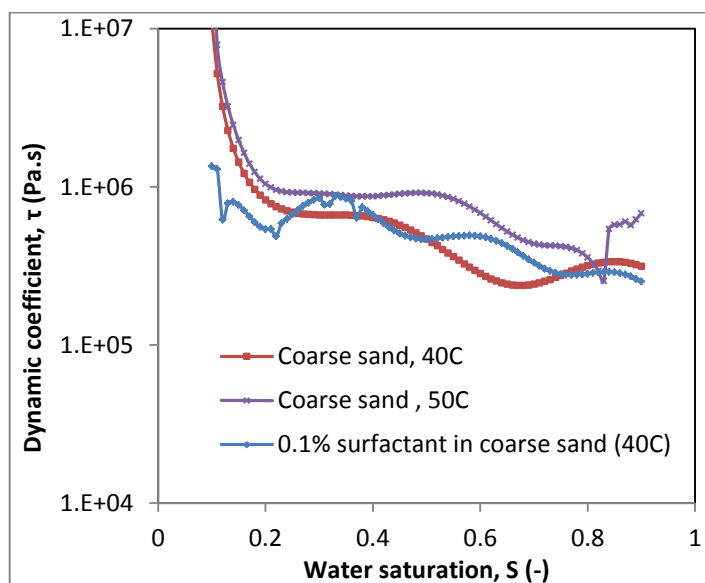


Figure 6.4: Dynamic coefficients in coarse sand at 40°C, coarse sand at 50°C, and coarse sand saturated with 0.1% surfactant at 40°C. All dynamic experiments conducted at 80.5 bar.

### 6.3.5 Effect of porous media permeability on $\tau$

It is well known that the porous domains in actual sequestration aquifers and oil reservoirs are characterised with heterogeneity in porous media property (e.g., permeability, grain size distributions, etc.) (Yang et al. 2013; Das et al. 2006; Aggelopoulos and Tsakiroglou 2008). Two-phase flow experiments on soils with different properties (e.g., particle and pore size distribution, permeabilities, etc.) result in different  $P^c$ - $S$ - $K_r$  relationships, i.e., causing non-uniqueness in these curves (Das et al. 2006). Therefore, this section looks into the impact of porous media property (i.e., permeability) on  $\tau$  for the scCO<sub>2</sub>-water system, using finer silica sand (CH30) than the one used in the previous experiments (DA14/25). Properties of these two porous media are listed in Table 6.1.

The  $P^c$ - $S$  curve for scCO<sub>2</sub>-water system in fine silica sand is shown in Figure 6.5(A). Similar to the behaviour of  $P^c$ - $S$  curves shown in Figure 6.2, the  $P^c$ - $S$  relationships remain higher under the dynamic condition. This is an indication of the dynamic  $P^c$  effect (Das et al. 2014; Khudaida and Das 2014; Abidoye et al. 2014; Hassanizadeh and Gray 1990). Comparison of the behaviour of the dynamic  $P^c$ - $S$  curves for coarse (DA14/25) and fine (CH30) silica sand is given in Figure 6.5(B). Figure 6.5(B) shows that the  $P^c$ - $S$  curve is higher in fine sand than the coarse type. This can be attributed to the increased pore pressure as a result of reduced

pore space in the fine sand domain. A similar finding was reported by Das and Mirzaei (2013). They found the  $P^c$ - $S$  curve higher in fine sand than the coarse type. The entry pressure is noticeably higher in fine sand. This can be attributed to the lower permeability of the fine sand sample as shown in Table 6.1. Low permeability has earlier been identified as one of the factors responsible for higher dynamic effect in porous media (Tian et al. 2012; Das et al. 2007). Figure 6.5(C) compares the desaturation rate of the water in the porous domains made of finer and coarse silica sand. Figure 6.5(C) shows that the desaturation rate (absolute value) is higher in coarse sand than in the fine sand domain.

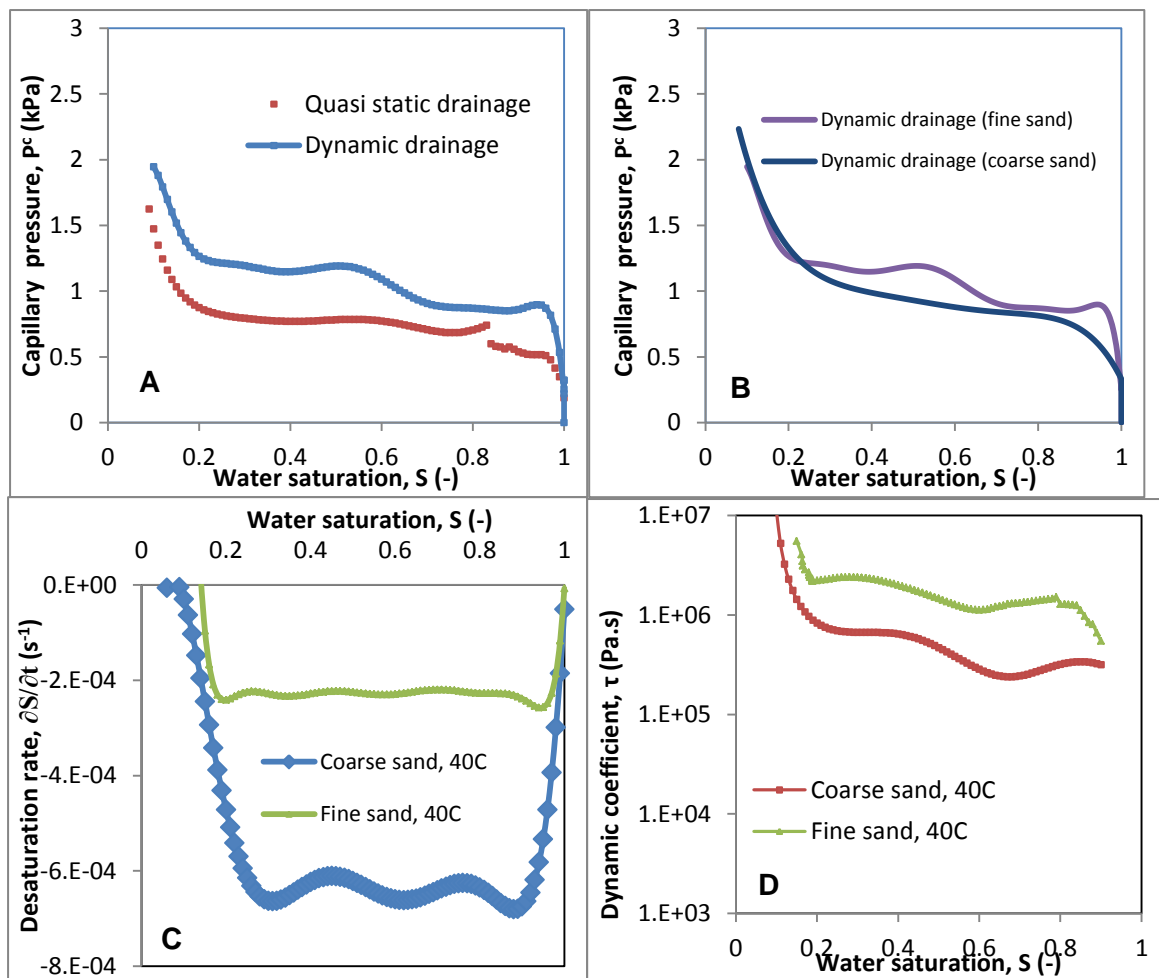


Figure 6.5: (A)  $P^c$ - $S$  relationships for the  $scCO_2$ -water system under dynamic and quasi static condition in fine sand (CH30) at 40°C (B) Comparison of dynamic  $P^c$ - $S$  relationship for  $scCO_2$ -water system in coarse and finer silica sand at 40°C. (C) Comparison of desaturation rate in coarse and fine silica sand at 40°C (D) Comparison of dynamic coefficients in coarse and fine silica sand at 40°C. All dynamic experiments conducted at 80.5 bar.

This can again be attributed to reduced pore space in the fine sand medium, leading to slow movement of fluids. Furthermore, the increase in surface area as a result of the finer grains

in the fine sand domain might also contribute to the slowing down of the displacement process.

The curve follows similar pattern as in the coarse sand sample, with short rise in desaturation rate followed by almost uniform desaturation rate until a saturation value of around 0.3. In the fine sand sample, the average peak in  $\partial S/\partial t$  value (absolute) is  $2.6 \times 10^{-4} \text{ (s}^{-1}\text{)}$  while the corresponding value in the coarse sand sample is above  $6.75 \times 10^{-4} \text{ (s}^{-1}\text{)}$ . This shows that displacement of water in the coarse sand sample is faster than in the fine sand. Figure 6.5(D) shows the  $\tau$ -S relationship in coarse and finer silica sand at 40°C. Figure 6.5(D) clearly indicates that the  $\tau$ -S curve is higher in lower-permeability medium, i.e., higher in fine sand. Thus, going by the interpretation of  $\tau$ , as explained by Das et al. (2007), it takes longer in fine sand medium to reach the equilibrium than in the coarse sand domain.

### 6.3.6 Numerical analyses

Numerical simulation was conducted to provide further basis for the results of the experimental investigations discussed, using the simulator STOMP. This will also affirm the reliability of the experimental measurements discussed. Figure 6.6 shows the  $P^c$ -S curves for the different porous media samples at different conditions. Figure 6.6 shows similarities in the  $P^c$ -S curves for the coarse sand samples at 40 and 50°C. For wide range of water saturation, the  $P^c$ -S curves in Figure 6.6 show that the dynamic  $P^c$ -S curves lie higher than the  $P^c$ -S curves under equilibrium conditions.

The curves in Figure 6.7 compare numerical simulation results of the  $\tau$ -S relationship with the experimental results in coarse sand at 40 and 50°C. In Figure 6.7, it can be appreciated that the numerical  $\tau$ -S relationship compares well with the corresponding experimental results for wide range of water saturation. Departure of the numerical results from the experimental values only become noticeable at low water saturation. Comparison of numerical results of  $\tau$ -S relationship in coarse sand at 40 and 50°C is shown in Figure 6.7(C). Figure 6.7(C) shows that the  $\tau$ -S curve at 50°C lies slightly above the curve a 40°C. This corroborates the experimental findings which show that the magnitude of  $\tau$  increases with temperature.

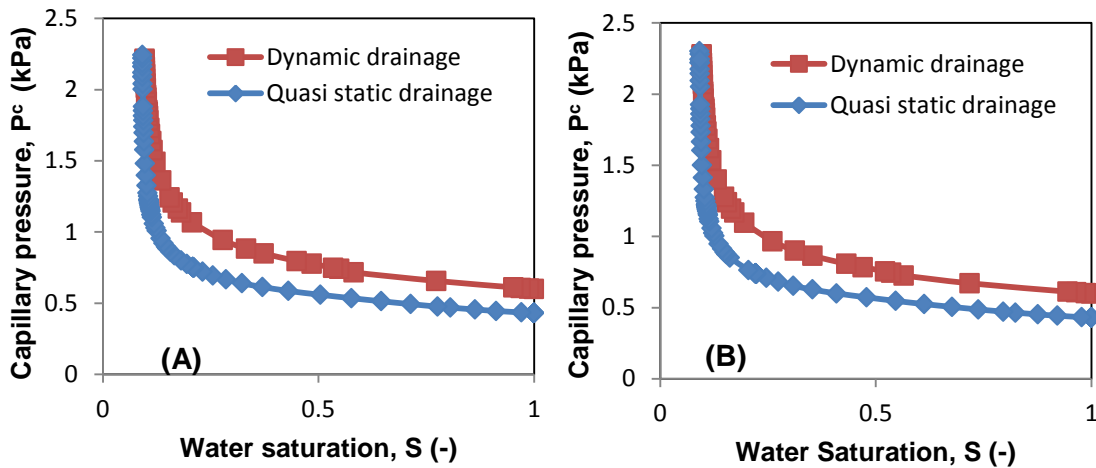


Figure 6.6:  $P^c$ - $S$  curves from the numerical simulations of the dynamic and quasi static displacements of water by  $scCO_2$  in the coarse sand medium (A) at  $40^\circ C$  (B) at  $50^\circ C$ .

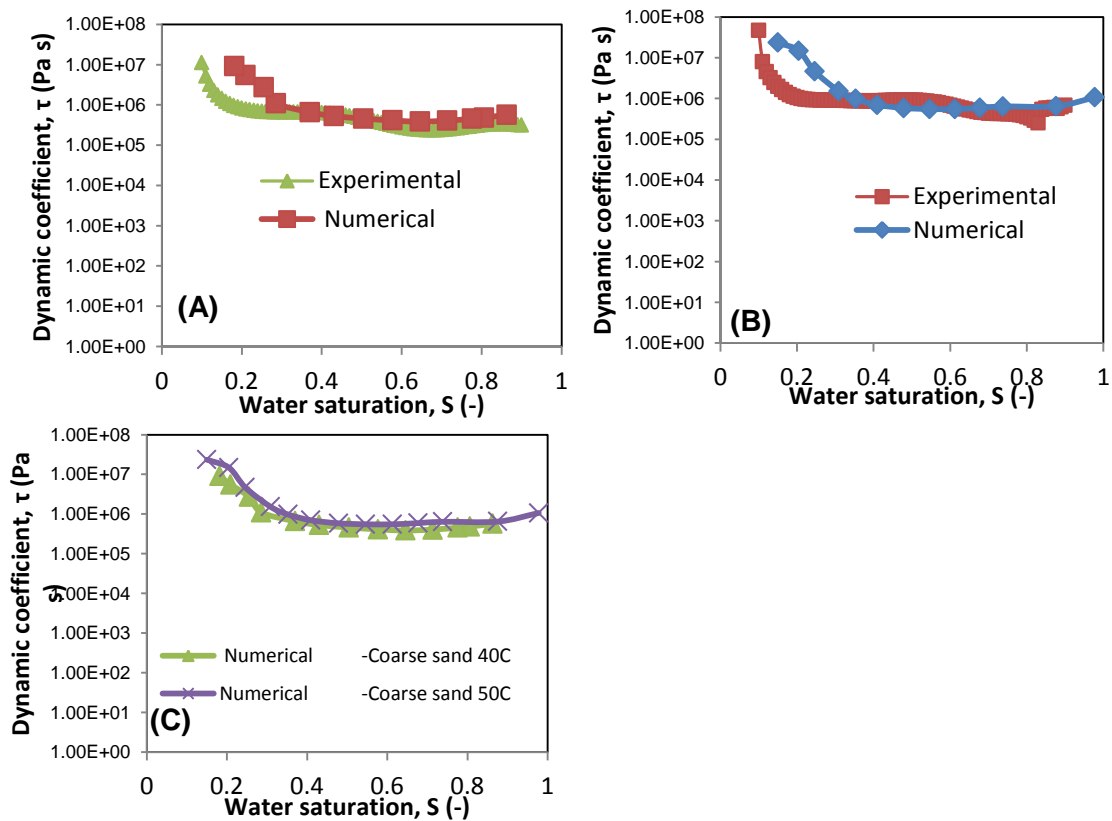


Figure 6.7: Numerically and experimentally determined  $\tau$ - $S$  relationships in the coarse sand medium at (A)  $40^\circ C$  (B)  $50^\circ C$  (C) comparison of  $\tau$ - $S$  at 40 and  $50^\circ C$ . Dynamic experiments and simulations are conducted at 80.5bar.

Numerical simulation of the behaviour of the  $\tau$ - $S$  relationship with porous media of different permeability from the simulation was conducted using properties of the fine sand (CH30) (see, Table 6.1). Figure 6.8 shows the results of the numerical simulations, using these characteristics. Figure 6.8(A) shows the  $P^c$ - $S$  curves under dynamic and quasi-static conditions in the fine sand medium. Similar to the  $P^c$ - $S$  curves in coarse sand medium,

Figure 6.8(A) shows that the  $P^c$ -S curve under dynamic condition is higher than under quasi-static condition.

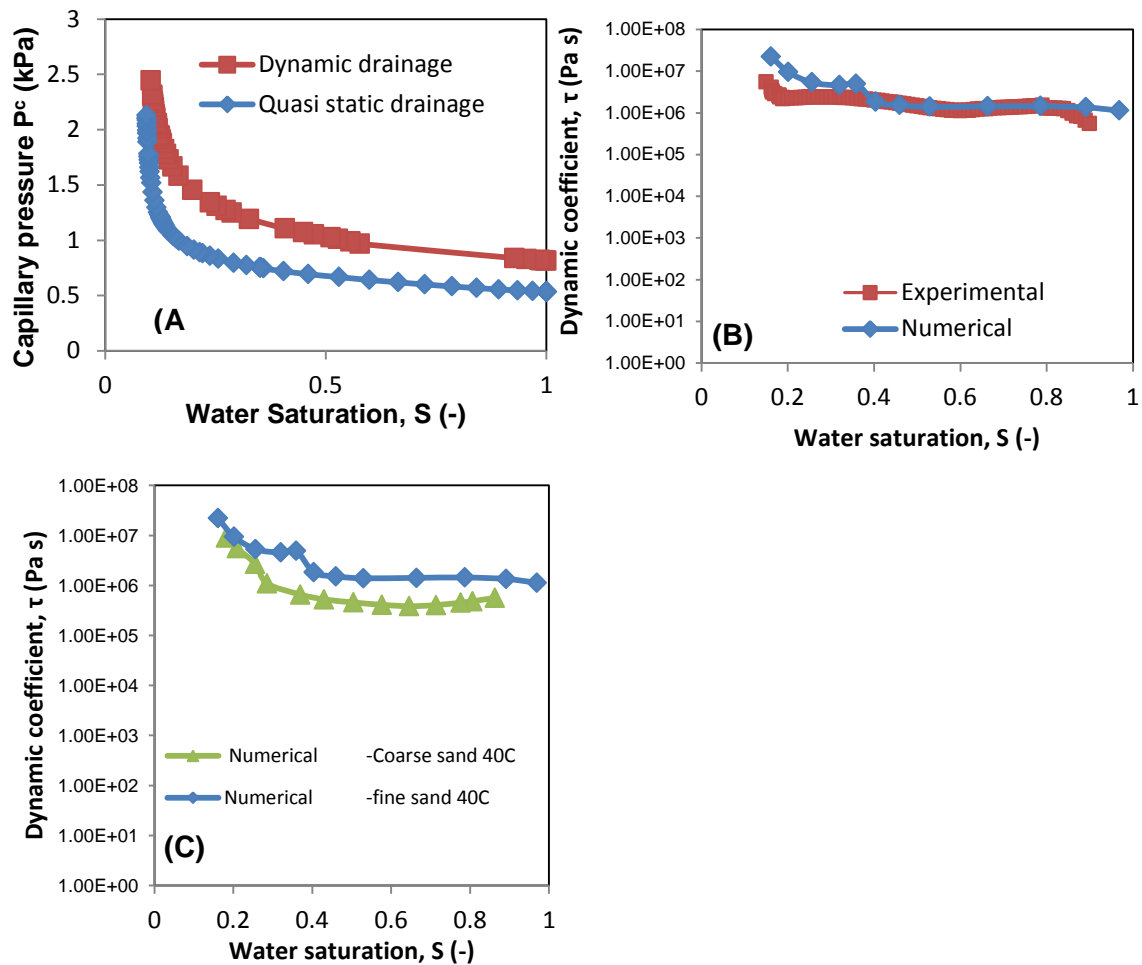


Figure 6.8: (A) Numerically determined  $P^c$ -S relationship in the fine sand medium at  $40^\circ\text{C}$  (B) Numerically and experimentally determined  $\tau$ -S relationship in the fine sand medium at  $40^\circ\text{C}$  (C) Comparison of numerically determined  $\tau$ -S relationship in the fine and coarse sand media at  $40^\circ\text{C}$ . Dynamic experiments and simulations conducted at 80.5 bar.

Figure 6.8(B) compares numerically simulated and the experimentally determined  $\tau$ -S relationship in the fine sand medium. Figure 6.8(B) shows that there is a good match between the numerical simulation and experimental results. This confirms the reliability of the experimental findings shown in Figure 6.5(D). Figure 6.5(C) shows that the  $\tau$ -S relationship is higher in the fine sand than the coarse type. Hence, with numerical simulations and appropriate material characteristics, the  $\tau$ -S relationship can be successfully investigated with both experiments and numerical simulations.

## 6.4 Dynamic $P^c$ effects in $scCO_2$ -water system and errors in the estimate of aquifer storage capacity

Capillary pressure and saturation relationship ( $P^c$ -S) is useful in the estimation of fluid (e.g., oil and water) distribution in the reservoir (Pini et al. 2012; Benson and Cole 2008; Tokunaga et al. 2013). Since the  $P^c$  varies with the change in water saturation, the value of measured  $P^c$  gives an indication of fractional space occupied by the oil/gas and water. In the case of carbon geological sequestration, the measured  $P^c$  offers information about the available space for storage.

Traditionally, the  $P^c$ -S relationship is determined under equilibrium conditions. With the dynamic  $P^c$  effect, error is introduced into the relationship if applied to two-phase system under flow conditions, i.e., non-equilibrium conditions. Considering the equilibrium  $P^c$ -S relationship for  $scCO_2$ -water system in coarse silica sand at 40°C, shown in Figure 6.2(A). Under equilibrium condition, when the  $P^c$  of around 0.69 kPa is measured, the domain is about 70% water-saturated. If the  $scCO_2$ -water is under non-equilibrium conditions, a measure of a similar amount of  $P^c$  indicates the domain is about 90% water-saturated. Therefore, if the equilibrium  $P^c$ -S relationship is applied under flow conditions, the porous domain water saturation is more than 28% overestimated. This is the implication of the dynamic  $P^c$  effect. This difference can affect the judgement of the aquifer storage capacity. The difference in the calculation is aggravated by increased temperature. For example, at 50°C (Figure 6.2(B)), applying the equilibrium  $P^c$ -S relationship for measurement at 70% water saturation to the  $scCO_2$ -water under flow condition introduces an error of around 37% to the domain water saturation. Furthermore, the effect of permeability raises the error in overestimation of the domain water saturation to above 41% at around the same saturation as above.

Thus, by using equation (3.2), the errors can be eliminated with the knowledge of dynamic coefficient,  $\tau$ , which correlates the error in the measured  $P^c$  to desaturation rate data. The relation in equation (3.2) can be used to estimate the expected error under the prevailing desaturation rate value. This can then be applied to quantify the true equilibrium  $P^c$ , which can then be used to estimate the actual saturation value of the porous domain.

The results bring to light the fundamental disparity that can be encountered in the application of  $P^c$ -S relationship in the study, monitoring, and control of  $scCO_2$ -water system in the porous media under the dynamic and quasi-static conditions. The results are important in the context of geological carbon sequestration. The dynamic effect has been widely found in the  $P^c$ -S relationship for oil-water and gas-water system, but little has been reported about the

phenomenon for scCO<sub>2</sub>-water system. Recently, numerical investigations by Khudaida and Das (2014), and Das et al. (2014) show that there is significant dynamic effect in the scCO<sub>2</sub>-water system. Thus, this work serves as good complimentary experimental confirmation of the phenomenon for the scCO<sub>2</sub>-water system.

## 6.5 Summary

Experiments and numerical investigations have been performed to determine the presence of dynamic effects in scCO<sub>2</sub>-water systems. Unconsolidated porous media samples of different properties were used under different conditions applicable to the geological carbon sequestration where CO<sub>2</sub> remains in a supercritical state. Findings in this work show that there is the existence of dynamic effect in the capillary pressure-saturation relationship (P<sup>c</sup>-S) for the scCO<sub>2</sub>-water system. The P<sup>c</sup>-S curve under dynamic condition lies considerably higher than P<sup>c</sup>-S curve for the quasi-static condition. Displacement of water in the water-saturated porous domain by scCO<sub>2</sub> shows a unique displacement pattern in which desaturation rate remains largely uniform for a wide range of wetting phase saturation except under the influence of surfactant where the desaturation rate declines linearly for a wide range of saturation. Thus, mobility reduction induced by the presence of the surfactant has the ability to alter the displacement pattern of the scCO<sub>2</sub>-water system in the porous media.

The magnitude of the dynamic effects was quantified using the dynamic coefficient,  $\tau$  and the results show that  $\tau$  increases with the decrease in wetting phase saturation. The slope of the rise in  $\tau$ -S is less steep for almost all the samples considered except near irreducible water saturation. It is found that  $\tau$ -S curve rises with the temperature of the system. Furthermore,  $\tau$ -S relationship is found to increase with the decreasing porous media permeability. Numerical results of the  $\tau$ -S relationship compare well with the corresponding experimental results for a wide range of water saturation. Departure of the numerical results from the experimental values only becomes noticeable at low water saturation for all the samples under different conditions.

The magnitudes of  $\tau$  found in this work are in the range of  $2 \times 10^5$  and  $6 \times 10^5$  Pa s at high water saturation and  $1.3 \times 10^6$  and  $8 \times 10^6$  Pa s around the irreducible saturation. Finally, this work expatiates the errors in the estimation of porous domain water saturation from using equilibrium P<sup>c</sup>-S relationship, as a result of dynamic P<sup>c</sup> effects. As a result of the dynamic P<sup>c</sup> effect alone, the porous domain water saturation is more than 28% overestimated. With increased temperature, the error in the estimation of the domain water saturation increases to above 37%. With decrease in sample permeability, more than 41% overestimation was found.

## CHAPTER SEVEN

# GEOELECTRICAL CHARACTERIZATION OF CARBONATE AND SILICATE POROUS MEDIA IN THE PRESENCE OF SUPERCRITICAL CO<sub>2</sub>-WATER FLOW\*

### Overview

*The relative permittivity ( $\epsilon$ ) and the electrical conductivity ( $\sigma$ ) of porous media are known to be functions of water saturation ( $S$ ). As such, their measurements can be useful in effective characterisations and monitoring of geological carbon sequestration using geoelectrical measurement techniques. In this work, the effects of pressure, temperature and salt concentration on bulk  $\epsilon$ - $S$  and  $\sigma$ - $S$  relationships were investigated for carbonate (limestone) and silicate porous media (both unconsolidated domains) under dynamic and quasi-static supercritical CO<sub>2</sub> (scCO<sub>2</sub>)-brine/water flow. In the silica sand sample, the bulk  $\epsilon$  ( $\epsilon_b$ ) for scCO<sub>2</sub>-water decreases as the temperature increases. On the contrary, a slight increase was seen in the  $\epsilon_b$  with temperature in the carbonate sample for the system. These trends are more conspicuous at high water saturation. The  $\epsilon_b$ - $S$  curves for the scCO<sub>2</sub>-water flow in the silica sand also show clear dependency on the domain pressure, where  $\epsilon_b$  increases as the domain pressure increases. Furthermore, the bulk  $\sigma$  ( $\sigma_b$ ), at any particular saturation for the scCO<sub>2</sub>-brine system rises as the temperature increases with a more significant increase found around 100% water saturation. Both  $\epsilon_b$  and  $\sigma_b$  values are found to be greater in the limestone than silica sand porous samples for similar porosity values. Based on different injection rates investigated, no significant dynamic effect was found in the  $\epsilon_b$ - $S$  and  $\sigma_b$ - $S$  relationships for the scCO<sub>2</sub>-brine/water system. As such, geoelectrical characteristics can be taken as reliable in the monitoring of two-phase flow system in the porous media. It can be inferred from the results that the geoelectrical techniques are highly dependent on water saturation. However, below 50% water saturation, the relationships appear less-dependent on operating pressure, temperature and brine/water saturation in the porous media.*

### 7.1 Introduction

The issue of global warming and the possibility of geological carbon sequestration have increased the interests on studying supercritical CO<sub>2</sub> (scCO<sub>2</sub>) and brine/water flow in porous medium (Abidoye et al. 2014; Khudaida and Das 2014; Benson and Cole 2008). Logically, a carbon sequestration operation in an aquifer should be safe guarded from CO<sub>2</sub> leakage into the atmosphere and/or CO<sub>2</sub> migration into a potable water aquifer that might lie above a sequestration aquifer (Dethlefsen et al. 2013). Thus, the efficient operation of CO<sub>2</sub>

---

\*Abidoye, L.K. and Das, D.B. Geoelectrical characterization of carbonate and silicate porous media in the presence of supercritical CO<sub>2</sub>-water flow, Geophysical Journal International (submitted).

sequestration activities and effective monitoring are keys to the success/safety of the overall process. Effective monitoring of geological carbon sequestration requires not only prior understanding of any adverse effects of different aspects of the operations but also the *in situ* mechanisms in the subsurface that may affect the sequestration process. In this regard, there are needs to understand the constitutive relationships that govern immiscible flow in porous media, namely, the capillary pressure-saturation and relative permeability relationships ( $P^c$ - $S$ - $K_r$ ) (see, e.g., Aggelopoulos and Tsakiroglou 2008; Doughty 2007; Khudaida and Das 2014) and/or geoelectrical characteristics of the system (see, e.g., Nakatsuka et al. 2010; Abidoye et al. 2014).

Interestingly, the capillary pressure ( $P^c$ ), relative permeability ( $K_r$ ) and electrical properties of a two-phase flow system in porous media are functions of water saturation (Plug et al. 2007). There are two principal electrical properties, namely, (i) the relative permittivity ( $\epsilon$ ), which is a measure of the electrical polarization of the material (Mahmood et al. 2012) that takes place when an electric field is applied, and (ii) the electrical conductivity ( $\sigma$ ), which is a measure of the conduction current resulting from an electric field through the material (Solymar et al. 2014; Keller 1966). These properties can provide valuable information about the macro- and microscopic properties of geological formations. For example, understanding of the electrical parameters have shown good promises in the subsurface characterization activities at sites contaminated with dense non-aqueous phase liquids (DNAPLs) (Power et al. 2013). The applications of geoelectrical techniques in two-phase flow systems and the interpretations of the resultant information depend on the knowledge of the relationships between the effective electrical parameters and the physical properties of the constituent parts of the porous domain (i.e., solid minerals and interstitial fluid) (Ellis et al. 2010). These parameters are mainly utilised based on the advantages of their sensitivities to change in the saturation of the aqueous phase. As such, the geoelectrical techniques have been proposed in research and industries for monitoring the behaviours of two-phase flow systems. These techniques are useful in monitoring strong contrasts in electrical resistivity when the aquifer brine is replaced with compressed gas (Al Hagrey et al. 2013; Dethlefsen et al. 2013). Since preferential pathways may exist in the subsurface for the upward migration of  $\text{CO}_2$  while contaminating near surface aquifers, the use of these techniques should be developed prior to the commencement of the sequestration processes (Lamert et al. 2012). Thus, geoelectric techniques can be successfully applied in the characterization and monitoring of the  $\text{scCO}_2$ -water flow system.

However, one of the challenges in the two-phase flow characterization parameters (i.e.,  $P^c$ - $S$ - $K_r$  functions) include their non-unique behaviour as the functions seem to vary with a number

of factors (Abidoye et al. 2014). Factors found to contribute to the non-uniqueness of the  $P^c$ - $S$ - $K_r$  functions in two-phase flow systems in porous media have also been reported to affect the geoelectrical properties and saturation relationships in such systems. For example, hysteresis is reported for  $P^c$ - $S$  relationships depending on phase distribution, saturation history ascribed to contact angle hysteresis, irreversible changes in pore-scale fluid distribution and the interfacial area (Mirzaei and Das 2013; Plug et al. 2007b). The electrical characteristics of the two-phase flow system also exhibit hysteresis, e.g., the electrical resistivity curve of a two-phase flow system is higher under drainage than imbibition (Verwer et al. 2011; Longeron et al. 1989; Knight and Abad 1995). This invariably translates to similar phenomenon but it has the opposite effect of electrical conductivity, as it is the reciprocal of the electrical resistivity. Nguyen et al. (1999) reported the same effect for complex relative permittivity though it is partly higher for imbibition at saturation ( $S > 0.6$ ) and vice versa at lower saturation values.

In the same vein, water content and temperature of the fluid-fluid-porous media system are some of the factors, which affect the bulk relative permittivity-saturation relationship ( $\epsilon_b$ - $S$ ) as well as the bulk electrical conductivity-saturation relationship ( $\sigma_b$ - $S$ ) in the porous media. Plug et al. (2007b) and Drnevich et al. (2001) showed that the bulk relative permittivity ( $\epsilon_b$ ) of a unconsolidated porous medium increases with the increase in water saturation. This can be attributed to the high value of  $\epsilon$  for water over the sand medium. Thus, as the water saturation decreases,  $\epsilon_b$  decreases. Similarly, Knight and Nur (1987) have found that the dielectric response of a porous domain is dependent on the layer of water formed around the grains which make the media. As such, water-wet media samples should have higher  $\epsilon_b$  under flow conditions. Also, the temperature is reported to influence the value of  $\epsilon_b$  in a number of ways. The  $\epsilon$  for water ( $\epsilon_w$ ) decreases significantly with increase in temperature but that of most solids seem independent of temperature (Drnevich et al. 2001). Accordingly, the  $\epsilon_b$  for fluid-media system will be affected by the influence of temperature, which will be directly related to the amount of water present in the sample. The work of Knight and Nur (1987) can be related to the findings of Wraith and Or (1999) on the influence of bound and free water in different soil types. It has been shown that while  $\epsilon_b$  decreases with temperature, it increases with the release of bound water at high temperature. This is the case with the medium, which has a tendency to retain a high amount of bound water, e.g., clay. Drnevich et al. (2001) show these phenomena with temperature effects using consolidated (cohesive) and unconsolidated (non-cohesive) soils. While relative permittivity increases with temperature in a consolidated soil system, e.g., water and clay, the opposite trend is found in an unconsolidated soil system such as sand saturated with water.

Also, the bulk electrical conductivity,  $\sigma_b$ , was reported to increase with increase in temperature (Wraith and Or 1999). This was explained to be due to increased electrical conductivity of the materials together with elevated mobility of ions, at higher temperatures. The electrical conductivity is particularly important in scCO<sub>2</sub>-water systems as sequestration is mostly performed in aquifers of high salinity (Lagneau et al. 2005). Since CO<sub>2</sub> is a resistive gas (Breen et al. 2012), it will definitely have a reverse effect on the  $\sigma_b$ -S relationship for the scCO<sub>2</sub>-brine system in the porous medium. Breen et al. (2012) showed the application of the electrical resistivity technique in the monitoring of scCO<sub>2</sub> injection, volume and spatial distribution in quartz sand. Also, Plug et al. (2007b) showed a work on the dielectric properties of CO<sub>2</sub>-water systems using a novel method of parallel –plate capacitor, which doubles as the porous medium sample holder. However, the measurements were made at below the supercritical conditions of CO<sub>2</sub>.

The discussions show the strong dependency of the electrical parameters on the wetting phase saturation, media characteristics, temperature and others. Concerning geoelectrical characterization of the scCO<sub>2</sub>-brine/water system, one can readily observe that the existing works are far from being exhaustive. Most of the works reported so far are related to water-sand system primarily under ambient conditions. The limited work on the CO<sub>2</sub>-brine/water system that have been done deal with either single phase flow in porous medium (Breen et al. 2012) or sub-critical condition for CO<sub>2</sub> (Plug et al. 2007b).

Geological sequestration of scCO<sub>2</sub> often takes place in silicate and carbonate aquifers. So, an important question arises, i.e., how do the geoelectrical characteristics of the scCO<sub>2</sub>-brine/water system depend on these media? Also, the desaturation rate has been shown to affect the P<sup>c</sup>-S-K<sub>r</sub> relationships in oil/gas-water flow systems in porous media (see, e.g., Kalaydjian 1992; Hassanizadeh et al. 2002; Das et al. 2007). Similar behaviour has been numerically investigated and reported for the scCO<sub>2</sub>-brine/water system (Khudaida and Das 2014). Therefore, there are needs for the experimental investigation of the impact of the desaturation rate on the  $\epsilon_b$ -S and  $\sigma_b$ -S relationships for the scCO<sub>2</sub>-brine/water system. To address these questions, this work aims to comprehensively investigate the effects of the media characteristics, temperature and pressure as well as salinity on the geoelectrical characteristics of the scCO<sub>2</sub>-water system in the silicate and carbonate unconsolidated porous media using a technique of time domain reflectometry (TDR). Furthermore, the effect of desaturation rate will be systematically investigated in repetitive experiments. The principle and the techniques of the TDR applications are explained in the methodology.

## 7.2 Materials and methods

### 7.2.1 Unconsolidated porous materials

The porous media used in this work were silica sand, referred to as DA 14/25 and limestone, referred to as Trucal 6. DA 14/25 and Trucal 6 were obtained from Minerals Marketing Company (Cheshire, UK) and the Tarmac Buxton Lime and Cement (Buxton, UK), respectively. Physical and chemical properties of the samples are listed in Table 7.1. Table 7.1 shows that the physical properties of the two porous media are very similar. Before use, they were pre-treated by washing in deionised water and dried for at least 24 hours to remove any clay content. To ensure uniform deposition in every experimental run, the sand was poured through a large sieve into the cell, which initially contains water to minimise air trap. The size of the domain utilized in this experiment was 4 cm in height by 10.2 cm in diameter.

### 7.2.2 Instrumentations and sample holder set up

*In situ* bulk relative permittivity and electrical conductivity measurements were made with the help of three-pin time domain reflectometry probes (TDR probes). The pins were locally constructed and held together with high temperature PTFE base holder to be used under high pressure and high temperature conditions. The rods were insulated in the region of contact with the steel cell to avoid interference with the signal. The TDR probes cable was connected to a multiplexer, which was attached to a TDR100 reflectometer (Campbell Scientific Ltd, Shepshed, UK). This was then connected to a CR10X datalogger (Campbell Scientific Ltd, Shepshed, UK). 12V and 50 Hz dual rail power supply (Rapid Electronics Ltd, Essex, UK) was used to supply power to the CR10X datalogger (Campbell Scientific Ltd, Shepshed, UK) which was connected to the computer for automatic logging of data collected from the TDR probes inserted into the porous medium. At the start of the experiment, the TDR probes were calibrated to get the offset and multiplier following the Campbell Scientific Instruction manual. The readings were used in developing the program used in communicating the TDR100 to the datalogger. The TDR100 has a timing resolution of 12.2 picoseconds for 2-way travel and the pulse length of 14 microseconds.

Figure 7.1 is a schematic diagram of the experimental set up. Figure 7.1 illustrates the domain size as well as the TDR probes at the centre of the sample holder. Pressure transducers (PTs) are included at the centre of the domain to measure the *in situ* system pressure for different experiments.

Table 7.1: Material Properties

Sample	CaCO <sub>3</sub> particles (Trucal 6)	SiO <sub>2</sub> Particles (DA14/25)
Permeability, K (m <sup>2</sup> )	4.53 x 10 <sup>-10</sup>	3.65 x 10 <sup>-10</sup>
Porosity, $\phi$ (-)	0.39	0.37
Particle Density, (kg/m <sup>3</sup> )	2690	2740
Average Particle Diameter, D <sub>p</sub> ( $\mu$ m)	1200	946.1
SiO <sub>2</sub> (%)	-	99 <sup>a</sup>
CaCO <sub>3</sub> content (%)	>98 <sup>b</sup>	-

<sup>a</sup> [www.sibelco.co.uk](http://www.sibelco.co.uk) (accessed May 2014)

<sup>b</sup> [www.lafargetarmac.com](http://www.lafargetarmac.com) (accessed May 2014)

Detailed description of the PTs configuration is not included in this work because measurements of the PTs are not reported. The sample holder was situated in a heating cabinet. To maintain predetermined temperature in the system, electric heaters were placed at the corners of the heating cabinet while the system temperature was regulated using a PID temperature controller (West Control Solutions, Brighton, UK). The set temperature was left overnight to ensure equilibration. The sample holder is a 4 cm high stainless steel cell with 10 cm diameter having stainless steel end-pieces at the top and bottom. Narrow steel tubes run upstream and downstream of the cell with an inlet for scCO<sub>2</sub> (at top) and outlet for water (at the bottom). The inner parts of the top and bottom end pieces are overlaid with hydrophobic polytetrafluoroethylene, PTFE (0.1  $\mu$ m) and hydrophilic nylon (1  $\mu$ m), respectively. The membranes were purchased from Porvair Filtration Group Ltd (Hampshire, UK). It was reported that hydrophilic membrane minimises scCO<sub>2</sub> escape from the bottom of the sample holder (Plug and Brunning 2007) while hydrophobic membrane was used to prevent excursion of water out of the top of the sample holder into the scCO<sub>2</sub> pump. A distributor was used above the hydrophobic membrane to ensure even infiltration of the scCO<sub>2</sub>. For fine control of outflow, a metering valve (Swagelok, Kings Langley, UK) was located at the exit of the sample holder. Following the metering valve was the precision back pressure regulator (BPR) (Equilibar, Fletcher, USA) that kept the system and outflow at the set pressure. The back pressure regulator was a dome loaded type using PTFE-glass

diaphragm and was loaded with nitrogen gas from a nitrogen cylinder (BOC gases, Leicester, UK) controlled with a single stage regulator.

## 7.2.3 Experimental procedure

### 7.2.3.1 Equipment set up

All experiments were conducted in a 4cm sample holder cell. At the start of the experiment, the equipment was set up from the bottom upward. After placing the sample holder on the bottom end piece with overlaying of the hydrophilic membrane, a small amount of water was poured into the cell to a certain position followed by pouring of sand through a metal sieve of appropriate size to ensure uniform sand deposition and prevent air trap.

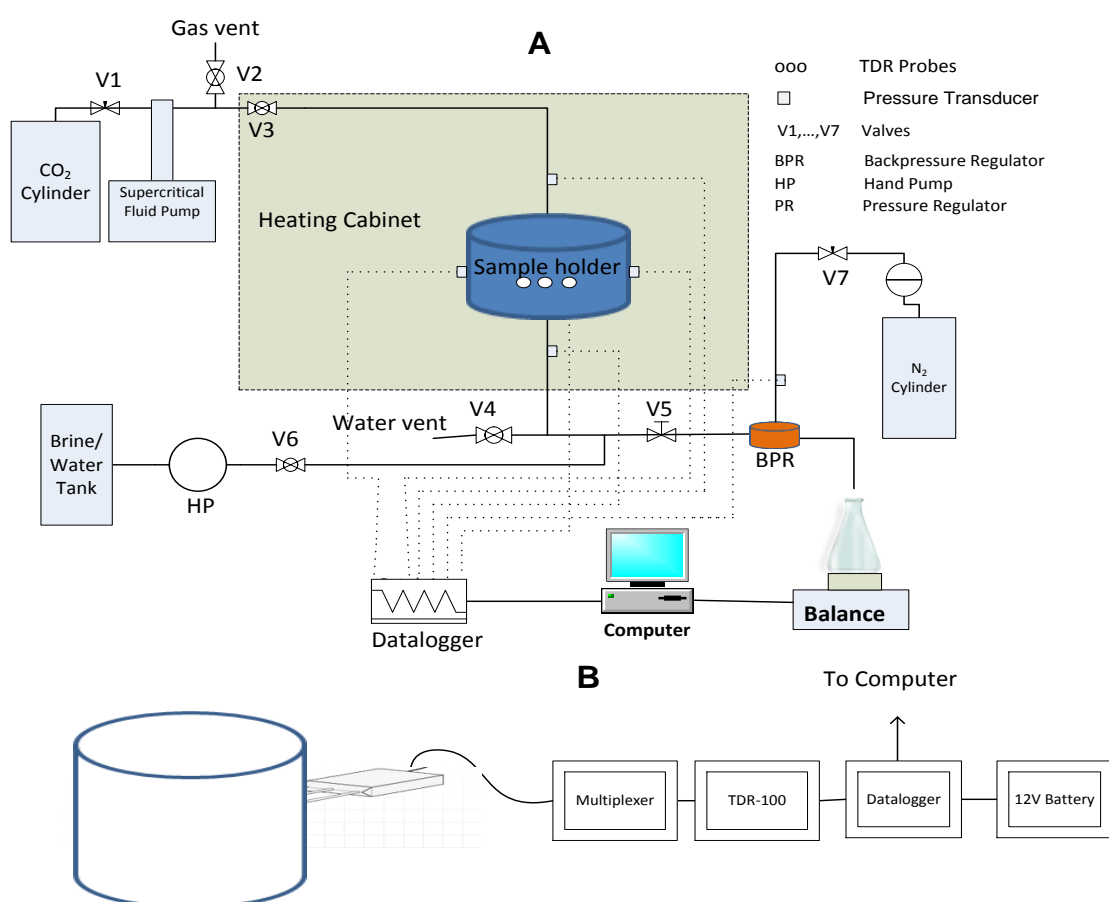


Figure 7.1: (A) High-pressure experimental set-up for the scCO<sub>2</sub>-water system (B) Schematics of TDR measurement system.

Equal amounts of sand (500g) was used in all cases. Then, the top end piece with the hydrophobic membrane was put in position.

After tightening all the joint bolts, deionised water or brine was passed into the sample from tank and pressurised up to the experimental set pressure using a hand pump. At this pressure, all air present in the tubing and sand was considered dissolved (Plug and Bruining, 2007). Water tank valve (V6) was then closed. CO<sub>2</sub> used in this work was obtained from BOC gases (Leicester, UK) at 99.9% purity. The supercritical fluid pump (Teledyne Isco, Lincoln NE) was filled with liquid CO<sub>2</sub> from the CO<sub>2</sub> cylinder by opening of valve 1 and setting the pump on refill mode. Then the cylinder valve 1 was closed and the supercritical fluid pump was set at the experimental pressure. This supplied the liquid CO<sub>2</sub> to the tubing from the exit of the supercritical fluid pump up to valve 3 (Figure 7.1) which serves as the interface between water and CO<sub>2</sub>. When the scCO<sub>2</sub> pump is set at the experimental condition, the heater is switched on and set at the experimental temperature. When the experimental conditions (Temperature and Pressure) reached equilibrium, V3 and V5 are opened and the displacement of brine/water began by scCO<sub>2</sub>. At the end of each experiment, the porous media sample was vacuumed and washed by passage of several volumes of deionised water. Details of the experimental procedure under dynamic and quasi-static conditions are explained in the following section.

#### **7.2.3.2 Dynamic and quasi static drainage experiments**

For the dynamic drainage, the backpressure regulator (BPR) was set at a constant pressure as monitored on the regulator situated on the nitrogen cylinder as well as the pressure transducer installed on the nitrogen cylinder line close to the BPR. The supercritical fluid pump was set at constant flow rate mode at a minimum rate of 5 ml/min for the dynamic drainage. This corresponds to about 2.3 pore volume per hour. For the quasi-static drainage, constant flow rate was set at 0.1 ml/min corresponding to about 0.05 pore volume per hour (PV/h). Plug and Bruining (2007) used range of injection rates between 0.01-0.1 PV/h to demonstrate quasi-static displacement of water by scCO<sub>2</sub> in porous media. Therefore, judging from the injection rate (0.05 PV/h), the displacement in this work can be taken as sufficiently quasi static. The objective of this was to find the effect of desaturation rate on the bulk properties considered (relative permittivity and electrical conductivity). Drainage or displacement of brine/water continued till there was no appreciable change in the amount of brine/water collected in the outflow bottle placed on the accurate weighing balance. The weighing balance (AandD Engineering, San Jose, USA) was also connected to the computer to log the collected data in sync with the data obtained from the CR10X datalogger. Some experiments were repeated two or three times to allow for statistical analysis. Measurements were performed at different temperatures (20, 40 and 50°C) as well as different pressures (20 and 80 bar). Much noise appeared in the data from the bulk relative permittivity measurements and were smoothed using the 'rloess' function in MATLAB. The function

carries out a regression of the reference data by using a combined weighted linear least square and second-degree polynomial model. It assigns lower weight to outliers in the regression.

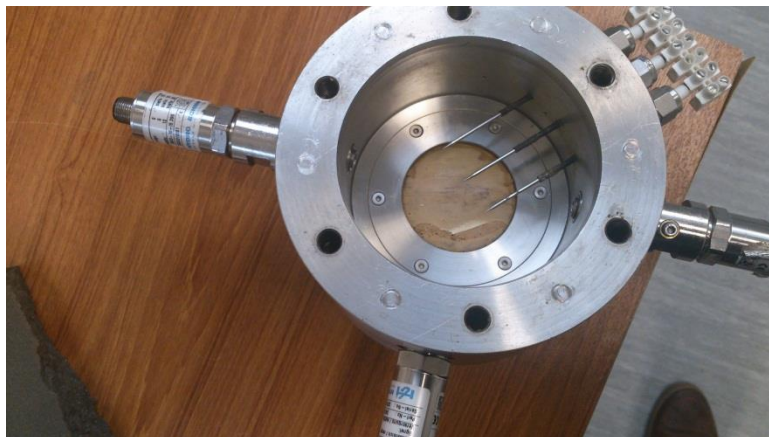


Figure 7.2: A photograph of the sample holder showing the TDR probes with insulation (cell internal diameter: 10cm, sample height: 4cm)

#### 7.2.4 Bulk relative permittivity ( $\epsilon_b$ ) and electric conductivity ( $\sigma_b$ ) measurements

The TDR probes used in this work were calibrated to obtain the probe offset and electrical conductivity constant ( $K_p$ ) as instructed in the manual (Campbell Scientific Ltd, Shepshed, UK) and were then inserted into the sample holder. They served as the waveguide extension on the coaxial cable connected to the TDR100. The TDR100 generates the electrical impulses, which travel through the coaxial cable connected to the TDR probes. Owing to contrast in impedance resulting from materials surrounding the TDR probes, reflection occurs which is sent back to the source (TDR100). TDR100 samples and digitizes the reflection waveforms to infer the impedance value. The impedance value is related to the geometrical configuration of the probe and inversely related to the relative permittivity of the surrounding medium. Complex permittivity ( $\epsilon^*$ ) of a material indicates the extent to which the charge distribution within a material is polarised under the influence of external electric field. Polar molecules such as water became polarised in the presence of the applied electric field owing to the absorbed energy by its molecules. The real (energy storage) and the imaginary (ionic conduction) parts (Robinson et al. 1999) constitute the impedance which can be used in characterising the fluid-fluid-media system. Owing to sharp contrast between the relative permittivity of the porous medium and the surrounding fluids, a change in fluid content causes a change in the bulk relative permittivity, which is seen as a change in probe impedance affecting the shape of the reflected waveform. Information from the differences in

shape of the reflection is used by the TDR measurement system to determine the relative permittivity and the electrical conductivity. Since the presence of a high amount of salt in the medium causes attenuation of the signal at the probe, the experiments in this work did not perform simultaneous measurements of both  $\epsilon_b$  and  $\sigma_b$ . Instead, separate experiments with 1, 5 and 10% reagent grade sodium chloride (Fisher Scientific, Loughborough, UK) were performed to determine  $\sigma_b$  for the scCO<sub>2</sub>-water system.

## 7.3 Results and discussions

### 7.3.1 Relative permittivity

The effective monitoring of scCO<sub>2</sub>-water flow in the subsurface will depend on the adequate characterization of the scCO<sub>2</sub>-brine/water and porous media system. Since different aquifers will likely exist at different conditions, the effects of the prevalent conditions on the geoelectrical characteristics of the scCO<sub>2</sub>-brine/water-porous media system will go a long way to determine reliability of the monitoring process. Here, the results of various factors investigated are discussed in connection with the  $\sigma_b$ -S and  $\epsilon_b$ -S relationships for scCO<sub>2</sub>-brine/water-porous media systems. As reproducibility of the measurements is important,

Figure 7.3 is included in this work, which demonstrates that the results of this work are reproducible. Figure 7.3 shows two separate measurements (A and B) for  $\epsilon_b$ -S relationships under the similar conditions. One can observe that the two runs (A and B) for  $\epsilon_b$ -S curves are essentially similar in values and patterns. Similar reproducibility in results is found for the  $\sigma_b$ -S relationship (not shown). Figure 7.3 further shows that the  $\epsilon_b$ -S relationship is a strong function of water saturation and it decreases as the water saturation reduces.

Effects of desaturation rate on the measured bulk relative permittivities and bulk electrical conductivity during the drainage process were determined. This is related to the 'dynamic effect' widely reported in the  $P^c$ -S relationships for many two-phase flow systems (Kalaydjian 1992; Hassanizadeh et al. 2002; Das and Mirzaei 2013; Goel and O'Carroll 2011; Camps-Roach et al. 2010; Hou et al. 2012). It refers to the dependence of the system properties on the desaturation rate in the medium (Das et al. 2007; Hou et al. 2012). Findings in this work do not show significant dynamic effects in the  $\epsilon_b$ -S and  $\sigma_b$ -S relationships. Figure 7.4 displayed this fact for the  $\epsilon_b$ -S relationships, respectively. In Figure 7.4, the data from quasi static displacement appeared dense because the drainage takes place over 24 hours with data collected every 10 seconds while the drainage under faster injection rate (5 ml/min) takes place in less than 2 hours at the same data collection rate. It could be seen that the data from both drainage conditions overlaid each other for most part of the water saturation

with the exception of much noise in the data from quasi-static drainage. Similar results are found for the  $\sigma_b$ -S relationship, which will be discussed in the following section.

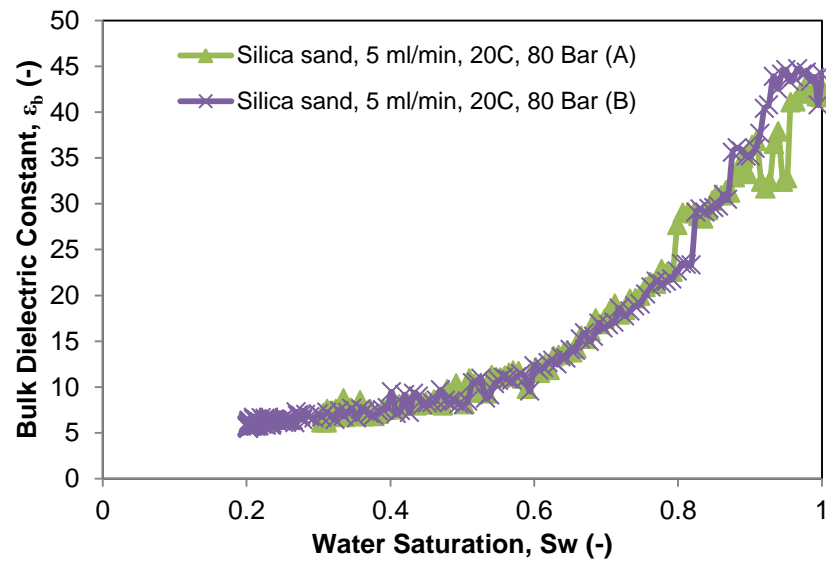


Figure 7.3: Reproducibility plot of  $\epsilon_b$ -S relationship for CO<sub>2</sub>-water-silica sand system.

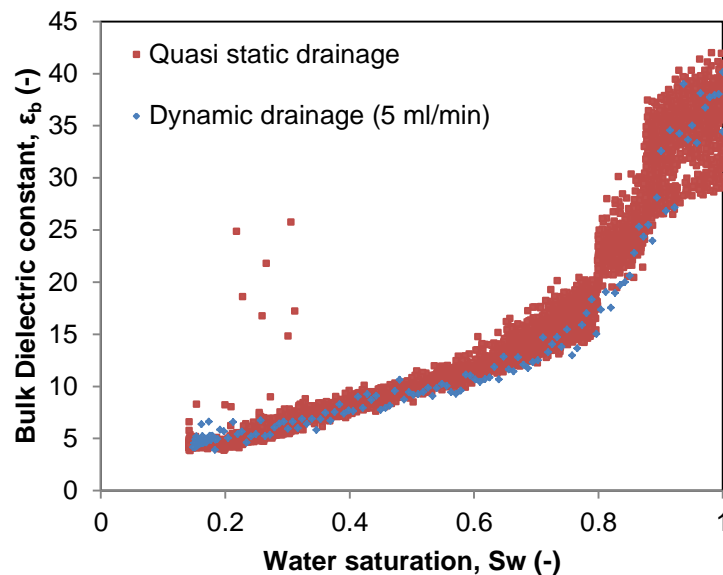


Figure 7.4: Drainage under quasi static and faster injection rate (5 ml/min) in scCO<sub>2</sub>-water-silica sand system at 80 bar and 40°C.

From Figures 7.3 and 7.4, it can be seen that the  $\epsilon_b$ -S relationship decreases as the water saturation reduces. This trend continues until a region of low water saturation where there is minimal change in the relationship as the water saturation reduces further. This was also shown in the work of Plug et al. (2007b).

This behaviour can be explained to be a result of the reducing influence of water. Water has a higher relative permittivity than the silica sand and the scCO<sub>2</sub> (Drnevich et al. 2001) and,

thus seems to determine the overall trend of the  $\epsilon_b$ -S curve as the displacement proceeds. Interestingly, the final value of the relative permittivity corresponds to what would be expected considering the bulk material present. For example, the silica sand has the relative permittivity value in the range 2.5-3.5 while that of the water is approximately 80 at ambient conditions. At the start of the drainage when the influence of water is very high,  $\epsilon$  of water dominates and the bulk relative permittivity starts at a high value. Close to the end of the drainage, with minimal amount of water present in the bulk sand, one expects the property of sand to dominate with little amount of water present together with high saturation of CO<sub>2</sub> which is a resistive gas (Breen et al. 2012). Thus, the bulk relative permittivity is slightly higher than the value of  $\epsilon$  in dry silica sand owing to the traces of the water remaining.

### 7.3.1.1 Effect of pressure

Sequestration of CO<sub>2</sub> in saline aquifers takes place at different depths (Benson and Cole 2008). These correspond to different conditions of pressure and temperature. It is, therefore, important to understand the effect of pressure on the geoelectrical characteristics of the scCO<sub>2</sub>-water-sand system. In order to simulate these conditions in the laboratory, the injection pressure was varied in a way that corresponds to varying injection depths.

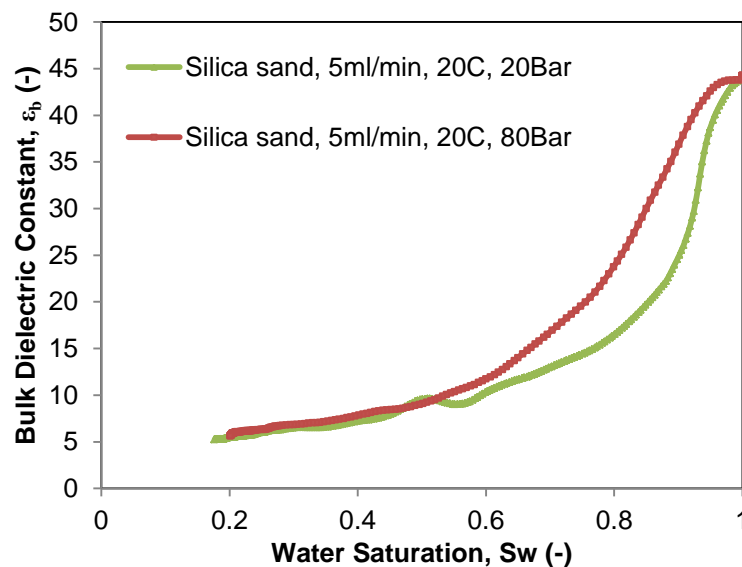


Figure 7.5: Effect of pressure on  $\epsilon_b$ -S relationship in CO<sub>2</sub>-water-silica sand system.

Our investigation of the effect of pressure on the  $\epsilon_b$ -S relationship for scCO<sub>2</sub>-water-silica sand system shows that the  $\epsilon_b$  increases as the pressure increases especially at higher water saturation ( $S \geq 50\%$ ). The finding is displayed in Figure 7.5. The  $\epsilon_b$ -S relationships at 20 and 80 bars have different profiles as water saturation reduces.  $\epsilon_b$  values are higher at 80 bar than 20 bar for every comparable water saturation value.

The difference remains conspicuous until around fifty percent saturation where the difference in the  $\epsilon_b$ -S relationships for the two conditions becomes insignificant. It is believed that this behaviour has to do with the compressibility of the unconsolidated porous media (Sawabini et al. 1974) and the CO<sub>2</sub>. Increasing pressure may increase the amount of soil-bound water as explained in the theory of soil-bound and bulk water by Wraith and Or (1999) and the results of Drnevich et al. 2001).

### 7.3.1.2 Effect of porous media sample chemical properties

Carbon sequestration is being carried out in many geological sites, especially those of carbonates and the silicates (Zhang et al. 2013; Lacinska et al. 2014). This makes it important to determine the effects of media sample characteristics on the  $\epsilon_b$ -S relationship important. The effects of the carbonate and silicate porous media chemical properties are shown in Figure 7.6 for the Trucal6 (limestone) and silica sand sample. It can be seen that the  $\epsilon_b$ -S profile is generally higher in Trucal6 than the silica sand for the entire range of the water saturation. As shown in Table 7.1, the physical properties of the two sand samples are very similar but their chemical constituents are different. These chemical characteristics are expected to play a more prominent role in the  $\epsilon_b$ -S relationship for the scCO<sub>2</sub>-water system.

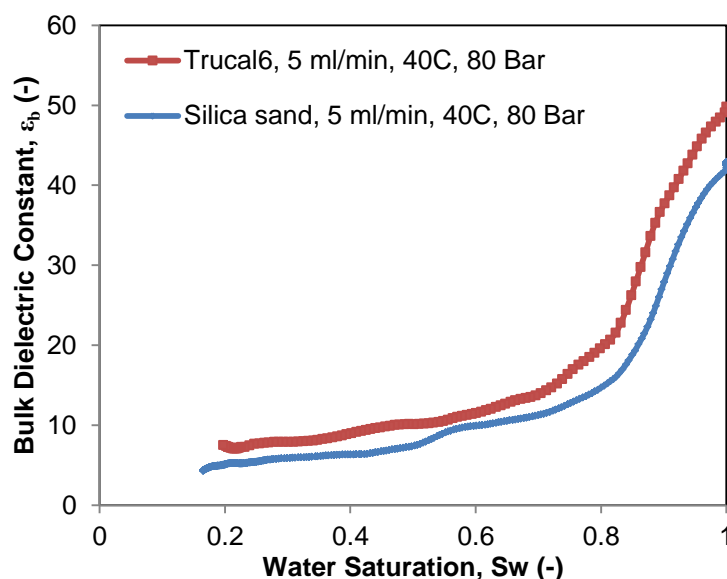


Figure 7.6: Effect of porous media chemical properties on  $\epsilon_b$ -S relationships in scCO<sub>2</sub>-water-silica/limestone sand system.

Thus, the type of chemical properties of the porous media through which scCO<sub>2</sub>-water system passes affects the  $\epsilon_b$ -S relationship. According to Keller (1966), relative permittivity is a measure of the electrical polarization that takes place in a material when an electric field is applied across it. This might imply higher polarisation in the carbonate media with the

presence of the electric field. As such, different profiles of  $\epsilon_b$ -S relationship are expected as the strength of media and fluid polarity increases.

### 7.3.1.3 Effect of temperature

Carbon sequestration at different geological depths correspond to different conditions of temperature and pressure. Here, the impact of temperature on the  $\epsilon_b$ -S relationship is also investigated. It was found that the  $\epsilon_b$ -S profile decreases as the temperature increases in the silica sand system.

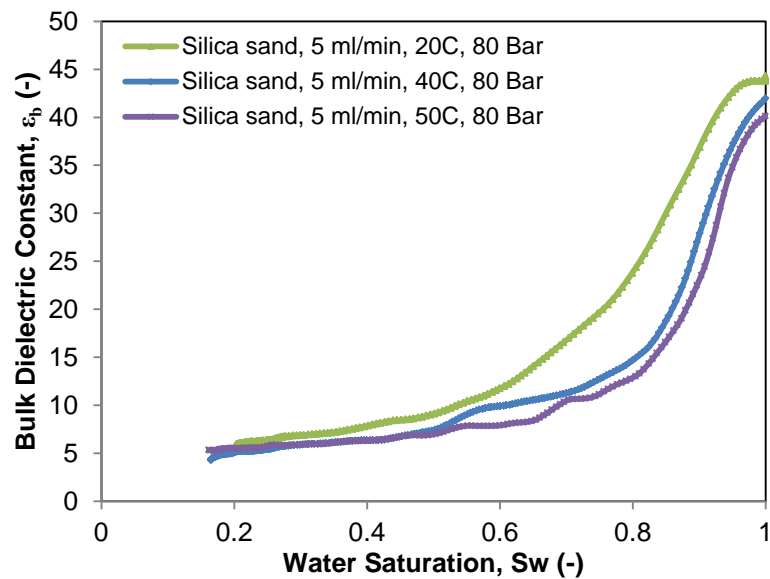


Figure 7.7: Effect of temperature on  $\epsilon_b$ -S relationships in CO<sub>2</sub>-water-silica sand system.

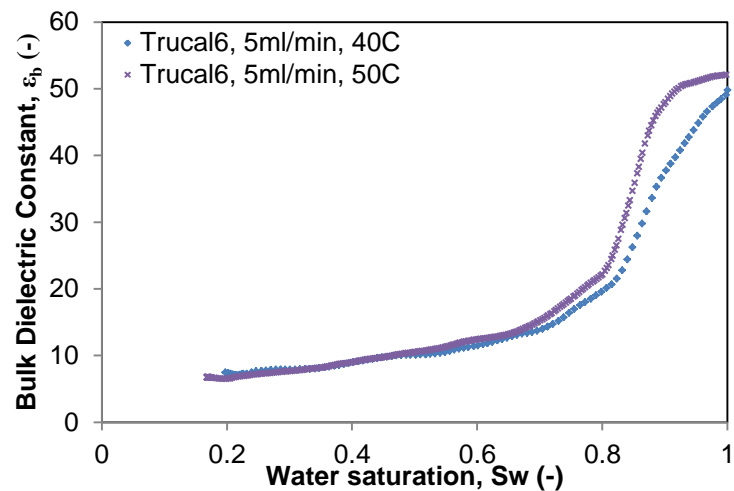


Figure 7.8: Effect of temperature on  $\epsilon_b$ -S relationships at 80 bar in the scCO<sub>2</sub>.limestone (Trucal 6)-water system.

Figure 7.7 shows the plots for the effect of temperature in silica sand. At 20°C, the profile is highest for almost the entire water saturation range.

Though, this is at subcritical state of CO<sub>2</sub> but the similar behaviour can be found in the supercritical state at 40°C and 50°C. The  $\epsilon_b$ -S profile is higher at 40°C than at 50°C. In the same way, the behaviour of  $\epsilon_b$ -S relationships in the limestone exhibits similar patterns. This is shown in Figure 7.8. It can be seen that the  $\epsilon_b$ -S profile at 50°C is lower than at 40°C. Drnevich et al. (2001) reported similar behaviour in unconsolidated soil samples. They further show that the effect of temperature becomes more important at temperatures above 20°C and can be ignored below this temperature. However, carbon sequestration is often carried out at temperatures above 20°C while possible leakage can follow different paths of various temperature and pressure conditions. Thus, the effect of temperature is essential for the geoelectrical monitoring techniques for the scCO<sub>2</sub>-water system. This behaviour can be used to monitor the change in aquifer conditions, especially when scCO<sub>2</sub> migrate in the aquifer to regions of different temperature conditions.

### 7.3.2 Electrical conductivity

Electrical conductivity,  $\sigma$ , is one of the fluid-fluid-media properties whose value is a function of water saturation (Huang et al. 2005; Keller 1966; Plug et al. 2007b). It is important to know the factors influencing the  $\sigma_b$ -S relationships in porous media especially as related to geological carbon sequestration. Characterising the supercritical CO<sub>2</sub>-water system with respect to these factors will enhance the prediction and understanding of the system especially in design of the monitoring procedures. The effect of CO<sub>2</sub> injection rate on the  $\epsilon_b$ -S relationships in silica sand was tested and the result shown in Figure 7.4.

Figure 7.9 is an illustration of  $\sigma_b$ -S relationships under different injection rates in silica sand. Though in Figure 7.9, the relationship was examined under two different fast injection rates (5 and 10 ml/min), it is visible that there exists close similarity in the two  $\sigma_b$ -S profiles. Thus, it can be inferred that the  $\epsilon_b$ -S and  $\sigma_b$ -S relationships are not affected by the desaturation rate in the unconsolidated sand unlike the P<sup>c</sup>-S relationships. As such, dynamic effects are not found in the  $\epsilon_b$ -S and  $\sigma_b$ -S relationships for scCO<sub>2</sub>-brine/water. This is an important result in relation to the effective monitoring of the geological carbon sequestration as CO<sub>2</sub> migration can be reliably monitored using the same characterization function under dynamic displacement conditions, especially at the time close to the start of CO<sub>2</sub> injection prior to the attainment of equilibrium in the aquifer. Challenges of non-uniqueness in the two-phase flow characterization functions, especially P<sup>c</sup>-S-K<sub>r</sub> relationships, are of considerable concerns to

researchers of two-phase flow systems in porous media (see e.g., Das et al. 2006; Joekar-Niasar and Hassanizadeh 2011; Khudaida and Das 2014; Abidoye et al. 2014).

The influence of media sample type on  $\sigma_b$ -S curves is shown in Figure 7.10 for the carbonate and silicate porous media. At all water saturation values, the  $\sigma_b$ -S curve is higher in limestone (Trucal6) than silica sand. This indicates that the conductivity of electric current is higher in the limestone. This can be attributed to the dissolution of the limestone in water thereby increasing the concentration of ions in the system. Carbonate rock is known for high dissolution rate (Assayag et al. 2009; Plan 2005).

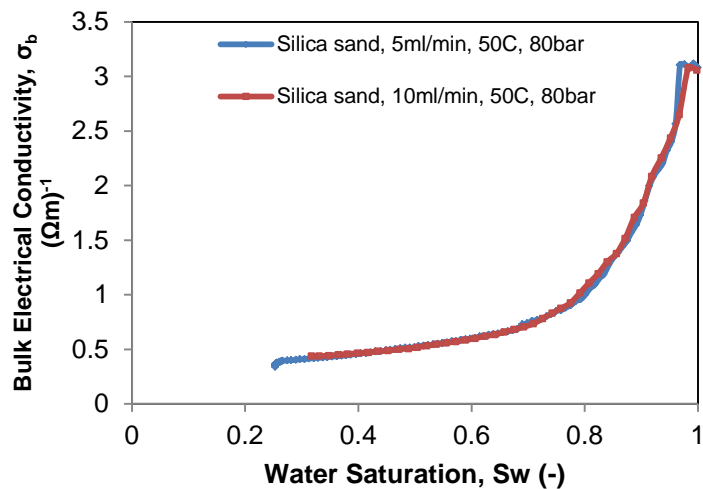


Figure 7.9: Effect of  $\text{CO}_2$  injection rates on  $\sigma_b$ -S relationships in the  $\text{scCO}_2$ -water-silica sand system (5% NaCl).

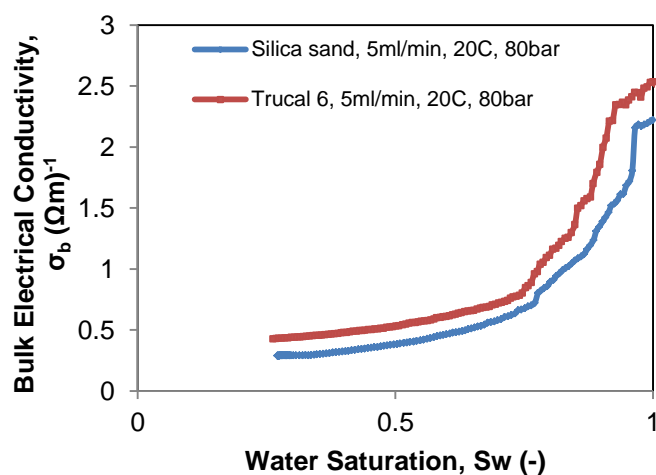


Figure 7.10: Effect of media sample types on  $\sigma_b$ -S relationships in the  $\text{CO}_2$ -water-sand system at 5% NaCl.

Temperature also shows impact on  $\sigma_b$ -S relationship as shown in Figures 7.11 and 7.12 for the CO<sub>2</sub> in silica sand and limestone, respectively. The  $\sigma_b$ -S curve increases as the temperature rises.

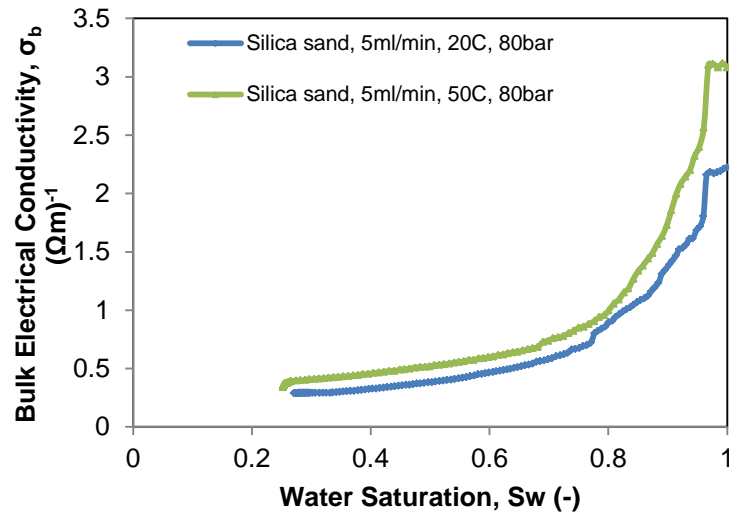


Figure 7.11: Effect of temperature on  $\sigma$ -S relationships in CO<sub>2</sub>-brine system in silica sand at 5% NaCl. This is more prominent at high water saturation. The trend in  $\sigma_b$ -S relationships appeared opposite to the effect of temperature in  $\epsilon_b$ -S relationships in silica sand. For example, the  $\epsilon_b$ -S curve decreases as the temperature increases while the  $\sigma_b$ -S curve increases with temperature in silica sand.

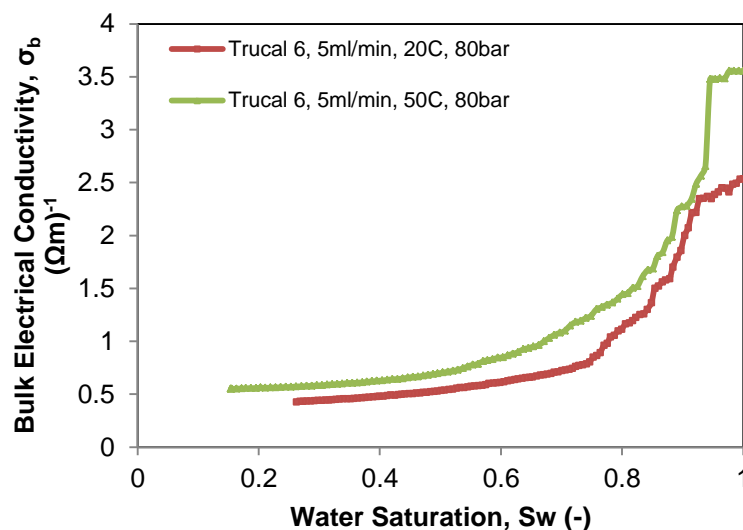


Figure 7.12: Effect of temperature on  $\sigma_b$ -S relationships in limestone (Trucal 6) (5% NaCl).

Also, it is interesting to see that the increase in  $\sigma_b$  -S curve with temperature is highest around 100 % water saturation and becomes less conspicuous as saturation decreases. This

observation is similar to the report of Huang et al. (2005). They found that the electrical conductivity of the minerals in the earth's mantle depends strongly on water content but only weakly on temperature. The trends of  $\epsilon_b$ -S and  $\sigma_b$ -S relationships are consistent in the limestone with respect to temperature. Both relationships show increments as the temperature increases.

### 7.3.3 Salt concentration

Saline aquifers in which carbon sequestrations take place may vary in the degree of salinity. Salinity can vary between 0.5 g/L to 153 g/L in deep saline aquifers (Buttinelli et al. 2011).

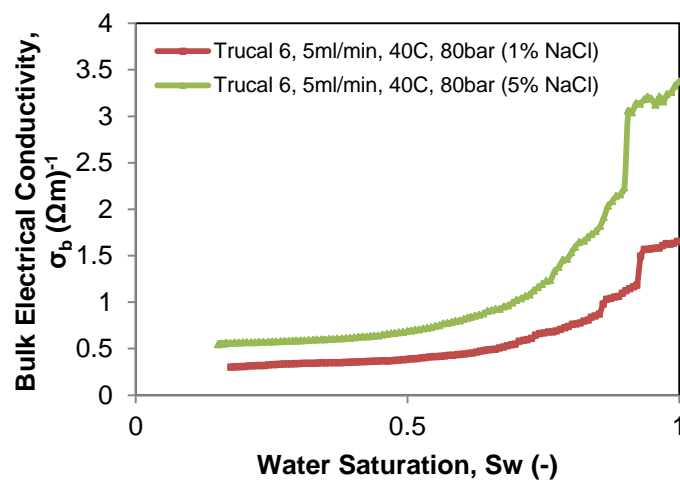


Figure 7.13:  $\sigma_b$ -S relationships at different salt concentrations at 40°C in limestone (Trucal 6).

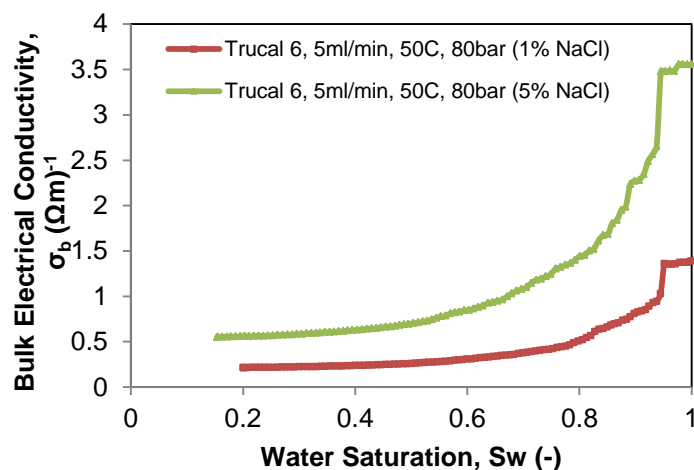


Figure 7.14:  $\sigma_b$ -S relationships at different salt concentrations at 50°C in limestone (Trucal 6). The effect of the variability of salinity is therefore examined on the  $\sigma_b$ -S relationship in this study. The  $\sigma_b$ -S relationships at different salt concentrations and temperatures in limestone (Trucal 6) are shown in Figures 7.13 and 7.14.

As expected,  $\sigma_b$ -S curves increase with the increase in salt concentration and the gap increases with temperature. Since carbon sequestration takes place at geological sites of different salt concentrations, the results show that geoelectrical characteristics of the scCO<sub>2</sub>-water system are site-specific.

### 7.3.4 Mathematical description of results

In this section, the results of the electrical parameters are discussed with the aid of the petrophysical and mathematical relationships. It must be pointed out that the experiments to determine the  $\sigma_b$  and  $\epsilon_b$  were separately conducted. Archie's law (see, equation 7.1) (Archie 1942) was used to predict the  $\sigma_b$  in the silica sand and the limestone in this work. The exponents in Archie's law were determined for each sample (silica sand or limestone). Also, the exponents were determined for the generalised case, by the combination of data from  $\sigma_b$ -S experiments from the silica sand and the limestone, respectively.

$$\sigma_b = \frac{S^n}{\phi^{-m}} \sigma_w \quad (7.1)$$

S is the water saturation,  $\sigma_w$  is the pore water conductivity,  $\phi$  denotes the connected porosity, n and m are the Archie's empirical parameters, which depend on the formation characteristics (Börner et al. 2013). Equation (7.1) was linearized using logarithm rules. Then, the equation was solved for the exponents ('m' and 'n') using MATLAB (Mathworks 2011).

Table 7.2: The electrical conductivity of the water used in the experiments

Salt (NaCl) content (%) (w/w)	Electrical Conductivity ( $\sigma$ ) ( $\Omega\text{m}$ ) <sup>-1</sup>
0	$2 \times 10^{-3}$
1	1.4
5	5.7

Values of the exponents in the equations (7.1), (7.2) and (7.3) appeared to be in agreement with reports from literature. In loose sands and quartz, values in the range of 1.2 to 1.7 are reported for 'm' in the literature (see, Archie 1942; Jackson et al., 1978; Atkins and Smith 1961). Also, values for 'n' in the literature are similar to that listed in the equations (see, Hamamoto et al., 2010; Vinegar and Waxman, 1984).

$$\sigma_b = \frac{S^{1.2}}{\phi^{-1.4}} \sigma_w \quad (7.2)$$

$$\sigma_b = \frac{S^{1.5}}{\phi^{-1.2}} \sigma_w \quad (7.3)$$

For generalised case, the model becomes:

$$\sigma_b = \frac{S^{1.3}}{\phi^{-1.3}} \sigma_w \quad (7.4)$$

The  $R^2$  value of 0.8 was obtained for the determination of the exponents ('n' and 'm'), in the generalised case (equation 7.4).

Furthermore, the results discussed in this work show that the  $\varepsilon_b$  is a function of many parameters including: water saturation (S), system temperature (T), pressure (P) and the initial value of  $\varepsilon_b$  (i). The initial value of  $\varepsilon_b$  is important because it indicates the porous media characteristics, which eventually determines the  $\varepsilon_b$ -S profile. Thus, it can be written that:

$$\varepsilon_b = f(S, T, P, i) \quad (7.5)$$

The nonlinear regression model in the XLSTAT (Microsoft 2014) was used to predict the observed  $\varepsilon_b$  values in this work. The nonlinear regression model of polynomial degree 2 is shown in equation (7.6):

$$\varepsilon_b = 213.86 - 47.17S - 0.074T + 0.048P - 9.18i + 72.71S^2 - 0.002T^2 + 0.11i^2 \quad (7.6)$$

The results of the prediction using equation (7.6) are shown in Figure 7.15 and Figure 7.16. Figure 7.15 shows that the model captures the trend in the observed values of  $\varepsilon_b$  very well. As shown in Figure 7.6, the  $\varepsilon_b$  values are higher in limestone than silica sand under similar conditions. This behaviour was predicted using equation (7.6) and the result is shown in Figure 7.16. Figure 7.16 shows that the  $\varepsilon_b$  values in limestone are higher than corresponding values in silica sand. Thus, the model in equation (7.6) is reliable in the prediction of  $\varepsilon_b$ -S characteristics in different porous media samples.

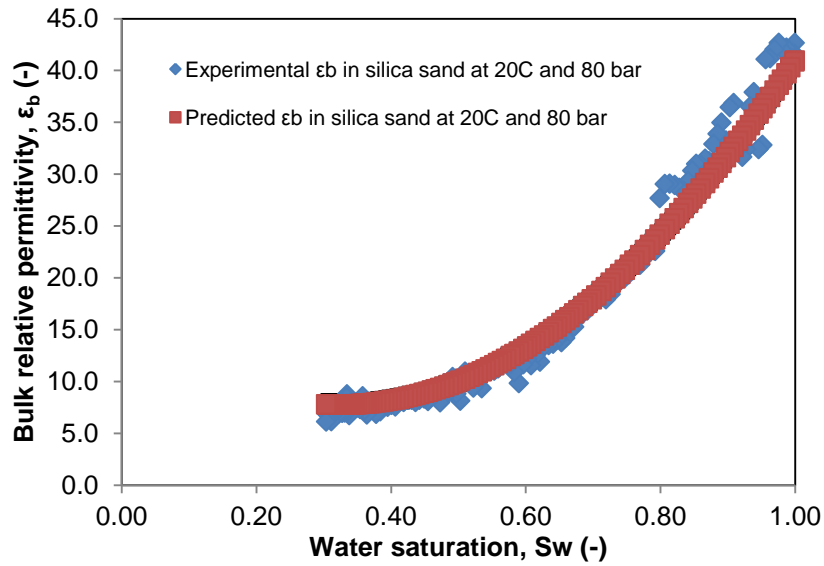


Figure 7.15: Prediction of the  $\epsilon_b$  values using nonlinear regression in water-silica sand system

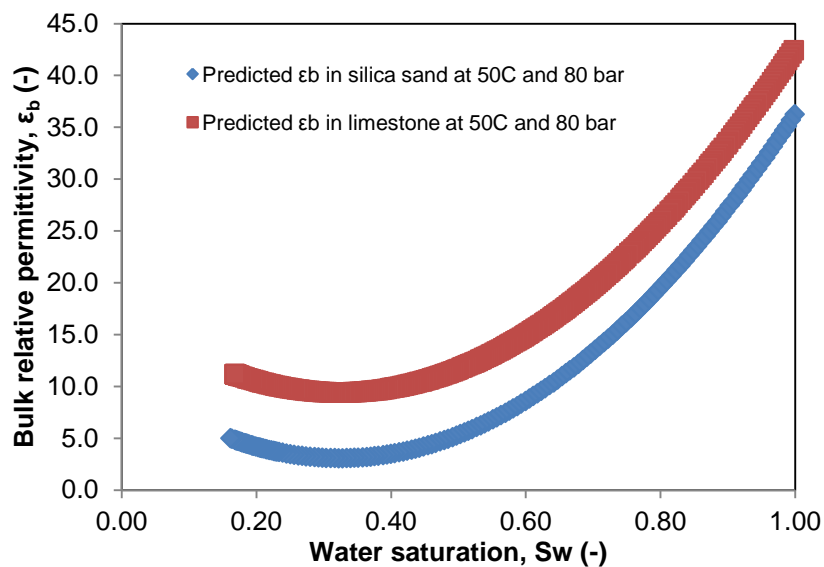


Figure 7.16: Comparisons of model predictions of the  $\epsilon_b$  values in silica sand and limestone.

## 7.4 Summary

The relative permittivity ( $\epsilon$ ) and the electrical conductivity ( $\sigma$ ) are known to be functions of water saturation and the porous media samples. These relationships have been successfully investigated for the supercritical  $\text{CO}_2$ -brine/water system in both the carbonate (limestone) and silica sand samples. The bulk  $\epsilon$  ( $\epsilon_b$ ) and  $\sigma$  ( $\sigma_b$ ) values decrease as the water saturation decreases in the two sand samples. While  $\epsilon_b$  decreases with increase in temperature in silica sand, the trend in the limestone shows a slight increase with temperature, especially at high water saturation. Also, the  $\epsilon_b$ - $S$  relationship is shown to be affected by the pressure in

unconsolidated silica sand, which increases, with the pressure of the domain. Contrarily, the  $\sigma_b$ -S relationship increases as the temperature increases with more significance at higher water saturation in the silica sand sample. The effect of media sample type on both the  $\epsilon_b$ -S and  $\sigma_b$ -S curves showed that the relationships remain higher in the limestone than silica sand under comparable conditions.

Based on the different injection rates investigated, there is no significant dynamic effect in  $\epsilon_b$ -S and  $\sigma_b$ -S relationships for the supercritical CO<sub>2</sub>-water system unlike P<sup>c</sup>-S-K<sub>r</sub> relationships. As such, geoelectrical characteristics are very reliable in the monitoring of two-phase flow systems in the porous media. It can be inferred from the results that the geoelectrical techniques are highly dependent on water saturation. However, below 50% water saturation, the relationships appear less dependent on pressure, temperature and brine/water saturation in the porous media. The petrophysical and mathematical relationships developed in this work are useful in the prediction of the geoelectrical parameters in different porous media, under different conditions.

## CHAPTER EIGHT

# POTENTIAL OF SILICONE RUBBER MEMBRANE IN THE MONITORING OF SUBSURFACE GASES AND ITS APPLICATIONS IN GEOLOGICAL CARBON SEQUESTRATION\*

### Overview

*The possibility of leakage of CO<sub>2</sub> from the geological storage site is of serious concern to stakeholders. While every effort should be made to secure the CO<sub>2</sub> in the storage aquifer, simple and less expensive techniques should equally be made available to the public and field investigators to monitor CO<sub>2</sub> and other gases in the subsurface. This will be beneficial in detecting the CO<sub>2</sub> leakage before the plume reaches the earth's surface or contaminates the potable water in the aquifer. In this work, a high pressure experimental rig was constructed consisting of a porous domain to which a flat sheet of silicone rubber together with pressure transducer (sensor) was fitted for monitoring of the different gases in the domain under different pressures and temperatures, which correspond to different geological depths. Under constant pressure and temperature in the porous domain, the dynamic responses of the membrane-sensor system in terms of the mass of permeated gas, membrane resistance to gas permeation and the gas flux across the membrane are reported for two gases, namely, CO<sub>2</sub> and N<sub>2</sub>. Mass permeation of CO<sub>2</sub> through the membrane was more than ten times higher than that of N<sub>2</sub> under similar conditions. It was also found to increase with the geological depths. The profile of gas flux remains higher for CO<sub>2</sub> as compared to N<sub>2</sub>. There are rapid, less rapid, constant and declining stages in the curves of gas flux across the membrane as the mass of the permeated gas increases. This is attributed to the reduction in the driving force with increased mass of the permeated gas. The permeability of the membrane to a gas was found to be independent on total pressure. However, the permeability varies for different gases, and it was much higher for CO<sub>2</sub> than N<sub>2</sub>. From the results, a simple criterion for distinguishing the presence of the different gases at various geological depths was established based on the rate at which the mass permeation of gas through the membrane occurs.*

### 8.1 Introduction

Global warming problems arising from climate change (Chandrappa et al. 2011) have led to the practice of geological carbon sequestration so as to limit the amount of greenhouse gases in the atmosphere (Ward et al. 2013; Khudaida and Das, 2014). However, the

---

\*Abidoeye, L.K., and Das, D.B. Potential of Silicone Rubber Membrane in the Monitoring of Subsurface Gases and its Applications in Geological Carbon Sequestration. Industrial & Engineering Chemistry Research (submitted)

possibility of CO<sub>2</sub> leakage from geological sequestration site is a major concern to many stakeholders (Abidoye et al. 2014; Itaoka et al. 2005). This is because the leakage of CO<sub>2</sub> from the storage site may pose serious danger to potable water aquifers that may lie along the CO<sub>2</sub> migration path. It also poses hazards to human and plant lives if the CO<sub>2</sub> finds its way to the earth's surface. On the other hand, leakage of CO<sub>2</sub> may give rise to hazards to the marine lives if it leaks through the ocean leading to water acidification (Klapper et al. 2013). These possibilities and their adverse effects hinder public acceptance and investors' confidence in the long term safety of the sequestration process (Krause et al. 2014; Itaoka et al. 2005).

The safety of a CO<sub>2</sub> storage site can be compromised due to the migration of CO<sub>2</sub> from the storage site, e.g., migration through fractures or high permeability pathways in or around the storage aquifer, resulting in leakage. The migration of the CO<sub>2</sub> from the storage site can also occur as a result of gravity override and/or viscous instability in the porous media initially filled with brine (Taku Ide et al. 2007; Berg and Ott 2012). This causes the CO<sub>2</sub> to move to the top of the injection layer and bypass large quantities of brine in the storage aquifer (Tao and Bryant 2014; Gasda et al. 2009; Saripalli et al. 2001). Similarly, wettability alteration of the caprock can lead into the migration of the CO<sub>2</sub> through overlying caprock (Saraji et al. 2013; Al-Garni and Al-Anazi 2008; Chiquet et al. 2007), which can lead to the leakage of CO<sub>2</sub>. Overcoming these challenges requires the design of efficient sequestration processes, together with the effective monitoring strategies to convince the public and win the investors' confidence on the reliability of the sequestration process in the long run.

Existing monitoring technologies for carbon sequestration are generally built upon the measurements of physico-chemical properties of the CO<sub>2</sub>-brine-rock system or the detectability of the reaction by-products, e.g., precipitation of carbonates in limestone-rich aquifer (Espinoza et al. 2011a). Electromagnetic techniques (Nakatsuka et al. 2010), infrared monitoring (Charpentier et al. 2009), and temperature signals (Bielinski et al. 2008) have been demonstrated either in the laboratory or pilot applications for subsurface monitoring of gases. Methods, such as electromagnetic techniques utilise large differences in the values of the dielectric permittivities of CO<sub>2</sub> and water to establish contrasts between the original and current amounts of water and CO<sub>2</sub> at any time in the domain (Vilamajó et al. 2013). Near surface monitoring involves the analysis of near surface water, air and soil samples on a regular basis as CO<sub>2</sub> leaks can acidify the water and create conspicuous contrast between the original and current soil and air compositions (Spangler et al. 2010).

Looking at the listed techniques, the conclusion may be drawn that a number of techniques are already proposed for the monitoring of the carbon sequestration process. However, the

costs of the instruments involved in the above techniques as well as the complexity of their operations are generally beyond the reach of many concerned households and investigators. This view was shared by Zimmer et al. (2011). These authors state that the conventional techniques for porous media gas sampling are time consuming, expensive, or limited in temporal sampling density and volume. Thus, research into the possibility of low cost and simple monitoring systems in the tracking of subsurface gas migration for use by investigators and common households especially those around the sequestration sites or CO<sub>2</sub> pipelines is highly desired.

In addressing the issues discussed, the potential of silicone rubber as a low-cost membrane for the monitoring of the presence of gas in the porous media is examined in this work. Silicone rubber is a widely used elastomer in a wide range of industries. It is also one of the most gas permeable elastomers (Zhang and Cloud 2006). The high permeability of silicone rubber to gas is due to the high flexibility of the silicone-oxygen chain, which enables easy diffusion of gas molecules. This property of silicone rubber has been exploited in gas separation, drug delivery, blood oxygenation and so on (Barnes et al. 2012).

Earlier, Zimmer et al. (2011) and Lazik et al. (2009) demonstrated the applicability of silicone rubber as a membrane in the detection of gases present in the underground and boreholes. Investigations by Zimmer et al. (2011) were connected to the geological carbon sequestration project (CO<sub>2</sub>SINK) in Ketzin, Germany. They have successfully demonstrated the detection of the CO<sub>2</sub> front at observation wells, located at different distances to the injection well, using the gas membrane sensor that includes the silicone rubber. However, the analyses of the gases through the device rely on the mass spectrometer located on the ground surface, making the system complex and expensive to use. This however raises a question, i.e., whether or not a low-cost membrane-sensor system can be effectively applied in the monitoring of subsurface gas migration under high pressure and temperature conditions, as found in the geological carbon sequestration. As shown in the works of Cheng and Luo (2014) and Zimmer et al. (2011), there are many gases that can migrate in the subsurface apart from CO<sub>2</sub>. Considering the scenario where unknown gas possibly permeates into the membrane-sensor system, how can the presence of a particular gas in the subsurface be possibly distinguished using such system?

To respond to these questions, this work attempts to characterize the performances of the flat sheet silicone rubber devised with a pressure sensor for the detection of CO<sub>2</sub> and N<sub>2</sub> in porous media. Previously, Lazik et al. (2009) demonstrated the application of membrane-sensor system in the continuous monitoring of O<sub>2</sub> and CO<sub>2</sub> in a sand-filled Lysimeter. However, they used tubular membrane unlike the flat-sheet membrane used in this work.

The tubular nature of the membrane used in their work seems to make the measurement of the gas concentration more tedious unlike the straightforward measurement obtained in this work. This is because the tubular membrane used required sensors with tubular geometry to achieve the measurement objective. Furthermore, the authors (Lazik et al. 2009) show that the subsurface gas concentration can be determined by simple measurement of physical quantities (e.g., pressure or volume) only. This principle was utilised in this work by the measurement of the pressure of the gas that permeated through the membrane into the measurement chamber of the membrane-sensor system.

In this work,  $N_2$ , as one of the abundant gases in the subsurface (Bednarek et al. 2014), is included as a model gas to create comparison for the responses of the membrane-sensor system to the presence of different gases. The characterization will be done in terms of the mass permeation of the gases through the membrane, dynamic profiles of gas fluxes across the membrane and membrane resistance to gas permeation. This work will utilize the differences in the performances of the membrane-sensor system under the influences of the different gases to establish distinguishing criterion for real-time monitoring of the gas migration in the subsurface.

The experiments involved the preparation of a porous domain with well-characterised silica sand particles. The domain was made of a steel cell to withstand the high pressure and temperature conditions, applicable to geological carbon sequestration. A flat sheet silicone rubber was fitted into a steel holder together with a pressure transducer (sensor) as a membrane-sensor system, which was attached to the port at the centre of the wall of the porous domain. The experiments were designed to mimic the conditions of temperature and pressure that can be encountered by gases escaping from shallow subsurface. According to Best (2013), the geobaric gradient in the continental crust is around 270 bar/km. Assuming linearity in pressure gradient, this gives the idea of the pressure prevailing for the matters existing at different depths in the geological domain. Also, geothermal gradients were reported to be 45 and 25°C/km for the warm and cold basins, respectively (Nordbotten et al. 2004; Das et al. 2014). In this work, a warm basin is considered, and the calculated conditions for different geological depths, based on the above reports, were used to design the experiments.

## 8.2 Materials and methods

### 8.2.1 Porous domain and materials

The porous domain used in this work was prepared using commercially available silica sand particles, similar to that described in subsection 7.2. The properties of the silica sand can be found in Table 7.1. The silicone rubber sheet (part number: RS 340-2689) used in the experiments was obtained from RS Components Ltd (Northants, UK). The sheet has an average thickness of 3mm. The gases used were high purity CO<sub>2</sub> and N<sub>2</sub>, which were obtained from BOC Industrial Gases (Loughborough, UK).

### 8.2.2 Instruments and sample holder set up

The pressure of the gas that permeated through the silicone rubber membrane was measured with the HySense PR 140 pressure transducer (Hydrotechnik, GmbH, Holzheimer Strasse, Germany) with operating pressure of 0 to 100 bar. The head of the pressure transducer (PT) was fitted into locally manufactured steel holder that also holds the silicone rubber membrane in a tight position. Figure 8.1 shows the photograph of the sample holder filled with sand, and the steel holder, which holds the membrane and the pressure transducer (sensor). The silicone membrane was cut to the appropriate diameter to fit into the steel holder with the average diameter of the membrane being  $7.3 \times 10^{-3}$  m while the infiltration area available for permeation is  $3.8 \times 10^{-3}$  m in diameter. The reason for the reduction in diameter for effective permeation was the metal cap on the top of the holder, which screwed down the membrane against a sintered metal disc at its base. The sample holder is a stainless steel cell with a sample height of 4cm and 10cm diameter. The sample holder for the porous medium is a stainless steel with end-pieces at the top and bottom. It was designed with ports centrally located at its wall to hold the steel holders. Two pressure transducers in the steel holders were used at the opposite sides of the wall of the sample holder to measure simultaneously the pressure of the gas that permeates through the membrane. The mathematical average of the pressure readings by the two PTs is reported for each experiment. The pressure transducers' cables were connected to a data logger (National Instrument, Newbury, UK). The data from the pressure transducers were logged into the computer using Labview (2011) (National Instrument, Newbury, UK). The gap between the membrane in the steel holder and the face of the PT at the base of the steel holder provides the space for the accumulation of gas that permeates through the membrane. This space has an average volume of  $1 \times 10^{-6}$  (m<sup>3</sup>). The pressure transducers were calibrated using a portable pressure calibrator, DPI 610 (Druck Limited, Leicester, UK).

Electric heaters were located at the convenient corners of the heating cabinet and the system temperature was regulated using PID temperature controller (West Control Solutions, Brighton, UK). Readings were collected every 10 s.

Figure 8.2 is a schematic diagram of the experimental set up. The experimental set up was similar to that described in subsection 7.2.3, except that, in this case, there is the use of the membrane and pressure sensors. Also, in the present experiment, there is no outflow of fluid from the porous domain and only CO<sub>2</sub> was used. Figure 8.2 illustrates the sample holder and the positions of the PTs. Narrow steel tubes run upstream and downstream of the cell with an inlet for scCO<sub>2</sub> via the upstream tube connected to the supercritical fluid pump. The outlet pipe from the bottom of the sample holder has a metering valve (Swagelok, Kings Langley, UK) to shut or control outflow from the sample holder. In all experiments, it was shut to prevent the leakage of the gas in the sample holder. Furthermore, to ensure that there is no gas leakage and that the system is at the desired pressure, a precision backpressure regulator, BPR (Equilibar, Fletcher, NC, USA) is located further down the outlet tube. The back pressure regulator is a dome loaded type using peek materials as diaphragm and was loaded with nitrogen gas (BOC Industrial Gases, Loughborough, UK) from a cylinder with appropriate gas regulator (Gas-Arc Group Ltd, Norfolk, UK). The pressure imposed on the porous domain from the supercritical fluid pump was recorded by a CR10X data logger (Campbell Scientific, Shepshed, UK).

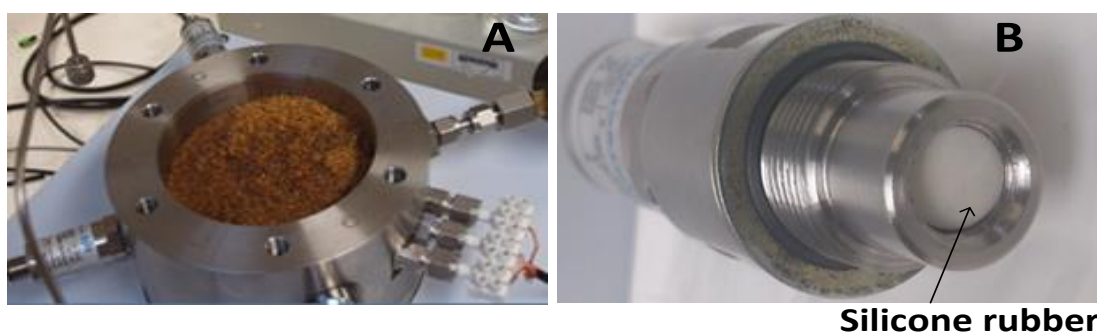


Figure 8.1: Photographs of (A) The sample holder showing silica sand and pressure transducer (B) Steel holder showing the pressure transducer and the silicone rubber sheet (metal cap not shown).  
Sample holder size: internal diameter=10cm, sample height=4cm

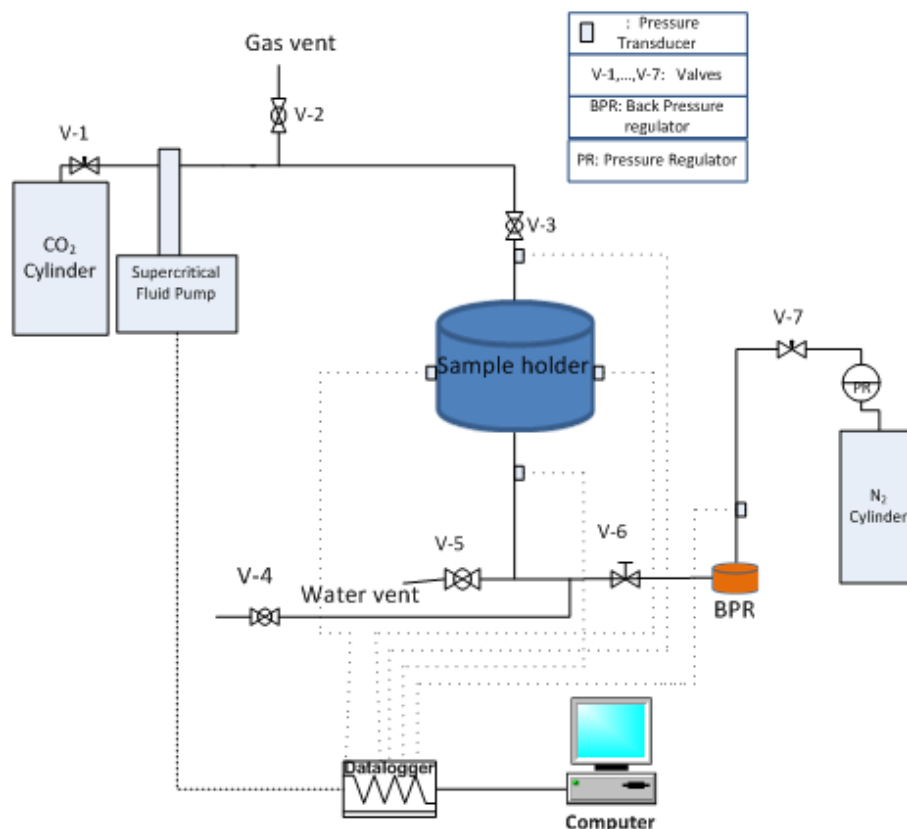


Figure 8.2: High-pressure experimental set-up for the investigation of gas migration in the porous media using membrane-sensor system (The set-up is slightly different from Figure 7.1)

### 8.2.3 Experimental design

Geological sequestration of CO<sub>2</sub> can take place at depth of 1km or more (Abidoye et al. 2014; Hosseini et al. 2013). However, migration of leaked CO<sub>2</sub> from the storage site may occur through several geological sediments, situated at different depths that lie above the storage site, before reaching the earth's surface. Based on this scenario, the experiments in this work were designed to mimic the presence of CO<sub>2</sub> at the hypothetical geological depths above the storage site. As pointed out in the introductory part of this work, the reports of Best (2013) and Nordbotten et al. (2004) were used to determine the pressure and temperature, respectively at the hypothetical geological depths for the experiments. Conditions at various geological depths, which were considered in this work, are listed in Table 8.1. For safety concerns during the experiments, the experimental conditions were chosen up to the limit of 300m depth (for N<sub>2</sub>). Fresh samples of silicone rubber membranes were used at the start of each experiment. At the start of the experiment, the equipment was set up by placing the body of the sample holder on the bottom end piece (sample holder base). Ports on the

sample holder were plugged with steel holders, which hold the PTs and the membrane. These were then connected to the peripheral devices as discussed above. The silica sand was poured through a metal sieve of appropriate size with regular tamping to ensure uniform sand deposition. Equal amounts of sand (500g) was used in all experiments. Then, the top end piece was placed in position. The weight of the top end piece compressed the sand to conditions suitable for a high-pressure system. After tightening all the tubing joints, high pressure was imposed on the BPR system from the N<sub>2</sub> cylinder. The peek diaphragm in the BPR prevents the passage of the N<sub>2</sub> through the downstream tubing into the porous domain. The sample holder and some portions of the tubing were contained within a heating cabinet fitted with electric heaters. The heaters were turned on and set at the appropriate temperature for the experiment. A supercritical fluid pump (Teledyne Isco, Lincoln, USA) was filled with liquid CO<sub>2</sub> from the cylinder by opening of the valve, v-1, and setting the pump on refill mode. Following this, v-1 was closed and the supercritical fluid pump was set at the experimental pressure. This procedure supplied the CO<sub>2</sub> to the tubing from the exit of the supercritical fluid pump up to the valve, v-3 (Figure 8.2). The constant pressure mode of the supercritical fluid pump was used throughout all the experiments. This mode imposed constant pressure of CO<sub>2</sub> on the porous domain. The constant pressure mode of the pump continued to maintain set pressure of gas on the domain, even when the gas in the domain starts infiltrating or permeating through the membrane into the space between the membrane and the sensor in the steel holder. When the temperature in the heating cabinet had reached the target condition, v-3 was opened and CO<sub>2</sub> was supplied into the sand in the sample holder. The pump being in constant pressure mode, any pressure fluctuation owing to the opening of the v-3 was quickly eliminated. The experiment continued for a varying number of hours as convenient for the investigator. Measurements were performed at different temperatures and pressures following the conditions listed in Table 8.1. In addition, for each experiment, the result presented was the arithmetic average of the readings from the two sensors. The silicone rubber used in this work is a non-porous flat sheet membrane. Gas permeates the membrane by diffusion under the influence of the driving force, e.g., the pressure difference across the membrane. Commonly, concentration gradient is normally taken as the driving force in the permeation of gas through a membrane in the mixture of gases (see, Lazik et al. 2009). In this work, only pure gas was used in each experiment. Therefore, pressure gradient across the membrane is rightly considered to be the driving force. Fresh and used silicone rubber membranes scanned with the field emission gun scanning electron microscopy (FEGSEM) (LEO 1530VP, Carl Zeiss SMT, Oberkochen, Germany) are shown in Figure 8.3. No significant pores were detected in the membrane by the scan after the CO<sub>2</sub> permeation.

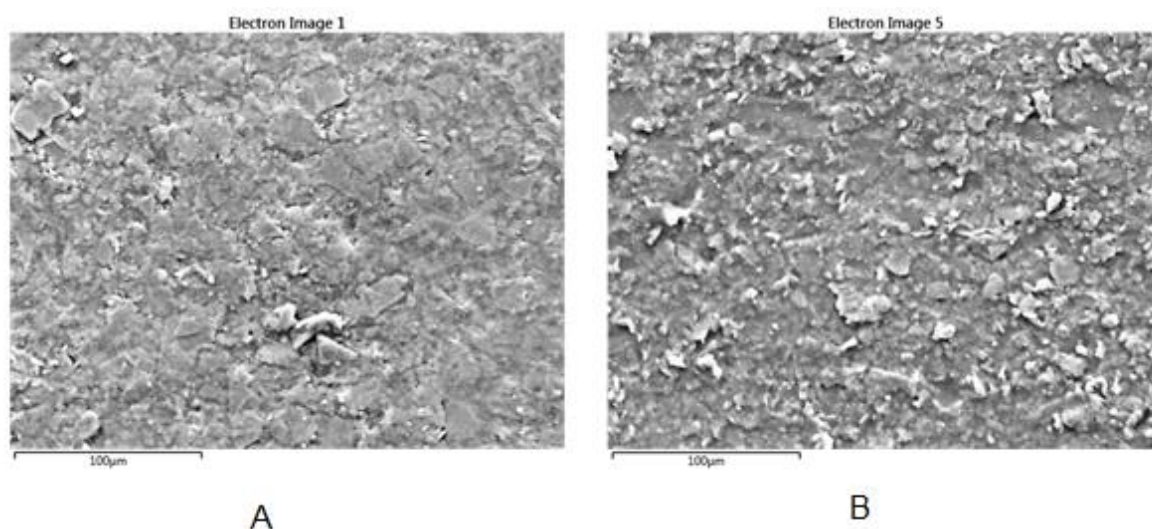


Figure 8.3: Scans of (A) Fresh (B) Used (experiment at 67.5 bar, 31.25°C, i.e., 200m depth) silicone rubber membrane using FEGSEM (LEO 1530VP, Carl Zeiss SMT, Oberkochen, Germany)

Table 8.1: List of Experimental Conditions and State of CO<sub>2</sub>

Depth (m)	Domain Temperature (°C)	Domain/Injection Pressure (bar)	CO <sub>2</sub> State
50	22.25	13.5	gas
150	26.75	40.5	gas
200	29	54	gas
250	31.25	67.5	Gas

For the experiments involving N<sub>2</sub>, the N<sub>2</sub> gas was supplied from the N<sub>2</sub> cylinder via the BPR. Here, v-3 was closed to prevent N<sub>2</sub> from entering the supercritical fluid pump. The diaphragm on the BPR was removed to provide a path for the N<sub>2</sub> to enter into the sand in the domain through the downstream tubing. The N<sub>2</sub> pressure was set on the gas regulator on top of the N<sub>2</sub> cylinder. All other procedures remained as defined above for the CO<sub>2</sub> experiments.

#### 8.2.4 Calculation of mass transfer parameters

The silicone rubber membrane selectively permits the transfer of gas across it. The permeation of a gas through the membrane was recorded as a rise in the pressure reading of membrane-sensor system. The pressure reading at different time was used to determine the mass of the gas in the measurement chamber of the membrane-sensor system. In order to obtain real properties of the gases, Van der Waals equation was used to determine the mole

of the gases. The mass of the gas was obtained from their respective mole at different time. Van der Waals equation is shown in equation (8.1):

$$[P + (n^2a/V^2)](V - nb) = nRT \quad (8.1)$$

$P$  (Pa),  $n$  (mol),  $V$  ( $m^3$ ) and  $T$  (K) are the pressure, number of mole, volume and temperature, respectively, of the gas in the measurement chamber of the membrane-sensor system.  $R$  (J/mol K) is the universal gas constant,  $a$  ( $kg\ m^5/s^2mol^2$ ) and  $b$  ( $m^3/mol$ ) are constants, which fit the experiment closely to individual gas molecule. The mole,  $n$ , is obtained from equation (8.1) by approximating  $V$  in the term  $n^2a/V^2$  (see, equation (8.1)) using the ideal gas equation (i.e.,  $V=nRT/P$ ). After rearrangement,  $n$  is obtained as:

$$n = \frac{V(PR^2T^2 + aP^2)}{bPR^2T^2 + baP^2 + R^3T^3} \quad (8.2)$$

The mass,  $m$ , of the gas was obtained by multiplying the mole,  $n$ , with the molar mass of the gas.

To assess the performance of a membrane in term of the mass of gas that permeates through its matrix, Shahrabi et al. (2012) describe the gas permeate flux ( $J$ ) ( $kg/m^2hr$ ) through the membrane as:

$$J = \frac{m}{A \cdot t} \quad (8.3)$$

where  $m$  (g) is the total mass of the permeate at the experimental time interval,  $t$  (h), and  $A$  is the effective membrane area for permeation ( $m^2$ )

The permeability of a membrane to gas is also mathematically described by equation (8.4) (Baker 2012; Zhang and Cloud 2006; Van Amerongen 1964):

$$P = \frac{v \cdot \delta}{A \cdot t \cdot (p_1 - p_0)} \quad (8.4)$$

Where  $\delta$  (m) is the thickness of the membrane,  $p_1$  and  $p_0$  (bar) are the higher and lower gas pressures, respectively, on either side of the membrane. In this work, the difference between these pressures, i.e.,  $p_1-p_0$ , is considered as the driving force for gas permeation through the membrane. In equation (8.4),  $v$  is often taken as the volume of the gas that penetrates the membrane under standard conditions (STP). However, it was used as the mass of the

permeated gas in this work since the mass of the gas is conserved under different conditions unlike the volume of a gas.

The mass transfer across a gas/membrane/gas system consists of three distinct stages. In this work, the stages are (1) mass transfer of gas across the gas boundary layer in the porous medium (2) the transfer of gas through the membrane, (3) transfer of gas across the gas boundary layer in the open space between the membrane and the pressure transducer (sensor). Each of these stages acts as a resistance to mass transfer. For a non-porous membrane, the total resistance ( $1/K_T$ ) can be expressed in series sum of the above resistances:

$$\frac{1}{K_T} = \frac{1}{k_{g1}} + \frac{1}{k_m} + \frac{1}{k_{g2}} \quad (8.5)$$

Where  $K_T$ ,  $k_{g1}$ ,  $k_m$ , and  $k_{g2}$  are the mass transfer coefficients for overall, gas boundary in the porous medium, gas permeation through the membrane, and the gas boundary in the measurement chamber of membrane-sensor system, respectively. In this work, it can be assumed that the resistances in the gas boundary layer in the porous medium ( $1/k_{g1}$ ) and in the open space between the membrane and the sensor ( $1/k_{g2}$ ) are negligible. Thus, it is defined that  $K_T \cong k_m$ . This assumption is reasonable considering that the gas transfer in the porous medium was rapid because of the automatic pressure regulation from the supercritical fluid pump, which imposed constant pressure on the domain throughout the experiment. De Bo (2003) similarly assumes the overall mass transfer resistance in gas/membrane/gas system is equivalent to the resistance in the non-porous membrane, like the one used in this work. The resistance to pure gas in the membrane can be determined from the equation (8.6) (Ozturk and Hughes 2012):

$$\frac{1}{k_m} = \frac{\delta}{P} \quad (8.6)$$

Calculations in this work using the equations (8.2) and (8.3) extend over the entire duration of the experiments. This approach enables understanding of the response of the membrane-sensor system from the beginning of gas permeation through the membrane. The primary aim of this work is to understand the response of the membrane-sensor system at simulated different geological depths in the event of the CO<sub>2</sub> leakage from a storage site and to establish a suitable distinguishing criterion with which a membrane-sensor system can be programmed to detect different gases that permeate through a non-porous membrane in the porous media at different depths. Therefore, it is important to know the response of the

membrane-sensor system at the start of the permeation, which can be used to characterise the gas leakage detection using the membrane-sensor system.

In all experiments, constant pressure and temperature were maintained on the porous domain. As mentioned earlier, the main driving force for the gas permeation through the membrane was the difference between the domain pressure and the pressure in the membrane-sensor system, i.e.,  $p_1 - p_0$ .

### 8.3 Results and discussions

The results of the investigations of the behaviours of the flat sheet silicone rubber membrane-sensor system to the presence of different gases ( $\text{CO}_2$  and  $\text{N}_2$ ) at various conditions corresponding to different geological depths are discussed in this section. The responses of the membrane-sensor system to the different imposed conditions of  $\text{CO}_2$  and  $\text{N}_2$  are discussed in the context of various parameters, which may affect the leakage/migration of  $\text{CO}_2$  from a storage site. For each experiment, simultaneous pressure readings were taken from the two pressure transducers located at the opposite sides of the centre of the porous domain. Arithmetic average of these readings was reported for each experiment in this work. Typical behaviour of the membrane-sensor system is shown in Figure 8.4 for  $\text{CO}_2$  permeation into the membrane at conditions corresponding to the 250m depth (see, Table 8.1). The simultaneous readings of the two sensors (PTs) are close, having the maximum standard deviation of 4.7 bar. For all experiments, the standard deviations of the simultaneous sensors' readings reduce with the decreasing depth. At 50 and 200m depths, the standard deviations are 0.9 and 2.8bar, respectively.

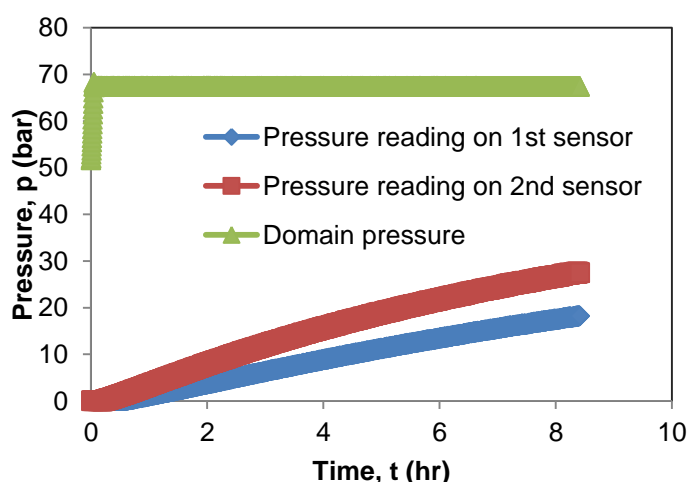


Figure 8.4: Simultaneous responses of the two pressure transducers to the  $\text{CO}_2$  gas that permeated through the membrane at imposed conditions corresponding to 250m depth.

The figure also shows that the domain pressure, which was imposed from the CO<sub>2</sub> pump, remained constant until the end of the experiment. In some experiments, the gas may leak through connections at the tubing joints, which seems to arise due to the high pressure of the system. This resulted in the decline of the pump and domain pressure. These results were discarded.

### 8.3.1 Gas permeation in the membrane

The permeation of gas through the membrane is recorded as a change in the pressure reading of the pressure transducer. Using the Van der Waals gas equation (8.1), the pressure reading was used to determine the mass of the gas that has penetrated through the silicon rubber. The volume of the measurement chamber between the membrane and the sensor in the steel holder is  $1 \times 10^{-6} \text{ m}^3$ . This volume is assumed constant and it is occupied by permeated gas under different conditions. In all experiments, no significant deformation of the membrane is visible. Therefore, the volume of the measurement chamber can be confidently assumed constant. The mass of the gas that permeates the membrane is an important parameter since it is known that the mass is conserved. Mass of N<sub>2</sub> that permeated into the membrane is shown in Figure 8.5 at the conditions corresponding to the depths of 150 and 300m. Under these conditions, Figure 8.5 shows that the time of the detection of the N<sub>2</sub> (i.e., start of the rise in the mass of the gas) is not significantly different for the two conditions. It takes more than an hour for any significant mass of N<sub>2</sub> gas to be recorded. In Figure 8.6, the responses of the membrane-sensor system to the presence of CO<sub>2</sub> at different conditions corresponding to different geological depths are shown. The rate of change of mass of CO<sub>2</sub> increases with depth. This can be seen as the effect of increasing pressure and temperature with depth. Comparing Figures 8.5 and 8.6, it can be seen that under similar conditions, the magnitudes of the responses of the system to the presence of the CO<sub>2</sub> far outweigh that of N<sub>2</sub>. Figure 8.7 displays this comparison clearly. At the same depth (150m), a significant amount of CO<sub>2</sub> is detected at less than 10 minutes compared to detection of N<sub>2</sub>, which takes more than 1 hour. This shows the quick response of the membrane-sensor system to the presence of CO<sub>2</sub>.

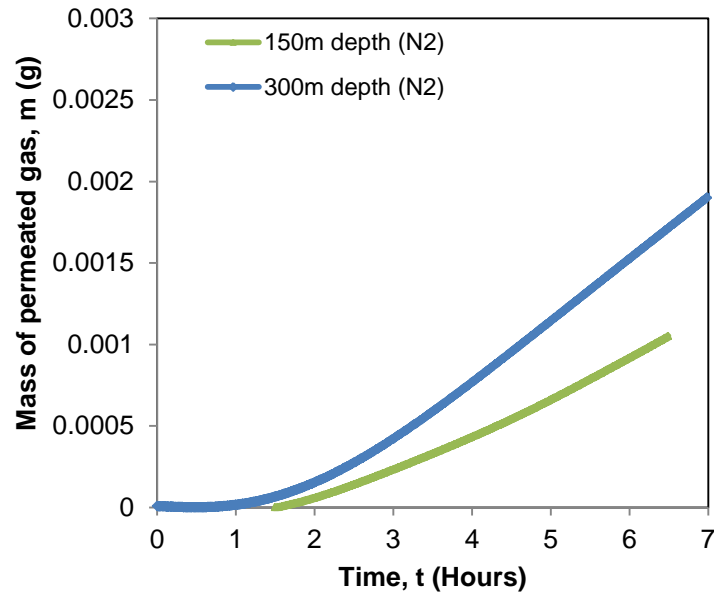


Figure 8.5: Mass of permeated gas ( $N_2$ ) under conditions that mimic different depths.

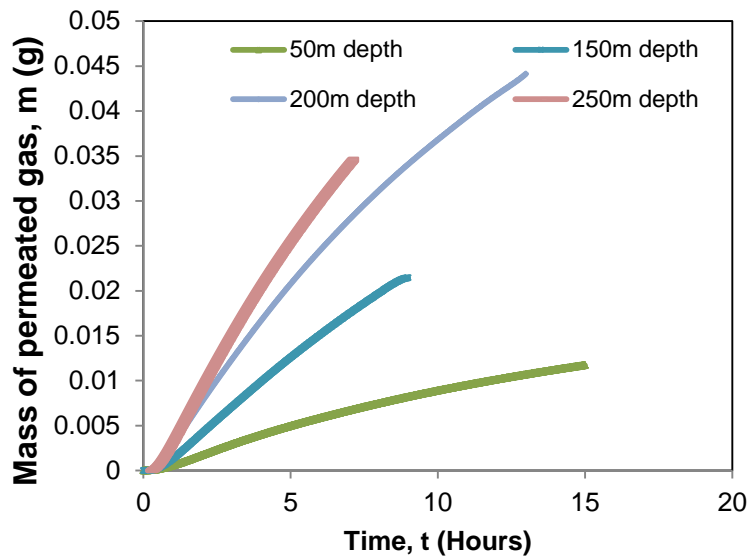


Figure 8.6: Mass of permeated gas ( $CO_2$ ) through the membrane under conditions that mimic different depths

Observations above are similar to the findings of many authors on the high permeation rate of  $CO_2$  in the silicone rubber membrane (see, e.g., Zimmer et al. 2011; Kesson 1984; Staude 1992; Praveen et al. 2006; Merkel et al. 2001; Egli et al. 1984), but the methods and units of estimations by different authors make comparison of the results less straightforward.

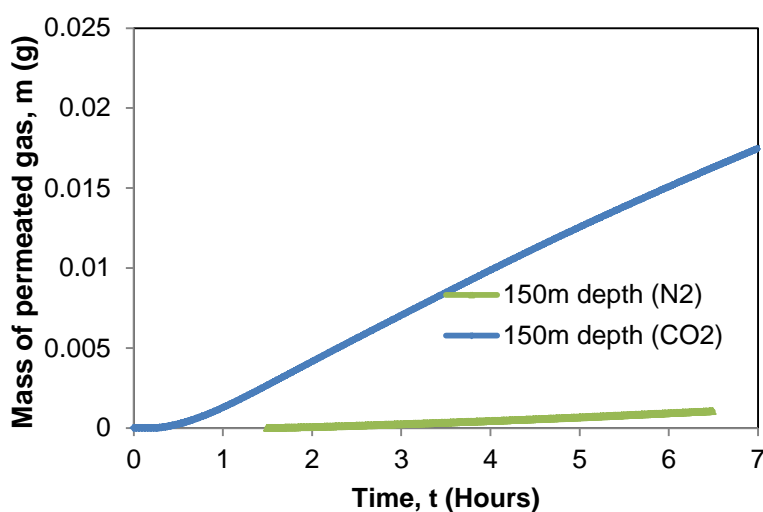


Figure 8.7: Mass of permeated gases (CO<sub>2</sub> and N<sub>2</sub>) through the membrane under similar conditions

### 8.3.2 Gas flux across the membrane

The flux of gas across the membrane is calculated using equation (8.3). The gas flux across the membrane is plotted across the mass of the permeated gas in order to show the influence of the driving force on the flux profile. The driving force represents the pressure difference across the membrane. The mass of the gas in the membrane-sensor system is proportional to the pressure reading by the pressure transducer. Therefore, the plot of the gas flux against mass of permeated gas gives information about the profile of the gas flux in relation to the change in the driving force. Flux across the membrane with the permeation of N<sub>2</sub> is shown in Figure 8.8. Several stages can be discerned in the flux profile of the gas. In the first part of the curve (Figure 8.8, 300m depth), the gas flux increases rapidly with the mass of permeated gas. This continues until the second stage is reached where the increase in gas flux persists but at a reduced rate compared to the first stage. This is succeeded by the third stage, which is characterised by a virtually constant flux regime. These first three stages can be discerned at 300m depth in Figure 8.8. In Figure 8.8, owing to the short duration of the experiment at 150m depth, only the first and part of the second stages are depicted.

Figure 8.9 shows the existence of a further stage in the profile of gas flux into the membrane with CO<sub>2</sub>. Here, there is higher permeation rate for the CO<sub>2</sub>. This enables clear visibility of the behaviour of the flux profile more readily. Following the third stage that was characterised by virtually constant flux of the gas into the membrane, it is clear in Figure 8.9 that the fourth stage of the profile is characterised by a decline in flux for all the conditions investigated. Thus, the third stage represents the peak value of the flux following which there is gradual

decline in the gas flux. Figures 8.8 and 8.9 show that the flux of the permeated gas increases with the depth. The value of flux recorded with  $\text{CO}_2$  on the silicone rubber far outweighs that of  $\text{N}_2$  under similar conditions. The results show that  $\text{CO}_2$  diffuses faster through the silicone membrane than  $\text{N}_2$ . Reasons for the decline in the flux profile with the mass of the permeated gas can be explained in term of the driving force, which is defined to be the difference in pressures across the membrane. It will be recalled that the increase in the mass of the gas that permeates through the membrane actually signifies an increase in the pressure of the permeated gas in the measurement chamber of the membrane-sensor system. Thus, increase in the mass of the permeated gas increases the pressure in the measurement chamber of the membrane-sensor system. Since the pressure in the porous domain remains constant throughout the experiment, the increase in the pressure on the side of the membrane-sensor system leads to the decrease in the driving force. Since the driving force reduces with increase in mass of the permeated gas, the gradient of the gas flux profile continues to decline, as shown in Figures 8.8 and 8.9. Zimmer et al. (2011) calculated the  $\text{CO}_2$  gas flux through silicone rubber and found that the flux values increase with the partial pressure of  $\text{CO}_2$ . However, their approach was different from this work as they only calculated the flux value at a steady state in gas permeation. They also show that the flux of  $\text{CO}_2$  increases with temperature. The trends in their results conform with the findings (shown in Figure 8.9) for  $\text{CO}_2$  flux values at different depths, corresponding to different pressure and temperature. Figure 8.9 shows that the flux values increase with depth.

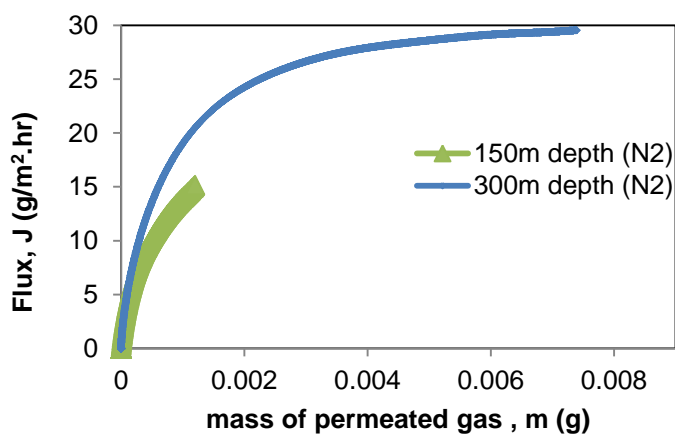


Figure 8.8: Change in the flux of permeated gas ( $\text{N}_2$ ) under conditions that mimic different depths

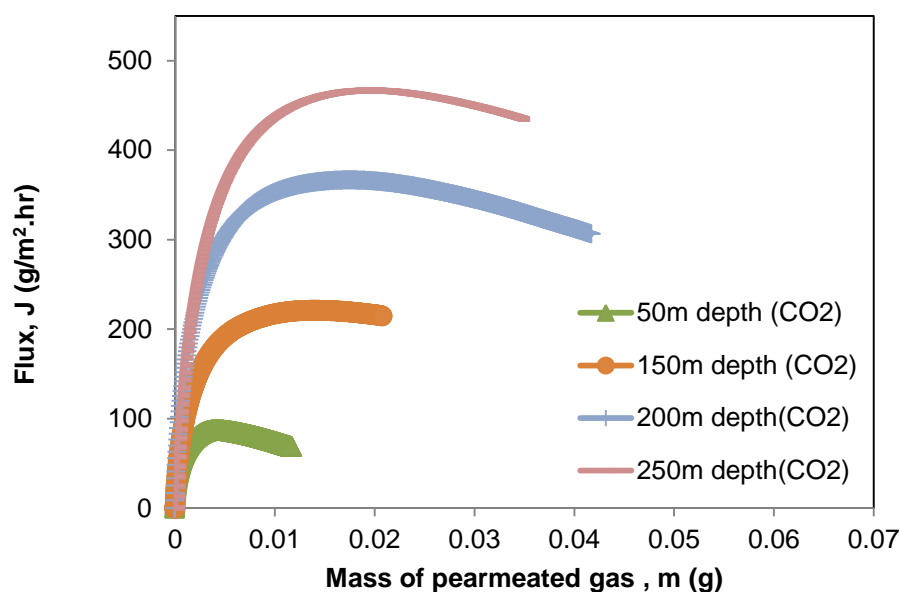


Figure 8.9: Change in the flux of permeated gas (CO<sub>2</sub>) under conditions that mimic different depths

### 8.3.3 Membrane permeability to gases

The permeability of the membrane to the gas provides information about the resistance of the membrane to the gas permeation. Equation (8.4) was used to calculate the permeability of the membrane to CO<sub>2</sub> and N<sub>2</sub>. The values of the permeability of the membrane to CO<sub>2</sub> and N<sub>2</sub> are  $3.1 \times 10^{-5}$  and  $1.2 \times 10^{-6}$  (kg m /m<sup>2</sup> hr bar), respectively. The results show that the membrane permeability to CO<sub>2</sub> is one order of magnitude higher than to N<sub>2</sub>. Thus, CO<sub>2</sub> readily permeates through the silicone rubber membrane than N<sub>2</sub>. The results also indicate that there is higher resistance of the membrane to N<sub>2</sub> permeation. Equation (8.6) shows that there is inverse relationship between the membrane resistance and the permeability. In equation (8.6), since the membrane thickness ( $\delta$ ) is constant for each experiment, therefore the membrane resistance to N<sub>2</sub> permeation is higher since the permeability of N<sub>2</sub> is lower than that of CO<sub>2</sub>. Once the gas breaks through the membrane, it creates pathway that seem to depend on the characteristics of the gas. Thus, the best mechanism to increase the overall mass transfer coefficient is to reduce the thickness of the membrane (Scholes et al. 2014). Experiments in this work show that the permeability of the silicone rubber membrane is less dependent on pressure. This is because under different conditions of the experiments (see, Table 8.1), the permeability value for the pure gas converges at steady state. This corroborates the assertion of Zhang and Cloud (2006) that the type of gas affects the permeability of the silicone rubber. They have also argued that there is no effect of pressure on membrane permeability on the premise that pressure

parameters in equation (8.4) will normalise under different conditions. Thus, the high-pressure experiments in this work seem to confirm the assertion of Zhang and Cloud (2006). Mainly, permeability in this work can be seen to vary with gas characteristics only. Explaining the effects of gas characteristics on the permeability, Jordan and Koros (1990) describe CO<sub>2</sub> as highly condensable compared to N<sub>2</sub>, which has low sorption property. They state that the plasticization effects are more pronounced in CO<sub>2</sub> while hydrodynamic compression effects dominate with N<sub>2</sub>. The plasticization effect of the CO<sub>2</sub> will naturally tend to create free pathway for its passage in the membrane while the hydrodynamic compression characteristic of N<sub>2</sub> tends to reduce its membrane permeability, as it leads to reduction of free volume in the membrane, thereby restricting the gas passage.

Zimmer et al. (2011) and Zhang and Cloud (2006) have reported values of CO<sub>2</sub> permeability in a silicone rubber membrane. However, as stated before, the methods and units of these reports make the comparisons of results less straightforward. But, the work of Zimmer et al. (2011) show that the permeability of the membrane to CO<sub>2</sub> remains very close at different partial pressures of CO<sub>2</sub>. Also, Zhang and Cloud (2006) show that the permeability is independent of pressure. This work mainly considers the effect of pressure, since there is a great change in pressure magnitude with depth, while the temperature change is seen as minimal (see, Table 8.1).

#### **8.3.4 Distinguishing criterion for permeated gas**

From the foregoing discussions of the results, it is possible to deduce the distinctive criterion to identify the presence of different gases that permeated through the silicone rubber membrane in the porous media, using the membrane-sensor system. For CO<sub>2</sub> and N<sub>2</sub> considered in this work, wide differences in permeability, flux and mass of gas permeated are scrutinised. Since mass is conserved irrespective of the measurement chamber volume under different temperature and pressure, the rate of change of mass of the permeated gas in the system was considered. This is very feasible since the rate of mass permeation of CO<sub>2</sub> through the membrane is more than 10 times higher than that of N<sub>2</sub> under similar conditions. Thus, the slope (i.e., mass permeation rate) obtained from mass versus time curves at various depths can be used to obtain the needed model. The model/equation obtained will be useful in the programming of the membrane-sensor system to uniquely detect the presence of a gas and possibly alert investigators to the presence of gas in the measurement chamber. The rate of permeation of the gas through the membrane was obtained from the slope of the linear equation fitted to the initial permeation stage of the mass versus time curve. For the CO<sub>2</sub> and N<sub>2</sub> at 150m depth, the mass permeation rates are  $2 \times 10^{-6}$  and  $2 \times 10^{-7}$  kg/hr, respectively. The rate was determined from the portion of the mass permeation

versus time curve, where the permeation became noticeable, i.e., at the initial stage of permeation. This stage of permeation was chosen because the response of the membrane-sensor system, at this point, is related to the early detection of the subsurface gas or leakage from the gas storage site. Thus, programming the membrane-sensor system with parameters obtained at this crucial stage is advantageous for the quick detection of gas leakage in the subsurface. The mass permeation rate of CO<sub>2</sub> is one order of magnitude higher than that of N<sub>2</sub> at the 150m depth. The trends are similar at other corresponding depths. Thus, the presence of CO<sub>2</sub> can be detected if the gradient of the mass with time recorded by the system is around  $2 \times 10^{-6}$  kg/hr at the 150m depth. For CO<sub>2</sub> at the other geological depths, Figure 8.10 shows the variation of the mass permeation rate with depth for the two gases considered in this work. The data points are fitted to power law models, which provide the means of predicting the behaviour at various depths.

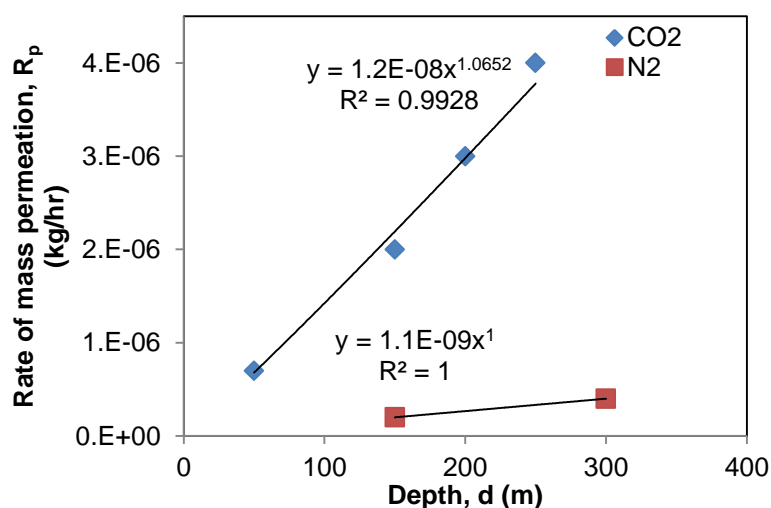


Figure 8.10: Models of mass permeation rate for different gases at different geological depths for application in the distinction of the presence of the different gases in the porous medium.

The above method is useful in the early detection of CO<sub>2</sub> migration or leakage from geological sites. Early detection at depth will allow for more time to tackle technical tasks before the CO<sub>2</sub> arrives in shallow groundwater or the earth's surface (Zimmer et al. 2011). In application, alarm system can be triggered to signify the presence of CO<sub>2</sub>, if the mass permeation rate follows the power law model provided in Figure 8.10. This model can be used to program the membrane-sensor system. The analysis above shows that the CO<sub>2</sub> has unique mass permeation rate that is different from that of N<sub>2</sub>. This can also be said of other gases found in the porous media. As shown, this rate is a function of depth. With the relation of the mass permeation rate to geological depth, using power law equation, this work has shown that the membrane-sensor system can be used to monitor gas leakage under different

geological conditions. Thus, at any depth, the system can be applied to give unique indication of gas present. From a practical point of view, one may wonder whether membrane-sensor system can be successfully applied at deep geological sediment. The work of Lamert et al. (2012) demonstrated the field measurements of electrical parameters to monitor the subsurface CO<sub>2</sub> movement by installing several copper electrodes at various depths up to 18.5m below the ground level around the CO<sub>2</sub> injection site. This enables the investigators to monitor the movement of injected CO<sub>2</sub> in the space surrounding the injection site. From this practical applications of sensors at depth by Lamert et al. (2012), it is believed that miniaturised pressure sensor with membrane can be for application at various depths.

However, further efforts will be needed to improve on this study. For example, the miniaturised sensor can be configured with the membrane for better application. Also, future work should require similar characterization for other gases found in the subsurface, in order to obtain a broad spectrum of mass permeation rates for different gases for complete programming of membrane-sensor system. Future work should also include the field application of the membrane sensor system.

## 8.4 Summary

In this work, the potentials of silicone rubber in the monitoring of gas migration in porous media have been demonstrated with well-defined laboratory experiments relating to the geological carbon sequestration. For this purpose, an experimental rig was constructed which consists of the domain of porous media to which the silicone rubber together with the pressure transducer (sensor) was fitted for monitoring of the different gases in the porous domain under different conditions corresponding to different geological depths. The responses of the membrane-sensor system in terms of the mass of permeated gas, membrane permeability to gas and the gas flux across the membrane are reported for both CO<sub>2</sub> and N<sub>2</sub>. The results showed the existence of distinguishable stages of permeation for the gases. In terms of the gas flux across the membrane, the first stage involves rapid rise in the flux across the membrane. This was followed by the less rapid stage of flux, where the gradient reduces and was succeeded by the stage of constant flux for a period, before the gas flux finally started to decline because of the reduction in the driving force across the membrane. The results differed considerably for the two gases with CO<sub>2</sub> flux occurring in multiples of that of N<sub>2</sub>, under similar conditions. The membrane shows different permeability to the gases and that of the CO<sub>2</sub> is higher than that of N<sub>2</sub>. The mass permeation with time for N<sub>2</sub> was more than ten times less than that for the CO<sub>2</sub>. Based on the mass permeation rate for the different gases, simple criterion for distinguishing the presence of the gases at various

geological depths using the membrane-sensor system was derived. The power law model of the distinguishing criterion is applicable in the monitoring of the subsurface gas migration.

## CHAPTER NINE

### PH, GEOELECTRICAL AND MEMBRANE FLUX PARAMETERS FOR THE MONITORING OF WATER-SATURATED SILICATE AND CARBONATE POROUS MEDIA CONTAMINATED BY CO<sub>2</sub> \*

#### Overview

*Characteristics of potable water aquifer contaminated by CO<sub>2</sub> are investigated using well-defined laboratory experiments. The porous media domain was prepared with silica sand and limestone in separate experiments. The investigations used combinations of techniques to measure various parameters in the water-saturated porous media domain on which pressure of CO<sub>2</sub> was imposed, under various conditions, which correspond to different geological depths. Measured parameters included the pH, geoelectrical parameters, and the diffusion of the CO<sub>2</sub> gas through the water-saturated porous media domain using a non-porous silicone rubber sheet. Experimental results revealed the existence of three stages in the profile of pH change with time as CO<sub>2</sub> dissolved and diffused in the water-saturated porous media domain, which was composed of silica sand. The first stage was characterised by rapid decline in the pH. This is associated with quick dissolution of CO<sub>2</sub> and the formation of carbonic acid together with bicarbonate. The second stage showed a short rise in pH value, which was attributed to the reverse reaction, i.e., the formation of aqueous and gaseous CO<sub>2</sub> and water from the carbonic acid. The third stage was that of the equilibrium in the forward and the reverse reactions, marked by steady state in pH value, which remained unchanged till the end of the experiment. The bulk electrical conductivity ( $\sigma_b$ ) of the water-saturated porous domain increased in the presence of CO<sub>2</sub>. This is attributed to the formation of ionic species, especially bicarbonate, as CO<sub>2</sub> dissolved in the domain. The rise in  $\sigma_b$  coincided with the first stage of the change in the pH of the system. In addition, the  $\sigma_b$  was higher in limestone than silica sand, and it increased with pressure of the domain. But, the bulk relative permittivity ( $\epsilon_b$ ) showed no change with the dissolution of the CO<sub>2</sub> under different conditions. Furthermore, permeation of CO<sub>2</sub> through the silicone rubber indicated the diffusion of the CO<sub>2</sub> gas through the water-saturated domain. CO<sub>2</sub> flux through the membrane was shown to increase with depth or pressure of the domain. A mathematical expression derived in this work shows the dependence of  $\sigma_b$  on the pH and the initial value of  $\sigma_b$ . Predictions of the changes in the  $\sigma_b$  for different porous domains show the reliability of the mathematical expression developed in this work.*

---

\*Abidoeye, L.K. and Das, D.B., (2015). pH, Geoelectrical and Membrane Flux Parameters for the Monitoring of Water-Saturated Silicate and Carbonate Porous Media Contaminated by CO<sub>2</sub>, Chemical Engineering Journal, 262, pp. 1208–1217, DOI: 10.1016/j.cej.2014.10.036

## 9.1 Introduction

Geological carbon sequestration has been proposed as a possible approach, which can significantly limit the amount of CO<sub>2</sub> in the atmosphere (Vuuren et al. 2013; Abidoye et al. 2014). However, the goal of the sequestration may be compromised by leakage of stored CO<sub>2</sub> which can take place due to high permeability pathways around the existing well bore (Tao and Bryant, 2014), nearby leaky wells (Humez et al. 2011; Nordbotten et al. 2004), fractures around caprocks (Huo and Gong, 2010), wettability alteration of the caprocks (Chiquet et al. 2007), and so on. In certain circumstances, it is feared that the vertical or upward migration of the leaked CO<sub>2</sub> from the sequestered aquifer may encounter overlying aquifers with potable water resulting in contamination of the water (Dethlefsen et al. 2013; Humez et al. 2011).

The assurance of a secure geological carbon sequestration practice should be accompanied with deployment of monitoring technologies and approaches that detect the movement of the CO<sub>2</sub> plume around the CO<sub>2</sub> storage formation before possible contamination of the potable water resources (Dethlefsen et al. 2013; Zimmer et al. 2011). Characteristics of the potable water contaminated by CO<sub>2</sub> can be determined using various combinations of techniques and tools. Methods based on geoelectrical measurement techniques (Dafflon et al. 2012; Drnevich et al. 2001; Nakatsuka et al. 2010), pH measurements (Yang et al. 2014; Dethlefsen et al. 2013; Dafflon et al. 2012), and membrane sensor (Zimmer et al. 2011) have been used to study the scenarios of CO<sub>2</sub> migration or water contamination by CO<sub>2</sub> in the subsurface.

Dethlefsen et al. (2013) state that the most significant geochemical processes, which occur during the CO<sub>2</sub> contamination of potable water are the changes in the pH and the resultant changes in the electrical conductivity ( $\sigma$ ) of the fluid-fluid-porous media system (i.e., CO<sub>2</sub>-water-porous media system). A lowering of pH during CO<sub>2</sub> dissolution in water is attributed to the formation of carbonic acid, which increases with the partial pressure of the CO<sub>2</sub> (Dafflon et al. 2012). The change in  $\sigma$  during the process is attributed to mineral dissolution from the rock/porous material, which is more pronounced in the carbonate formation. The dynamics of the change in electrical characteristics of CO<sub>2</sub>-contaminated water in the aquifer is discussed by Dafflon et al. (2012). They show the impact of the transition between bicarbonate and carbonic acid in the CO<sub>2</sub>-contaminated water on the electrical resistivity of the system. An increase in the amount of dissolved CO<sub>2</sub> was shown to lead to an initial decrease in the resistivity as a result of an increase in the amounts of bicarbonate and dissolved species in the system. Following the initial decrease in its value, the resistivity value rises at higher

partial pressure of CO<sub>2</sub> in a process attributed to the continued lowering of pH and the related transition of bicarbonate into non-dissociated carbonic acid, which reduces the total concentration of dissociated species (Dafflon et al. 2012). Dethlefsen et al. (2013) show that the change in  $\sigma$  is detectable with geoelectric measurement. The detectability is enhanced by the dissolution of the carbonate, and is reduced in the non-calcareous aquifers. Yang et al. (2014) developed a multicomponent geochemical model that simulated CO<sub>2</sub> dissolution in groundwater, aqueous complexation, mineral reactions (dissolution/precipitation), and surface complexation on clay mineral surfaces. Their study has shown that there is a greater threat of groundwater acidification in a non-carbonate aquifer in the presence of CO<sub>2</sub>. A number of authors (see, Dethlefsen et al. 2013) acknowledge the need for the evaluation of the sensitivity of a geoelectric measurement technique, with respect to the variations in the geological parameters and boundary conditions of the CO<sub>2</sub>. Earlier, Drnevich et al. (2001) investigated the effect of temperature on relative permittivity ( $\epsilon$ ) of water in porous media. Their findings show that  $\epsilon$  decreases with an increase in temperature. But, the study was conducted under atmospheric conditions with only one liquid phase (water) present in the porous medium.

The work of Zimmer et al. (2011) shows the application of silicone rubber as a selective membrane in conjunction with other analytical instruments for the detection of gases present in the underground and borehole. Their work was related to the carbon sequestration project (CO<sub>2</sub>SINK) at Ketzin, Germany. They successfully demonstrate the detection of CO<sub>2</sub> front at observation wells, located at different distances to the injection well, using the gas membrane sensor system.

Considering the above points, the applications of the geoelectric techniques, pH measurements and gas permeation through membrane in the monitoring of the potable water aquifer contaminated by CO<sub>2</sub> can be appreciated. However, some of the above studies were conducted under or near ambient conditions (see e.g., Dafflon et al. 2012; Drnevich et al. 2001). Also, the studies were mainly conducted in sediments consisting of a mixture of materials and metals making it difficult to distinguish the influence of pure minerals and metal content on the measurements made.

From a flow system point of view, the CO<sub>2</sub> contamination of the potable water aquifers can be visualised as a two-phase static system with the water in porous media remaining static while the contaminating plume of CO<sub>2</sub> imposed a pressure head at the boundary (Humez et al. 2011; Das et al. 2014). However, some of the experiments in the above-cited publications consider the detection of the CO<sub>2</sub> as a contaminant alone (see e.g., Zimmer et al. 2011) rather than the effects of the contamination on the potable water in the aquifer.

In light of the foregoing discussions, the threat posed by leakage of CO<sub>2</sub> from the storage aquifer on the potable water aquifer that might lie on its path can easily be acknowledged. The migration of leaked CO<sub>2</sub> from the sequestered site will pass through layers of geological sediments, where potable water aquifers might be found. This scenario calls for the investigations of the behaviour of the CO<sub>2</sub>-contaminated water in the porous media at different temperatures and pressures corresponding to different geological depths in which potable water aquifers might be found in the geological domain. Furthermore, common geological aquifers are rich in silicate and/or carbonate minerals (Espinoza et al. 2011a; Shukla et al. 2010; Verwer et al. 2011; Little and Jackson 2010; Dethlefsen et al. 2013). These minerals might influence the characteristics of the potable water in the aquifers contaminated by CO<sub>2</sub>. Therefore, it is necessary to conduct investigations with well-characterised porous media (e.g., using silicate or carbonate rich materials).

To bridge the above-identified gaps in the current knowledge, this work aims to utilize well-characterised unconsolidated porous media, rich in silicate and carbonate minerals, respectively, to investigate the characteristics of the water-saturated porous media contaminated by CO<sub>2</sub>. Investigation methods to be used include pH measurements, application of silicone rubber as a membrane in the monitoring of CO<sub>2</sub> diffusion in the contaminated water-saturated porous media, and the geoelectrical measurement techniques for the determination of the bulk relative permittivity ( $\epsilon_b$ ) and the bulk electrical conductivity ( $\sigma_b$ ) of the CO<sub>2</sub>-water-porous media system. The investigations are designed to mimic contamination of the potable water aquifer by CO<sub>2</sub> at different geological depths. Thus, different pressure and temperature of CO<sub>2</sub> are imposed on the experimental domain. This design satisfies the call by Dethlefsen et al. (2013) for the evaluation of the sensitivity of the boundary conditions of CO<sub>2</sub> on geoelectrical measurement methods. Unlike the works previously discussed, the present investigation discusses simultaneous measurements of pH, geoelectrical parameters and gas permeation through a membrane, as a comprehensive procedure for the monitoring of the water-saturated silicate and carbonate porous media contaminated by CO<sub>2</sub>.

In this work, the porous media domain was prepared using well-characterised particles of silica sand and limestone. The domain was used in the experimental investigations of the effects of CO<sub>2</sub> contamination on the water-saturated porous media. This work involves the measurements of the pH and geoelectrical parameters ( $\epsilon_b$  and  $\sigma_b$ ) to monitor changes in the characteristics of the water-saturated porous media contaminated by CO<sub>2</sub>. The permeation of CO<sub>2</sub> through the nonporous silicone rubber was also recorded using a membrane-sensor system. The results of the investigations are discussed in relation to different geological

depths where potable water aquifers might be encountered by a plume of CO<sub>2</sub> migrating from the storage aquifer, where leakage occurs. The time domain reflectometry (TDR) method was used to measure the bulk relative permittivity ( $\epsilon_b$ ), and the bulk electrical conductivity ( $\sigma_b$ ) of the CO<sub>2</sub>-water-porous media system. Further details about the TDR measurement techniques and principles are expatiated in the methodology section (Section 9.2).

## 9.2 Methodology

### 9.2.1 Porous domain and materials

The experiments in this work were conducted using two materials, namely, silica sand (DA 14/25) and limestone particles (Trucal 6). They have been chosen so as to provide two porous domains (silicate and carbonate domains) with different chemical but similar physical properties for separate experiments. The silica sand was purchased from Minerals Marketing (Buxton, UK), while the limestone was purchased from the Tarmac Buxton Lime and Cement (Buxton, UK). The physical and chemical properties of the samples are listed in Table 7.1. From the Table 7.1, it can be seen that the physical properties of the two materials are very similar. The constant-head permeameter technique (Bear 2013) was used to determine the permeability of the packed particle bed. Before use, the porous domains were pre-treated by washing in tap water and dried for at least 24 hours to remove any clay content. To ensure uniform particle deposition in every experiment, the sand was poured through a large sieve into the cell, which initially contains water to minimise air trap. The characterizations of the water-saturated porous media in the presence of CO<sub>2</sub> relied on the measurements of the system electrical parameters, pH and CO<sub>2</sub> permeation through a non-porous silicone rubber membrane. The silicone rubber sheet (part number: RS 340-2689) used in the gas permeation experiments was obtained from RS Components Ltd (Northants, UK) with a thickness of 3mm.

### 9.2.2 Instrumentations and sample holder

*In situ* bulk relative permittivity and electrical conductivity measurements were made with the three-pin time domain reflectometry probes (TDR probes) already described in subsection 7.2.2. Figure 9.1(A) is a schematic diagram of the experimental set up, which is similar to that described in Figure 7.1. indicates the port for the TDR probes at the centre of the sample holder. Two pressure transducers (PTs) HySense PR 140 (Hydrotechnik, GmbH, Limburg an der Lahn, Germany) were included at the directly opposite ports at the centre of the domain. The PTs were held in steel holders together with the silicone rubber membranes. The arrangement permits the *in situ* measurement of the pressure of CO<sub>2</sub> that diffuses

through the water-saturated porous domain and permeates through the membrane. This is already illustrated in Chapter eight. Fresh samples of silicone rubber were used at the start of each experiment to measure diffusion of the gas through the water-saturated domain. Some important procedures and features of the experimental diagram are previously described in Chapters 7 and 8. The pH measurement was performed with the aid of the digital pH meter (Hydrus 500) (Fisher Scientific, Loughborough, UK).

## 9.2.3 Experimental Procedure

### 9.2.3.1 Equipment set up

All experiments were conducted in a 4cm sample holder cell. The sample holder was set up by placing the body of the sample holder on the bottom end piece (sample holder base). Ports on the sample holder were plugged with steel holders, which hold the PTs and the membrane. These were then connected to the peripheral devices as discussed above. A small amount of tap water was poured into the cell to a certain position followed by pouring of sand through a metal sieve of appropriate size to ensure uniform sand deposition and prevent air trap. Equal amount of sand (500g) was used in all experiments. A distributor was placed on the top of the sand bed. Then, the top end piece with the hydrophobic membrane was placed over the sand bed. After tightening all the tubing connection points, more tap water was passed into the sample from the water tank and pressurised up to the experimental set pressure using the hand pump (see, Figure 9.1). At high pressure, all air present in the tubing and the sand was considered dissolved (Plug and Bruining, 2007). Water tank valve (V-4) was then closed. Level of the water in the tubing was then adjusted by letting off some water through the outlet valve, V-5. This was done to ensure that the water level stays at the surface of the sand bed in the sample holder, so that the incoming CO<sub>2</sub> will make contact with the water at the sand surface. CO<sub>2</sub> used in this work was obtained from BOC Industrial gases (Loughborough, UK) at 99.9% purity. The supercritical fluid pump (Teledyne Isco, Lincoln NE, USA) was filled with liquid CO<sub>2</sub> from the CO<sub>2</sub> cylinder by opening of the valve, V-1, and setting the pump on refill mode. When the pump tank was full, the CO<sub>2</sub> cylinder valve, V-1, was closed and the pressure on the supercritical fluid pump was raised to the experimental pressure while valve, V-2 remained closed. When the supercritical fluid pump was set at the experimental pressure, the heater was switched on and set at the experimental temperature. When the temperature and pressure are at equilibrium, valve, V-2 was opened and the CO<sub>2</sub> was supplied into the upstream tubing up to the top of the sand bed in the sample holder, forming interface with water-saturated domain.

### 9.2.3.2 Design of the experimental conditions

As explained under the introduction of this work, the experiments were designed to fulfil the conditions of temperature and pressure that are likely to be encountered by CO<sub>2</sub> migrating or escaping from the geological sequestration site into the shallow subsurface. Figure 9.2 illustrates this scenario. In Figure 9.2, potable water aquifers are located at different depths in the sediment. The leaked CO<sub>2</sub> follows a pathway (e.g., fracture in caprock, high permeability pathway, etc.) to reach the water aquifer. The water aquifers in Figure 9.2, can be viewed separately (i.e., one aquifer in one sediment) or collectively (i.e., all aquifers at different depths of a single sediment). The hypothetical geological conditions were determined using the reports of the Best (2013) for geobaric pressure gradients and that of the Nordbotten et al. (2004) for warm basin geothermal gradient. The conditions were listed in Table 9.1. For safety concerns, the experiments were limited to conditions corresponding to 200m depth. In Table 9.1, temperature and pressure at which injections of CO<sub>2</sub> were done differ for each depth considered. This is because temperature and pressure vary together with depth in geological sediment (Best 2013; Nordbotten et al. 2004). Table 9.1 further shows the varying density and dynamic viscosity of CO<sub>2</sub> under different conditions. Under these conditions, the *in situ* measurements of the electrical parameters (bulk relative permittivity ( $\epsilon_b$ ) and the bulk electrical conductivity ( $\sigma_b$ )) and the responses of membrane-sensor system were conducted. But the pH measurements were conducted under atmospheric conditions by immediate measurements of small sample taken from the domain.

Table 9.1: List of conditions which were experimentally simulated in this study

Depth (m)	Temperature (°C)	Pressure (bar)	CO <sub>2</sub> Density (kg/m <sup>3</sup> ) <sup>a</sup>	CO <sub>2</sub> Dynamic viscosity (10 <sup>-6</sup> Pa s) <sup>a</sup>
50	22.25	13.5	26.34	14.98
100	24.5	27	56.87	15.37
200	29	54	144.0	17.20

a. [http://www.peacesoftware.de/einigewerte/CO2\\_e.html](http://www.peacesoftware.de/einigewerte/CO2_e.html)

From a practical point of view, it may be surprising whether a membrane-sensor system can be successfully applied at deep geological sediment. Earlier, Lamert et al. (2012) demonstrated the field measurements of electrical parameters to monitor the subsurface CO<sub>2</sub> movement. They installed several copper electrodes at various depths up to 18.5m below the ground level around the CO<sub>2</sub> injection site in order to monitor the movement of injected CO<sub>2</sub>

in the space surrounding the injection site. Therefore, if copper electrodes can be buried at such geological depths, it is believed that miniaturised pressure sensor can be coupled with highly selective non-porous membranes at various depths for similar practical applications.

### 9.2.3.3 pH measurement

The pH of the solution was measured at intervals using the pH meter (Hydrus 500, Fisher Scientific, Loughborough, UK). At any particular time of interest, a solution sample was taken by opening of the valve, V-6 (see, Figure 9.1). The BPR ensured that the system pressure remained stable after the short disturbance of the opening of the valve. The sample pH was immediately measured using the pH meter. The pH meter was regularly calibrated to ensure consistent and reliable measurements.

### 9.2.4 Time domain reflectometry

For the measurements of the geoelectrical parameters in the water-saturated domain contaminated by CO<sub>2</sub>, time domain reflectometry (TDR) method (Lamert et al. 2012; Drnevich et al. 2001; Plug et al. 2007b) was used. The TDR probes serve as the waveguide extension on the coaxial cable connected to the TDR100 (electrical impulse generator). It will be recalled that the TDR probes used in this work are made in the workshop in order for them to be suitable for high temperature and pressure conditions of this work. But, the impulse generator (TDR100) to which the cable of the TDR probes was connected, the multiplexer, and the datalogger are branded products (Campbell Scientific Ltd, Shepshed, UK). The TDR system was calibrated to determine the necessary parameters (e.g., offset and multiplier) following the instruction manual of Campbell Scientific Ltd (Shepshed, UK). The TDR100 generates the electrical pulses, which travel through the coaxial cable connected to the TDR probes. Owing to the contrast in impedance resulting from materials surrounding the TDR probes, reflections occur, which are sent back to the source (TDR100). TDR100 samples and digitizes the reflection waveforms to infer the impedance value. The impedance value is related to the geometrical configuration of the probe and inversely related to the relative permittivity of the surrounding medium. Owing to sharp contrast between the relative permittivity of the porous medium and the surrounding fluids, a change in fluid content causes a change in the bulk relative permittivity, which is seen as a change in probe impedance affecting the shape of the reflected waveform. Information from the differences in shape of the reflection is used by the TDR measurement system to determine the bulk relative permittivity ( $\epsilon_b$ ) and the bulk electrical conductivity ( $\sigma_b$ ) of the system.

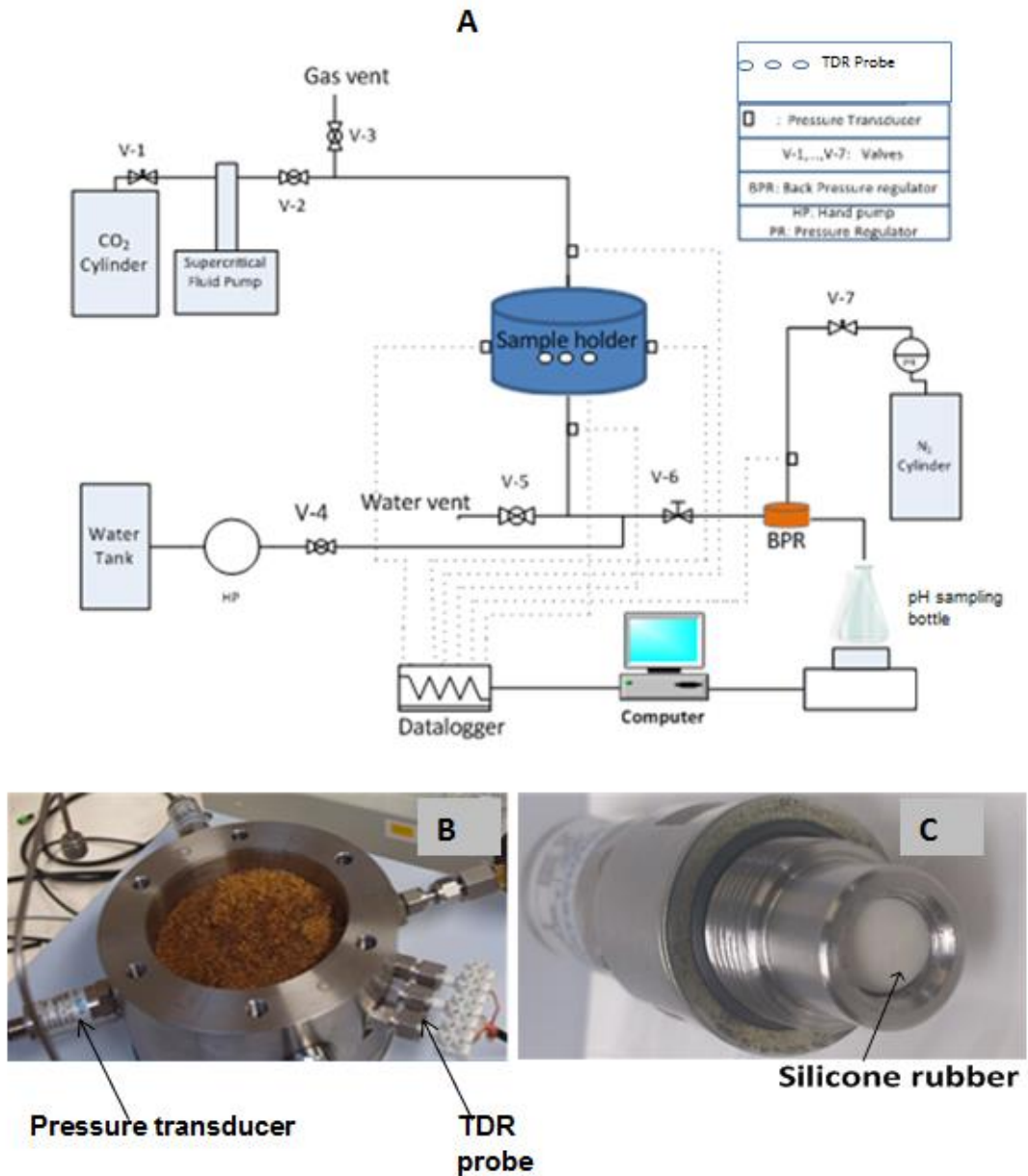


Figure 9.1: (A) Schematic diagram of experimental rig for the investigation of CO<sub>2</sub>-contamination of water in porous media. (B) Photograph of the sample holder showing silica sand, pressure transducer and TDR (C) Steel holder showing the pressure transducer and the silicone rubber sheet (metal cap not shown). Sample holder size: internal diameter=10cm, sample height=4cm.

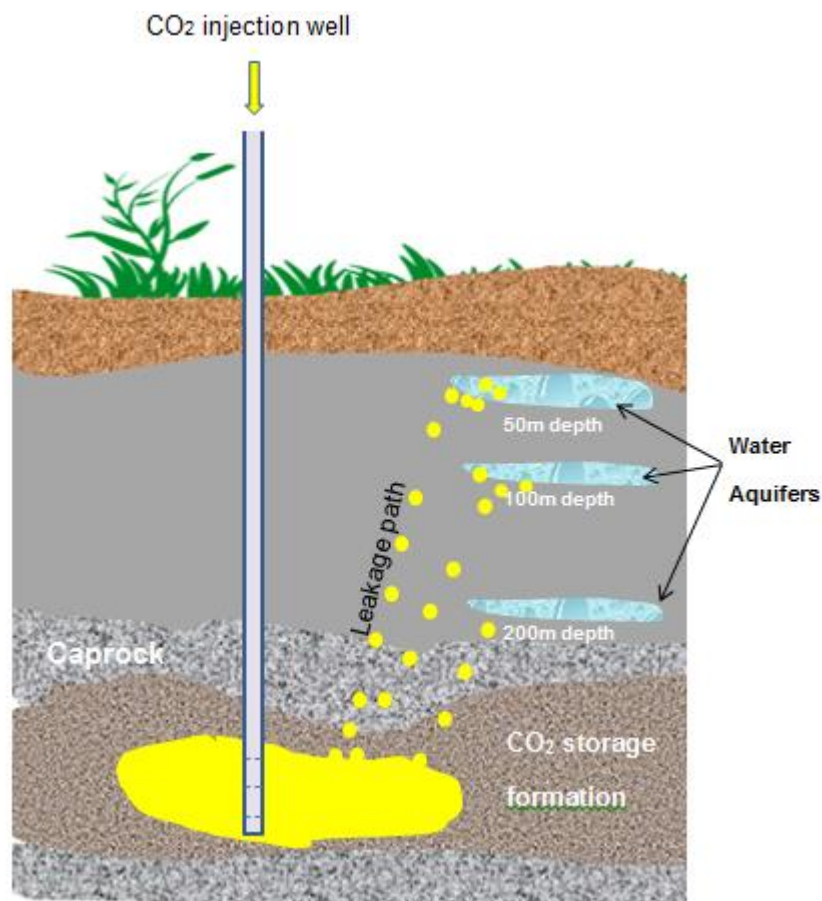


Figure 9.2: Hypothetical representation of geological sediment with potable water aquifers located at different depths. This work considers the effect of aquifer depth on CO<sub>2</sub> contamination of water-saturated aquifer.

### 9.2.5 Calculation of CO<sub>2</sub> flux through the non-porous membrane

To assess the performance of a membrane in terms of the mass of gas that permeate through its matrix, Shahrabi et al. (2012) describe the gas permeate flux ( $J$ ) through the membrane. The mathematical expression is already stated in equation (8.3). The mass of the gas that permeates through the membrane was calculated by assuming the ideal gas relation for the CO<sub>2</sub>. Since the gas volume of the membrane-sensor system is known while the pressure change (in the membrane-sensor system), as a result of the increase in the amount of permeated gas is automatically recorded, the mass of the CO<sub>2</sub> present in the open volume of the membrane-sensor system can be readily determined, using the ideal gas equation.

## 9.3 Results and discussions

The leakage of CO<sub>2</sub> from the geological carbon sequestration aquifer may result in the contamination of potable water aquifers that lie above the aquifer (Dethlefsen et al. 2013;

Tao and Bryant 2014; Little and Jackson 2010). This will affect the pH and the electrical properties of the water-filled porous media, as a result of the interactions among the CO<sub>2</sub>, water and the rock minerals leading to geochemical changes (Dafflon et al. 2012). The changes in the characteristics of the water-saturated porous domain as a result of the contamination by CO<sub>2</sub> are expected to be different depending on whether the contamination takes place in a carbonate or silicate aquifer. It is therefore important to understand the behaviours of the CO<sub>2</sub>-contaminated water in porous media together with the influence of mineral content of the porous media. The results of the investigations of the scenarios described above using geoelectrical, pH and membrane measurement techniques are presented and discussed below for various conditions corresponding to different geological depths at which potable water aquifers might be found in the geological domain.

### 9.3.1 Change in pH of the water-saturated domain contaminated by CO<sub>2</sub>

Migration of leaked CO<sub>2</sub> from a storage site might encounter a potable water aquifer that lies along its path. As such, the change in the pH of the CO<sub>2</sub>-contaminated water in the aquifer can be used to monitor this scenario (Little and Jackson 2010; Dethlefsen et al. 2013). In the laboratory experiment, the change of pH with time for water-saturated silica sand contaminated by CO<sub>2</sub> is shown in Figure 9.3 at conditions corresponding to 200m depth (see, Table 9.1). The scenario in Figure 9.3 shows the existence of three stages in the profile of pH with time for CO<sub>2</sub>-contaminated water in silica sand. Following the start of the experiment, there was a decline in the pH value with time. After this initial decline, the second stage begins with a short rise in pH value. This is then followed by the third stage, which is a period of steady state in the pH value, and it remains till the end of the experiment. In Figure 9.3, the immediate fall in the pH value at the start of the experiment can be attributed to the quick dissolution of CO<sub>2</sub> in the water in the porous sample. The decrease in pH continues after the start of the experiment before it rises again and finally levels off at the steady pH value, which lasts until the end of the experiment. However, the final steady state value of the pH is still lower than the original pH value of the uncontaminated water.

The behaviour described can be interpreted as follows: The region of continued reduction of pH indicates the increase in the amount of dissolved CO<sub>2</sub> leading to the formation of carbonic acid, thereby lowering the pH. Increase in the concentration of carbonic acid results in the lowering of pH (Dafflon et al. 2012). The rise of pH following the initial decline indicates a reverse reaction leading to the formation of aqueous and possibly gaseous CO<sub>2</sub> and water from the carbonic acid. Following the period of forward and reverse reactions, the system attains equilibrium. This is represented by the steady state value of pH, which remains until

the end of the experiment. Furthermore, Figure 9.3 shows the repeatability of the experiments (run 1 and run 2).

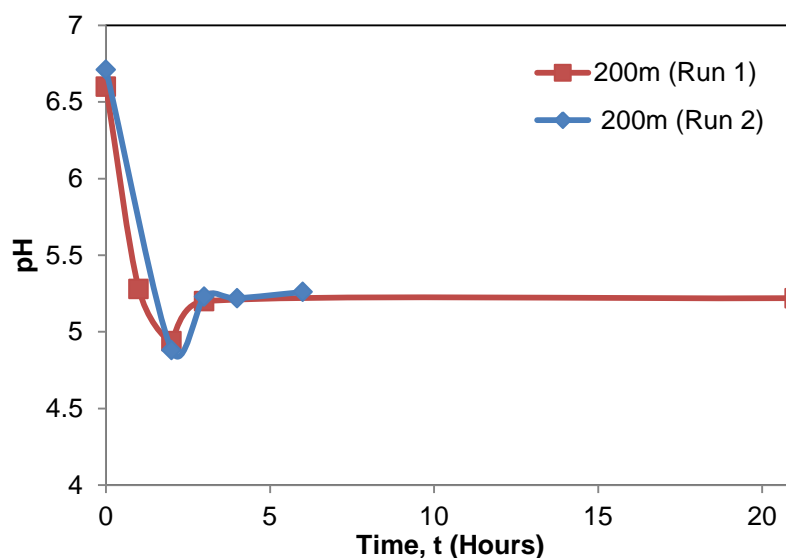


Figure 9.3: Replicate experimental results showing the three stages of changes in pH for water-saturated silica sand contaminated by CO<sub>2</sub> at conditions corresponding to 200m depth.

Table 9.2 shows the results of the changes in pH for all the experiments performed in this work under different conditions and in different porous media. The results in Table 9.2 show the pH values at the start of the experiment and at the steady state. Judging from Figure 9.3, the pH in the system reaches a steady state value quite readily (i.e., at less than 3 hours). The results reported for steady state values in Table 9.2 were obtained at the end of each of the experiments, which often took more than 20 hours. Table 9.2 shows that the steady state value of pH decreases from the initial value at the start of the experiment, as a result of the CO<sub>2</sub> dissolution in the water-saturated silica sand. The decrease in pH can be seen to be an indication of the formation of carbonic acid as a result of the dissolution of CO<sub>2</sub> in the water. Also, it is shown in Table 9.2 that the change in pH increases with depth. This implies that the pH change is a function of pressure and temperature because the pressures and temperatures, listed in Table 9.1, are dependent on depth. But, looking at the temperature and pressure values for different depths in Table 9.1, the temperature only increases by approximately 10% from 50 to 100m depth while the pressure increases by over 100% for the same change in depth. Thus, it can be said that the change in pH with depth is mainly due to the effect of pressure. It is known that the dissolution of CO<sub>2</sub> in water increases with pressure (Omambia and Li 2010; Duan and Sun 2003; Chang et al. 1998; Dafflon et al. 2012).

Table 9.2: Changes in pH of water-saturated silicate and carbonate porous media in the presence of CO<sub>2</sub> at various depths

Depth (m)	pH			
	pH at Start		pH at Steady state	
	Silica	Limestone	Silica	Limestone
50	6.7	7.01	5.34	6.02
100	6.7		5.26	
200	6.7	7.01	5.22	5.85

In the limestone porous domain, the steady state value of pH of the water contaminated by CO<sub>2</sub> also changes with depth. This is also shown in Table 9.2 for conditions corresponding to the 50 and 200m depths. To understand the influence of mineral contents of the porous medium on the pH of the contaminated water, comparison was made between the behaviours of the CO<sub>2</sub>-contaminated water in silica sand and limestone. The properties of the media are already listed in Table 7.1. As shown in Table 9.2, the changes in pH value (i.e., percent difference in starting and the steady state pH values) for water-saturated limestone in the presence of CO<sub>2</sub> were approximately 14 and 17% at 50 and 200m depths, respectively. In water-saturated silica sand, the corresponding changes in pH values were 20 and 22%, respectively. Thus, pH change is more severe in silicate than carbonate porous domains. The results indicate that in the presence of CO<sub>2</sub>, severe groundwater acidification will occur in non-carbonate aquifers (Yang et al. 2014) with time and still remains higher in limestone than silica sand. This can be attributed to the alkaline nature of the limestone. It is known that alkalinity raises the value of the pH.

### 9.3.2 Bulk relative permittivity of the water-saturated domain in the presence of CO<sub>2</sub>

Investigations of the CO<sub>2</sub>-contaminated water in the porous media using geoelectrical measurement techniques further reveals the responses of the bulk electrical parameters ( $\epsilon_b$  and  $\sigma_b$ ) with the dissolution of CO<sub>2</sub> in the water-saturated domain. It is known that the bulk electrical parameters of the water-saturated porous media domain change with decrease in the saturation of the wetting phase (water) (Plug et al. 2007a, b; Drnevich et al. 2001). But, in the case of CO<sub>2</sub> contamination of the water in porous media, static conditions are envisaged, where there is no noticeable change in the water saturation. Thus, in this work, the

behaviours of the geoelectrical parameters in the contaminated porous media domain are plotted against time instead of the water saturation as in the studies cited previously. Figure 9.4 shows the trend in the bulk relative permittivity ( $\epsilon_b$ ) for the water-saturated silica sand contaminated by  $\text{CO}_2$ . There is no sign of change in the  $\epsilon_b$  for the entire duration of the experiment. Figure 9.4 also shows repeatability of the measurements under similar conditions. This is indicated by run 2 in the Figure 9.4.

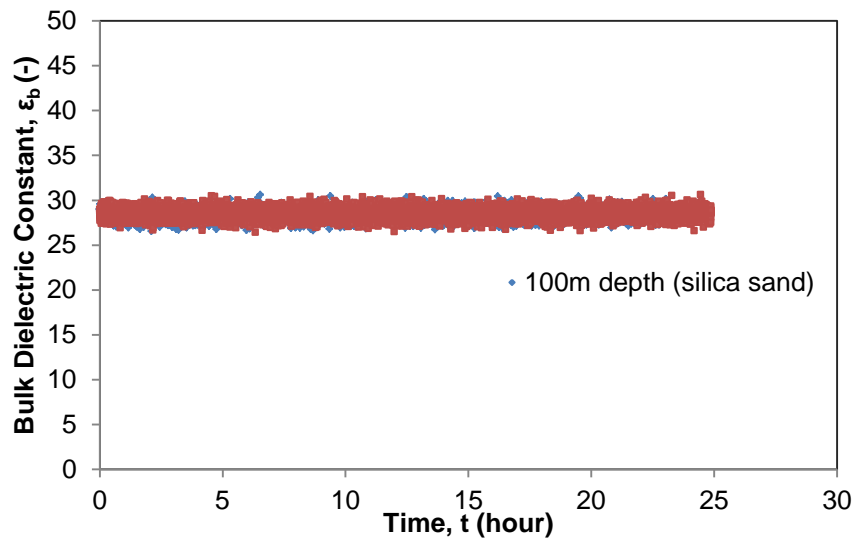


Figure 9.4: Replicate experiments for bulk relative permittivity of water-saturated silica sand contaminated by  $\text{CO}_2$  at conditions corresponding to 100m depth.

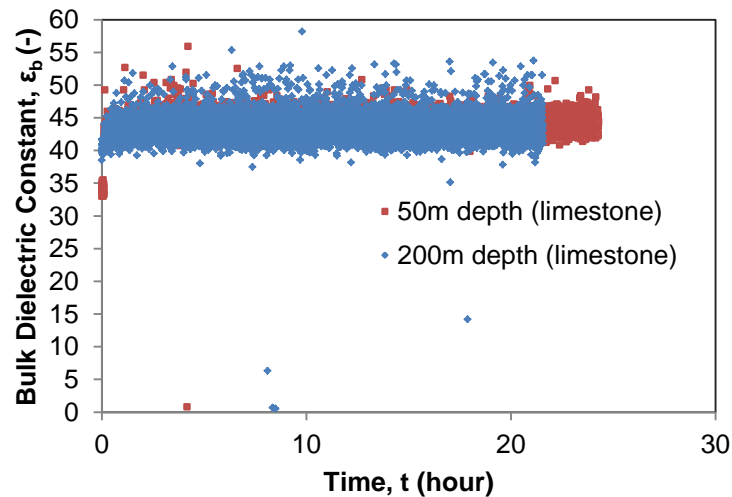


Figure 9.5: Bulk relative permittivity for water-saturated limestone contaminated by  $\text{CO}_2$  at conditions corresponding to 50 and 200m depths.

In addition, Figure 9.5 shows the  $\epsilon_b$  for the water-saturated limestone contaminated by  $\text{CO}_2$  at conditions corresponding to 50 and 200m geological depths.

The curve of  $\epsilon_b$  in Figure 9.5 shows no sign of change at different depths in the limestone porous domain. Thus, it can be inferred that the  $\epsilon_b$  for the water-saturated porous media

contaminated by CO<sub>2</sub> does not change with increase in the dissolution of CO<sub>2</sub> in the water. It must be distinguished that investigations in this work were done under static conditions where the saturation of water in porous media domain does not change. This is unlike the work of Plug et al. (2007b) where the  $\epsilon_b$  was shown to vary with change in water saturation as CO<sub>2</sub> displaces the resident water in the porous media. Thus,  $\epsilon_b$  is dependent on the flow condition of the two-phase system in the porous medium.

### 9.3.3 Bulk electrical conductivity of the water-saturated domain in the presence of CO<sub>2</sub>

Another electrical parameter of importance is the electrical conductivity. The behaviour of the bulk electrical conductivity ( $\sigma_b$ ) in a potable water aquifer contaminated by CO<sub>2</sub> was also examined. Figure 9.6 shows the replicate experimental results for the  $\sigma_b$  in the water-saturated silica sand contaminated by CO<sub>2</sub>. There appears short rise in the  $\sigma_b$  for the system before constant value was attained. This can be interpreted as a period of increase in ionic strength of the pore fluid owing to the dissolution of CO<sub>2</sub>, leading to the increase in the electrical conductivity, as a result of the formation of readily-dissociated bicarbonate from the carbonic acid. At the period of increase in  $\sigma_b$ , the reaction seems to produce more bicarbonate from the carbonic acid. The short rise in  $\sigma_b$  can be seen to coincide with the initial period of decrease in the pH shown in Figure 9.3, where the rate of bicarbonate formation from nondissociated carbonic acid seems high. This period is characterised with the rise in the ionic concentration of water-saturated porous domain contaminated by CO<sub>2</sub> (Dafflon et al. 2012). Thus,  $\sigma_b$  rises during this period as shown in Figure 9.6. As the process continues, equilibrium was reached at which the value of  $\sigma_b$  becomes steady as shown in Figure 9.6. In Figure 9.3, the second stage of short rise in the pH after initial decrease was explained to be due to the reverse formation of aqueous and possibly gaseous CO<sub>2</sub> and water from the carbonic acid. This stage seems to provide an ionic equilibrium state in the system, leading to the steady state value in  $\sigma_b$ . Thus,  $\sigma_b$  behaviour in Figure 9.6 does not reflect the second stage in pH since ionic species may not change at this period, i.e., second stage of pH change in Figure 9.3 may be concerned with reverse reaction of nondissociated carbonic acid, leaving the amount of ionic species from dissociated bicarbonate unchanged. Figure 9.6 further shows the repeatability of the measurements under similar conditions (indicated by run2).

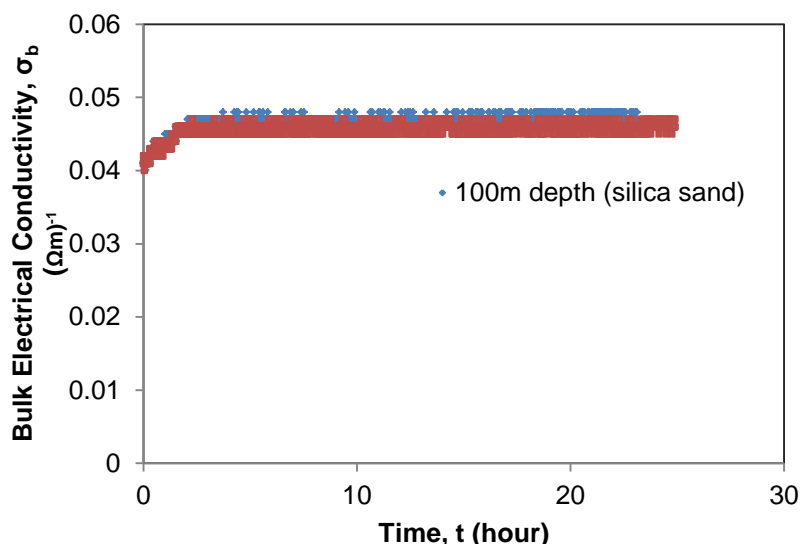


Figure 9.6: Replicate experiments showing bulk electrical conductivity of water-saturated silica sand contaminated by  $\text{CO}_2$  at conditions corresponding to 100m depth.

A similar scenario was observed in  $\sigma_b$  for water-saturated limestone contaminated by  $\text{CO}_2$ . This is shown in Figure 9.7 for conditions corresponding to 50 and 200m depths (see, Table 9.1). The  $\sigma_b$  increases with depth. This can be seen as the effect of pressure on  $\sigma_b$ . The results imply that the  $\text{CO}_2$  dissolution and the amount of bicarbonate increase with pressure (depth) prior to the attainment of equilibrium. Furthermore, a comparison of Figure 9.6 and 9.7 shows that the  $\sigma_b$  in limestone is far higher than in silica sand under similar conditions of injected  $\text{CO}_2$ .

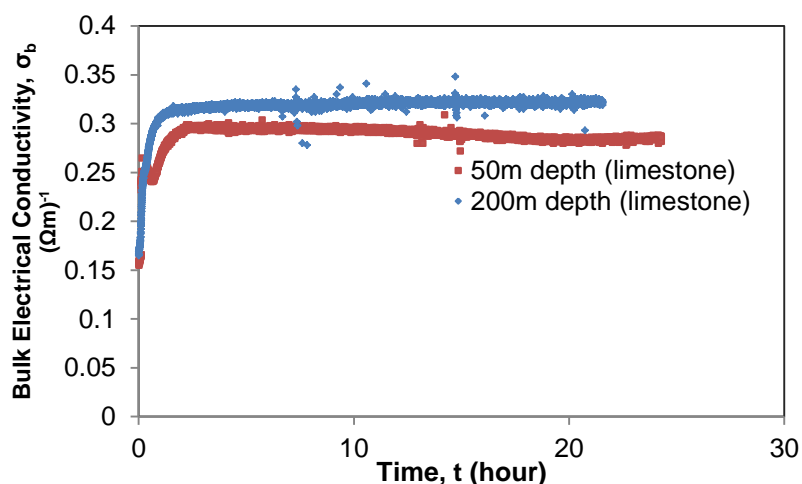


Figure 9.7: Bulk electrical conductivity of water-saturated limestone at conditions corresponding to 50 and 200m depths.

A model by Yang et al. (2014) found increasing trend in concentrations of major ions in the carbonate sediment (i.e., limestone). Therefore, mineral dissolution is more pronounced in limestone, leading to higher ion concentration in the domain and, in effect, higher,  $\sigma_b$ .

### 9.3.4 Diffusion of CO<sub>2</sub> in the water-saturated domain and its permeation through silicone rubber membrane

When CO<sub>2</sub> contacts the potable water aquifer, contamination of the water will occur via dissolution and diffusion of CO<sub>2</sub> through the water-saturated domain. Keeping this in mind, this section discusses the results of the monitoring of the diffusion process using a silicone rubber membrane devised with pressure sensors. The change in the pressure reading on the membrane-sensor system occurring via permeation of the CO<sub>2</sub> through the membrane was recorded as an indicator of the diffusion process.

Figure 9.8 shows experimental results of CO<sub>2</sub> permeation through silicone rubber membrane at different conditions corresponding to 50, 100, and 200m depths. As the depth increases, the permeation rate increases. The start of the permeation was characterised by a rise in the pressure of the permeated gas. At 50m depth, the permeation starts after 8 hours of contamination of the water-saturated domain by CO<sub>2</sub>. This reduces to around 4hrs at 100m depth and less than an hour at 200m depth.

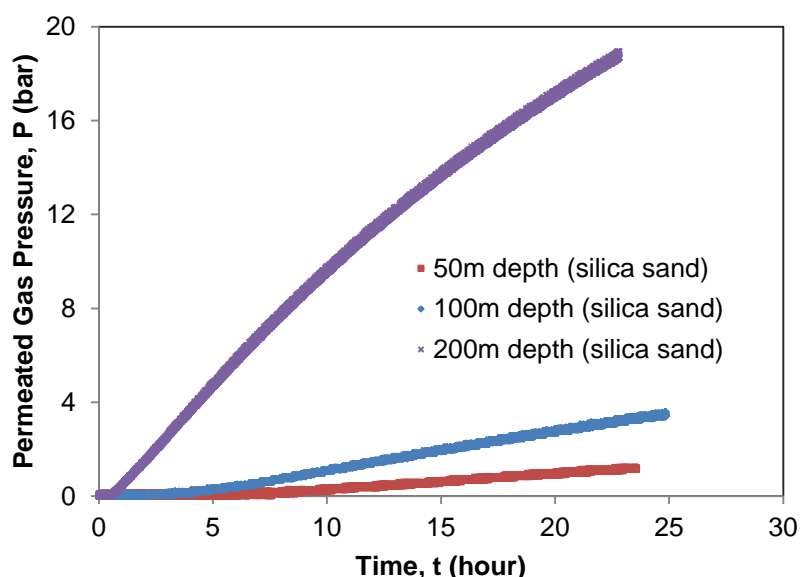


Figure 9.8: Permeation of CO<sub>2</sub> into silicone rubber membrane via diffusion through water-saturated silica sand.

Thus, the permeation rate of CO<sub>2</sub> through the non-porous membrane increases, as the pressure or depth increases. Therefore, CO<sub>2</sub> leakage and contamination of a potable water

aquifer can be quickly detected at greater geological depths using the membrane-sensor system.

The flux of CO<sub>2</sub> through the membrane is shown in Figure 9.9. The flux values are very small, but Figure 9.9 shows that the CO<sub>2</sub> flux increases with depth. At 200m depth, the flux values show geometrical rise in comparison to the flux values at 50 and 100m depths. This can be due to the ease at which membrane resistance is overcome at greater depth or higher pressure. Therefore, at greater geological depth, flux of CO<sub>2</sub> through non-porous membrane can be easily detected and can give indication of the presence of CO<sub>2</sub>.

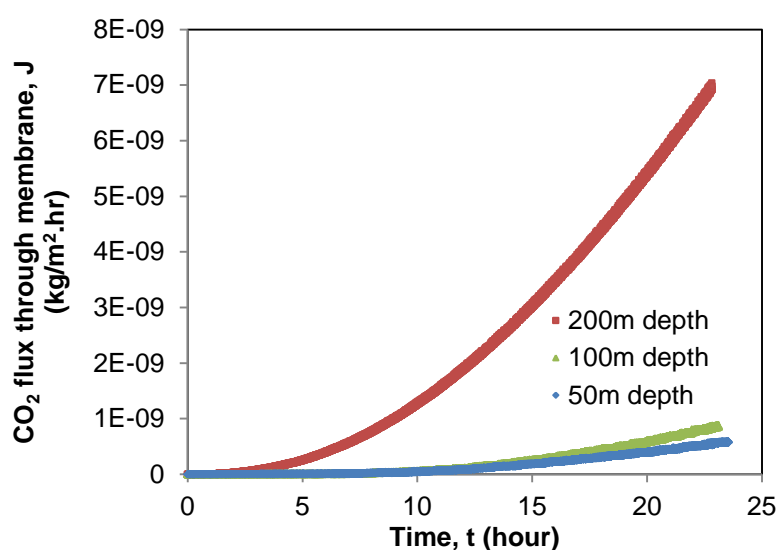


Figure 9.9: CO<sub>2</sub> flux through the silicone rubber membrane via diffusion through water-saturated silica sand.

### 9.3.5 A mathematical expression between pH and $\sigma_b$

The previous discussions show the existence of a relationship between the pH and  $\sigma_b$  of the porous domain. It was earlier stated that the short rise in  $\sigma_b$  appears to coincide with the initial period of decrease in the pH as shown in Figure 9.3, which seems to indicate a high rate of bicarbonate formation from non-dissociated carbonic acid. An assessment of the results shows that the  $\sigma_b$  is dependent on the pH and the initial value of  $\sigma_b$ . Its dependence on the former is evident in the increase of  $\sigma_b$  as the pH decreases while its dependence on the latter is shown by higher  $\sigma_b$  values in water-saturated limestone than the water-saturated silica sand. The water-saturated limestone domain has a higher initial  $\sigma_b$  value. In order to generalise this behaviour a mathematical expression is developed between these parameters, which is expressed as follows:

$$\sigma_{br} = f(\text{pH}_r, \sigma_{b1}) \quad (9.1)$$

$\sigma_{br}$  is the ratio of the steady state value of  $\sigma_b$  (i.e., the value of  $\sigma_b$  when the pH is at steady state) to the initial value of  $\sigma_b$  (i.e.,  $\sigma_{bi}$ ).  $\sigma_{bi}$  is the initial value of  $\sigma_b$  before the injection of  $\text{CO}_2$ .  $\text{pH}_r$  is the ratio of the steady state value (i.e., pH value at steady state) to the initial value of the pH (i.e., the pH value before the injection of  $\text{CO}_2$ ). This arrangement enables the determination of the change in  $\sigma_b$  at different conditions and porous media properties provided the data of the initial  $\sigma_b$  and  $\text{pH}_r$  are available. An attempt to develop a mathematical expression has been made using the combined data from the experiments involving silica sand and limestone porous domains. A regression has been performed using MATLAB (Matrix Laboratory, Mathworks, Cambridge, UK) and the resulting expression is shown in equation (9.2):

$$\sigma_{br} = 3.87\sigma_{bi}^{0.42}\text{pH}_r^{-0.4} \quad (9.2)$$

The regression has a  $R^2$  value of 0.997. Comparisons of the results from the experiments and predictions by equation (9.2) are shown in Figure 9.10. In Figure 9.10, it is found that the experimental results and the mathematical predictions by equation (9.2) match well for different porous media samples at different depths. This gives the possibility that the final  $\sigma_b$  of a water-saturated porous domain into which  $\text{CO}_2$  is injected can be determined if the changes in pH and the initial values of  $\sigma_b$  are known.

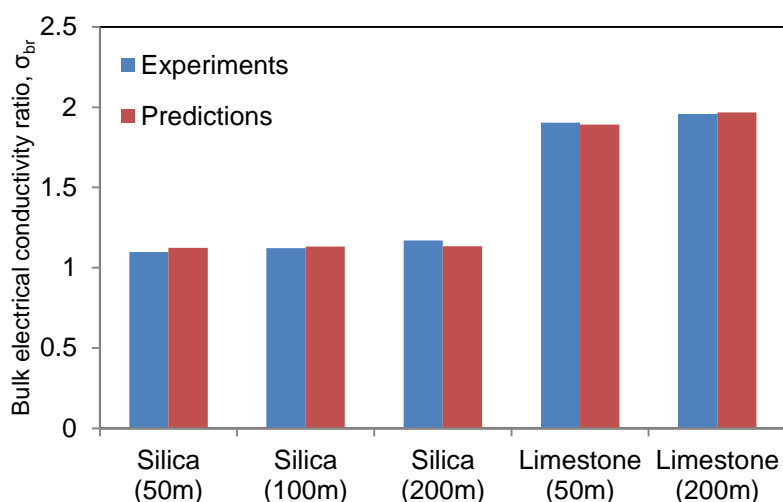


Figure 9.10: Comparison of the ratios of the bulk electrical conductivity ( $\sigma_{br}$ ) from the experiments and mathematical predictions

The results and discussions examine experimental techniques to monitor a plume of  $\text{CO}_2$  around the potable water aquifers. Since a  $\text{CO}_2$  plume resulting from leakage of  $\text{CO}_2$  from carbon storage aquifer can migrate through different depths of geological sediments, the

studies were conducted at conditions corresponding to different geological depths using geoelectrical, pH and membrane flux parameters. The results showed the applicability of multi-parameter characterization techniques in the monitoring of CO<sub>2</sub>-contaminated water in the different aquifers. A mathematical expression developed for the relationship among various parameters can provide an estimate of the change in the  $\sigma_b$  and pH of the water-saturated silica sand and the limestone into which CO<sub>2</sub> is injected. However, further studies are needed in the application of the techniques at field scale. Also, there is a need for more experiments to establish a distinguishing criterion between different gases that can permeate the membrane in the subsurface.

## 9.4 Summary

This work looked into the characteristics of potable water contaminated by CO<sub>2</sub> in the silicate and carbonate porous media domain, respectively. The results showed three stages in the profile of pH change with time as CO<sub>2</sub> dissolved and diffused in water-saturated silica sand. The first stage was characterised by rapid decline in the pH from the start of the experiment associated with quick dissolution of CO<sub>2</sub> and the formation of carbonic acid along with bicarbonate. This was followed by the second stage, showing a short rise in pH value, which is attributed to the reverse reaction, leading to the formation of aqueous and gaseous CO<sub>2</sub> and water from carbonic acid. The third stage was that of the equilibrium in the forward and the reverse reactions, marked by steady state in pH value, which remained unchanged until the end of the experiment. The bulk electrical conductivity ( $\sigma_b$ ) increased at the contact of the CO<sub>2</sub> with the water-saturated porous media domain in a process attributed to the formation of ionic species, especially bicarbonate from the dissolution of CO<sub>2</sub> in water. The rise in  $\sigma_b$  coincided with the first stage of the change in the pH of the system. The  $\sigma_b$  was higher in limestone than silica sand, and it increased with depth or domain pressure. But, the bulk relative permittivity ( $\epsilon_b$ ) showed no change with time and pressure. A silicone rubber membrane showed the promise of detecting the diffusion of the CO<sub>2</sub> through the water-saturated domain and the rate of permeation of CO<sub>2</sub> through the membrane was shown to increase with depth. A mathematical relationship developed in this work shows the dependence of  $\sigma_b$  on the pH and initial value of  $\sigma_b$ .

## CHAPTER TEN

### CONCLUSIONS AND RECOMMENDATIONS

#### 10.1 Conclusions

Two-phase systems in porous media are important in the Chemical Engineering process industries with significant impacts on the global economy and environments. This work consists of experiments and numerical simulations conducted to investigate the two-phase flow/static systems in porous media. The fluids used in this work to investigate two-phase systems were silicone oil/water and CO<sub>2</sub>/water. The former was used in relation to the study of secondary/tertiary oil recovery in the oil industry, while the latter was studied in connection with the *in situ* process involved in the geological carbon sequestration. The investigations examine the factors affecting the characterization parameters that are important in the monitoring, control and prediction of the behaviours of two-phase systems in the porous media. These characterisation parameters include the capillary pressure-saturation relationship ( $P^c$ -S), relative permeability and saturation relationship ( $K_r$ -S), bulk relative permittivity-saturation relationship ( $\epsilon_b$ -S) and the bulk electrical conductivity-saturation relationship ( $\sigma_b$ -S). The effects of factors like the non-equilibrium flow condition (dynamic effect), porous media properties, domain scales, system temperature, pressure, salt concentration, etc., on the above parameters, were considered. Broad conclusions on the two categories of the two-phase systems investigated (i.e., silicone oil/water, CO<sub>2</sub>-water) are deduced.

##### 10.1.1 Silicone oil/water system

Results of the experimental investigations show that the capillary pressure-saturation relationship ( $P^c$ -S) for the silicone oil-water system in silica sand sample is affected by the dynamic capillary pressure effect. This effect, quantified by the parameter named the dynamic coefficient,  $\tau$ , was found to be dependent on domain scale and fluid-fluid viscosity ratio. It is confirmed that  $\tau$  increases with the domain scale and the viscosity ratio of the silicone oil/water. It is further shown that its value is inversely affected by the desaturation rate ( $\partial S/\partial t$ ), which is related to the degree of resistance to the fluid motion, namely, viscosity. In almost all cases,  $\tau$  is found to decrease monotonically with increase in water saturation, S, although there are some instances where the  $\tau$ -S relationship is non-monotonic. An order increase in magnitude of  $\tau$  is observed as the domain scale changes

from the 4cm scale to the 8cm domain scale. A similar order of increase with higher magnitude is found in the 12cm domain scale. Furthermore, there is an order increase in the value of  $\tau$  for silicone oil-water systems as the viscosity ratio increases from 200 to 500. The observed scale dependency of  $\tau$  appeared related to  $\partial S/\partial t$ , whose magnitude decreases with the increase in depth of the domain from the injection point. This can also be said of  $\tau$  dependency on viscosity ratios of the two-phase fluids. As the viscosity ratio increases, the  $\partial S/\partial t$  reduces and hence,  $\tau$  increases.

Dimensionless analysis on the experimental results shows that by constructing non-dimensional groups of quantities expressing a relationship among different variables, on which  $\tau$  depends, it is possible to summarise experimental results and determine their functional relationship. A generalised scaling relationship for  $\tau$  was derived from the dimensionless analysis which was then validated against independent literature data. The results show that the  $\tau$ -S relationships obtained from the literature and the scaling relationship match reasonably well.

Dynamic effects in the  $K_r$ -S relationship for silicone oil-water systems are further demonstrated. Investigations reveal that the  $K_r$ -S relationship is susceptible to the influence of fluid properties (i.e., viscosity) and porous media characteristics, under non-equilibrium flow. Results show that the dynamic relative permeability curves are different from the static relative permeability curves.  $K_{rw}$  increases with increasing wetting phase saturation and decreases with the increase in viscosity ratio, while  $K_{rnw}$  increases with increasing non-wetting phase saturation as well as with the increase in viscosity ratio. Also,  $K_{rw}$  decreases while the oil relative permeability increases with the increasing boundary pressure. The boundary pressure effect is significant in comparison to fluid viscosity ratio and scale dependency. At 40% water saturation and for a 8cm high domain, the  $K_{rnw}$  increased by 24.5% when viscosity ratio was increased from 200 to 1000. The same is true for the 12 cm high domain. The boundary pressure, location of pressure sensors and the fluid viscosity play significant role in the  $K_r$ -S relationship.

A computationally efficient and simple alternative platform for the prediction of the domain scale dependence of the  $\tau$ , is demonstrated using artificial neural networks (ANN). The input parameters consist of the phase saturation, media permeability, capillary entry pressure, viscosity ratio, density ratio, temperature, pore size distribution index, porosity and domain volume with the corresponding output  $\tau$  obtained at different domain scales. Good generalization of the model was achieved by acquiring data from independent sources comprising experiments and numerical simulations. Different ANN configurations as well as

linear and non-linear multivariate regression models were tested using a number of performance criteria. Findings in this work showed that the ANN structures with two hidden layers perform better than those with a single hidden layer. In particular, the ANN configuration with 13 and 15 neurons in the first and second hidden layers, respectively, performed the best. Using this best-performing ANN, effects of increased domain size were predicted for three separate experimental results obtained from literature and the in-house laboratory experiments with different domain scales. Results showed increased magnitude of  $\tau$  as the domain size increases for all the independent experimental data considered.

### 10.1.2 CO<sub>2</sub>/water system

The presence and influence of the dynamic capillary pressure effect in the  $P^c$ - $S$  relationship for scCO<sub>2</sub>-water systems in porous media were investigated, experimentally and numerically. Though, the effect of domain scale was not investigated in this case, the  $\tau$  was found to be affected by the system temperature and porous media permeability. The results show that  $\tau$  increases with the decrease in wetting phase saturation. The slope of the rise in  $\tau$ - $S$  is less steep for almost all the samples considered but it is found to increase with the temperature of the system. Furthermore, it is found to increase with the decreasing sample permeability. Towards irreducible saturation, the steepness of the  $\tau$ - $S$  curves becomes almost vertical. The magnitudes of  $\tau$  found for the scCO<sub>2</sub>-water system are in the range of  $2 \times 10^5$  and  $6 \times 10^5$  Pa s at high water saturation and  $1.3 \times 10^6$  and  $7 \times 10^6$  Pa s around the irreducible saturation.

However, no significant dynamic effect was found in the  $\epsilon_b$ - $S$  and  $\sigma_b$ - $S$  relationships for the scCO<sub>2</sub>-water system in carbonate and silicate porous media. The  $\epsilon_b$ - $S$  and  $\sigma_b$ - $S$  relationships decrease as the water saturation decreases in the two sand samples. While the  $\epsilon_b$ - $S$  relationship decreases with increase in temperature in silica sand, the trend in the limestone shows a slight increase with temperature, especially at high water saturation. Also, the  $\epsilon_b$ - $S$  relationship is shown to be affected by pressure in unconsolidated silica sand, increasing with the pressure of the domain. Contrarily, the  $\sigma_b$ - $S$  relationship increases as the temperature increases with more significance at higher water saturation in the silica sand sample. Effect of porous media chemical properties on both the  $\epsilon_b$ - $S$  and  $\sigma_b$ - $S$  curves showed that the relationships remain higher in the limestone than silica sand under comparable conditions. It can be inferred from the results that the geoelectrical techniques are highly dependent on water saturation. However, below 50% water saturation, the relationships appear less-dependent on pressure, temperature and brine/water saturation in the porous media.

This work further demonstrates the application of membranes in the monitoring of CO<sub>2</sub> in geological carbon sequestration. Commercial silicone rubber coupled with pressure transducers shows potential in the detection of CO<sub>2</sub> leakage from geological sites. The response of the device in terms of the mass of permeated gas, permeability and gas flux are investigated for both CO<sub>2</sub> and N<sub>2</sub>. Findings showed the existence of different stages of permeation rate for both gases. In terms of gas flux across the membrane, the first stage involves rapid rise in the flux with gas mass. This is followed by the less rapid stage of flux where the gradient reduces and is succeeded by the stage of constant flux for a period before the gas flux starts to decline. The results differ considerably for the two gases with CO<sub>2</sub> flux occurring in multiples of that of N<sub>2</sub> under similar conditions. The membrane shows different permeability to the gases and that of the CO<sub>2</sub> is higher than that of N<sub>2</sub>. However, for the same gas, the permeability appears less dependent of pressure. The mass permeation rate of N<sub>2</sub> is more than ten times less than that for the CO<sub>2</sub>. Based on the mass permeation rate, simple criterion for distinguishing the two gases at various depths is developed from the slope of mass with time curve. Thus, the membrane can be used to effectively monitor the movement of the CO<sub>2</sub>, N<sub>2</sub> and other gases in the subsurface.

Finally, the monitoring of potable water contamination in a shallow aquifer by the migrating or leaked CO<sub>2</sub> is demonstrated with the combination of the geoelectrical measurement techniques together with the membrane-sensor system. The study shows the variation of pH with time and explained the transition between dissociated bicarbonate, which increases the conductivity, to nondissociated carbonic acid, which reduces the pH. Results further show how the successive regimes of the above reactions tend the CO<sub>2</sub> with water towards equilibrium indicated by a steady value of pH. While bulk electrical conductivity of the system rises briefly at the contact of the CO<sub>2</sub> with the water-saturated domain, the bulk relative permittivity shows no change. A silicone rubber membrane shows the promise of detecting the diffusion of the CO<sub>2</sub> through the water-saturated domain and the rate of permeation was shown to increase with depth. Thus, the pH, electrical conductivity and membrane measurement techniques can effectively be used in the monitoring of the potable water aquifer that might be contaminated by the potential leakage from geological carbon sequestration site.

## **10.2 Recommendations for future work**

From the experiences garnered over the period of the investigations owing recommendations and future work can be made:

- The inclusion of the dynamic coefficient,  $\tau$  in the two-phase model/simulator is recommended in order to account for the presence of dynamic capillary pressure effect for two-phase flow in porous media.
- In the monitoring of two-phase flow in porous media, with water being the wetting phase, the use of geoelectrical measurement techniques, as characterization parameters is more reliable, since electrical parameters are not affected by the 'dynamic capillary pressure effect'.
- Polymeric membranes are widely applied in the capture of CO<sub>2</sub> from flue gases, but they are rarely used in the subsurface monitoring of gases. Therefore, more work is recommended for the applications of polymeric membrane in the subsurface monitoring of gases, especially CO<sub>2</sub> that may leak from a storage aquifer.
- Other simpler platforms for the investigations of two-phase flow parameters are recommended in order to make computational techniques cheaper and time-saving for two-phase flow in porous media.
- Determination of the permeation rates for other geologically relevant gases apart from CO<sub>2</sub> and N<sub>2</sub> is recommended in order to have a model that can comprehensively predict the identity of gases that permeate the membrane.
- Simultaneous permeation of more than one gas in the polymeric membrane should be investigated. This could be used to establish criteria to distinguish the presence of more than one gas that permeates through membrane at any time.

## REFERENCES

- Abidoye, L.K., Das, D.B., and Khudaida, K., 2014. Geological carbon sequestration in the context of two-phase flow in porous media: A review. *Journal of Critical Reviews in Environmental Science and Technology*, DOI: 10.1080/10643389.2014.924184 (in press).
- Abidoye, L.K. and Das, D.B., 2014. Scale-dependent dynamic capillary pressure effect for two-phase flow in porous media. *Advances in Water Resources*. DOI: 10.1016/j.advwatres.2014.09.009 (in press).
- Abrams, A. 1975. The Influence of Fluid Viscosity, Interfacial Tension, and Flow Velocity on Residual Oil Saturation Left by Waterflood, *Society of Petroleum Engineers Journal*, 15 (5), pp. 437 - 447, <http://dx.doi.org/10.2118/5050-PA>.
- Abu-Khader, M.M., 2006. Recent Progress in CO<sub>2</sub> Capture/Sequestration: A Review. *Energy Sources, Part A: Recovery, Utilization, and Environmental Effects*, 28(14), pp.1261–1279.
- Adamson, A.W., and Gast, A.P.: *Physical Chemistry of Surfaces*, 6th edition. Wiley-Interscience Publications, New York, ISBN 0-471-14873-3, (1997).
- Aggelopoulos, C. A. and Tsakiroglou, C.D., 2008. The effect of micro-heterogeneity and capillary number on capillary pressure and relative permeability curves of soils. *Geoderma*, 148(1), pp.25–34.
- Aggelopoulos, C. A., Robin, M., Perfetti, E., and Vizika, O., 2010. CO<sub>2</sub>/CaCl<sub>2</sub> solution interfacial tensions under CO<sub>2</sub> geological storage conditions: Influence of cation valence on interfacial tension. *Advances in Water Resources*, 33(6), 691–697. doi:10.1016/j.advwatres.2010.04.006
- Ahmadi, M.A., Ebadi, M., Shokrollahi, A., and Majidi, S.M.J., 2013. Evolving artificial neural network and imperialist competitive algorithm for prediction oil flow rate of the reservoir. *Applied Soft Computing*, 13(2), pp.1085–1098.
- Ahmadlouydarab, M., Liu, Z.-S. S. and Feng, J. J., (2012). Relative permeability for two-phase flow through corrugated tubes as model porous media, *International Journal of Multiphase Flow* 47, 85-93. Alabi, O.O., 2011. Fluid Flow in Homogeneous and Heterogeneous Porous Media. *Electronic Journal of Geotechnical Engineering*, 16.

Alabi, O. O., 2011. Fluid Flow in Homogeneous and Heterogeneous Porous Media. *Electronic Journal of Geotechnical Engineering*, 16.

Al-Garni, M.T. and Al-Anazi, B.D., 2008. Investigation of wettability effects on capillary pressure, and irreducible saturation for Saudi crude oils, using rock centrifuge. *Oil and Gas Business*, 2008(2).

Algive, L., Bekri, S., and Vizika-kavvadias, O., 2009. Reactive pore network modeling dedicated to the determination of the petrophysical property changes while injecting CO<sub>2</sub>. In *SPE Annual Technical conference and Exhibition*.

Al Hagrey, S. A., Köhn, D., and Rabbel, W., 2013. Feasibility Study of Applying Geoelectric and Gravity Techniques for CAES Reservoir Monitoring. In *Sustainable Earth Sciences 2013*. DOI: 10.3997/2214-4609.20131622

Alkan, H., Cinar, Y. and Ülker, E.B., 2010. Impact of Capillary Pressure, Salinity and In situ Conditions on CO<sub>2</sub> Injection into Saline Aquifers. *Transport in Porous Media*, 84(3), pp.799–819.

Alnes, H., Eiken, O. and Stenvold, T., 2008. Monitoring gas production and CO<sub>2</sub> injection at the Sleipner field using time-lapse gravimetry. *Geophysics*, 73(6), pp.WA155–WA161.

Amaefule, J. O. and Handy, L. L., 1982. The effect of interfacial tensions on relative oil/water permeabilities of consolidated porous media, *Soc. Pet. Eng. J.*, 22, 371–381.

Amato, F., López, A., Peña-Méndez, E., Vañhara, P., Hampl, A., and Havel, J., 2013. Artificial neural networks in medical diagnosis. *Journal of Applied Biomedicine*, 11(2), pp.47–58.

Anderson, W., 1987. Wettability Literature Survey Part 5: The Effects Of Wettability On Relative Permeability. *Journal of Petroleum Technology*, 39(11), pp.1453–1468.

Archie, G., 1942. The electrical resistivity log as an aid in determining some reservoir characteristics. *Transaction of the american institute of mining and metallurgical engineers*, 146:54–61.

Assayag, N., Matter, J., Ader, M., Goldberg, D., and Agrinier, P., 2009. Water--rock interactions during a CO<sub>2</sub> injection field-test: Implications on host rock dissolution and alteration effects. *Chemical geology*, 265(1), pp.227–235.

Ataie-Ashtiani, B., S. M. Hassanizadeh, and M. A. Celia, 2002. Effects of heterogeneities on capillary pressure-saturation-relative permeability relationships, *Journal of Contaminant Hydrology*, 56(3-4), 175-192.

Ataie-Ashtiani, B., Hassanizadeh SM, Oostrom M, Celia MA, and White MD., 2001. Effective parameters for two-phase flow in a porous medium with periodic heterogeneities. *Journal of contaminant hydrology*, 49(1), pp.87–109.

Atkins, E. R. and G. H. Smith, 1961. The significance of particle shape in formation factor-porosity relationships. *Petroleum Technology* 13: 285-291

Avraam, D. G., and Payatakes, A. C., 1995. Flow regimes and relative permeabilities during steady-state two-phase flow in porous media, *Journal of Fluid Mechanics*, 293, 207–236.

Babchin, A., Brailovsky, I., Gordon, P. and Sivashinsky, G., 2008. Fingering instability in immiscible displacement. *Physical Review-Series E-*, 77(2), 026301.

Baker, R.W., 2012. *Membrane Technology and Applications* 3rd ed., John Wiley & Sons.

Barker, J. W., and Thibeau, S., 1997. A Critical Review of the Use of Pseudorelative Permeabilities for Upscaling, *SPE Reservoir Engineering (Society of Petroleum Engineers)*, 12(2), 138-143.

Barnes, A. C., Dejuan Jr, E., Humayun, M., Shelley, T., and Varner, S. E., 2012. Devices for intraocular drug delivery. U.S. Patent No. 8,096,972. Washington, DC: U.S. Patent and Trademark Office.

Bear, J., 2013. *Dynamics of fluids in porous media*, Courier Dover Publications.

Bednarek, A., Szklarek, S., and Zalewski, M. (2014). Nitrogen pollution removal from areas of intensive farming—comparison of various denitrification biotechnologies. *Ecohydrology & Hydrobiology*.

Beni, A.N., Kühn, M., Meyer, R., and Clauser, C., 2012. Numerical modeling of a potential geological CO<sub>2</sub> sequestration site at Minden (Germany). *Environmental Modeling & Assessment*, 17(4), pp.337–351.

Bennion, B. and Bachu, S., 2008. and imbibition relative permeability relationships for supercritical CO<sub>2</sub>/brine and H<sub>2</sub>S/brine systems in intergranular sandstone, carbonate, shale, and anhydrite rocks. *SPE Reservoir Evaluation & Engineering*, 11(3).

- Benson, S.M. and Cole, D.R., 2008. CO<sub>2</sub> sequestration in deep sedimentary formations. *Elements*, 4(5), pp.325–331.
- Bentham, M., 2006. An assessment of carbon sequestration potential in the UK--Southern North Sea case study. Tyndall Centre for Climate Change Research and British Geological Survey. Keyworth, Nottingham, UK: Kingsley Dunham Centre.
- Berg, S. and Ott, H., 2012. Stability of CO<sub>2</sub>-brine immiscible displacement. *International Journal of Greenhouse Gas Control*, 11, pp.188–203.
- Best, M.G., 2013. *Igneous and Metamorphic Petrology*, John Wiley & Sons.
- Bickle, M., Chadwick, A., Huppert, H. E., Hallworth, M., and Lyle, S., 2007. Modelling carbon dioxide accumulation at Sleipner: Implications for underground carbon storage. *Earth and Planetary Science Letters*, 255(1), pp.164–176.
- Bielinski, Andreas, Kopp, A., Schütt, H. and Class, H., 2008. Monitoring of CO<sub>2</sub> plumes during storage in geological formations using temperature signals: Numerical investigation. *International Journal of Greenhouse Gas Control*, 2(3), pp.319–328.
- Bissell, R.C., Vasco, D. W., Atbi, M., Hamdani, M., Okwelegbe, M., and Goldwater, M. H., 2011. A full field simulation of the in Salah gas production and CO<sub>2</sub> storage project using a coupled geo-mechanical and thermal fluid flow simulator. *Energy Procedia*, 4, pp.3290–3297.
- Blunt, Martin J., Jackson, M. D., Piri, M., and Valvatne, P. H., 2002. Detailed physics, predictive capabilities and macroscopic consequences for pore-network models of multiphase flow. *Advances in Water Resources*, 25(8-12), pp.1069–1089.
- Börner, J.H., Herdegen, V., Repke, J.U., Spitzer, K., 2013. The impact of CO<sub>2</sub> on the electrical properties of water bearing porous media—laboratory experiments with respect to carbon capture and storage. *Geophysical Prospecting*, 61(s1):446–460.
- Bottero, S., Hassanizadeh, S. M., Kleingeld, P. J., and Bezuijen, A., 2006. Experimental study of dynamic capillary pressure effect in two-phase flow in porous media. In *Proceedings of the XVI International Conference on Computational Methods in Water Resources (CMWR)*, Copenhagen, Denmark. pp. 18–22.
- Bottero, S., Hassanizadeh, S. M., Kleingeld, P. J. and Heimovaara, T. J., 2011a. Nonequilibrium capillarity effects in two-phase flow through porous media at different scales. *Water Resources Research*, 47(10), p.W10505.

Bottero, S. (2009), 2009. *Advances in the Theory of Capillarity in Porous Media*. PhD Thesis, Universiteit Utrecht, The Netherlands.

Bottero, S., Hassanizadeh, S. M. and Kleingeld, P. J., 2011b. From Local Measurements to an Upscaled Capillary Pressure–Saturation Curve. *Transport in Porous Media*, 88(2), pp.271–291.

Bourgeat, M. and Panfilov E., 1998. Effective two-phase flow through highly heterogeneous porous media: capillary non-equilibrium effects. *Comput. Geosci.*, 2(3), pp.191–215.

Bower, K.M. and Zyvoloski, G., 1997. A numerical model for thermo-hydro-mechanical coupling in fractured rock. *International Journal of Rock Mechanics and Mining Sciences*, 34(8), pp.1201–1211.

Breen, S.J., Carrigan, C. R., LaBrecque, D. J., and Detwiler, R. L., 2012. Bench-scale experiments to evaluate electrical resistivity tomography as a monitoring tool for geologic CO<sub>2</sub> sequestration. *International Journal of Greenhouse Gas Control*, 9, pp.484–494.

Brooks, R. and Corey, A., 1964. *Hydraulic Properties of Porous Media*. Hydrology Papers. Colorado State University.

BS 1377-5:1990: Methods of test for soils for civil engineering purposes. Compressibility, permeability and durability tests. ISBN 0 580 18030 1. Published by BSI

Burdine, N., 1953. Relative permeability calculations from pore size distribution data. *Journal of Petroleum Technology*, 5(03), pp.71–78.

Burdine, N.T., Gournay, L.S. and Reichertz, P.P., 1950. No Title“Pore Size Distribution of Petroleum Reservoir Rocks.” *Trans. AIME*, 198, pp.195–204.

Buttinelli, M., Procesi, M., Cantucci, B., Quattrocchi, F., and Boschi, E., 2011. The geo-database of caprock quality and deep saline aquifers distribution for geological storage of CO<sub>2</sub> in Italy. *Energy*, 36(5), pp.2968–2983.

Camps-Roach, G., D. M. O’Carroll, T. A. Newson, T. Sakaki, and T. H. Illangasekare, 2010. Experimental investigation of dynamic effects in capillary pressure: Grain size dependency and upscaling. *Water Resources Research*, 46(8), p.W08544.

Chadwick, A., Arts, R., Bernstone, C., May, F., Thibeau, S., and Zweigel, P., 2008. *Best Practice for the Storage of CO<sub>2</sub> in Saline Aquifers-Observations and Guidelines from the SACS and CO<sub>2</sub>STORE projects*,

Chalbaud, C., Robin, M., Lombard, J. M., Bertin, H., and Egermann, P., 2010. Brine/CO<sub>2</sub> Interfacial Properties and Effects on CO<sub>2</sub> Storage in Deep Saline Aquifers. , 65(4), pp.541–555.

Chandrappa, R. and Das, Diganta B, 2014. Sustainable Water Engineering: Theory and Practice, John Wiley & Sons.

Chandrappa, R., Gupta, S. and Kulshrestha, U.C., 2011. Coping with climate change: principles and Asian context, Springer.

Chang, Y.-B., Coats, B. and Nolen, J., 1998. A Compositional Model for CO<sub>2</sub> Floods Including CO<sub>2</sub> Solubility in Water. SPE Reservoir Evaluation & Engineering, 1(2), pp.155–160.

Charpentier, F., Bureau, B., Troles, J., Boussard-Plédel, C., Michel-Le Pierrès, K., Smektala, F., and Adam, J. L., 2009. Infrared monitoring of underground CO<sub>2</sub> storage using chalcogenide glass fibers. Optical Materials, 31(3), pp.496–500.

Chen, L., Miller, G.A. and Kibbey, T.C.G., 2007. Rapid pseudo-static measurement of hysteretic capillary pressure-saturation relationships in unconsolidated porous media. ASTM geotechnical testing journal, 30(6), pp.474–483.

Cheng, J. and Luo, Y., 2014. Modeling Atmosphere Composition and Determining Explosibility in a Sealed Coal Mine Volume. Archives of Mining Sciences, 59(1), pp.25–40.

Chiquet, P., Broseta, D. and Thibeau, S., 2007. Wettability alteration of caprock minerals by carbon dioxide. Geofluids, 7(2), pp.112–122.

Chun, B.-S. and Wilkinson, G.T., 1995. Interfacial tension in high-pressure carbon dioxide mixtures. Industrial & Engineering Chemistry Research, 34(12), pp.4371–4377.

Class, Holger, Anozie Ebigbo, Rainer Helmig, Helge K. Dahle, Jan M. Nordbotten, Michael A. Celia, Pascal Audigane, Melanie Darcis, Jonathan Ennis-King, Yaqing Fan, Bernd Flemisch, Sarah E. Gasda, Min Jin, Stefanie Krug, Diane Labregere, Ali Naderi Beni, Rajesh J. Pawar, Adil Sbai, Sunil G. Thomas, Laurent Trenty, Lingli Wei 2009. A benchmark study on problems related to CO<sub>2</sub> storage in geologic formations. Computational Geosciences, 13(4), pp.409–434.

Cuesta, C, van Dujin, C.J. and H.J., 2000. Infiltration in porous media with dynamic capillary pressure: travelling waves. European. Journal of Applied Mathematics, pp.381–397.

Dafflon, B., Yuxin Wu, Susan S. Hubbard, Jens T. Birkholzer, Thomas M. Daley, John D. Pugh, John E. Peterson, and Robert C. Trautz., 2012. Monitoring CO<sub>2</sub> intrusion and associated geochemical transformations in a shallow groundwater system using complex electrical methods. *Environmental science & technology*, 47(1), pp.314–321.

Dahle, Helge K., Celia, M. A. and Majid Hassanizadeh, S., 2005. Bundle-of-Tubes Model for Calculating Dynamic Effects in the Capillary-Pressure- Saturation Relationship. *Transport in Porous Media*, 58(1-2), pp.5–22.

Danish, M. and Jacquin, C., 1983. Influence du Contraste des Viscosités sur les Perméabilités Relatives lors du Drainage. *Expérimentation et Modélisation. Rev. Inst. Franc. Pétrole*, 33(6), pp.723–733.

Das, D. B., Hassanizadeh, S. M., Rotter, B. E. and Ataie-Ashtiani, B., 2004. A numerical study of micro-heterogeneity effects on upscaled properties of two-phase flow in porous media, *Transp. Porous Media*, 56(3), 329-350

Das, D B and Hassanizadeh, S M, 2005. *Upscaling Multiphase Flow in Porous Media*, Springer.

Das, D.B., Gill, B. S., Abidoye, L. K., and Khudaida, K. J. 2014. A numerical study of dynamic capillary pressure effect for supercritical carbon dioxide-water flow in porous domain. *AIChE Journal*, p.n/a–n/a.

Das, D. B., Gaudie, R. and Mirzaei, M., 2007. Dynamic Effects for Two-Phase Flow in Porous Media : Fluid Property Effects. *AIChE*, 53(10), pp.2505–2520.

Das, D. B. and Mirzaei, M., 2012. Dynamic effects in capillary pressure relationships for two-phase flow in porous media: Experiments and numerical analyses. *AIChE Journal*, 58(12), pp.3891–3903.

Das, D. B. and Mirzaei, M., 2013. Experimental measurement of dynamic effect in capillary pressure relationship for two-phase flow in weakly layered porous media. *AIChE Journal*, 59(5), pp.1723–1734.

Das, D. B., Mirzaei, M. and Widdows, N., 2006. Non-uniqueness in capillary pressure–saturation–relative permeability relationships for two-phase flow in porous media: Interplay between intensity and distribution of random micro-heterogeneities. *Chemical Engineering Science*, 61(20), pp.6786–6803.

Das, D.B., Hanspal, N.S., and Nassehi, V., 2005. Analysis of hydrodynamic conditions in adjacent free and heterogeneous porous flow domains. *Hydrological Processes*, 19(14), pp.2775–2799.

De Bo, I., Van Langenhove, H., Pruuost, P., De Neve, J., Pieters, J., Vankelecom, I. F., and Dick, E. 2003. Investigation of the permeability and selectivity of gases and volatile organic compounds for polydimethylsiloxane membranes. *Journal of Membrane Science*, 215(1-2), pp.303–319.

Dethlefsen, F., Ralf Köber, Dirk Schäfer, Said Attia al Hagrey, Götz Hornbruch, Markus Ebert, Matthias Beyer, Jochen Großmann, and Andreas Dahmke, 2013. Monitoring Approaches for Detecting and Evaluating CO<sub>2</sub> and Formation Water Leakages into Near-surface Aquifers. *Energy Procedia*, 37, pp.4886–4893.

Demond, A. H. and Roberts, P. V., 1987. An examination of relative permeability relations for two-phase flow in porous media, *Water Resour. Bull.*, 23, 617-628.

Diamantopoulos, E. and Durner, W., 2012. Dynamic Nonequilibrium of Water Flow in Porous Media: A Review. *Vadose Zone Journal*, 11(3).

DiCarlo, D. A., 2013. Stability of gravity-driven multiphase flow in porous media: 40 Years of advancements. *Water Resources Research*, 49(8), pp.4531–4544.

DiCarlo, D. A., 2004. Experimental measurements of saturation overshoot on infiltration. *Water resources research*, 40(4).

Dodds, W.S., Stutzman, L.F. and Sollami, B.J., 1956. Carbon dioxide solubility in water. *Chemical & Engineering Data Series*, 1(1), pp.92–95.

DOE, 2010. Fossil fuels, <http://www.energy.gov/energysources/fossilfuels.htm>, accessed on 11/14/2010.

Dollimore, D. and Heal, G.R., 1964. An improved method for the calculation of pore size distribution from adsorption data. *Journal of Applied Chemistry*, 14(3), pp.109–114.

Donaldson, E. C., Thomas, R. D., and Lorenz, P. B., 1969. Wettability determination and its effect on recovery efficiency. *Society of Petroleum Engineers Journal*, 9(01), pp.13–20.

Donaldson, Erle C, Ewall, N. and Singh, B., 1991. Characteristics of capillary pressure curves. *Journal of Petroleum Science and Engineering*, 6(3), pp.249–261.

Dou, Z., and Zhou, Z. F., 2013. Numerical study of non-uniqueness of the factors influencing relative permeability in heterogeneous porous media by lattice Boltzmann method, *International Journal of Heat and Fluid Flow*, 42, 23-32.

Doughty, C., 2007. Modeling geologic storage of carbon dioxide: Comparison of non-hysteretic and hysteretic characteristic curves. *Energy Conversion and Management*, 48(6), pp.1768–1781.

Downie, J., and Crane, F. E., 1961. Effect of viscosity on relative permeability, *Soc. Pet. Eng. J.*, 1, 59-60.

Drever, J.I. and Stillings, L.L., 1997. The role of organic acids in mineral weathering. *Colloids and Surfaces A: Physicochemical and Engineering Aspects*, 120(1), pp.167–181.

Drnevich, V.P., Lovell, J., Tishmack, J., Yu, X., and Zhang, J., 2001. "Temperature Effects on Relative permittivity Determined by Time Domain Reflectometry," TDR 2001: Innovative Applications of TDR Technology, Infrastructure Technology Institute, Northwestern University, Evanston, IL, September.

Duan, Z. and Sun, R., 2003. An improved model calculating CO<sub>2</sub> solubility in pure water and aqueous NaCl solutions from 273 to 533 K and from 0 to 2000 bar. *Chemical Geology*, 193(3), pp.257–271.

Dullien, F.A.L., Allsop, H.A., Chatzis, I., Macdonald, I.F., 1990. Wettability and miscible displacement in Pembina Cardium Sandstone. *Can. J.P.T.*, 29(4), p.63.

Egermann, P., Lombard, J.M. and Bretonnier, P., 2006. A fast and accurate method to measure threshold capillary pressure of caprocks under representative conditions. , pp.1–14.

Egli, S., Ruf, A. and Buck, A., 1984. Gastrennung mittels Membranen. Ein {Ü}berblick. *Swiss Chem*, 6(9), pp.89–122.

Ehrlich, R., 1993. Viscous coupling in two-phase flow in porous media and its effect on relative permeabilities, *Transp. Porous Media*, 11, 201-218.

Ekre, R., Johnson, P. C., Rittmann, B. E., and Krajmalnik-Brown, R., 2014. Method for Assessing Source Zone Natural Depletion at Chlorinated Aliphatic Spill Sites. *Groundwater Monitoring & Remediation*, 34(2), pp.60–70.

- Elenius, M. and Gasda, S., 2012. Impact of tight horizontal layers on dissolution trapping in geological carbon storage. XIX International Conference on Water Resources CMWR 2012 University of Illinois at Urbana-Champaign June 17-22,2012 pp. 1–8.
- Ellis, M.H., Sinha, M. C., Minshull, T. A., Sothcott, J., and Best, A. I., 2010. An anisotropic model for the electrical resistivity of two-phase geologic materials. *GEOPHYSICS*, 75(6), pp.E161–E170.
- El Tabach, E., Lancelot, L., Shahrour, I., and Najjar, Y. 2007. Use of artificial neural network simulation metamodelling to assess groundwater contamination in a road project. *Mathematical and Computer Modelling*, 45(7), pp.766–776.
- Emmanuel, S., Ague, J.J. and Walderhaug, O., 2010. Interfacial energy effects and the evolution of pore size distributions during quartz precipitation in sandstone. *Geochimica et Cosmochimica Acta*, 74(12), pp.3539–3552.
- Espinoza, D. N., Kim, S. H. and Santamarina, J. C., 2011. CO<sub>2</sub> geological storage — Geotechnical implications. *KSCE Journal of Civil Engineering*, 15(4), pp.707–719.
- Espinoza, D. N. and Santamarina, J. C., 2010. Water-CO<sub>2</sub> -mineral systems: Interfacial tension, contact angle, and diffusion-Implications to CO<sub>2</sub> geological storage. *Water Resources Research*, 46(7), p.n/a–n/a.
- Farajzadeh, R., 2009. Enhanced transport phenomena in CO<sub>2</sub> sequestration and CO<sub>2</sub> EOR, PhD thesis, Technical University Delft, The Netherlands.
- Fleury, M., J. Pironon, Y.M. Le Nindre, O. Bildstein, P. Berne, V. Lagneau, D. Broseta, T. Pichery, S. Fillacier, M. Lescanne and O. Vidal, 2010. Petrophysical measurements for CO<sub>2</sub> storage: application to the Ketzin site. *The Society of Core Analysts, SCA News SCA2010-06*, 22, pp.1–12.
- Fujii, T., Satomi Nakagawa, Yoshiyuki Sato, Hiroshi Inomata and Toshiyuki Hashida, 2010. Sorption Characteristics of CO<sub>2</sub> on Rocks and Minerals in Storing CO<sub>2</sub> Processes. *Natural Resources (2158-706X)*, 1(1).
- Gao, S.J. and Meegoda, L.H., 2013. Simulation of Dynamic Two-Phase Flow During Multistep Air Sparging. *Transp. Porous Media*, 96(1), pp.173–192.
- Garcia, J.E., 2001. Density of Aqueous Solutions of CO<sub>2</sub>. Lawrence Berkeley National Laboratory Report LBNL-49023, Berkeley, CA (2001).

Gasda, S. E. and Celia, M.A., 2005. Upscaling relative permeabilities in a structured porous medium, *Advances in Water Resources*, 28(5), 493-506.

Gasda, S E, Nordbotten, J M and Celia, M A, 2009. Vertical equilibrium with sub-scale analytical methods for geological CO<sub>2</sub> sequestration. *Computational Geosciences*, 13(4), pp.469–481.

Gasda, S.E., 2008. Numerical Models for Evaluating CO<sub>2</sub> Storage in Deep, Saline Aquifers : Leaky Wells and Large-Scale Geological Features . Princeton University.

Gaus, I., Azaroual, M. and Czernichowski-Lauriol, I., 2005. Reactive transport modelling of the impact of CO<sub>2</sub> injection on the clayey cap rock at Sleipner (North Sea). *Chemical Geology*, 217(3), pp.319–337.

Gawish, A., and Al-Homadhi, E., 2008. Relative permeability curves for high pressure, high temperature reservoir conditions, *Oil and Gas Business*(2).

Gerhard, J. I. and Kueper, B.H., 2003. Relative permeability characteristics necessary for simulating DNAPL infiltration, redistribution, and immobilization in saturated porous media,. *Water Resources Research*, 39(8).

Ghosal, S.K. and Datta, S., 1993. Introduction to Chemical Engineering, Tata McGraw Hill Education Private Limited 0074601407, 9780074601402.

Gielen, T., Hassanizadeh, S. M., Leijnse, A., and Nordhaug, H. F. 2005. Dynamic effects in multiphase flow: a pore-scale network approach. In *Upscaling multiphase flow in porous media*. Springer, pp. 217–236.

Goel, G. and O'Carroll, D.M., 2011. Experimental investigation of nonequilibrium capillarity effects: Fluid viscosity effects. *Water Resources Research*, 47(9), p.W09507.

Gunter, W.D., Bachu, S., Palombi, D., Lakeman, B., Sawchuk, W., and Bonner, D. 2009. Heartland Area Redwater reef saline aquifer CO<sub>2</sub> storage project. *Energy Procedia*, 1(1), pp.3943–3950.

Hamamoto, S., Moldrup, P., Kawamoto, K., and Komatsu, T., 2010. Excluded-volume expansion of Archie's law for gas and solute diffusivities and electrical and thermal conductivities in variably saturated porous media. *Water Resources Research*, 46(6).

Hansen, J., Makiko Sato, Pushker Kharecha, David Beerling, Robert Berner, Valerie Masson-Delmotte, Mark Pagani, Maureen Raymo, Dana L. Royer, and James C. Zachos., 2008. Target atmospheric CO<sub>2</sub>: Where should humanity aim? arXiv preprint arXiv:0804.1126.

Hanspal, N. and Das, D., 2012. Dynamic effects on capillary pressure–Saturation relationships for two-phase porous flow: Implications of temperature. *AIChE Journal*, 58(6), pp.1951–1965.

Hanspal, N.S., Allison, B. A., Deka, L., and Das, D. B., 2013. Artificial neural network (ANN) modeling of dynamic effects on two-phase flow in homogenous porous media. *Journal of Hydroinformatics*, 15(2), p.540.

Hassanizadeh, S. M., Celia, Michael A. and Dahle, H. K., 2002. Dynamic effect in the capillary pressure--saturation relationship and its impacts on unsaturated flow. *Vadose Zone Journal*, 1(1), pp.38–57.

Hassanizadeh, S. M. and Gray, W.G., 1990a. Mechanics and thermodynamics of multiphase flow in porous media including interphase boundaries. *Advances in water resources*, 13(4), pp.169–186.

Hassanizadeh, S. M. and Gray, W.G., 1993. Thermodynamic basis of capillary pressure in porous media. *Water Resources Research*, 29(10), pp.3389–3405.

Heimovaara, T. J., 1994. Frequency domain analysis of time domain reflectometry waveforms: 1. Measurement of the complex dielectric permittivity of soils. *Water Resources Research*, 30(2), 189-199.

Homsy, G.M., 1987. Viscous fingering in porous media. *Annual Review of Fluid Mechanics*, 19(1), pp.271–311.

Hosseini, S.A., Lashgari, H., Choi, J. W., Nicot, J. P., Lu, J., and Hovorka, S. D., 2013. Static and dynamic reservoir modeling for geological CO<sub>2</sub> sequestration at Cranfield, Mississippi, U.S.A. *International Journal of Greenhouse Gas Control*, 18, pp.449–462.

Hou, L., Chen, L. and Kibbey, T.C.G., 2012. Dynamic capillary effects in a small-volume unsaturated porous medium: Implications of sensor response and gas pressure gradients for understanding system dependencies. *Water Resources Research*, 48(11), p.W1152.

- Hou, L., Sleep, B.E. and Kibbey, T., 2014. The influence of unavoidable saturation averaging on the experimental measurement of dynamic capillary effects: A numerical simulation study. *Advances in Water Resources Research*, 66, pp.43–51.
- Houghton, J.T., Ding, Y. D. J. G., Griggs, D. J., Noguera, M., van der Linden, P. J., Dai, X., Maskell, K., and Johnson, C. A., 2001. *Climate change 2001: the scientific basis*, Cambridge university press Cambridge.
- Huang, X., Xu, Y. and Karato, S., 2005. Water content in the transition zone from electrical conductivity of wadsleyite and ringwoodite. *Nature*, 434(7034), pp.746–749.
- Huh, C., Seong-Gil Kang, Sup Hong, Jong-Su Choi, Jong-Hwa Baek, Chul-Soo Lee, Yong-Chan Park, and Jung-Suk Lee., 2009. CO<sub>2</sub> storage in marine geological structure: A review of latest progress and its application in Korea. *Energy Procedia*, 1(1), pp.3993–4000.
- Humez, P., Audigane, P., Lions, J., Chiaberge, C., and Bellenfant, G. 2011. Modeling of CO<sub>2</sub> leakage up through an abandoned well from deep saline aquifer to shallow fresh groundwaters. , 1, pp.153–181.
- Huo, D. and Gong, B., 2010. Discrete Modeling and Simulation on Potential Leakage through Fractures in CO<sub>2</sub> Sequestration. In *SPE Annual Technical Conference and Exhibition*.
- Ingham, D.B. and Pop, I., 2005. *Transport phenomena in porous media III*, Elsevier.
- Itaoka, K., Saito, A. and Akai, M., 2005. Public acceptance of CO<sub>2</sub> capture and storage technology: a survey of public opinion to explore influential factors. In *Proceedings of the 7. international conference on greenhouse gas control technologies*.
- Jackson, P. D., Smith, D. T., and Stanford, P. N., 1978. Resistivity-porosity-particle shape relationships for marine sands. *Geophysics*, 43(6), 1250-1268.
- Jain, A. and Indurthy, S., 2003. Comparative Analysis of Event-based Rainfall-runoff Modeling Techniques—Deterministic, Statistical, and Artificial Neural Networks. *Journal of Hydrologic Engineering*, 8(2), pp. 93-98, (doi: [http://dx.doi.org/10.1061/\(ASCE\)1084-0699\(2003\)8:2\(93\)](http://dx.doi.org/10.1061/(ASCE)1084-0699(2003)8:2(93)))
- Jain, Ashu and Ormsbee, L.E., 2002. Short-term water demand forecast modeling techniques: Conventional methods versus AI. *Journal-American Water Works Association*, 94(7), pp.64–72.

Jennings, J.B., 1987. Capillary pressure techniques: application to exploration and development geology. *AAPG Bulletin*, 71(10), pp.1196–1209.

Joekar-Niasar, V, Hassanizadeh, S Majid and Dahle, H K, 2010. Non-equilibrium effects in capillarity and interfacial area in two-phase flow: Dynamic pore-network modelling. *Journal of Fluid Mechanics*, 655, pp.38–71.

Joekar-Niasar, Vahid and Majid Hassanizadeh, S., 2011. Effect of fluids properties on non-equilibrium capillarity effects: Dynamic pore-network modeling. *International Journal of Multiphase Flow*, 37(2), pp.198–214.

Johnson, V.M. and Rogers, L.L., 2000. Accuracy of neural network approximators in simulation-optimization. *Journal of Water Resources Planning and Management*, 126(2), pp.48–56.

Jordan, S.M. and Koros, W.J., 1990. Permeability of pure and mixed gases in silicone rubber at elevated pressures. *Journal of Polymer Science Part B: Polymer Physics*, 28(6), pp.795–809.

Juanes, R., Spiteri, E. J., Orr, F. M., and Blunt, M. J. 2006. Impact of relative permeability hysteresis on geological CO<sub>2</sub> storage. *Water Resources Research*, 42(12).

Juanes, R., 2008. Nonequilibrium effects in models of three-phase flow in porous media. *Advances in Water Resources*, 31(4), pp.661–673.

Kalaydjian, Francois, 1987. A Macroscopic Description of Multiphase Flow in Porous Media involving Space-time Evolution of Fluid/Fluid Interface. *Transport in Porous Media*, 6(2), pp.537–552.

Kalaydjian, Francois, 1992. Effect of the Flow Rate on an Imbibition Capillary Pressure Curve-Theory Versus Experiment. In *SCA European Core Analysis Symposium*, Paris, France.

Kalogirou, S.A., 2013. Applications of artificial neural-networks for. *Energy Systems: Adaptive Complexity*, p.17. Elsevier, 31 May 2013 - Science - 244 pages.

Karimpouli, S., Fathianpour, N. and Roohi, J., 2010. A new approach to improve neural networks' algorithm in permeability prediction of petroleum reservoirs using supervised committee machine neural network (SCMNN). *Journal of Petroleum Science and Engineering*, 73(3), pp.227–232.

Karl, T.R., Melillo, J.M. and Peterson, T.C., 2009. Global climate change impacts in the United States, Cambridge University Press.

Kaveh, N. S., Rudolph, E. S. J., Rossen, W. R., van Hemert, P., and Wolf, K. H., 2013. Interfacial Tension and Contact Angle Determination in Water-sandstone Systems with Injection of Flue Gas and CO<sub>2</sub>. In IOR 2013-From Fundamental Science to Deployment.

Keller, G. V., 1966. SECTION 26: ELECTRICAL PROPERTIES OF ROCKS AND MINERALS. Geological Society of America Memoirs, 97, pp.553–577.

Kesson, J., 1984. The diffusion of gases through a silicon rubber membrane and its application to an in-line carbonation meter. MBAA Technical Quarterly 21 (3), 143–146. MBAA Technical Quarterly, 21(3), pp.143–146.

Khashei, M. and Bijari, M., 2013. Fuzzy artificial neural network (p, d, q) model for incomplete financial time series forecasting. Journal of Intelligent and Fuzzy Systems.

Khudaida, K. and Das, Diganta Bhusan, 2014. A numerical study of capillary pressure-saturation relationship for supercritical carbon dioxide (CO<sub>2</sub>) injection in deep saline aquifer. Chemical Engineering Research and Design.

Kissling, F. and Rohde, C., 2010. The computation of nonclassical shock waves with a heterogeneous multiscale method. NHM, 5(3), pp.661–674.

Klapper, R., Widdicombe, S. and Reitz, A., 2013. ECO2 Briefing Paper No. 2: Potential impacts of CO<sub>2</sub> leakage from sub-surface storage on seabed biology.

Knight, R. and Abad, A., 1995. Rock/water interaction in dielectric properties: Experiments with hydrophobic sandstones. Geophysics, 60(2), pp.431–436.

Knight, R.J. and Nur, A., 1987. The relative permittivity of sandstones, 60 kHz to 4 MHz. Geophysics, 52(5), pp.644–654.

relative permittivity Kopp, A, Class, H and Helmig, R, 2009. Investigations on CO<sub>2</sub> storage capacity in saline aquifers: Part 1. Dimensional analysis of flow processes and reservoir characteristics. International Journal of Greenhouse Gas Control, 3(3), pp.263–276.

Krause, R.M., Carley, S. R., Warren, D. C., Rupp, J. A., and Graham, J. D., 2014. "Not in (or Under) My Backyard": Geographic proximity and public acceptance of carbon capture and storage facilities. Risk Analysis, 34(3), pp.529–540.

Kvamme, B., Kuznetsova, T., Hebach, A., Oberhof, A., and Lunde, E., 2007. Measurements and modelling of interfacial tension for water+carbon dioxide systems at elevated pressures. *Computational Materials Science*, 38(3), pp.506–513.

Lacinska, A.M., Styles, M.T. and Farrant, A.R., 2014. Near-surface diagenesis of ophiolite-derived conglomerates of the Barzaman Formation, United Arab Emirates: a natural analogue for permanent CO<sub>2</sub> sequestration via mineral carbonation of ultramafic rocks. *Geological Society, London, Special Publications*, 392(1), pp.343–360.

Lagneau, V., Pipart, A. and Catalette, H., 2005. Reactive Transportmodelling and Long Term Behaviour of CO<sub>2</sub> Sequestration in Saline Aquifers. *Oil & gas science and technology*, 60(2), pp.231–247.

Lamert, H., H. Geistlinger, U. Werban, C. Schütze, A. Peter, G. Hornbruch, A. Schulz, M. Pohlert, S. Kalia, M. Beyer, J. Großmann, A. Dahmke and P. Dietrich, 2012. Feasibility of geoelectrical monitoring and multiphase modeling for process understanding of gaseous CO<sub>2</sub> injection into a shallow aquifer. *Environmental Earth Sciences*, 67(2), pp.447–462.

Lazik, D., Ebert, S., Leuthold, M., Hagenau, J., and Geistlinger, H., 2009. Membrane based measurement technology for in situ monitoring of gases in soil. *Sensors*, 9(2), 756-767. DOI: 10.3390/s90200756

Lenormand, R., Delaplace, P. and Schmitz, P., 1998. Can we really measure the relative permeabilities using the micropore membrane method? *Journal of Petroleum Science and Engineering*, 19(1-2), pp.93–102.

Lenormand, R., Touboul, E. and Zarcone, C., 1988. Numerical models and experiments on immiscible displacements in porous media. *J. Fluid Mech.* (1988),, 189(C), pp.165–187.

Leuning, R., Etheridge, D., Luhan, A., and Dunse, B., 2008. Atmospheric monitoring and verification technologies for CO<sub>2</sub> geosequestration. *International Journal of Greenhouse Gas Control*, 2(3), pp.401–414.

Leverett, M. C., 1939. Flow of Oil/Water Mixtures through Unconsolidated Sands, *Trans. AIME*, 132(1), pp.149 - 171.

Li, L., Peters, C.A. and Celia, Michael A, 2006. Upscaling geochemical reaction rates using pore-scale network modeling. *Advances in water resources*, 29(9), pp.1351–1370.

Little, M.G. and Jackson, R.B., 2010. Potential impacts of leakage from deep CO<sub>2</sub> geosequestration on overlying freshwater aquifers. *Environmental science & technology*, 44(23), pp.9225–32.

Longeron, D.G., Argaud, M. J., and Feraud, J. P., 1989. Effect of overburden pressure and the nature and microscopic distribution of fluids on electrical properties of rock samples. *SPE Formation Evaluation*, 4(02), pp.194–202.

Ma, K., Lopez-Salinas, J. L., Puerto, M. C., Miller, C. A., Biswal, S. L., and Hirasaki, G. J., 2013. Estimation of Parameters for the Simulation of Foam Flow through Porous Media. Part 1: The Dry-Out Effect,

Mahmood, A., Warsi, M. F., Ashiq, M.N., Sher, M., 2012. Improvements in electrical and dielectric properties of substituted multiferroic LaMnO<sub>3</sub> based nanostructures synthesized by co-precipitation method. *Materials Research Bulletin*, 47(12), pp.4197–4202.

Manthey, S., Hassanizadeh, S.M. and Helmig, R., 2005. Macro-Scale Dynamic Effects in Homogeneous and Heterogeneous Porous Media. *Transport in Porous Media*, 58(1-2), pp.121–145.

Manthey, S., 2006. Two-phase flow processes with dynamic effect in porous media-parameter estimation and simulation, PhD Dissertation thesis, pp. 212, University of Stuttgart.

Mariotti, A.D., Brandaleze, E. and Buscaglia, G.C., 2010. Parametric study of the interface behavior between two immiscible liquids flowing through a porous medium. *Papers in Physics*, 1, p.10007.

Markatos, N.C., 2012. Dynamic computer modeling of environmental systems for decision making, risk assessment and design. *Asia-Pacific Journal of Chemical Engineering*, 7(2), pp.182–205.

Marland, G. and Rotty, R.M., 1984. Carbon dioxide emissions from fossil fuels: A procedure for estimation and results for 1950--1982. *Tellus B*, 36(4), pp.232–261.

Marquardt, D.W., 1963. An algorithm for least-squares estimation of nonlinear parameters. *Journal of the Society for Industrial & Applied Mathematics*, 11(2), pp.431–441.

Mehta, H.B., Pujara, M.P. and Banerjee, J., 2013. Prediction of Two Phase Flow Pattern Using Artificial Neural Network. In International Conference on Chemical and Environmental Engineering (ICCEE'2013) April 15-16, 2013 Johannesburg (South Africa).

Merkel, T.C., Gupta, R. P., Turk, B. S., and Freeman, B. D., 2001. Mixed-gas permeation of syngas components in poly (dimethylsiloxane) and poly (1-trimethylsilyl-1-propyne) at elevated temperatures. *Journal of Membrane Science*, 191(1), pp.85–94.

Metz, B., Davidson, O., de Coninck, H., Loos, M., and Meyer, L., 2005. IPCC special report on carbon dioxide capture and storage, Intergovernmental Panel on Climate Change, Geneva (Switzerland). Working Group III. Cambridge University Press.

Michael, K., Golab, A., Shulakova, V., Ennis-King, J., Allinson, G., Sharma, S., and Aiken, T. 2010. Geological storage of CO<sub>2</sub> in saline aquifers. A review of the experience from existing storage operations. *International Journal of Greenhouse Gas Control*, 4(4), pp.659–667.

Mirzaei, M. and Das, D. B., 2007. Dynamic effects in capillary pressure–saturations relationships for two-phase flow in 3D porous media: Implications of micro-heterogeneities. *Chemical Engineering Science*, 62(7), pp.1927–1947.

Mirzaei, M. and Das, D. B., 2013. Experimental investigation of hysteretic dynamic effect in capillary pressure-saturation relationship for two-phase flow in porous media. *AIChE Journal*, 59(10), pp.3958–3974.

Miller, C. T., Christakos, G., Imhoff, P. T., McBride, J. F. and Pedit, J. A., 1998. Multiphase flow and transport modeling in heterogeneous porous media: Challenges and approaches, *Advances in Water Resources*, 21, 77-120.

Morris, J P, Hao, Y., Foxall, W., and McNab, W., 2011a. In salah CO<sub>2</sub> storage JIP: hydromechanical simulations of surface uplift due to CO<sub>2</sub> injection at in salah. *Energy Procedia*, 4, pp.3269–3275.

Morris, Joseph P., Detwiler, R. L., Friedmann, S. J., Vorobiev, O. Y., and Hao, Y., 2011b. The large-scale geomechanical and hydrogeological effects of multiple CO<sub>2</sub> injection sites on formation stability. *International Journal of Greenhouse Gas Control*, 5(1), pp.69–74.

Morrow, N. and Harris, C., 1965. Capillary Equilibrium in Porous Materials. *Society of Petroleum Engineers Journal*, 5(1), pp.418–420.

Mohanty, K. K. (2002), Impact of Capillary and Bond Numbers on Relative Permeability, Final Report, University of Houston, Houston, TX., DOE Award Number: DE-AC26-99BC15206, pp1-119.

Mualem, Y., 1976. A new model for predicting the hydraulic conductivity of unsaturated porous media. *Water Resour. Res.*, 12(3), pp.513–522.

Mueller, A. V and Hemond, H.F., 2013. Extended artificial neural networks: incorporation of a priori chemical knowledge enables use of ion selective electrodes for in-situ measurement of ions at environmentally relevant levels.. *Talanta*, 117, pp.112–118.

Müller, N., 2011. Supercritical CO<sub>2</sub>-Brine Relative Permeability Experiments in Reservoir Rocks—Literature Review and Recommendations. *Transport in Porous Media*, 87(2), pp.367–383.

Nakatsuka, Y., Xue, Z., Garcia, H., and Matsuoka, T., 2010. Experimental study on CO<sub>2</sub> monitoring and quantification of stored CO<sub>2</sub> in saline formations using resistivity measurements. *International Journal of Greenhouse Gas Control*, 4(2), pp.209–216.

Nejad, K., E. Berg, and J. Ringen, 2011. Effect of Oil Viscosity on Water/Oil Relative Permeability. Presentation at the International Symposium of the Society of Core Analysts edited, Austin, Texas, USA.

Nguyen, B.-L., Bruining, Johannes and Slob, E.C., 1999. Effects of wettability on dielectric properties of porous media. In SPE annual technical conference. pp. 153–160.

Nielsen, L.C., Bourg, I.C. and Sposito, G., 2012. Predicting CO<sub>2</sub>-water interfacial tension under pressure and temperature conditions of geologic CO<sub>2</sub> storage. *Geochimica et Cosmochimica Acta*, 81, pp.28–38.

Nick, H. M., and S. K. Matthäi, 2011. Comparison of Three FE-FV Numerical Schemes for Single- and Two-Phase Flow Simulation of Fractured Porous Media, *Transp. Porous Media*, 90(2), 421-444.

Nordbotten, J. M., Celia, M. A., Dahle, H. K., and Hassanizadeh, S. M., 2007. Interpretation of macroscale variables in Darcy's law. *Water Resources Research*, 43(8), DOI: 10.1029/2006WR005018

Nordbotten, J. M., Celia, M. A., Dahle, H. K., and Hassanizadeh, S. M. 2008. On the definition of macroscale pressure for multiphase flow in porous media. *Water Resources Research*, 44(6), pp.1–8.

Nordbotten, J. M., Nogués, J. P., and Celia, M. A., 2010. Appropriate choice of average pressure for upscaling relative permeability in dynamic flow conditions. *SPE J*, 15(1), pp.228–237.

Nordbotten, J. M., Celia, M. A. and Bachu, S., 2004. Analytical solutions for leakage rates through abandoned wells. *Water Resources Research*, 40(4), DOI: 10.1029/2003WR002997.

Nordbotten, Jan Martin, Celia, Michael A and Bachu, S., 2005. Injection and storage of CO<sub>2</sub> in deep saline aquifers: Analytical solution for CO<sub>2</sub> plume evolution during injection. *Transport in Porous media*, 58(3), pp.339–360.

O'Carroll, D M, Phelan, T.J. and Abriola, L M, 2005a. Exploring dynamic effects in capillary pressure in multistep outflow experiments. *Water Resour. Res.*, 41(11), p.W11419.

O'Carroll, D. M., Abriola, L. M., Polityka, C. A., Bradford, S. A., and Demond, A. H., 2005b. Prediction of two-phase capillary pressure--saturation relationships in fractional wettability systems. *Journal of contaminant hydrology*, 77(4), pp.247–270.

Odeh, A. S., 1959. Effect of Viscosity Ratio on Relative Permeability, *Transactions AIME*, 216, 346-353.

Olivella, S., Carrera, J., Gens, A., and Alonso, E., 1994. Nonisothermal multiphase flow of brine and gas through saline media. *Transport in porous media*, 15(3), pp.271–293.

Omambia, A.N. and Li, Y., 2010. Numeric modeling of carbon dioxide sequestration in deep saline aquifers in Wangchang Oilfield-Jiangnan Basin, China. *Journal of American Science*, 6(8).

Ouakad, H.M., 2013. Modeling the CO<sub>2</sub> Sequestration Convection Problem Using the Lattice Boltzmann Method. *Mathematical Problems in Engineering*, 2013, pp.1–10.

Ouellet, A., Thomas Bérard, Jean Desroches, Peter Frykman, Peter Welsh, James Minton, Yusuf Pamukcu, Suzanne Hurter, and Cornelia Schmidt-Hattenberger, 2011. Reservoir geomechanics for assessing containment in CO<sub>2</sub> storage: A case study at Ketzin, Germany. *Energy Procedia*, 4, pp.3298–3305.

Oung, O., Hassanizadeh, S. Majid and Bezuijen, Adam, 2005. Two-Phase Flow Experiments in a Geocentrifuge and the Significance of Dynamic Capillary Pressure Effect. *Journal of Porous Media*, 8(3), pp.247–257.

Ozgun, E. and Gumrah, F., 2009. Diffusive and Convective Mechanisms during CO<sub>2</sub> Sequestration in Aquifers. *Energy Sources, Part A*, 31(8), pp.698–709.

Ozturk, B. and Hughes, R., 2012. Evaluation of mass transfer characteristics of non-porous and microporous membrane contactors for the removal of CO<sub>2</sub>. *Chemical Engineering Journal*, 195-196, pp.122–131.

Patankar, S., 1980. *Numerical heat transfer and fluid flow*, CRC Press.

Pentland, C.H., 2011. *Measurements of Non-wetting Phase Trapping in Porous Media*. , 2010 (Awarded).

Pentland, C.H., El-Maghraby, R., Iglauer, S., and Blunt, M. J. 2011. Measurements of the capillary trapping of super-critical carbon dioxide in Berea sandstone. *Geophysical Research Letters*, 38(6), pp.2007–2010.

Petersen, R. T., Balhoff, M. T. and Bryant, S., 2011. Coupling multiphase pore-scale models to account for boundary conditions: Application to 2D quasi-static pore networks, *Journal of Multiscale Modelling*, 03(03), 109-131.

Petvipusit, K.R., Elsheikh, A. H., Laforce, T. C., King, P. R., and Blunt, M. J., 2014. Robust optimisation of CO<sub>2</sub> sequestration strategies under geological uncertainty using adaptive sparse grid surrogates. *Computational Geosciences*, pp.1–16.

Pickup, G.E., Stephen, K. D., Ma, J., Zhang, P., and Clark, J. D. 2005. Multi-Stage Upscaling: Selection of Suitable Methods. In D B Das and S M Hassanizadeh, eds. *Upscaling Multiphase Flow in Porous Media SE - 10*. Springer Netherlands, pp. 191–216.

Pini, R., Krevor, S.C.M. and Benson, S.M., 2012. Capillary pressure and heterogeneity for the CO<sub>2</sub>/water system in sandstone rocks at reservoir conditions. *Advances in Water Resources*, 38, pp.48–59.

Pistone, S., Stacey, R. and Horne, R., 2011. The significance of CO<sub>2</sub> solubility in geothermal reservoirs. In *Proceedings Thirty-Sixth Workshop on Geothermal Reservoir Engineering*, Jan-2011.

Plan, L., 2005. Factors controlling carbonate dissolution rates quantified in a field test in the Austrian alps. *Geomorphology*, 68(3), pp.201–212.

Plug, W.-J, Slob, E., Bruining, J., and Moreno Tirado, L. M., 2007a. Simultaneous measurement of hysteresis in capillary pressure and electric permittivity for multiphase flow through porous media. , 72(3).

Plug, W.J., Moreno, L. M., Bruining, J., and Slob, E. C. 2007b. Simultaneous Measurement of Capillary Pressure and Relative permittivity in Porous Media. *PIERS Online*, 3(4), pp.549–553.

Plug, W.-J. and Bruining, J., 2007. Capillary pressure for the sand–CO<sub>2</sub>–water system under various pressure conditions. Application to CO<sub>2</sub> sequestration. *Advances in Water Resources*, 30(11), pp.2339–2353.

Plug, W-J, Mazumder, S. and Bruining, J, 2006. Capillary pressure and wettability behavior of the coal-water-carbon dioxide system at high pressures. *International CBM ...*, pp.1–15.

Power, C., Gerhard, J. I., Tsourlos, P., and Giannopoulos, A., 2013. A new coupled model for simulating the mapping of dense nonaqueous phase liquids using electrical resistivity tomography. *Geophysics*, 78(4), pp.EN1–EN15.

Praveen, J., Larry W. Mason, and J. Douglas Way, 2006. Characterization of silicon rubber membrane materials at low temperature and low pressure conditions. *Journal of Membrane Science*, 272, pp.125–136.

Preisig, M. and Prévost, J.H., 2011. Coupled multi-phase thermo-poromechanical effects. Case study: CO<sub>2</sub> injection at In Salah, Algeria. *International Journal of Greenhouse Gas Control*, 5(4), pp.1055–1064.

Pruess, K., García, J., Kavscek, T., Oldenburg, C., Rutqvist, J., Steefel, C., & Xu, T. (2004). Code intercomparison builds confidence in numerical simulation models for geologic disposal of CO<sub>2</sub>. *Energy*, 29(9), 1431-1444.

Pruess, K., 2004. Numerical Simulation of CO<sub>2</sub> Leakage from a Geologic Disposal Reservoir, Including Transitions from Super- to Sub-Critical Conditions , and Boiling of Liquid CO<sub>2</sub>. *SPE Journal* 9(02), pp. 237 – 248. DOI: <http://dx.doi.org/10.2118/86098-PA>

Pruess, Karsten, Oldenburg, C.M. and Moridis, G.J., 1999. TOUGH2 User's Guide Version 2. In *TOUGH2 User's Guide Version 2*. Lawrence Berkeley National Laboratory.

Pusch G, May, F, Bernstone C, Höllwart J, Lillie J, Mundhenk N, W.H., 2010. Common Features of Carbon Dioxide and underground Gas Storage (2). Oil Gas European Magazine, 36(3/4), pp.131–136.

Rafati, R., Hamidi, H., Idris, A. K., and Manan, M. A., 2012. Application of sustainable foaming agents to control the mobility of carbon dioxide in enhanced oil recovery. Egyptian Journal of Petroleum, 21(2), pp.155–163.

Riaz, A. and Tchelepi, H.A., 2004. Linear stability analysis of immiscible two-phase flow in porous media with capillary dispersion and density variation. Physics of Fluids (1994-present), 16(12), pp.4727–4737.

Ritter, L.C. and Drake, R.L., 1945. Pore Size Distribution in Porous Materials. Industrial & Engineering Chemistry Analytical Edition, 17(12), pp.782–786.

Renard, P., and G. De Marsily, 1997. Calculating equivalent permeability: A review, Advances in Water Resources, 20(5-6), 253-278.

Robinson, D.A., Gardner, C.M.K. and Cooper, J.D., 1999. Measurement of relative permittivity in sandy soils using TDR, capacitance and theta probes: comparison, including the effects of bulk soil electrical conductivity. Journal of Hydrology, 223(3), pp.198–211.

Rogers, L.L. and Dowla, F.U., 1994. Optimization of groundwater remediation using artificial neural networks with parallel solute transport modeling. Water Resources Research, 30(2), pp.457–481.

Rohde, C., and F. Kissling, 2010. The computation of nonclassical shock waves with a heterogeneous multiscale method, Networks and Heterogeneous Media (NHM), 5(3), 661-674.

Rutqvist, J., Wu, Y. S., Tsang, C. F., and Bodvarsson, G. 2002. A modeling approach for analysis of coupled multiphase fluid flow, heat transfer, and deformation in fractured porous rock. International Journal of Rock Mechanics and Mining Sciences, 39(4), pp.429–442.

Rutqvist, Jonny, 2011. Status of the TOUGH-FLAC simulator and recent applications related to coupled fluid flow and crustal deformations. Computers & Geosciences, 37(6), pp.739–750.

Rutqvist, Jonny, 2012. The Geomechanics of CO<sub>2</sub> Storage in Deep Sedimentary Formations. Geotechnical and Geological Engineering, 30(3), pp.525–551.

- Saffman, P.G. and Taylor, G., 1958. The penetration of a fluid into a porous medium or Hele-Shaw cell containing a more viscous liquid. *Proceedings of the Royal Society of London. Series A. Mathematical and Physical Sciences*, 245(1242), pp. 312–329.
- Sakaki, T., O'Carroll, Denis M. and Illangasekare, T.H., 2010. Direct Quantification of Dynamic Effects in Capillary Pressure for Drainage–Wetting Cycles. *Vadose Zone Journal*, 9(2), p.424.
- Shahrabi, S.S., Mortaheb, H. R., Barzin, J., and Ehsani, M. R. 2012. Pervaporative performance of a PDMS/blended PES composite membrane for removal of toluene from water. *Desalination*, 287, pp.281–289.
- Salimi, H., Wolf, K.-H. and Bruining, Johannes, 2012. The influence of capillary pressure on the phase equilibrium of the CO<sub>2</sub>–water system: Application to carbon sequestration combined with geothermal energy. *International Journal of Greenhouse Gas Control*, 11, pp.S47–S66.
- Saraji, S. Goual, L., Piri, M., and Plancher, H., 2013. Wettability of supercritical carbon dioxide/water/quartz systems: simultaneous measurement of contact angle and interfacial tension at reservoir conditions. *Langmuir: the ACS journal of surfaces and colloids*, 29(23), pp.6856–6866.
- Saripalli, K.P., Mcgrail, B.P. and White, Mark D, 2001. Modeling the sequestration of CO<sub>2</sub> in deep geological formations. In *First National Conference on Carbon Sequestration*. pp. 1–19.
- Sawabini, C.T., Chilingar, G. V and Allen, B.R., 1974. Compressibility of unconsolidated, arkosic oil sands: 11F, 31R Soc. Petroleum engrs. J. V14, N2, Apr. 1974, P132--139. In *International Journal of Rock Mechanics and Mining Sciences & Geomechanics Abstracts*. p. 201.
- Scholes, C. A., Qader, A., Stevens, G. W., and Kentish, S. E. 2014. Membrane gas-solvent contactor pilot plant trials of CO<sub>2</sub> absorption from flue gas. *Separation Science and Technology*, (August), p.140731131036000.
- Schwartz, M.O., 2014. Modelling leakage and groundwater pollution in a hypothetical CO<sub>2</sub> sequestration project. *International Journal of Greenhouse Gas Control*, 23, pp.72–85.
- Seaton, N.A. and Walton, J.P.R.B., 1989. A new analysis method for the determination of the pore size distribution of porous carbons from nitrogen adsorption measurements. *Carbon*, 27(6), pp.853–861.

Shafrin, E.G. and Zisman, W.A., 1960. Constitutive relations in the wetting of low energy surfaces and the theory of the retraction method of preparing monolayers<sup>1</sup>. *The Journal of Physical Chemistry*, 64(5), pp.519–524.

Sharifi, M., and M. Kelkar, 2013. New dynamic permeability upscaling method for flow simulation under depletion drive and no-crossflow conditions, *Pet. Sci.*, 10(2), 233-241.

Shojai Kaveh, N., Rudolph, E. S. J., Wolf, K. H. A., and Ashrafizadeh, S. N. 2011. Wettability determination by contact angle measurements: hvbB coal-water system with injection of synthetic flue gas and CO<sub>2</sub>. *Journal of colloid and interface science*, 364(1), pp.237–47.

Shukla, R., Ranjith, P., Haque, A., and Choi, X. 2010. A review of studies on CO<sub>2</sub> sequestration and caprock integrity. *Fuel*, 89(10), pp.2651–2664.

Silin, D., Patzek, T. and Benson, S.M., 2008. A Model of Buoyancy-Driven Two-Phase Countercurrent Fluid Flow. *Transport in Porous Media*, 76(3), pp.449–469.

Singh, V.P., Cavanagh, A., Hansen, H., Nazarian, B., Iding, M., and Ringrose, P. S., 2010. Reservoir Modeling of CO<sub>2</sub> Plume Behavior Calibrated Against Monitoring Data From Sleipner Norway. In *SPE annual technical conference and exhibition*.

Smiles, D.E., Vachaud, G. and Vauclin, M., 1971. A test of the uniqueness of the soil moisture characteristic during transient, nonhysteretic flow of water in a rigid soil. *Soil Science Society of America Journal*, 35(4), pp.534–539.

Solomon S, Qin D, Manning M, Chen Z, Marquis M, Averyt K B, Tignor M and Miller H L (ed), 2007 *Climate Change 2007: The Physical Science Basis. Contribution of Working Group I to the Fourth Assessment Report of the Intergovernmental Panel on Climate Change* (Cambridge: Cambridge University Press).

Solyman, L., Walsh, D. and Syms, R.R.A., 2014. *Electrical properties of materials*, Oxford University Press.

Spalding, D.B., 1981. A general purpose computer program for multi-dimensional one-and two-phase flow. *Mathematics and Computers in Simulation*, 23(3), pp.267–276.

Spangler, L.H., Dobeck, L. M., Repasky, K. S., Nehrir, A. R., Humphries, S. D., Barr, J. L., 2010. A shallow subsurface controlled release facility in Bozeman, Montana, USA, for testing near surface CO<sub>2</sub> detection techniques and transport models. *Environmental Earth Sciences*, 60(2), pp.227–239.

- Srinivasulu, S. and Jain, A., 2006. A comparative analysis of training methods for artificial neural network rainfall--runoff models. *Applied Soft Computing*, 6(3), pp.295–306.
- Stanmore, B.R. and Gilot, P., 2005. Review—calcination and carbonation of limestone during thermal cycling for CO<sub>2</sub> sequestration. *Fuel Processing Technology*, 86(16), pp.1707–1743.
- Stauder, E., 1992. *Membranen und Membranprozesse*. VCH Weinheim, p.325 pp.
- Stauffer, 1978. Time Dependence of the Relations between Capillary Pressure, Water Content and Conductivity During Drainage of Porous Media. In paper presented at IAHR Symp. on Scale Effects in Porous Media. pp. 766–776.
- Stephens, J.C., 2006. Growing interest in carbon capture and storage(CCS) for climate change mitigation. *Sustainability: Science Practice and Policy*, 2(2), pp.4–13.
- Sweijen, T., Hartog, N., Marsman, A., and Keijzer, T. J., 2014. The transport behaviour of elemental mercury DNAPL in saturated porous media: Analysis of field observations and two-phase flow modelling. *Journal of contaminant hydrology*, 161, pp.24–34.
- Taku Ide, S., Jessen, Kristian and Orr Jr, F.M., 2007. Storage of CO<sub>2</sub> in saline aquifers: Effects of gravity, viscous, and capillary forces on amount and timing of trapping. *International Journal of Greenhouse Gas Control*, 1(4), pp.481–491.
- Tao, Q. and Bryant, S.L., 2014. Well permeability estimation and CO<sub>2</sub> leakage rates. *International Journal of Greenhouse Gas Control*, 22, pp.77–87.
- Tiab, D. and Donaldson, E C, 2004. *Petrophysics: Theory and Practice of Measuring Reservoir Rock and Fluid Transport Properties* 2nd ed., Oxford: Gulf Professional Publishing (Elsevier).
- Tian, S., Lei, G., He, S., and Yang, L., 2012. Dynamic effect of capillary pressure in low permeability reservoirs. *Petroleum Exploration and Development*, 39(3), pp.405–411.
- Tokunaga, T.K., Wan, J., Jung, J. W., Kim, T. W., Kim, Y., and Dong, W. 2013. Capillary pressure and saturation relations for supercritical CO<sub>2</sub> and brine in sand: High-pressure P<sub>c</sub>(S<sub>w</sub>) controller/meter measurements, and capillary scaling predictions. *Water Resources Research*, 49(8), 4566-4579.
- Topp, G.C., Zebchuk, W. D., Davis, J. L., and Bailey, W. G., 1984. The measurement of soil water content using a portable tdr hand probe. *Canadian Journal of Soil Science*, 64(3), pp.313–321.

- Topp, G.C., Klute, A. and Peters, D.B., 1967. Comparison of water content-pressure head data obtained by equilibrium, steady-state, and unsteady-state methods. *Soil Science Society of America Journal*, 31(3), pp.312–314.
- Tsakiroglou, C. D., D. G. Avraam, and A. C. Payatakes, 2007. Transient and steady-state relative permeabilities from two-phase flow experiments in planar pore networks, *Advances in Water Resources*, 30(9), 1981-1992.
- Tsang, Chin-Fu, Birkholzer, J. and Rutqvist, Jonny, 2007. A comparative review of hydrologic issues involved in geologic storage of CO<sub>2</sub> and injection disposal of liquid waste. *Environmental Geology*, 54(8), pp.1723–1737.
- Van Duijn, C.J. and Floris, F.J., 1992. Instability of a sharp interface in polymer flooding. *Engineering Computations*, 9(4), pp.453 – 467.
- Van Duijn, C.J., Fan, Y., Peletier, L. A., and Pop, I. S., 2013. Travelling wave solutions for degenerate pseudo-parabolic equations modelling two-phase flow in porous media. *Nonlinear Analysis: Real World Applications*, 14(3), pp.1361–1383.
- van Genuchten, M. T., 1980. A closed form equation for predicting the hydraulic conductivity of unsaturated soils, *Soil Science Society of America Journal*, 44, 892-898.
- Van Amerongen, G.J., 1964. Diffusion in elastomers. *Rubber Chemistry and Technology*, 37(5), pp.1065–1152.
- Van Lingen, P., Bruining, J. and C.P.J.W., V., 1996. Capillary Entrapment Caused by Small-Scale Wettability Heterogeneities. *SPE Reservoir Engineering*, 11(2), pp.93–100.
- Van Meurs, P., 1957. The use of transparent three-dimensional models for studying the mechanism of flow processes in oil reservoirs. In In: *SPE Annual Technical Conference and Exhibition*, Anaheim, CA, vol. 210. Society of Petroleum Engineers, pp. 295–301.
- Van Wunnik, J.N.M. and Wit, K., 1989. A simple analytical model of the growth of viscous fingers in heterogeneous porous media. In In: *1st European Conference on the Mathematics of Oil Recovery*. University of Cambridge.
- Versteeg, H.K. and Malalasekera, W., 1995. An introduction to computational fluid dynamic: The finite volume method, John Wiley & Sons Inc, New York (1995).
- Verwer, K., Eberli, G.P. and Weger, R.J., 2011. Effect of pore structure on electrical resistivity in carbonates. *AAPG bulletin*, 95(2), pp.175–190.

- Vilamajó, E., Queralt, Pilar Ledo, Juanjo Marcuello, Alex 2013. Feasibility of Monitoring the Hontom{in} (Burgos, Spain) CO<sub>2</sub> Storage Site Using a Deep EM Source. *Surveys in Geophysics*, 34(4), pp.441–461.
- Vilarrasa, V., Bolster, D., Olivella, S., and Carrera, J., 2010. Coupled hydromechanical modeling of CO<sub>2</sub> sequestration in deep saline aquifers. *International Journal of Greenhouse Gas Control*, 4(6), pp.910–919.
- Vinegar, H. J., and Waxman, M. H., 1984. Induced polarization of shaly sands. *Geophysics*, 49(8), 1267-1287.
- Vinegar, H.J. and Waxman, M.H., 1987. In-situ method for determining pore size distribution, capillary pressure and permeability.
- Virnovsky, G.A., 1995. Steady-State Relative Permeability Measurements Corrected for Capillary Effects. *SPE Journal*, (3), pp.85–95.
- Vuuren, D.P., Sebastiaan Deetman, Jasper van Vliet, Maarten van den Berg, Bas J. van Ruijven, Barbara Koelbl 2013. The role of negative CO<sub>2</sub> emissions for reaching 2°C—insights from integrated assessment modelling. *Climatic Change*, 118(1), pp.15–27.
- Wang, L. and Fu, K., 2008. *Artificial neural networks*, Wiley Online Library.
- Wang, S., Edwards, I.M. and Clarens, A.F., 2012. Wettability phenomena at the CO<sub>2</sub>--brine--mineral interface: Implications for geologic carbon sequestration. *Environmental science & technology*, 47(1), pp.234–241.
- Wang, W. and Kolditz, O., 2007. Object-oriented finite element analysis of thermo-hydro-mechanical (THM) problems in porous media. *International journal for numerical methods in engineering*, 69(1), pp.162–201.
- Wang, Y., Zhang, C., Wei, N., Oostrom, M., Wietsma, T. W., Li, X., and Bonneville, A., 2013. Experimental study of crossover from capillary to viscous fingering for supercritical CO<sub>2</sub>-water displacement in a homogeneous pore network. *Environmental science & technology*, 47(1), pp.212–8.
- Wang, J., M. Dong, and K. Asghari, 2006. Effect of Oil Viscosity on Heavy Oil-Water Relative Permeability Curves, in *SPE/DOE Symposium on Improved Oil Recovery*, edited, Society of Petroleum Engineers, Tulsa, Oklahoma, USA.

Ward, S.E., Ostle, N. J., Oakley, S., Quirk, H., Henrys, P. A., and Bardgett, R. D., 2013. Warming effects on greenhouse gas fluxes in peatlands are modulated by vegetation composition. *Ecology letters*, 16(10), pp.1285–1293.

Water, M., Abaci, S. and Whittaker, N., 2006. Relative permeability measurements for two phase flow in unconsolidated sands. *Mine Water and the Environment*, 26(2), pp.12–26.

Wedlake, G.D. and Robinson, D.B., 1979. Solubility of carbon dioxide in silicone oil. *Journal of Chemical and Engineering Data*, 24(4), pp.305–306.

White, H., 1989. Learning in artificial neural networks: A statistical perspective. *Neural computation*, 1(4), 425-464.

White, D.J., G. Burrowes, T. Davis, Z. Hajnal, K. Hirsche, I. Hutcheon, E. Majer, B. Rostron, and S. Whittaker, 2004. Greenhouse gas sequestration in abandoned oil reservoirs: The International Energy Agency Weyburn pilot project. *GSA today*, 14(7), pp.4–11.

White, M.D., 2002. Example Problem 9 Simulation of supercritical CO<sub>2</sub> into a deep saline aquifer, USA: Pacific Northwest Laboratory.

White, M.D., Watson, D.J., Bacon, D.H., White, S.K., McGrail, B.P. and Zhang, Z.F., 2012. Subsurface Transport Over Multiple Phases STOMP-CO<sub>2</sub> and -CO<sub>2e</sub> Guide PNNL-21268th ed., Pacific Northwest National Laboratory.

White, Mark D et al., 2003. Numerical Investigations of Multifluid Hydrodynamics During Injection of Supercritical CO<sub>2</sub> into Porous Media, In Sixth International Conference on Greenhouse Gas Control Technologies, Vol. I (ed. J. Gale and Y. Kaya), pp. 449-455. Elsevier Science Ltd., Kidlington, Oxford, United Kingdom.

White, Mark D and McGrail, B Peter, 2005. Stomp (subsurface transport over multiple phase) version 1.0 addendum: ECKEchem equilibrium-conservationkinetic equation chemistry and reactive transport. Pacific Northwest National Laboratory, PNNL-15482, Richland, Washington.

White, SP, Weir, G. and Kissling, W.M., 2001. Numerical simulation of CO<sub>2</sub> sequestration in natural CO<sub>2</sub> reservoirs on the Colorado Plateau. This volume, (64).

Wielopolski, L. and Mitra, S., 2010. Near-surface soil carbon detection for monitoring CO<sub>2</sub> seepage from a geological reservoir. *Environmental Earth Sciences*, 60(2), pp.307–312.

Wildenschild, D., Hopmans, J.W. and Simunek, J., 2001. Flow rate dependence of soil hydraulic characteristics. *Soil Science Society of America Journal*, 65(1), pp.35–48.

Woods, E.G., and Comer, A.G. 1962. Saturation distribution and injection pressure for a radial gas-storage reservoir. *Journal of Petroleum Technology*, 14(12), pp.1–389  
<http://dx.doi.org/10.2118/401-PA>.

Wraith, J.M. and Or, D., 1999. Temperature effects on soil bulk dielectric permittivity measured by time domain reflectometry: Experimental evidence and hypothesis development. *Water Resources Research*, 35(2), pp.361–369.

Xu, T., Sonnenthal, E., Spycher, N., Pruess, K., 2006. TOUGHREACT—A simulation program for non-isothermal multiphase reactive geochemical transport in variably saturated geologic media: Applications to geothermal injectivity and CO<sub>2</sub> geological sequestration. *Computers & Geosciences*, 32(2), pp.145–165.

Yan, S. and Minsker, B., 2006. Optimal groundwater remediation design using an Adaptive Neural Network Genetic Algorithm. *Water Resources Research*, 42(5). DOI: 10.1029/2005WR004303

Yang, Z., Tian, L., Niemi, A. and Fagerlund, F., 2013. Upscaling of the constitutive relationships for CO<sub>2</sub> migration in multimodal heterogeneous formations, *International Journal of Greenhouse Gas Control*, 19, 743-755.

Yang, C., Dai, Z., Romanak, K. D., Hovorka, S. D. and Treviño, R. H, 2014. Inverse modeling of water-rock-CO<sub>2</sub> batch experiments: Potential impacts on groundwater resources at carbon sequestration sites. *Environmental science & technology*, 48(5), pp.2798–2806.

Yang, Z., Dai, Z., Romanak, K. D., Hovorka, S. D., and Treviño, R. H 2013. The role of geological heterogeneity and variability in water infiltration on non-aqueous phase liquid migration. *Environmental Earth Sciences*, 68(7), pp.2085–2097.

Yiotis, A. G., J. Psihogios, M. E. Kainourgiakis, A. Papaioannou, and A. K. Stubos, 2007. A lattice boltzmann study of viscous coupling effects in immiscible two-phase flow in porous media, *Colloids and Surfaces A: Physicochemical and Engineering Aspects*, 300, 35-49.

Yortsos, Y.C. and Hickernell, F.J., 1989. Linear stability of immiscible displacement in porous media. *SIAM Journal on Applied Mathematics*, 49(3), pp.730–748.

- Yurdakul, M. and Akdas, H., 2013. Modeling uniaxial compressive strength of building stones using non-destructive test results as neural networks input parameters. *Construction and Building Materials*, 47, pp.1010–1019.
- Zahid, U., Lim, Y., Jung, J., and Han, C., 2011. CO<sub>2</sub> geological storage: A review on present and future prospects. *Korean Journal of Chemical Engineering*, 28(3), pp.674–685.
- Zakkour, P. and Haines, M., 2007. Permitting issues for CO<sub>2</sub> capture, transport and geological storage: A review of Europe, USA, Canada and Australia. *International Journal of Greenhouse Gas Control*, 1(1), pp.94–100.
- Zhang, C., Oostrom, M., Wietsma, T. W., Grate, J. W., and Warner, M. G., 2011. Influence of Viscous and Capillary Forces on Immiscible Fluid Displacement: Pore-Scale Experimental Study in a Water-Wet Micromodel Demonstrating Viscous and Capillary Fingering. *Energy & Fuels*, 25(8), pp.3493–3505.
- Zhang, G., Eddy Patuwo, B. and Y. Hu, M., 1998. Forecasting with artificial neural networks: *International Journal of Forecasting*, 14(1), pp.35–62.
- Zhang, H. and Cloud, A., 2006. The permeability characteristics of silicone rubber. In *Proceedings of the 2006 SAMPE Fall Technical Conference“ Global Advances in Materials and Process Engineering”*, Coatings and Sealants Section.
- Zhang, Y.-Q., Radha, A. V and Navrotsky, A., 2013. Thermochemistry of two calcium silicate carbonate minerals: scawtite, Ca<sub>7</sub> (Si<sub>6</sub>O<sub>18</sub>)(CO<sub>3</sub>) 2H<sub>2</sub>O, and spurrite, Ca<sub>5</sub> (SiO<sub>4</sub>)<sub>2</sub>(CO<sub>3</sub>). *Geochimica et Cosmochimica Acta*, 115, pp.92–99.
- Zhang, H., S. He, C. Jiao, G. Luan, S. Mo, and G. Lei (2014), Investigation of Dynamic Effect of Capillary Pressure in Ultra-Low Permeability Sandstones, *Indian Geotech J*, 1-10. DOI 10.1007/s40098-014-0109-3
- Zimmer, M., Erzinger, J. and Kujawa, C., 2011. The gas membrane sensor (GMS): A new method for gas measurements in deep boreholes applied at the CO<sub>2</sub>SINK site. *International Journal of Greenhouse Gas Control*, 5(4), pp.995–1001.

## APPENDIX A MATERIAL CHARACTERIZATIONS

### A.1 Particle characterization

Different sizes of silica sand particles (99% silicon dioxide from Sibelco, UK) were prepared to conduct two-phase flow experiments in the homogeneous domain. The coarse type (DA 14/25) and the fine or medium type (CH30 or DA30) were characterised as to their sizes using sieve analysis and microscope scanning. Porosity, bulk density and particle density were also determined using various techniques.

#### A.1.1 Sieve analysis

The sieve shaker (FRITCH, Idar-Oberstein, Germany) was used for the analysis of particle sizes. The sieves were arranged in the descending order of sizes from the top. Shaking was done for several minutes at different amplitudes to ensure complete segregation and the calculations were done assuming the particles found on a sieve were of average size in the median of the sieve and the immediate higher size. The average size obtained for the coarse size particle was 946 $\mu\text{m}$  and for the fine size was 482  $\mu\text{m}$ . Analyses of mass retention on each sieve for the samples are shown in Table A.1 and Table A.2 for the coarse and fine silica sand samples, respectively. The distribution coefficients derived for the coarse grains (DA 14/25) are shown in Table A.3. Other particle properties can be found in Table 3.1.

Table A.1: Sieve analysis for coarse silica sand particles

Sieve size ( $\mu\text{m}$ )	Sand Trapped (g)	Average Diameter ( $\mu\text{m}$ )	Phi size ( $\Phi$ )	mass Fraction	Cumulative mass Fraction
1700	—	—	—	—	—
1400	0.18	1550	-10.598	0.0009	0.0009
1000	70.47	1200	-10.229	0.3524	0.3533
850	46.82	925	-9.854	0.2341	0.5874
710	74.04	780	-9.608	0.3702	0.9576
600	7.78	655	-9.356	0.0389	0.9965
0	0.71	300	-8.229	0.0036	1.0001

Table A.2: Sieve analysis for fine silica sand particles

Sieve size ( $\mu\text{m}$ )	Sand Trapped (g)	Average Diameter ( $\mu\text{m}$ )	Phi size ( $\Phi$ )	mass Fraction	Cumulative mass Fraction
1400	-	-	-	-	
1000	0.1	1200	-10.23	0.0005	0.0005
710	0.8	855	-9.74	0.004	0.0045
500	82.42	605	-9.241	0.4122	0.4167
420	52.83	460	-8.846	0.2642	0.6809
300	56.57	360	-8.492	0.2829	0.9638
0	7.22	150	-7.229	0.0361	0.9999

Table A.3: Distribution coefficients in the silica sand samples

Sample	$D_{10}$	$D_{60}$	$D_{10}/D_{60}$
DA 14/25	649.1	888	1.37
CH 30	324.3	485	1.5

$D_{10}/D_{60}$  is the uniformity coefficient and its closeness to unity indicates the degree of uniformity in the particle sizes. The values for the coarse and fine sand samples are shown in Table A.3 and are close to 1. The coarse sample has a  $D_{10}/D_{60}$  value closer to 1. This implies more uniform size distribution in its range. Thus, the samples can be said to be uniform in size. This is somehow obvious in the plot of % mass retention on a sieve against the sieve diameter (Figures A1-A4) where that of the coarse range looks symmetrical while the other appears lopsided.

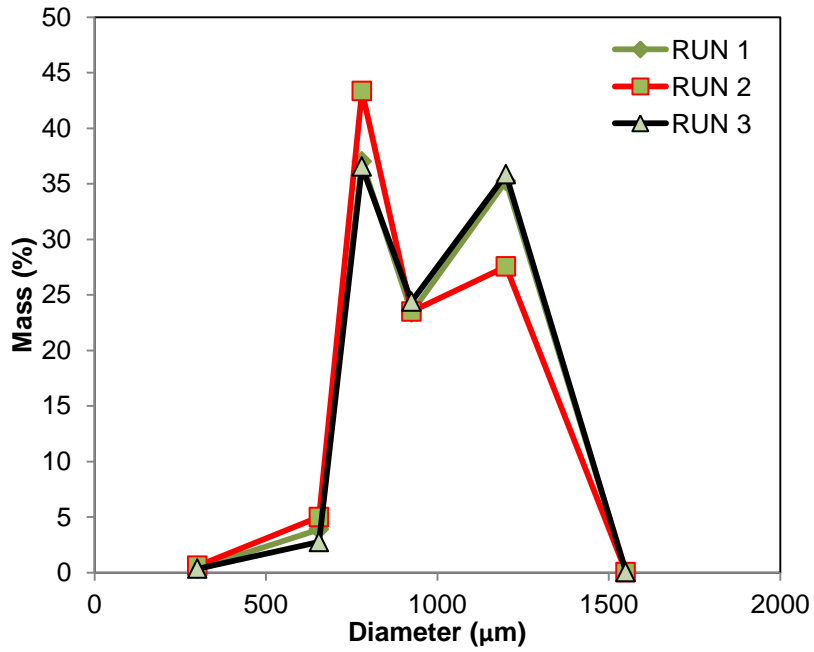


Figure A.1: Plot of % mass retention on each sieve versus average sieve diameter for DA 14/25 (coarse particle)

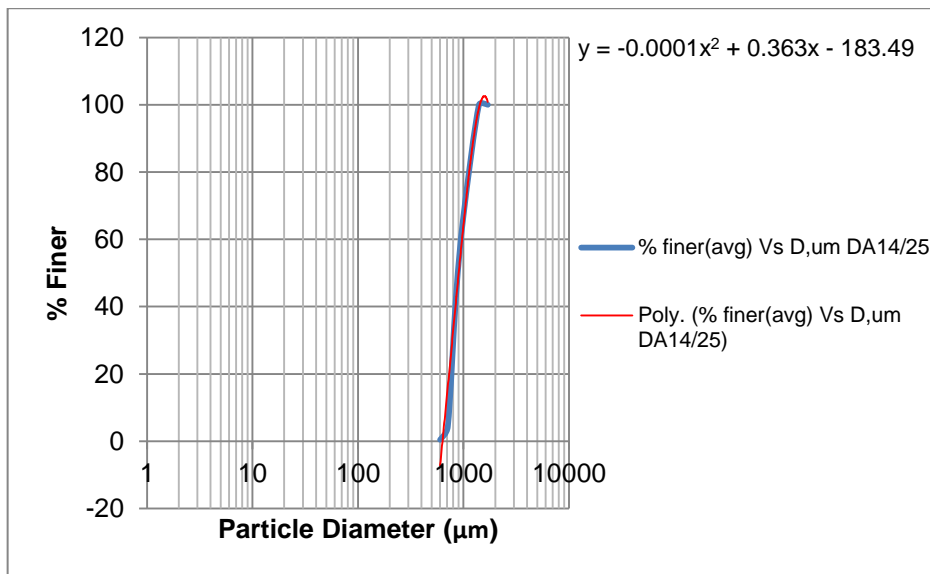


Figure A.2: Semi-log plot of % finer particle mass against average particle diameter for da14/25 (coarse particle)

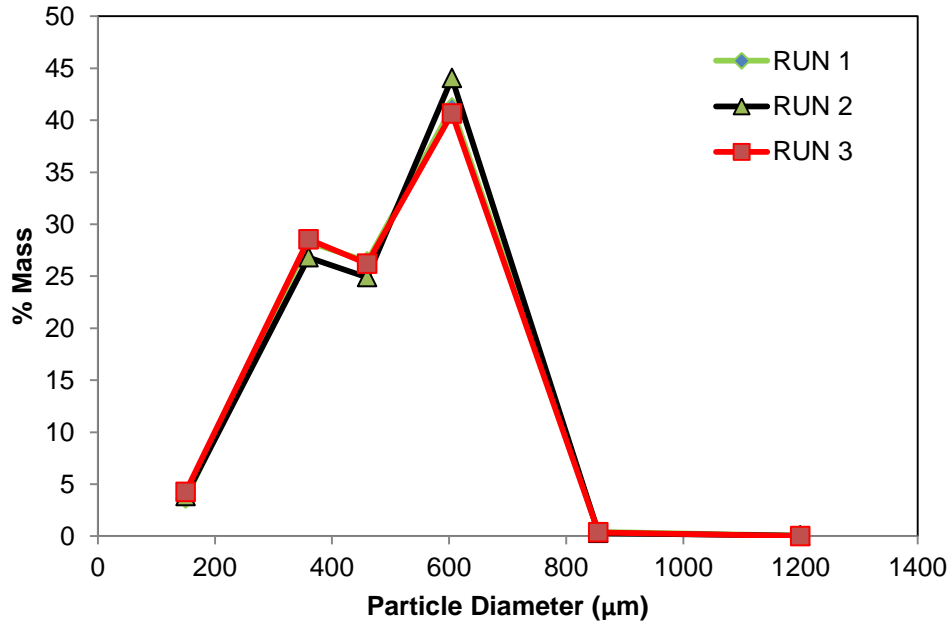


Figure A.3: Plot of % mass retention on each sieve versus average sieve diameter for DA 30 (fine particle)

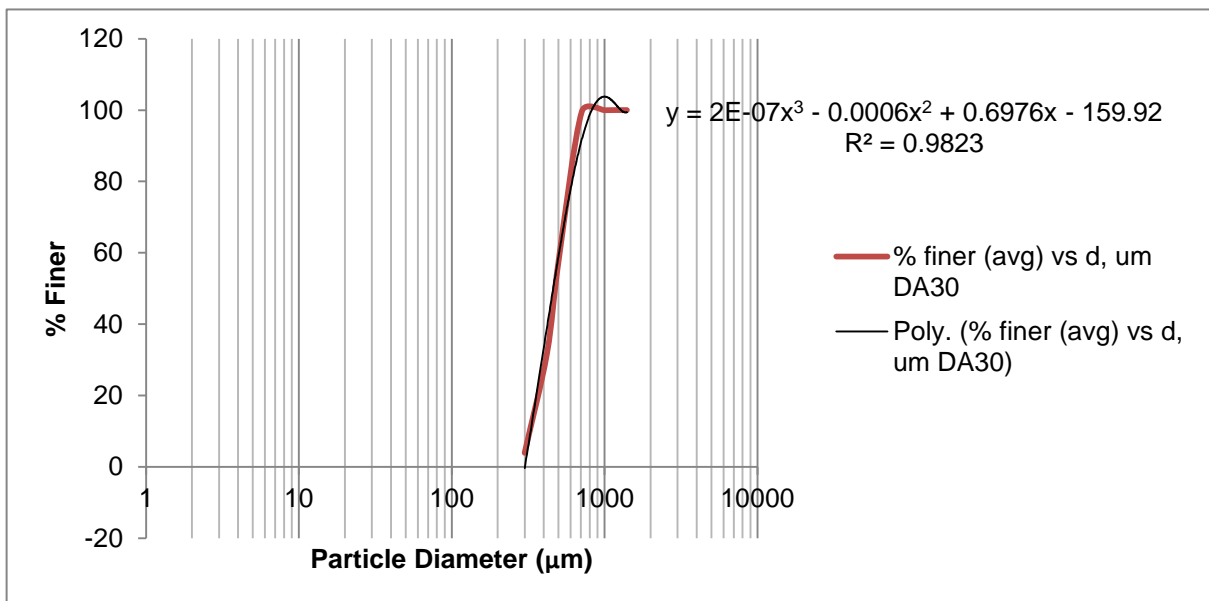


Figure A.4: Semi-log plot of % finer particle mass against average particle diameter for DA30 (fine particle)

### A.1.2 Microscope scan

Microscope scans of the coarse (DA 14/25) and fine (DA 30) silica sand particles were performed. The scanned images were analysed with ImageJ application software (National Institutes of Health, USA). Figures A.5 and A.6 show the scan images of the samples, while Figures A.7 and A.8 show the histogram depictions of the size distribution as obtained from image analysis software- **ImageJ** (rsbweb.nih.gov).

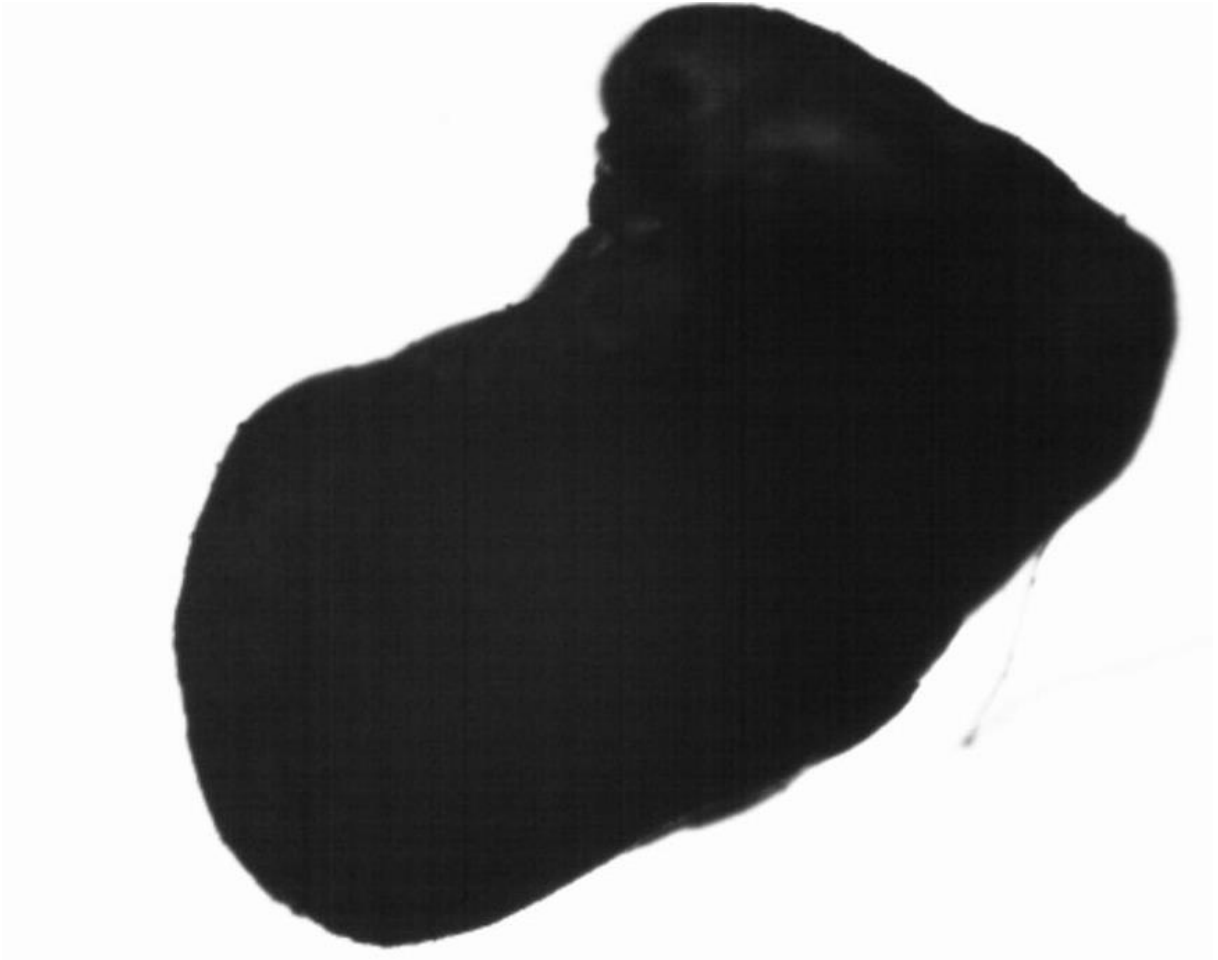


Figure A.5: Microscope scan (DA 14/25) (Magnification:x4)



Figure A.6: Microscope scan (DA 30) (Magnification:x4)

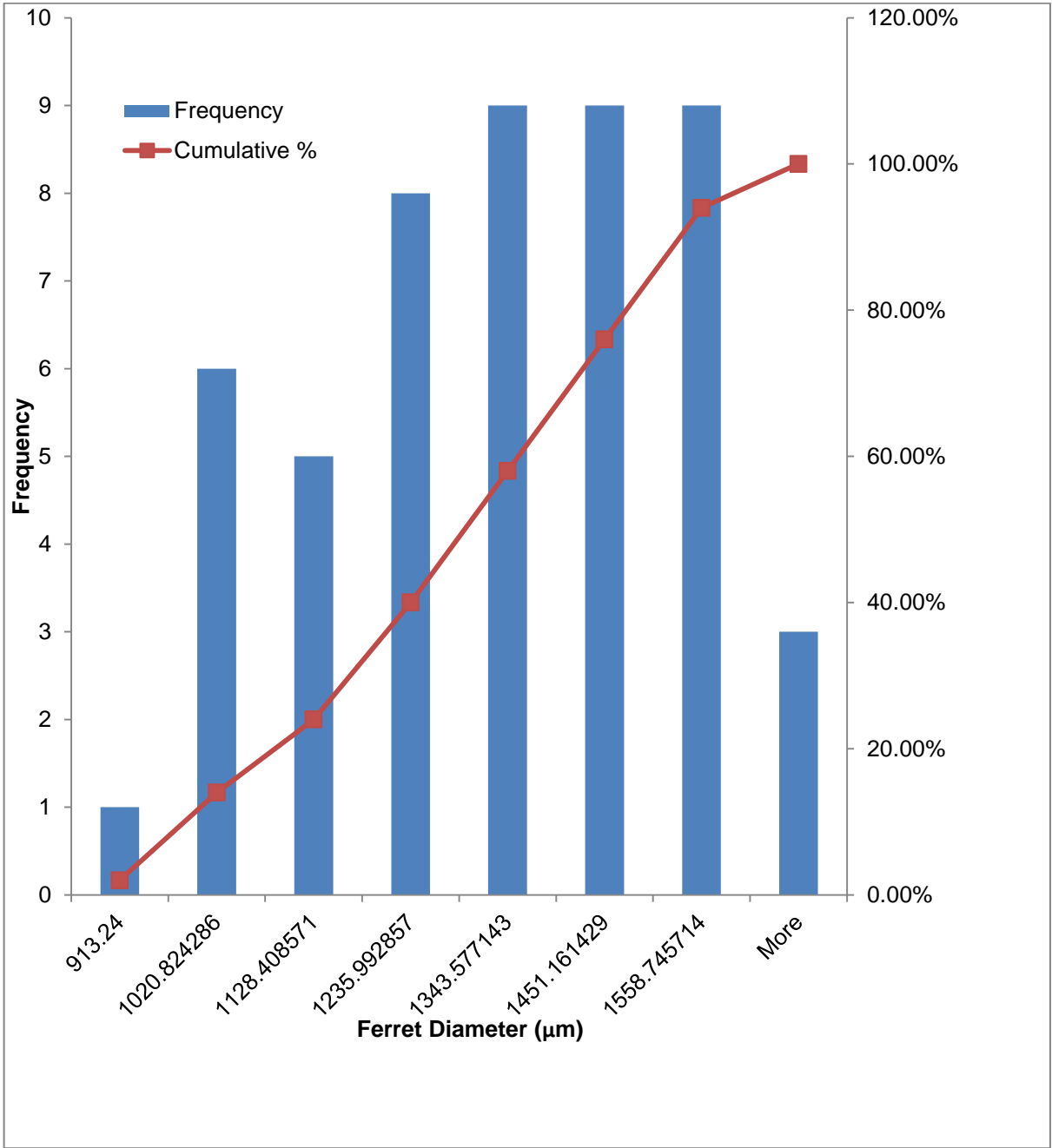


Figure A.7: Histogram of particle size distribution based on imageJ analysis of microscope scan of particles (DA 14/25)

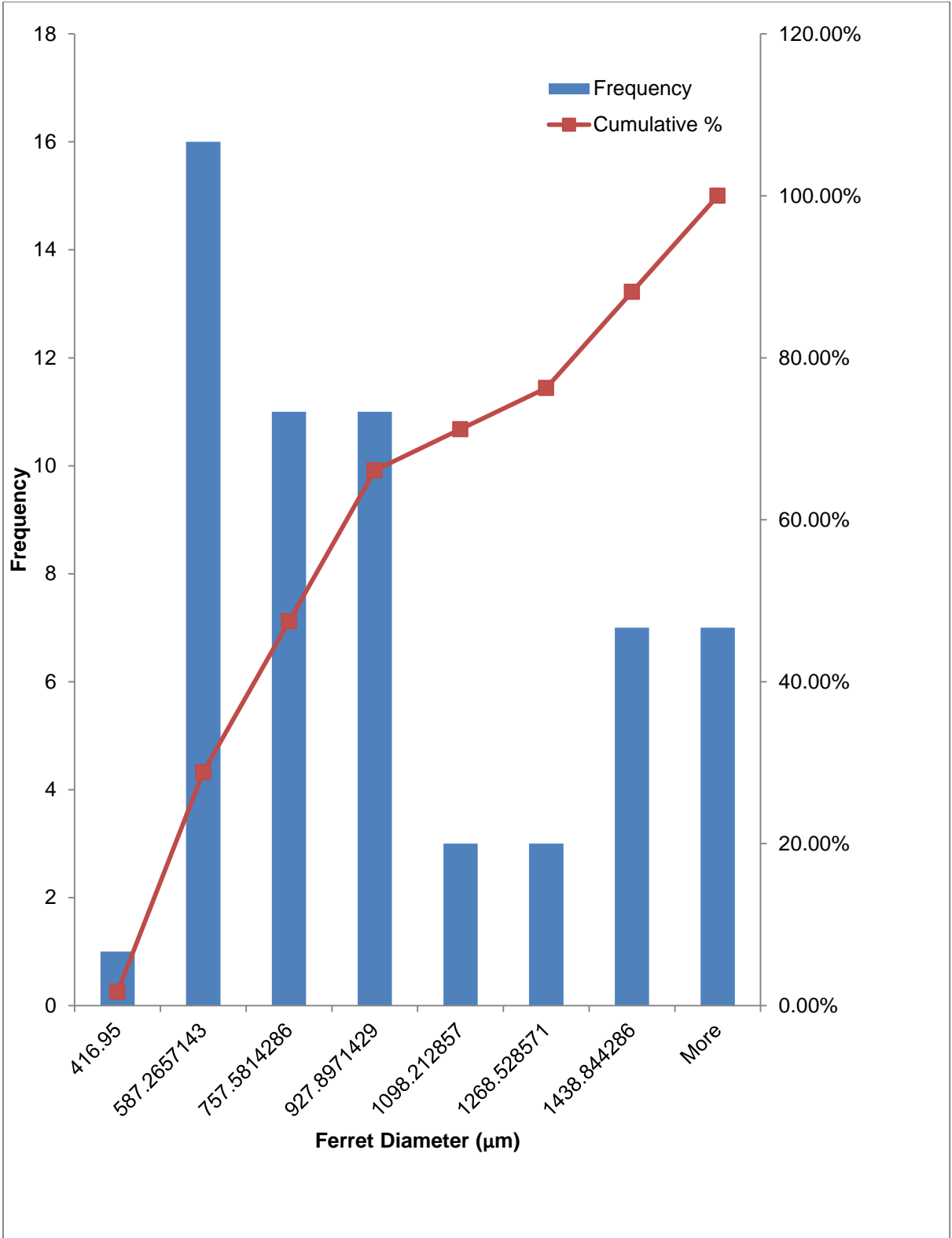


Figure A.8: Histogram of particle size distribution based on imageJ analysis of microscope scan of particles (DA 30)

### A.1.3 Absolute density

Absolute density was determined using a helium pycnometer (Micromeritics model 1305). A weighed quantity of silica sand in a sample cell was placed in a sample chamber and purged with helium. The chamber was later filled with helium, allowing pressure to build. The chamber was then vented and the procedure repeated for the sample up to five times. Average density for the coarse sample is in the range  $2.66 \text{ gcm}^{-3}$  while the fine sample is  $2.74 \text{ gcm}^{-3}$ . Difference in the densities may be attributed to different proportions of non –silica elements present in the two samples.

### A.2 Particle bed permeability

Permeability of the sample was determined using a constant-head permeameter following the British Standard (BS 1377-5:1990). After initial preparation of the sample, the assembly of the apparatus was done followed by imposition of constant head by setting of the outlet flow valve. The flow of water through the sample was set to be laminar. The volume of water through the sample in a known time was measured while the manometer gives the hydraulic gradient over the sample column. The coefficient of permeability ( $k$ ) was directly calculated using :

$$k = \left( \frac{q}{i} \right) \left( \frac{R_t}{A} \right) \quad (\text{A.1})$$

$q$  is the volumetric flow rate,  $i$  is the pressure head,  $A$  is the surface area of the particle bed and  $R_t$  is the temperature correction factor. Permeability coefficient is then converted to absolute permeability,  $K$ , by:

$$K = \left( \frac{k\mu}{\rho g} \right) \quad (\text{A.2})$$

where  $\mu$  is the fluid viscosity,  $\rho$  is the density and  $g$  is the acceleration due to gravity

Details of the results will be found in the Figure A.0. From the plot, it was discernible that the coarse medium had a higher permeability than the fine sample. The behaviours of the various proportions of the blend of coarse and fine samples also exhibit an interesting pattern where zero mark on the abscissa corresponds to 100% fine sample. As the percentage of the fine sample grows in the coarse, the permeability of the blend decreases but yet still maintains an edge over the fine sample value. However, at 75% proportion of the fine or 25 % of the coarse, the permeability value dips lowest getting even below the fine sample value. This is well marked on the curve and it can be explained by increasing level of heterogeneity

and tortuosity created by high quantity of fine grains interspersed in the coarse sample. So, the value returns higher at 100% fine sample i. zero mark, since there is higher homogeneity.



Figure A.9: Set up of constant-head permeameter for permeability experiment

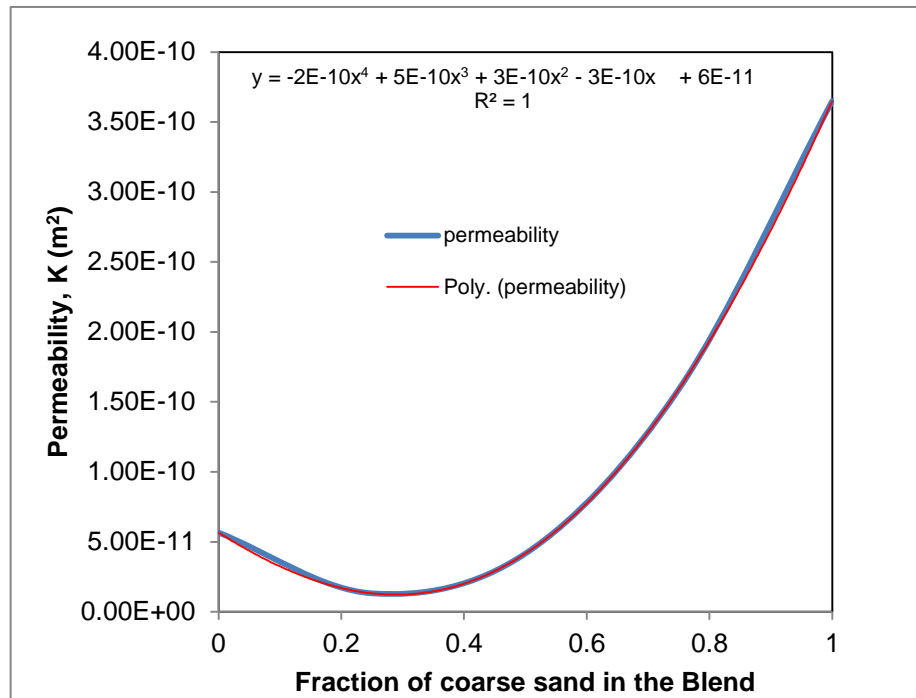


Figure A.10: Permeability of the sand blend

## APPENDIX B CALIBRATION OF TDR

### B.1 Time domain reflectometry

Time domain reflectometry (TDR) measures the propagation velocity of a step pulse with a bandwidth of around 20kHz to 1.5GHz (Heimovaara 1994). It is a broadband technique that produces a waveform composing of several frequencies. It is used in the telecommunications industry to identify locations of discontinuities in cables. The signal propagation velocity,  $V_s$ , as function of the cable relative permittivity along with a reflection at a point of discontinuity in a cable, allows the operator to determine locations of line breaks or other damage to cables using travel time ( $t$ ) analysis.

In addition to conductive loss, the velocity of the signal is primarily a function of the permittivity of the medium through which it travels. Figure B.1 is the waveform as the signal reaches the TDR probe head causing characteristic reflection peculiar to the surrounding medium. In Figure B.1, the starting dip in the reflection was caused by the electrical marker in the head of TDR probe enabling the software to locate the start point for travel time analysis.

#### B.1.1 Relative permittivity

The propagation velocity,  $V_p$ , is given by:

$$V_p = \frac{1}{\sqrt{\mu_0 \mu_r \epsilon_0 \epsilon_r}} = \frac{c}{\sqrt{\mu_r \epsilon_r}} \quad (\text{B.1})$$

where  $c$  is the velocity of light;  $3 \times 10^8$  m/s,  $\mu_r$  is the relative magnetic permeability,  $\mu_0$  is the magnetic permeability of vacuum ( $1.257 \times 10^{-6}$  H m<sup>-1</sup>),  $\epsilon_r$  is the relative permittivity.

A step voltage applied by a pulse generator, TDR100, powered via a datalogger, CR10X, sends a signal that travels through the connecting cable to the probe. The velocity of propagation to the probe rods and return reflection from probe end, as sampled by the TDR device in a perfect dielectric is given by:

$$v = \frac{2l}{t} \quad (\text{B.2})$$

$l$  is the waveguide length and  $t$  is the travel time.

Usually,  $V_p = \frac{c}{\sqrt{\epsilon_r}}$  ; as relative magnetic permeability,  $\mu_r$ , in most earth material is unity.

Thus, it can be can be written that;

$$t = \frac{2t\sqrt{\epsilon_r}}{c} \quad (\text{B.3})$$

In a soil, complex relative permittivity  $K^*$  results from conductive losses and is correlated as:

$$K^* = K' - i \left( K'' + \frac{\sigma_{dc}}{2\pi f \epsilon_0} \right) \quad (\text{B.4})$$

where,  $K'$  is the real part of the complex relative permittivity,  $i = \sqrt{-1}$  is an imaginary number,  $K''$  is the imaginary part of the relative permittivity due to polarization,  $\sigma_{dc}$  is the zero-frequency conductivity,  $f$  is frequency of the electromagnetic wave and  $\epsilon_0$  is the free-space permittivity. If the electric loss in the soil is small, then the imaginary part can be neglected (Topp et al. 1984) reducing equation B.4 to:

$$K^* = K' \quad (\text{B.5})$$

A measurement of  $K'$  in a soil with low electric loss within the mentioned frequency range therefore in theory becomes only a function of the soil components. In practice, however, effects of electric loss and the different frequencies in the frequency range influence measurements of  $K'$  to a small extent. Therefore a measured  $K'$  value is called the apparent relative permittivity and is denoted as  $K_a$ . The TDR-measured relative permittivity in soil is approximately a function only of the soil constituents. The lower the permittivity, the faster the speed of the signal at the same frequency.

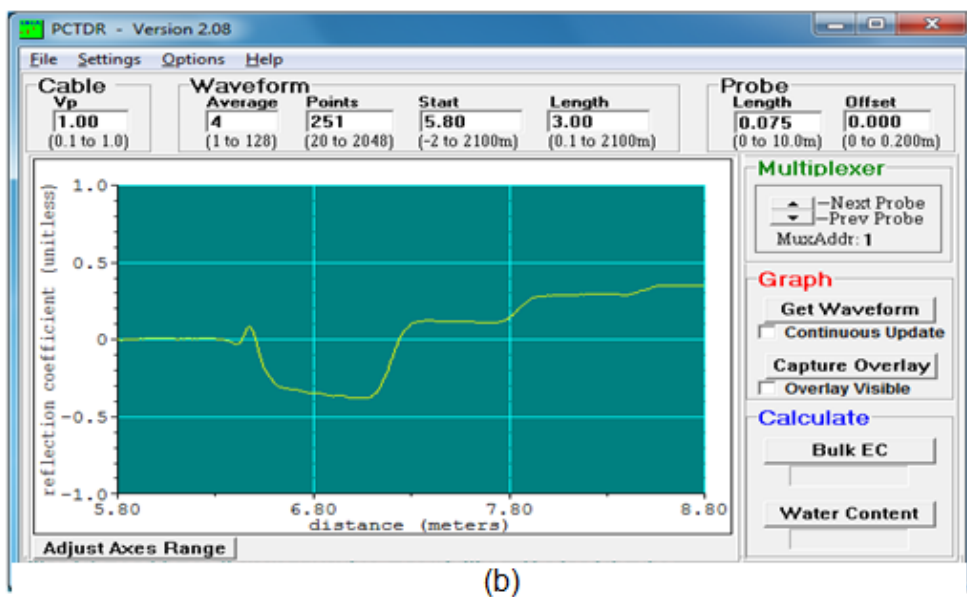
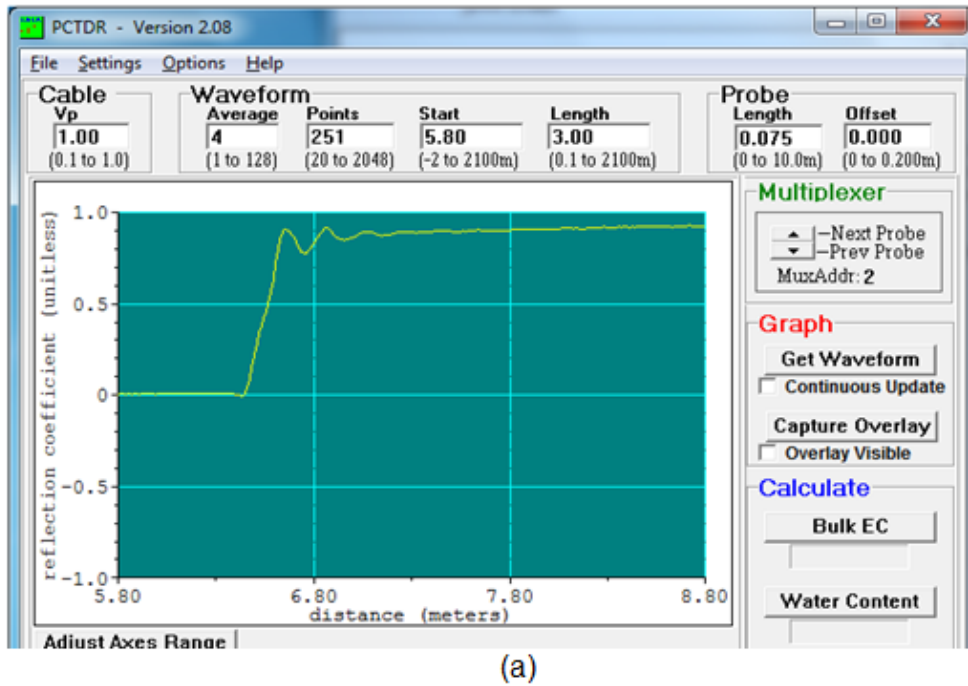


Figure B.1: Wave reflection in TDR probe visualised with PCTDR (a) in air, (b) in water

### B.1.2 Electrical conductivity (EC)

In addition to dielectric permittivity, TDR has the capacity to measure the electrical conductivity of the medium. The bulk electrical conductivity ( $\sigma_b$ ) at a given temperature depends on cell constant, or geometric factor ( $g$ ) of the probe conductor and is expressed as:

$$\sigma = \frac{1}{R_s g} \quad (\text{B.6})$$

$\sigma$  is the conductivity in Siemen/m ( $\Omega \text{ m}^{-1}$ ),  $R$  in ohm ( $\Omega$ ) and  $g$  in meter (m). Bulk soil EC leads to attenuation of the waveform which can limit the range in which permittivity can be measured and water content estimated.

### B.1.3 TDR calibration procedure

Water content measurement is hinged on the accurate measurement of the apparent permittivity of the medium. Getting travel time from the high quality waveform for permittivity determination is crucial and relies on the physical construction of the probes as well as the homogeneity of the dielectric material. In addition, the relaxation behaviour of the material had been identified as a factor. Calibrating in water or other suitable medium, analysis software like PCTDR can determine the travel time or distance by fitting tangents at the base of the hump emerging from the probe head to denote the start of the reflection in the probe. This is marked as the beginning of the mismatch between the impedance of the cable and the probe. Second reflection at the end of the sensor is also located by fitting tangents to the start of the rise of the reflection (see, Figure B.1). The mini-TDR probes (Campbell Scientific, Inc.) consist of three stainless-steel rods (7.5cm long) separated 8 mm at the probe head with epoxy between them as shown in Figure B.2.

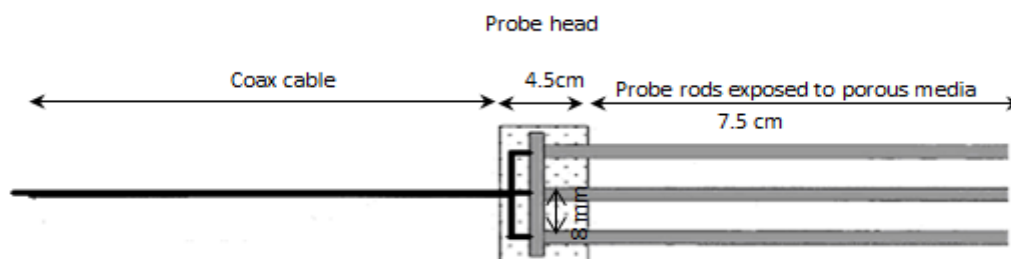


Figure B.2: A schematic overview of the mini-TDR with triple-rod probe and coax cable

The instrument used includes: SDMX50 multiplexer (Campbell Scientific Ltd. (CSL), Loughborough, UK), TDR100 unit (Campbell Scientific Ltd. (CSI), Loughborough, UK), CR10X Datalogger (Campbell Scientific Ltd. (CSL), Loughborough, UK), shielded coaxial interconnecting cable (Campbell Scientific Ltd. (CSI), Loughborough, UK), personal computer and 12-V Battery. The TDR100 contains the pulse generator for the signal applied to a TDR probe and also digitises the reflection and applies numerical algorithms for measuring volumetric water content or electrical conductivity. The CR10X is a fully programmable datalogger with robust ability for single-logger and network applications. The TDR100 communicates with the datalogger using SDM protocol or with a computer using PCTDR and serial communications. SDMX50 multiplexer serves as a hub of multiple connections of probes to the TDR100. The probe cable is connected to the SDMX50 multiplexer, which is then connected to the BNC connector of TDR100 unit by a shielded coaxial interconnecting cable. The photograph of the instruments and the interconnections is shown in Figure B.3.

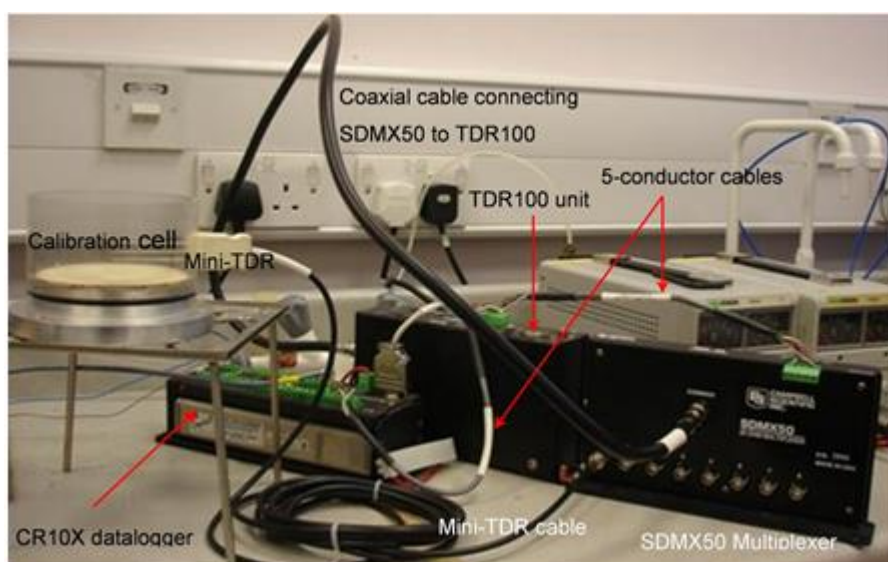


Figure B.3: TDR instruments and the interconnections

#### B.1.4 Probe offset determination

During initial characterization of the probes, the TDR100 unit, itself, is powered by 12 V battery source and is connected to computer running windows software PCTDR (Campbell Scientific Ltd. (CSL), Loughborough, UK) installed for automatic logging of the water content for single probe. The connection to the computer was made with 9-conductor cable using the RS232 port of the TDR100 unit. This port is used for communication between the computer and TDR100 unit. The characterisation is used to determine the window length, Start point or distance and the probe offset. It involves the following procedure:

The mini-TDR probe, connected to the SDMX50 multiplexer, which was also connected to the TDR100, was inserted into deionised water in a large open container with a minimum of 5cm from the container's wall. The temperature of the water was monitored with a thermocouple. The propagation velocity of the cable was set at 1.00, waveform point; 251, and average of 4.0 while the start point and window's length were initially set at 4.0m and 3.0m respectively. The probe length was entered and the offset was set 0.00 at this stage. Upon getting the waveform as shown in Figure B.1, the start point was adjusted to 5.8m to reflect the actual impedance change from the cable to the probe. Then, under the settings of the PCTDR menu, volume calibration was selected and La/L (apparent length to actual probe length) was picked for the calibration. The water content button was clicked. This gave the La/L result. Then, the menu option, "terminal emulation" was used to give results for the start and end indices. The apparent length was determined from the apparent permittivity of water corresponding to the temperature reading of the thermocouple as

$$\frac{L_a}{L} = \sqrt{K_a(T)} \quad (B.7)$$

Start and end distances determined from the indices by:

$$\text{Start}_{\text{distance}} = \frac{\text{Start}_{\text{index}}}{\text{datapoints} - 1} \times \text{Waveform length} \quad (B.8)$$

$$\text{End}_{\text{distance}} = \frac{\text{End}_{\text{index}}}{\text{datapoints} - 1} \times \text{Waveform length} \quad (B.9)$$

Above formulae were used in determining the probe offset as follows:

$$\text{Probe Offset} = \text{End}_{\text{distance}} - L_a - \text{Start}_{\text{distance}} \quad (B.10)$$

Table B.1 shows the offsets for the three different probes used in this experiment.

Table B.1: Probe Offset for the mini-TDR probes

	<b>Probe Offset (m)</b>	<b>Length (m)</b>
TDR1	0.029	0.075
TDR2	0.025	0.075
TDR3	0.023	0.075

### **B.1.5 Volumetric Water Correlation**

Following the determination of probe offset for the mini-TDR probes, the correlation for the saturation-permittivity relationship became necessary as an essential input in the datalogger programming for in-situ measurement of the saturation profile in the drainage experiment. After the offset determination, the TDR100 was powered from the CR10X datalogger, which itself was directly connected to a 12 V battery source using a short 5-conductor cable, while the 9-conductor cable was disconnected from the RS232 port of the TDR100 for that of CR10X.

When the TRD100 multivibrator switches states by any of the controlling programs, it generates a very short rise time electro-magnetic pulse that is applied to a coaxial SDM50 multiplexer which includes a mini-TDR probe. The electromagnetic wave travels along the rods and is reflected by the rod ends. This reflection provides feedback to switch the state of the multivibrator and initiate subsequent wave propagation on the rods. At the same time, the TDR100 unit samples and digitizes the resulting reflection waveform for analysis or storage. The elapsed travel time and pulse reflection amplitude contain information used by the on-board processor to quickly and accurately determine apparent distance for electrical conductivity of the media and fluid surrounding the probe rods and finally water content measurement. This information is sent to a datalogger or a PCTDR for waveform collection and water content measurement.

### **B.1.6 Data logger set up**

CR10X datalogger is a versatile and programmable controller used as a data processing, storage and management tool for the sensors used in this experiment. The datalogger must be programmed before it can make any measurement and communicate with any device connected to its serial I/O port. This program is a set of instructions entered in a program table and given an execution interval which determines how frequently a defined set of instructions is executed.

A program is created by entering it directly into the datalogger or on a computer using either of Campbell Scientific's programs Edlog or Short Cut. Short Cut is an easy to use program builder having a graphical interface which goes through the program building in four steps.

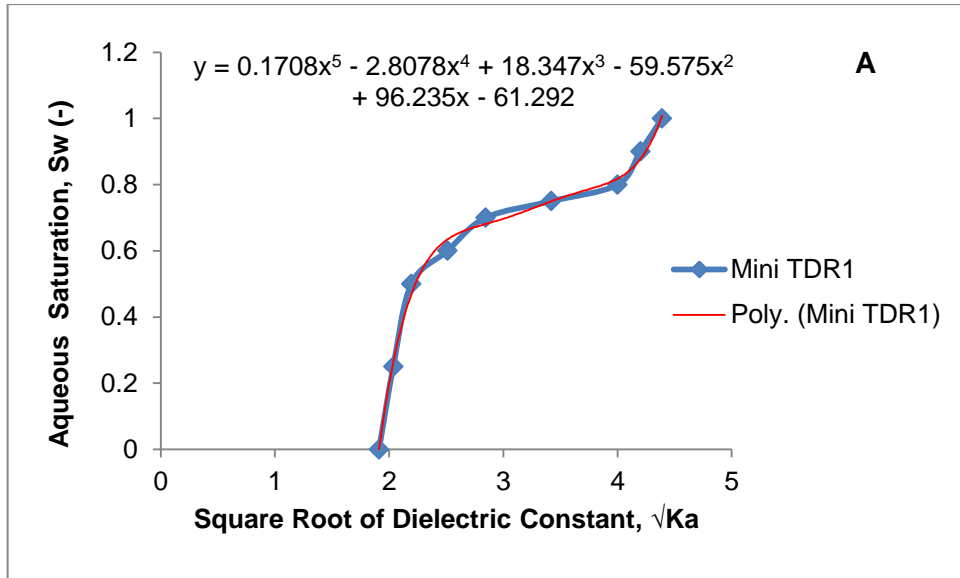
In this experiment, the program was created using a combination of Edlog and Short Cut. The program for the TDR100 measurements of water content and conductivity, battery voltage and system temperature were programmed using Edlog while pressure transducers

and thermocouple were imported from Short Cut. A sample program can be found in the APPENDIX D.

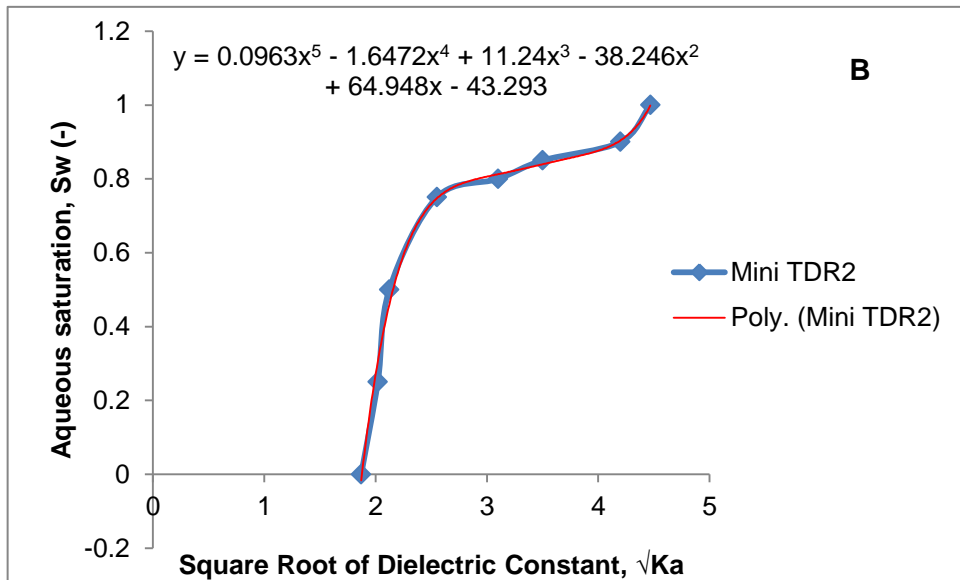
The multiplexer uses CSI's SDM communication protocols and may be controlled by the TDR100 unit via a computer running PCTDR software or a TDR100 instruction in CR10X datalogger programming for waveform collection in calibration measurements or automated measurements for two-phase flow, respectively. In this work, the LoggerNet 3.1 support software provides telecommunications, programming, data transfer, and data processing functions when multiplexer/TDR100 is controlled by CR10X datalogger. Mini-TDR probe calibration for correlation was done in a cell of 10 cm diameter and 4 cm height. The short cell was used to avoid water saturation inconsistencies that may arise due to the gravity segregation if a tall cell is used. If calibration is done in the taller experimental cell, it is likely that, for the two-phase mixture, water accumulates at the bottom and even distribution of both phases in porous media is not achieved. Therefore, mini-TDR probes do not read constant values. The gravity segregation effect may be more pronounced if the sample is left for a long time.

To start with, the cell is filled with a known amount of water and a pre-determined amount of sand is poured to the cell. Then vacuum is applied for 24 hours to take any possible trapped air out of the porous sample. Subsequently, the TDR100 unit is switched on and the mini-TDR probe readings are recorded with the datalogger.

Next, the water-saturated sand in the cell is replaced by the same mass of sand, fully saturated with oil and de-aired. Again, the datalogger records the data for this sample. These two measurements provide the limiting points for the calibration curve corresponding to 100% and 0% saturation points. Readings are then taken for different proportions of oil and water contents whilst the total mass of sand remains constant. This provides intermediate points on the calibration curve. The results of the calibration were correlated using Microsoft Excel data trending tool. Fifth order polynomial functions give good fits to these data points. These are displayed in Figure B.4 for three different mini-TDR probes while the coefficients are tabulated in Table B.2. The coefficients were implemented in the programming of the datalogger



(see the figure title after plot C)



(see the figure title after plot C)

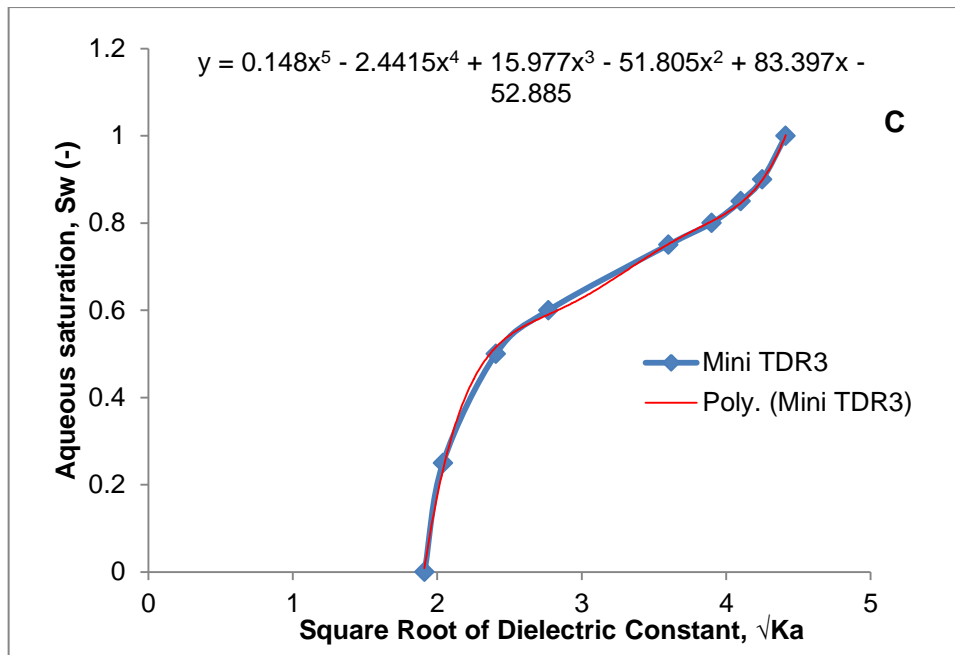


Figure B.4: Plots of aqueous saturation, ( $S_w$ ) against square root of relative permittivity,  $\sqrt{K_a}$ . (A) mini TDR1 (B) mini TDR2 (C) mini TDR3

Table B.2: Parameters for  $S_w$  calculation from fifth order polynomial equation ( $x = \sqrt{K_a}$ )

Probe	Probe Length (m)	Probe Offset (m)	Polynomial Coefficients					
			A	B (x)	C(x <sup>2</sup> )	D(x <sup>3</sup> )	E(x <sup>4</sup> )	F (x <sup>5</sup> )
TDR 1	0.075	0.029	61.292	96.235	59.575	18.347	2.8078	0.1708
TDR 2	0.075	0.025	43.293	64.948	38.246	11.24	1.6472	0.0963
TDR 3	0.075	0.023	52.885	83.397	51.805	15.977	2.4415	0.148

## APPENDIX C CALIBRATION OF THE PRESSURE TRANSDUCERS

In this work, pressure transducers (XTM 190, Kulite Semiconductor, New Jersey, USA) were used. The calibration was done using a portable pressure calibrator, DPI 610 (Druck Limited, Leicester, England) (shown in Figure C.1). Four wire connecting cable of the pressure transducers provides a full bridge circuit for datalogger programming. The LoggerNet 3.1 Support Software provides telecommunications, programming, data transfer, and data processing functions during calibration and through the experiment. The transducers were wired to the datalogger via the AM 16X32 device.

PV 411 pneumatic /hydraulic hand-pump (Druck Limited, Leicester, England) was used to generate the pressure for the calibration. Its scissor-action handles provide pneumatic pressure and vacuum generation while hydraulic pressure is generated in the hydraulic mode. The sensor was connected to the hand-pump, which was, itself, connected to the calibrator. In the hydraulic mode, the fluid reservoir was filled with appropriate fluid (Silicon oil, water or CO<sub>2</sub>) and screwed into the inlet port to complete the hydraulic circuit. Due to the high viscosity of the silicon oil (Basildon Chemicals, BDH, Oxford) used in this experiment (500 cSt) which exceeded the maximum working viscosity of the pump (22cSt), appropriate mineral based oil was substituted as the non-aqueous phase in the calibration. Vacuum priming was done to eliminate the air present in the pump, as its presence during the hydraulic operation cannot allow full pressure to be achieved owing to air compression. The system was vented to the reservoir using the selector valve and the pressure relief valve (PRV) was used to set the desired range of pressure.

Following priming, the selector valve was turned anticlockwise by one turn and the volume adjuster turned fully anticlockwise. Then the selector valve was closed while the initial pressure was generated using the scissor-action handles of the pump. The volume adjuster was later used to fine tune the appropriate pressure value while time was allowed for thermal stabilization. Voltage output in millibar was output, at each applied pressure on the Loggernet 3.1 and recorded automatically. The calibration was done stepwisely while equilibration was allowed between two steps or stages. After calibration, each transducer was immediately mounted on the cell, which was already filled with water to the transducer point, starting from the bottom, to avoid air infiltration of the membrane. Figure C.2 shows the graph of the plots of applied pressure to the output voltage together with polynomial fitting.

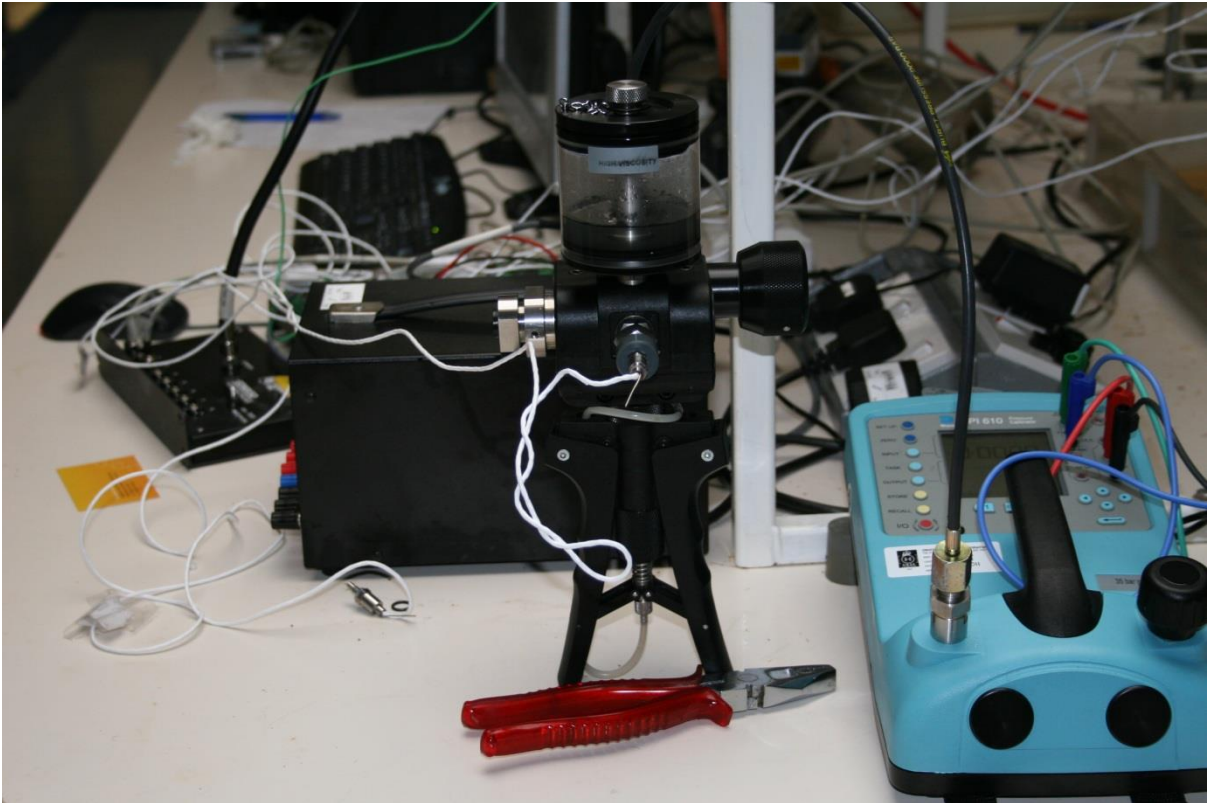


Figure C.1: DPI calibrator with pump used in the calibration of the pressure transducers.

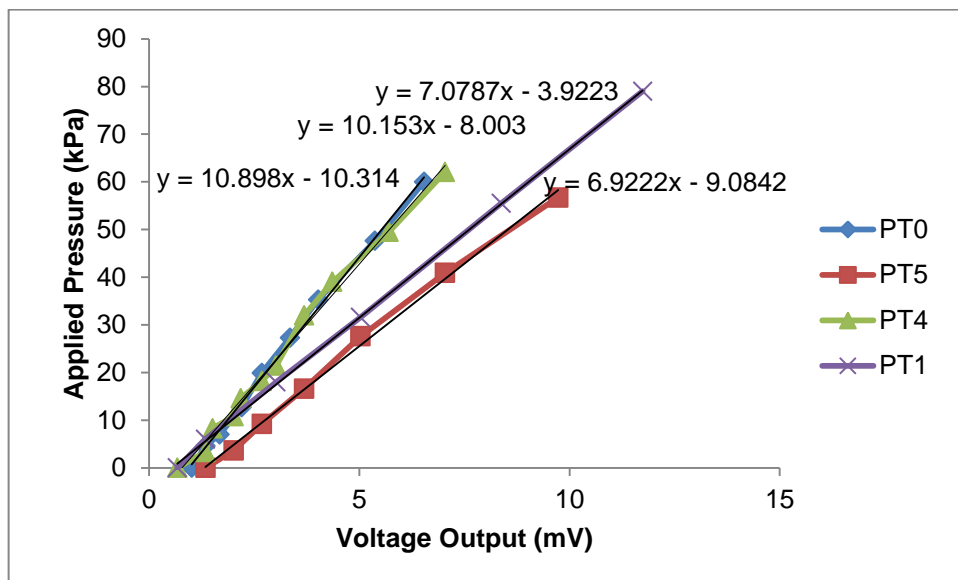


Figure C.2: Voltage output from the pressure transducers in response to the applied pressure (low-pressure pressure transducers)

**APPENDIX D SAMPLE DATALOGGER PROGRAM**

;{CR10X}

;

**\*Table 1 Program**

01: 10.000 Execution Interval (seconds)

**1: Batt Voltage (P10)**

1: 1 Loc [ BattV ]

**2: Internal Temperature (P17)**

1: 16 Loc [ DL\_Temp ]

**3: Do (P86)**

1: 45 Set Port 5 High

**4: Excitation with Delay (P22)**

1: 1 Ex Channel

2: 0 Delay W/Ex (0.01 sec units)

3: 15 Delay After Ex (0.01 sec units)

4: 0 mV Excitation

**5: Beginning of Loop (P87)**

1: 0 Delay

2: 8 Loop Count

**6: Do (P86)**

1: 74 Pulse Port 4

**7: Excitation with Delay (P22)**

1: 1 Ex Channel

- 2: 0 Delay W/Ex (0.01 sec units)
- 3: 1 Delay After Ex (0.01 sec units)
- 4: 0 mV Excitation

**8: Volt (Diff) (P2)**

- 1: 5 Reps
- 2: 35 2500 mV 50 Hz Rejection Range
- 3: 1 DIFF Channel
- 4: 4 -- Loc [ Diff\_V ]
- 5: 1.0 Multiplier
- 6: 0.0 Offset

**9: End (P95)****10: Beginning of Loop (P87)**

- 1: 0 Delay
- 2: 3 Loop Count

**11: Do (P86)**

- 1: 74 Pulse Port 4

**12: Excitation with Delay (P22)**

- 1: 1 Ex Channel
- 2: 0 Delay W/Ex (0.01 sec units)
- 3: 1 Delay After Ex (0.01 sec units)
- 4: 0 mV Excitation

**13: Thermocouple Temp (DIFF) (P14)**

- 1: 1 Reps

2: 31 2.5 mV 50 Hz Rejection Range  
3: 1 DIFF Channel  
4: 3 Type K (Chromel-Alumel)  
5: 16 Ref Temp (Deg. C) Loc [ DL\_Temp ]  
6: 3 -- Loc [ Temp\_C0 ]  
7: 1 Multiplier  
8: 0.0 Offset

**14: End (P95)****15: TDR100 Measurement (P119)**

1: 00 SDM Address  
2: 0 La/L for Water Content  
3: 2001 MMMP Mux & Probe Selection  
4: 4 Waveform Averaging  
5: 1 Vp  
6: 251 Points  
7: 6.5 Cable Length (meters)  
8: 3.0 Window Length (meters)  
9: 0.045 Probe Length (meters)  
10: 0.1907 Probe Offset (meters)  
11: 14 Loc [ La\_L2 ]  
12: 1 Multiplier  
13: 0.0 Offset

**16: TDR100 Measurement (P119)**

1: 00    SDM Address  
2: 3    Electrical Conductivity  
3: 2001    MMMP Mux & Probe Selection  
4: 4    Waveform Averaging  
5: 1    Vp  
6: 251    Points  
7: 6.5    Cable Length (meters)  
8: 3.0    Window Length (meters)  
9: 0.045    Probe Length (meters)  
10: 0.1907    Probe Offset (meters)

11: 15    Loc [ EC\_2    ]

12: 17.6345    Multiplier

13: 0.0    Offset

**17: Z=X\*F (P37)**

1: 8    X Loc [ DiffV\_4    ]

2: 0.0688    F

3: 17    Z Loc [ PT\_Isco    ]

**18: Do (P86)**

1: 55    Set Port 5 Low

**19: Do (P86)**

1: 10    Set Output Flag High (Flag 0)

**20: Real Time (P77)^16017**

1: 1220    Year,Day,Hour/Minute (midnight = 2400)

**21: Sample (P70)^30243**

1: 2 Reps

2: 14 Loc [ La\_L2 ]

**22: Sample (P70)^17476**

1: 1 Reps

2: 8 Loc [ DiffV\_4 ]

**23: Sample (P70)^15531**

1: 1 Reps

2: 3 Loc [ Temp\_C0 ]

**24: Sample (P70)^23235**

1: 1 Reps

2: 17 Loc [ PT\_Isco ]

**\*Table 2 Program**

02: 0.0000 Execution Interval (seconds)

**\*Table 3 Subroutines**

End Program

## APPENDIX E Numerical Simulation

### A Numerical Study of Dynamic Capillary Pressure Effect for Supercritical Carbon Dioxide-Water Flow in Porous Domain\*

Diganta B. Das<sup>#</sup>, Bhupinder S. Gill, Luqman K. Abidoye, Kamal Khudaida

Department of Chemical Engineering, Loughborough University, Loughborough LE11 3TU,  
Leicestershire

<sup>#</sup>Corresponding Author (Email: d.b.das@lboro.ac.uk)

#### Abstract

Numerical simulations for core-scale capillary pressure ( $P^c$ )–saturation (S) relationships have been conducted for a supercritical carbon dioxide-water system at temperatures between 35°C and 65°C at a domain pressure of 15 MPa as typically expected during geological sequestration of CO<sub>2</sub>. As the  $P^c$ -S relationships depend on both S and time derivative of saturation ( $\partial S/\partial t$ ) yielding what is known as the ‘dynamic capillary pressure effect’ or simply ‘dynamic effect’, this work specifically attempts to determine the significance of these effects for supercritical carbon dioxide-water flow in terms of a coefficient, namely dynamic coefficient ( $\tau$ ). The coefficient establishes the speed at which capillary equilibrium for supercritical CO<sub>2</sub>-water flow is reached. The simulations in this work involved the solution of the extended version of Darcy’s law which represents the momentum balance for individual fluid phases in the system, the continuity equation for fluid mass balance, as well as additional correlations for determining the capillary pressure as a function of saturation, and the physical properties of the fluids as a function of temperature. The simulations were carried for 3D cylindrical porous domains measuring 10 cm in diameter and 12 cm in height.  $\tau$  was determined by measuring the slope of a best-fit straight line plotted between (i) the differences in dynamic and equilibrium capillary pressures ( $P^{c,dyn} - P^{c,eq}$ ) against (ii) the time derivative of saturation ( $dS/dt$ ), both at the same saturation value. The results show rising trends for  $\tau$  as the saturation values reduce, with noticeable impacts of temperature at 50% saturation of aqueous phase. This means that the time to attain capillary equilibrium for the CO<sub>2</sub>-water system increases as the saturation decreases. From a practical point of view, it implies that the time to reach capillary equilibrium during geological sequestration of CO<sub>2</sub> is an important factor and should be accounted for while simulating the flow processes, e.g., to determine the CO<sub>2</sub> storage capacity of a geological aquifer. In this task, one would require

---

\* Das, D.B., Gill, B.S., Abidoye, L.K., and Khudaida, K.J., (2014). Numerical Simulation of Dynamic Effect in Capillary Pressure-Saturation Relationship for Supercritical Carbon dioxide-Water Flow in Porous Domain, *AIChE Journal*, 60(12), pp. 4266-4278, DOI: 10.1002/aic.14577

both the fundamental understanding of the dynamic capillary pressure effects for supercritical CO<sub>2</sub>-water flow as well as  $\tau$  values. These issues are addressed in this paper.